

Searching for ω -mesic state in Carbon

Inaugural-Dissertation zur Erlangung
des Doktorgrades der Naturwissenschaften
der Justus-Liebig-Universität Gießen
Fachbereich 07
(Mathematik und Informatik, Physik, Geographie)

vorgelegt von

Károly Makónyi
aus Mátészalka

II. Physikalisches Institut der
Justus-Liebig-Universität Gießen

June 21, 2011

Dekan: Prof. Dr. Bernd Baumann
1. Berichterstatter: Prof. Dr. Volker Metag
2. Berichterstatter: Prof. Dr. Alfred Müller
Tag der mündlichen Prüfung: 21. June 2011

Édesapámnak

Abstract

The existence of a bound pion-nucleus system has been experimentally demonstrated by embedding a charged pions in different nuclei like in a lead nucleus. This bound system, which is called deeply bound pionic atom, is held together by the interplay of Coulomb and strong interactions. This thesis concentrates on the investigation of the bound ω -mesic state in carbon nuclei. Since the ω meson does not carry an electric charge, this system, unlike the deeply bound pionic atoms, is governed by the strong interaction only. The study of such a system can lead to a better understanding of the basic meson-nucleus interaction.

In March 2007, an experiment was carried out at the **Elektronen-Stretcher-Anlage** (ELSA) in Bonn to observe bound mesic states in carbon. The photon beam used for the experiment was produced in a thin radiator via electron bremsstrahlung. The **Crystal Barrel** (CB), the **ForWard Plug** (FW-Plug) and the **Two Arm Photo-Spectrometer** (MiniTAPS) calorimeters provided an almost 4π coverage where the final-state photons were detected. The protons were identified with an aerogel Cherenkov detector and with the **Time-of-Flight** (TOF) technique.

A bound mesic nuclear state can only be produced if the participating meson has a small momentum. The momentum distribution of the produced ω s measured in this experiment showed that slow ω mesons can be produced in quasi-free photoproduction in coincidence with knocked-out protons that were registered in very forward direction. Based on this result, only such events were used for the further analysis where a proton was detected in the MiniTAPS forward wall.

Two reaction channels have been studied to explore bound ω mesons in nucleus:

In the first analysis the reaction channel has been studied in which the slow ω meson produces a resonance by being absorbed by a nucleon. In this case the produced resonance has to be slow as well and it can decay into a meson-nucleon pair - where the meson is either π^0 or η - with a relative angle of almost 180° between the decay products.

$$\gamma + {}^{12}\text{C} \rightarrow \omega + p \rightarrow N^* \rightarrow p + (\pi^0/\eta).$$

The kinematic constraints of this reaction channel and the possible background channels have been studied by using Monte Carlo simulations. These simulations have shown that reactions with a charged pion in the final state are the prominent background channels because the charged pions are misinterpreted as protons. Since these background channels have a much larger production yield than the bound ω -mesic state, this background might overwhelm the possible signal.

In the second analysis the neutral decay channel of the ω meson was investigated.

$$\gamma + {}^{12}\text{C} \rightarrow \omega + p + {}^{11}\text{B} \rightarrow \pi^0\gamma + p + {}^{11}\text{B} \rightarrow \gamma\gamma\gamma + p + {}^{11}\text{B}$$

If an ω meson decays into a π^0 and a photon and the π^0 decays further into two photons then the mass and energy of the ω can be reconstructed using the four-vectors of the final-state photons.

A bound state is indicated by an extra yield in the kinetic energy histogram at $E_{\pi^0\gamma} - m_{\omega}^{PDG} < 0$ MeV ($m_{\omega}^{PDG} = 782.65$ MeV/c² is the mass of the ω meson in vacuum, $E_{\pi^0\gamma}$ is the reconstructed energy of the $\pi^0\gamma$ system) together with an enhanced yield in the invariant mass histogram at $m_{\pi^0\gamma} < m_{\omega}^{PDG}$ ($m_{\pi^0\gamma}$ is the reconstructed invariant mass of the three registered photons if the invariant mass of two of them gives the mass of the π^0).

Using a simultaneous fit of the two distributions, the presence of a surplus of 83 ± 32 counts has been shown in the lowest momentum bin ($p_{\pi^0\gamma} \leq 300$ MeV/c) where the bound states were expected. The same kind of structure has not been observed either in the higher momentum bins or in the simulations where no bound state has been included.

Different backgrounds of this reaction channel have also been studied by means of Monte Carlo (MC) simulations. Based on the results of these simulations, kinematical cuts have been determined to reduce these background channels. Applying these cuts in the analysis of the measured data, a change has been found in the yields of the observed structure and of the quasi-free ω peak.

Theories predict a signature of the bound ω -mesic state in the kinetic energy distribution at $E_{\pi^0\gamma} - m_{\omega}^{PDG} \approx -60$ MeV. In this experiment no excess yield has been found in this region. An extra intensity has been, however, observed at $E_{\pi^0\gamma} - m_{\omega}^{PDG} \approx -100$ MeV where contributions from background channels are also expected although an effort has been made to suppress these background channels.

Nevertheless, the observed yield is comparable with the theoretical predictions (16 counts). In view of statistical and systematic uncertainties the experimentally registered yield of 83 ± 32 counts is considered as an upper limit. This yield corresponds to a differential cross section of $\approx 4 \mu\text{b}/\text{sr}$ for the incident photon energy range of $E_{\gamma} = 1250 - 3113$ MeV

This thesis has demonstrated that progress in the search for ω -mesic states requires two steps: a reference measurement on a LH₂ target to understand and control the background and improved experiment on carbon with higher statistics and a high resolution momentum measurement of the forward going proton.

Zusammenfassung

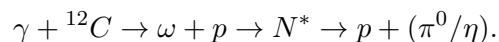
Gebundene Pion-Kern Zustände konnten experimentell durch den Einschluss von geladenen Pionen in verschiedene Kerne wie z.B. Blei nachgewiesen werden. Solche Zustände werden auch tiefgebundene pionische Atome genannt. Sie werden durch ein Zusammenspiel der Coulomb- und der starken Kraft zusammen gehalten. Der Schwerpunkt dieser Arbeit liegt in der Untersuchung von gebundenen ω -mesischen Zuständen in Kohlenstoff. Im Gegensatz zu den tiefgebundenen pionischen Atomen spielt hier nur die starke Kraft eine Rolle, da die ω Mesonen keine elektrische Ladung tragen. Das Ziel dieser Untersuchungen ist ein besseres Verständnis der grundlegenden Meson-Kern Wechselwirkung zu erlangen.

Das Experiment zur Untersuchung ω -mesischer Zustände in Kohlenstoff wurde an der Elektronen-Stretcher-Anlage (ELSA) in Bonn im März 2007 durchgeführt. Hierfür wurde ein energiemarkierter Photonenstrahl mit einer maximalen Energie von $E_\gamma = 2.9 \text{ GeV}$ verwendet, der über Bremsstrahlung Prozesse in einem dünnen Radiator erzeugt wurde. Das Detektorsystem bestehend aus den Kalorimetern Crystal Barrel (CB), ForWard Plug (FW-Plug) und Two Arm Photon-Spectrometer (TAPS) deckte nahezu den gesamten Raumwinkel von 4π ab und war damit ideal für den Nachweis der Photonen im Endzustand geeignet. Des Weiteren konnten Protonen mithilfe eines Cherenkov Detektors und über Flugzeitmessungen (Time-of-Flight, ToF) identifiziert werden.

Für die Erzeugung ω -mesischer Zustände muss das dazugehörige Meson langsam sein. Hier zeigte die im Experiment bestimmte Impulsverteilung, dass langsame ω Mesonen in quasi-freier Photoproduktion zusammen mit einem Rückstoß-Proton in Vorwärtsrichtung erzeugt werden. Daher wurden in der Analyse nur Ereignisse verwendet, bei denen das Proton im TAPS Detektor nachgewiesen wurde.

Im Rahmen dieser Arbeit wurden zwei verschiedene Reaktionskanäle zur Erzeugung gebundener ω -mesischer Zustände untersucht.

Im ersten Fall wurde der Reaktionskanal untersucht, bei dem das langsame ω Meson von einem Nukleon absorbiert wird und eine Resonanz erzeugt:



Die so erzeugte Resonanz ist ebenfalls langsam und kann in ein Meson-Nukleon Paar zerfallen mit einem relativen Winkel von etwa 180° zwischen den beiden Zerfallsprodukten. Die kinematischen Randbedingungen dieses Reaktionskanals sowie möglicherweise beitragende Untergrundkanäle wurden wiederum mit Monte Carlo Simulationen untersucht. Hier zeigte sich, dass Reaktionen mit geladenen Pionen im Endzustand durch Misidentifizierung als Protonen einen großen Beitrag zum Untergrund liefern. Da die Produktionsquerschnitte der Untergrundkanäle sehr viel größer sind als der Produktionsquerschnitt von gebundenen ω -mesischen Zuständen besteht die Möglichkeit, dass das Signal von den Untergrundbeiträgen überdeckt wird.

Diese Arbeit zeigt, dass für einen Fortschritt in der Suche nach ω -mesischen Zuständen zwei Schritte notwendig sind: eine Referenzmessung am LH_2 Target, um den Untergrund zu verstehen und besser kontrollieren zu können und ein verbessertes Experiment am Kohlenstoff Target mit einer höheren Statistik sowie einer Impulsmessung der Protonen in Vorwärtsrichtung mit sehr guter Auflösung.

Im zweiten Fall wurde der neutrale, hadronische Zerfallskanal des ω Mesons untersucht:

$$\gamma + {}^{12}\text{C} \rightarrow \omega + p + {}^{11}\text{B} \rightarrow \pi^0\gamma + p + {}^{11}\text{B} \rightarrow \gamma\gamma\gamma + p + {}^{11}\text{B}$$

Dabei wurde die invariante Masse des ω Mesons durch die Vierervektoren der drei Photonen im Endzustand rekonstruiert. Bei einem gebundenen Zustand würde man zusätzliche Intensität sowohl in der kinetischen Energie als auch in der invarianten Masse erwarten:

$$E_{\pi^0\gamma} - m_{\omega}^{PDG} < 0 \text{ MeV} \quad \text{und} \quad m_{\pi^0\gamma} < m_{\omega}^{PDG}$$

Hierbei ist $m_{\omega}^{PDG} = 782.65 \text{ MeV}/c^2$ die ω Meson Masse im Vakuum, $E_{\pi^0\gamma}$ die rekonstruierte Energie des $\pi^0\gamma$ -Systems und $m_{\pi^0\gamma}$ die rekonstruierte invariante Masse. Ein gleichzeitiger Fit der beiden Verteilungen lieferte eine Erhöhung von 83 ± 32 Ereignissen im niedrigsten Impulsbereich $p_{\pi^0\gamma} \leq 300 \text{ MeV}/c$. Dies ist der Bereich, für den gebundene Zustände vorhergesagt werden. Im Vergleich dazu konnten weder bei höheren Impulsen noch in Simulationen, für die keine gebundenen Zustände angenommen wurden, zusätzliche Intensität nachgewiesen werden.

Außerdem wurden Monte Carlo (MC) Simulationen benutzt, um die verschiedenen beitragenden Untergrundkanäle zu untersuchen. Daraus resultierten kinematische Schnitte, die die Untergrundbeiträge reduzierten. Dabei hatte sich allerdings auch die Ausbeute der beobachteten Struktur und des quasi-freien ω Signals reduziert.

Theoretische Rechnungen sagen einen gebundenen ω -mesischen Zustand bei einer Energie von $E_{\pi^0\gamma} - m_{\omega}^{PDG} \approx -60 \text{ MeV}$ mit etwa 16 Ereignissen unter den gegebenen Bedingungen des Experiments voraus. Dies konnte im Rahmen dieser Arbeit nicht verifiziert werden. Die experimentell beobachtete Struktur liegt bei $E_{\pi^0\gamma} - m_{\omega}^{PDG} \approx -100 \text{ MeV}$. Leider erwartet man an dieser Position ebenfalls Beiträge der Untergrundkanäle.

Zusammenfassend sind die theoretischen Vorhersagen vergleichbar mit dem experimentell erzielten Ergebnis. Angesichts der statistischen und systematischen Unsicherheiten ist das experimentelle Resultat von 83 ± 32 Ereignissen als obere Grenze anzusehen. Dies entspricht einem differentiellen Wirkungsquerschnitt von $\approx 4 \mu\text{b}/\text{sr}$ für Einschussenergien im Bereich $E_{\gamma} = 1250 - 3113 \text{ MeV}$.

Diese Arbeit zeigt, dass für einen Fortschritt in der Suche nach ω -mesischen Zuständen zwei Schritte notwendig sind: eine Referenzmessung am LH_2 Target, um den Untergrund zu verstehen und besser kontrollieren zu können und ein verbessertes Experiment am Kohlenstoff Target mit einer höheren Statistik sowie einer Impulsmessung der Protonen in Vorwärtsrichtung mit sehr guter Auflösung.

Contents

Abstract	v
1. Introduction	1
1.1. A historical timeline	2
1.2. The Standard Model	4
1.2.1. Forces of the Standard Model	4
1.2.2. Particle Zoo of the Standard Model	5
1.3. Hadrons	6
1.3.1. Mesons	7
1.3.2. Baryons	7
1.4. Hadrons in a medium	8
1.4.1. Chirality	9
1.4.2. Hadron properties in the nuclear medium	12
1.4.3. Former experiments	15
1.5. Bound ω -mesic states and the Crystal-ELSA/TAPS experiment	19
1.5.1. Bound ω -mesic states	19
1.5.2. Searching for bound ω -mesic states at the ELSA	21
2. Experimental setup	25
2.1. The accelerator and the beamline	26
2.1.1. The electron beam	26
2.1.2. γ -beam	28
2.1.3. The tagging system	29
2.1.4. Beam dump	30
2.1.5. The target	30
2.1.6. γ intensity monitor	31
2.2. The CB-MiniTAPS experiment	31
2.2.1. The Crystal Barrel detector	32
2.2.2. The Inner Detector	33
2.2.3. Forward Plug	34
2.2.4. The MiniTAPS detector	34
2.3. The aerogel Cherenkov detector	37
2.4. Electronics and data acquisition system	37
2.4.1. The tagger	37
2.4.2. The Crystal Barrel	38
2.4.3. The Inner Detector	38
2.4.4. The MiniTAPS	39
2.5. Trigger	40
2.5.1. First-level trigger	40

2.5.2.	Second-level trigger	41
2.5.3.	Stand-alone trigger	41
2.6.	Parameters during the experiment	41
3.	Data analysis	43
3.1.	Calibration	44
3.1.1.	Time calibration	44
3.1.2.	Energy calibration of the tagger	46
3.1.3.	Energy calibration of CB and MiniTAPS	48
3.1.4.	LED calibration	56
3.2.	Reconstruction of primary particles, mesons and reactions	57
3.2.1.	Reconstruction of the energy of primary particles	57
3.2.2.	Reconstruction of primary particles	59
3.2.3.	Suppressing random time coincidences	64
3.2.4.	PEDs and preselection	66
3.2.5.	Identification of the reaction	68
3.3.	Offline analysis chain	71
3.3.1.	Kinematical cuts on the neutral decay channel of the ω meson	71
3.4.	Simultaneous fit of the $m_{\pi^0\gamma}$ and the $E_{\pi^0\gamma}-m_{\omega}^{PDG}$ distributions	74
3.5.	Simulation	75
3.5.1.	Simulation of the kinematics	76
3.5.2.	Particle tracking with GEANT	78
3.5.3.	Event generators	80
3.5.4.	Background channels of the neutral decay channel of the ω meson	82
3.5.5.	Background rejection techniques	86
3.5.6.	Simulation of the conversion channels	90
3.6.	Detection efficiency	95
3.6.1.	Determining the detection efficiency	97
4.	Results and discussion	99
4.1.	Momentum distribution of the photo-produced ω mesons	100
4.2.	Searching for bound ω -mesic states	101
4.2.1.	Back-to-back analysis	101
4.2.2.	Study of the kinetic energy distribution (Marco-Weise analysis)	103
4.2.3.	Conclusion	110
	Frequently Used Abbreviations	115
	Appendices	
	A. Quantum numbers	117
	B. Trigger-scheme of the MiniTAPS	119
	C. Parameters during the experiment	121
	D. Calibration	123
D.1.	π^0 -calibration	123

D.2. η -calibration	123
D.2.1. η calibration in the Crystal Barrel/Forward Plug detectors	123
D.2.2. η calibration in MiniTAPS	124
D.3. Fine-tuning of the π^0 calibration	125
E. The kinematics of two-body reactions	127
E.1. Solution I.	127
E.1.1. Calculation of p_{nucleon}	128
E.1.2. Calculation of the momentum vector of the meson	128
E.2. Solution II.	129
F. An explanation for the structures on the 3-gamma invariant mass spectrum of the $\pi^0\eta$ channel	131
G. Simulated background channels	135
H. Kinematical Cuts and Background Rejection	143
Bibliography	149

1. Introduction

Contents

1.1. A historical timeline	2
1.2. The Standard Model	4
1.2.1. Forces of the Standard Model	4
1.2.2. Particle Zoo of the Standard Model	5
1.3. Hadrons	6
1.3.1. Mesons	7
1.3.2. Baryons	7
1.4. Hadrons in a medium	8
1.4.1. Chirality	9
1.4.2. Hadron properties in the nuclear medium	12
1.4.3. Former experiments	15
1.5. Bound ω-mesic states and the Crystal-ELSA/TAPS experiment	19
1.5.1. Bound ω -mesic states	19
1.5.2. Searching for bound ω -mesic states at the ELSA	21

Chapter summary

According to the presently accepted theory of subatomic particles (the **Standard Model** of Particle Physics (SM)), all processes in nature can be explained by four fundamental forces, namely, the electromagnetic, the weak, the strong and the gravitational force. The interaction between particles is mediated via exchange bosons.

1.1. A historical timeline

Richard Feynman once observed that if one had to reduce the scientific history into one sentence, the statement would be: “All things are made of atoms” [Bry04].

- Around 460 B.C. a Greek philosopher, Democritus, developed the idea of atoms. He asked the question: “If one breaks a piece of matter in half, and then break it in half again, how many breaks will you have to make before you can break it no further?”. Democritus believed that it ended at some point, a smallest possible bit of matter. He called these basic matter particles atoms¹. These atoms were all composed of the same primary matter with the only differences between them being their size, shape and weight. The differences in these characteristics explained the differences in the properties of matter.

Unfortunately, the atomic idea of Democritus had no lasting effects on other Greek philosophers, including Aristotle who dismissed the atomic idea as worthless.

- In the 1800’s, an English chemist, John Dalton performed experiments with various chemicals that showed that matter seems to consist of particles (atoms). Dalton is usually credited for developing the first coherent atomic theory.

Dalton’s theory can be summarized as follows:

- Matter is composed of small particles called atoms.
 - All atoms of an element are identical, but are different from those of any other element.
 - During chemical reactions, atoms are neither created nor destroyed, but are simply rearranged.
 - Atoms always combine in whole number multiples of each other (law of multiple proportions).
- In 1869, the Russian chemist Dmitri Mendeleev constructed a classification, which grouped all of the chemical elements known at that time according to their chemical properties. This is known as the Periodic Table of elements. This table later served to methodically classify all of the atoms, both natural and man made, by their atomic number².
 - In the 19th century, an important physical theory arose assuming the existence of atoms: the kinetic theory. This theory states that gases are made up of a large number of small particles, being in constant random motion.
 - In 1897, the English physicist J.J. Thomson discovered the electron and proposed a model for the structure of the atom. He postulated the first atom model, in which electrons with a negative charge are homogeneously embedded inside the positively charged atom.
 - In 1911, Ernest Rutherford performed scattering experiments of α particles on a thin gold foil. In most of the cases the particles penetrated the target foil without changing direction, but some deflected up to 180° . Based on this result Thomson’s atom model had to be revised. The new model of the atom was a tiny positively charged nucleus containing the major fraction of the mass (responsible for the large scattering angles). The space between the nuclei, which is large compared to size of the nuclei, is filled by a negatively charged

¹from the Greek “indivisible”

²The atomic number is also known as proton number.

electron cloud. Rutherford thought that the negative electrons orbited a positive center in a manner like the solar system where the planets orbit the sun.

- According to the theory of electricity and magnetism it was predicted that opposite charges attract each other and the electrons in the atom should gradually lose energy and spiral inward. This was contradicting Rutherford's model. In 1912, a Danish physicist, Niels Bohr came up with a theory which said that the electrons do not spiral into the nucleus. He came up with two rules that agreed with experiment:
 - Electrons in an atom can orbit only at certain allowed distances from the nucleus.
 - Atoms radiate energy when an electron jumps from a higher-energy orbit to a lower-energy orbit. Also, an atom absorbs energy when an electron gets boosted from a low-energy orbit to a high-energy orbit
- On this footpath, quantum mechanics, including the concept of anti-particles and the interpretation of the wave function as probability amplitude for its location, was developed by W. Heisenberg, P. M. A. Dirac and many others.
- In the 1940's and 50's, consistent relativistic quantum theory of charged particles was developed by R. Feynman, J. Schwinger and S. Tomonaga (**Quantum ElectroDynamics (QED)**).
- The nucleus contains most of the atom's mass as well as the positive charge. The protons supposedly accounted for this mass. However, a nucleus with twice the charge of another should have twice the number of protons and twice the mass. But this did not prove to be correct.

Rutherford speculated in 1920 that there existed electrically neutral particles that make up the missing mass but no one accepted his idea at the time. Not until 1932, when the English physicist James Chadwick finally discovered the neutron. He found it to be slightly heavier than the proton with a mass of 1840 electrons and with no charge. The proton and neutron together, received the name, "nucleon".

- In 1935, a Japanese physicist, Hideki Yukawa suggested that exchange forces might describe the strong force between nucleons which explains the stable nuclei in spite of the positive charge of proton. Yukawa used Heisenberg's uncertainty principle to explain that a virtual particle could exist for only a short time. He calculated that these particles must be about 250 times heavier than an electron. Later, in 1947, the physicist Cecil F. Powell detected this particle and called it the "pion".
- In the 1950's and 60's, new powerful particle accelerators were built and physicists discovered many more new particles. The various types of particles needed a new theory to explain their strange properties. In 1960, Murray Gell-Mann and Yuval Ne'emann independently proposed a method for classifying all the particles known at that time. The method became known as the *Eightfold Way*. What the periodic table did for the elements, the Eightfold Way did for the particles. In 1964, Gell-Mann went further and proposed the existence of a new level of elementary particles and called them quarks³. Well-established particles like protons, neutrons or pions were no longer seen as elementary. They are representatives of a family of particles called hadrons⁴. Hadrons are composite systems made of quarks. This

³The spelling derives from a phrase in James Joyce's book, *Finnegans Wake*, "Three quarks for Muster Mark".

⁴from the Greek "thick"

family of particles can be subdivided into two groups: mesons⁵ and baryons⁶. Mesons are made of a quark-antiquark pair, while baryons have a three-quark substructure.

Within this ordering scheme, the existence and the properties of the Ω^- baryon was predicted, which later was found providing evidence for the quark model.

- Similarly to QED, a theory can be established to describe the interaction of quarks with each other. This theory is called **Quantum Chromodynamics (QCD)**.
- The Standard Model of subatomic particles (SM) combines all the findings described above to provide a consistent picture of the structure of matter.

1.2. The Standard Model

The Standard Model of particle physics is a unified theory of the electromagnetic, weak and strong nuclear interactions which mediate the dynamics of the known subatomic particles. Developed throughout the early and middle 20th century, the current formulation was finalized in the mid-1970's upon experimental confirmation of the existence of quarks. Since then, discoveries of the bottom quark [H⁺77], the top quark [A⁺95] and the tau neutrino [K⁺01] have given credence to the Standard Model.

1.2.1. Forces of the Standard Model

1. Electroweak force

In particle physics, the electroweak interaction is the unified description of two of the four fundamental interactions of nature: electromagnetism and the weak interaction. Although these two forces appear very different at low energies, the theory models them as two different aspects of the same force. Above the unification energy, of the order of 100 GeV, they would merge into a single electroweak force. Thus if the universe is hot enough (approximately 10^{15} K, a temperature reached shortly after the Big Bang) then the electromagnetic force and weak force will merge into a combined electroweak force.

For contributions to the unification of the weak and electromagnetic interaction between elementary particles, A. Salam, S. Glashow and S. Weinberg were awarded the Nobel Prize in Physics in 1979. The existence of the electroweak interactions was experimentally established in two stages: the first being the discovery of neutral currents in neutrino scattering by the Gargamelle collaboration in 1973 [HFK⁺73], and the second in 1983 by the UA1 and the UA2 collaborations that involved the discovery of the W^\pm and Z^0 gauge bosons in proton-antiproton collisions at the **Super Proton Synchrotron (SPS)** [A⁺81, A⁺83a, A⁺83b].

- **Electromagnetic Force**

One of the four fundamental forces, the electromagnetic force manifests itself through the forces between electromagnetic charges (Coulomb's law) and the magnetic force, both of which are summarized in the Lorentz force law. Fundamentally, both magnetic and electric forces are manifestations of an exchange force involving the exchange of photons. The quantum approach to the electromagnetic force is called QED. The electromagnetic force is a force of infinite range which obeys the inverse square law.

⁵from the Greek "Intermediate"

⁶derived from the Greek "Heavy"

The electromagnetic force holds atoms and molecules together. On atomic scale the forces of electric attraction and repulsion of electric charges are so dominant over the other three fundamental forces that they can be considered to be negligible as determiners of atomic and molecular structure.

- **Weak Force**

One of the four fundamental forces, the weak interaction involves the exchange of the intermediate vector bosons, the W^\pm and the Z^0 . Since the mass of these particles is on the order of 80 GeV, the uncertainty principle dictates a range of about 10^{-18} meters which is about 0.1% of the diameter of a proton. The weak interaction is able to change one flavor of quark into another⁷. The weak interaction is the only process in which a quark can change to another quark, or a lepton to another lepton - the so-called “flavor changes”. The weak interaction acts between both quarks and leptons, whereas the strong force does not act between leptons.

The discovery of the W^\pm and Z^0 particles in 1983 was hailed as a confirmation of the theories connecting the weak force to the electromagnetic force in electroweak unification.

2. Strong Force

The force that can hold a nucleus together against the enormous forces of the electromagnetic repulsion of the protons is strong indeed. However, it is not an inverse square force like the electromagnetic force and it has a very short range. Yukawa modeled the strong force as an effective exchange force in which the exchange particles are pions and other heavier particles. The range of a particle exchange force is limited by the uncertainty principle. It is the strongest of the four fundamental forces on the sub-atomic level.

Protons and neutrons, which make up the nucleus, are considered to be made up of quarks, and the quarks are considered to be held together by the strong interaction. The force between nucleons may be considered to be a residual strong color force. In the Standard Model, therefore, the basic exchange particle is the gluon which mediates the forces between quarks. Since the individual gluons and quarks are contained within the proton or neutron, the masses attributed to them cannot be used to predict the range of the force. When something is viewed as emerging from a proton or neutron, then it must be at least a quark-antiquark pair, so it is then plausible that the pion as the lightest meson should serve as a predictor of the maximum range of the strong force between nucleons.

1.2.2. Particle Zoo of the Standard Model

According to the SM, in nature 61 elementary particles exist (see Table 1.1) and all the observed universe is constructed by them⁸. These are the 12 exchange bosons (8 gluons, W^\pm , Z^0 and the photon), the Higgs boson⁹ and 6 leptons and 6 quarks (with corresponding anti-particles). In addition the quarks carry color charge. This leads to a total of: 12 exchange bosons + Higgs boson + 6*2 leptons + 6*3*2 quarks = 61 particles.

⁷In fact, only the W^\pm boson has any role in the flavor changing of the quarks.

⁸Recently, the cosmic microwave background measurements suggests that the universe originated from the Standard Model (Hadronic Matter) makes only 4% of the whole universe. The rest is filled by Dark Matter and Dark Energy.

⁹The existence of the Higgs boson is experimentally not confirmed yet.

Particle	spin	b	l	I	I_Z	S	C	B	charge (e)	m_0 (MeV)
u	1/2	1/3	0	1/2	1/2	0	0	0	+2/3	5
d	1/2	1/3	0	1/2	-1/2	0	0	0	-1/3	9
s	1/2	1/3	0	0	0	-1	0	0	-1/3	175
c	1/2	1/3	0	0	0	0	1	0	+2/3	1350
b	1/2	1/3	0	0	0	0	0	-1	-1/3	4500
t	1/2	1/3	0	0	0	0	0	0	+2/3	173000
e^-	1/2	0	1	0	0	0	0	0	-1	0.511
μ^-	1/2	0	1	0	0	0	0	0	-1	105.658
τ^-	1/2	0	1	0	0	0	0	0	-1	1777.1
ν_e	1/2	0	1	0	0	0	0	0	0	0(?)
ν_μ	1/2	0	1	0	0	0	0	0	0	0(?)
ν_τ	1/2	0	1	0	0	0	0	0	0	0(?)
γ	1	0	0	0	0	0	0	0	0	0
gluon	1	0	0	0	0	0	0	0	0	0
W^+	1	0	0	0	0	0	0	0	+1	80220
Z	1	0	0	0	0	0	0	0	0	91187

Table 1.1.: An overview of particles and antiparticles. Here, b is the baryon number and l the lepton number. There are three different lepton numbers, one for e , μ and τ , which are separately conserved. I is the isospin, with I_Z the projection of the isospin on the third axis, S the strangeness, C the charmness and B the bottomness. The antiparticles have an opposite charge. The existence of all elementary particles, but the Higgs-boson, has been demonstrated experimentally.

1.3. Hadrons

Strongly interacting particles which are made of quarks and/or anti-quarks are called *hadrons*. Up to now, only colorless (“white”) particles are observed in nature. In analogy to the color theory, color neutral particles can be obtained either by quark - anti-quark ($q\bar{q}$) states where one quark carries one type of color and the other one carries the corresponding anti-color, or by qqq (and $\bar{q}\bar{q}\bar{q}$) where all the quarks have different colors. The $q\bar{q}$ states are called *mesons*, the qqq states are the *baryons*.

There are other possibilities to produce colorless particles. Exotic baryons have more than just the three quarks like in ordinary baryons and exotic mesons do not have one quark and one antiquark structure like ordinary mesons but also gluons contributing directly to the quantum number of the system. Exotic baryons like the pentaquark (like the $\Theta^+(1540)$ which was seen in some experiment while others experiments gave null-result) [Hic05] or the tetraquark (like the $X(3872)$ which was seen in the BELLE and BABAR experiments [C⁺03, AHA10]) are under debate. The existence of exotic mesons like glueballs¹⁰ (for example the $f_0(1540)$ which was seen by the LEAR collaboration with the Crystal Barrel detector) or hybrids¹¹ are neither widely accepted.

¹⁰Glueballs [Cre09, CP98] solely consists of gluon particles, without valence quarks. Such a state is possible because gluons carry color charge and experience the strong interaction.

¹¹Hybrid mesons consist of bound states of quarks and gluons, where the gluons contribute directly to the quantum numbers of the system (valance glue).

1.3.1. Mesons

The mesons are strongly interacting particles made of a pair of a quark and an anti-quark ($q\bar{q}$). The large number of observed hadronic states required the classification of those states. M. Gell-Mann (and independently Y. Ne'eman) made classification of these particles according to their quantum numbers. Considering only the 3 lightest quarks u, d, s the mesonic states can be described within a $3 \otimes 3$ symmetry.

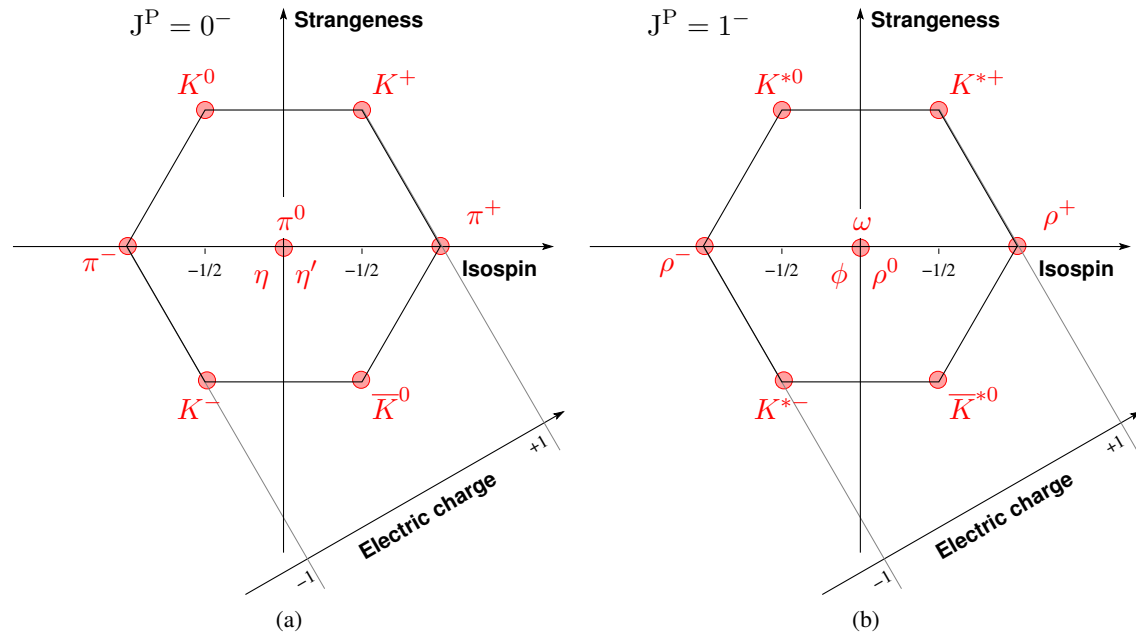


Figure 1.1.: The lightest pseudoscalar (a) and vector mesons (b) are listed, classified according to their isospin I_3 , strangeness S and electric charge.

First, it is assumed that quarks in the mesons have no relative orbital momentum ($L = 0$). Because quarks and anti-quarks have opposite intrinsic parity, the constructed mesons have parity $-1^{L+1} = -1$ (see Appendix A). The spin of the quarks determine the spin of the meson. They add up and result in $S = 1$ or they can be opposite and result in $S = 0$. The $J^P = 0^-$ states are called *pseudoscalar mesons* and the $J^P = 1^-$ states are called *vector mesons* (see Figure 1.1). Concentrating only on the three lightest quarks, 9 possible states can be formed. Using group theory, these 9 states can be split up into an octet and a singlet state ($3 \otimes 3 = 8 \oplus 1$). Due to very similar masses $u\bar{u}$, $d\bar{d}$ and $s\bar{s}$ states can mix with each other. The u and d quarks have smaller mass than the s quark, consequently the mixing of $s\bar{s}$ with $u\bar{u}$ or $d\bar{d}$ is smaller than the mixing of $u\bar{u}$ and $d\bar{d}$.

1.3.2. Baryons

Baryons, qqq states, can be arranged in a similar way as the mesons (see Figure 1.2). The increasing number of possible combinations of the three quarks, however, results in a richer spectrum of baryonic states. Again only the lightest three quarks will be considered where the orbital angular momentum of the quarks relative to each other is $L = 0$. The total baryonic spin results from adding the individual quark spins and must be either $S = 1/2$ or $S = 3/2$ and the total angular momentum of the baryon is (J) is the total spin of the three quarks.

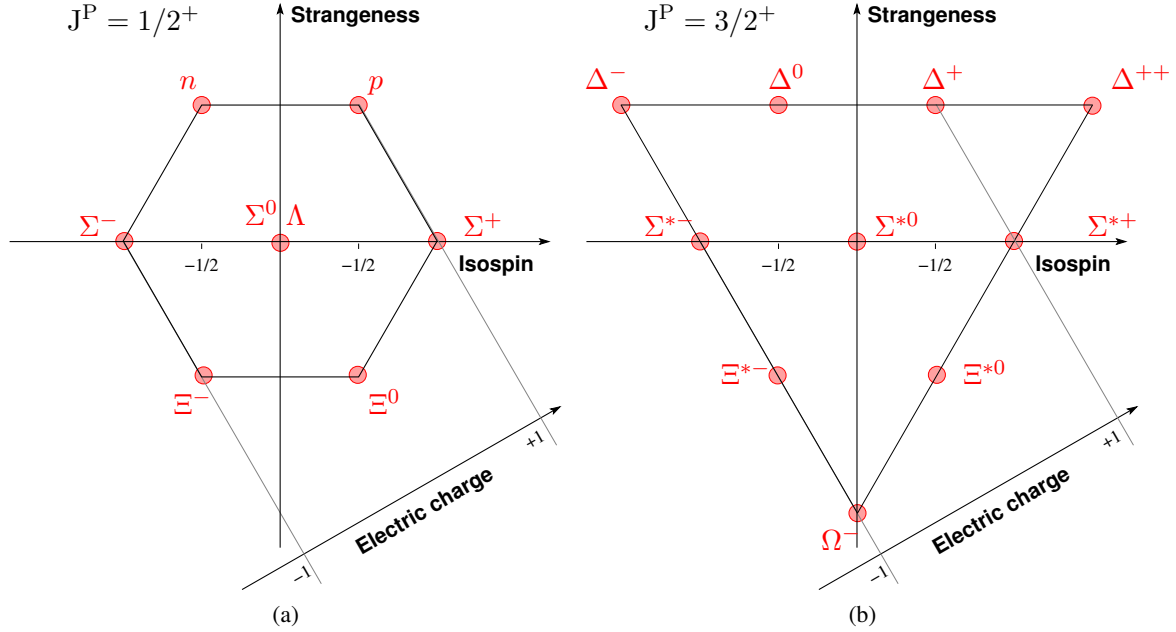


Figure 1.2.: The lightest baryon octet (a) and decuplet (b) are listed, classified according to their isospin I_3 , strangeness S and electric charge.

Extending the number of the quarks from two (mesons) to three (baryons), the system can be described within a $3 \otimes 3 \otimes 3 = 10_s \oplus 8_m \oplus 8_m \otimes 1_a$ symmetry: one symmetric decuplet, 2 octets with mixed symmetry and an antisymmetric singlet, referring to the behavior of the baryons under exchange of two quarks.

1.4. Hadrons in a medium

The Lagrangian of QCD can be written as:

$$\mathcal{L}_{QCD} = \bar{\psi}_q (i\gamma^\nu (D_\nu) - m) \psi_q - \frac{1}{4} G_{\alpha\mu}^{\nu} G_{\nu\mu}^{\alpha}, \quad (1.1)$$

where the field strength is

$$G_{\nu\mu}^{\alpha} = \partial_\mu \mathcal{A}_\nu^\alpha - \partial_\nu \mathcal{A}_\mu^\alpha - g f_{\alpha\beta\gamma} \mathcal{A}_\mu^\beta \mathcal{A}_\nu^\gamma. \quad (1.2)$$

the ψ_q is the quark-field, $m = \text{diag}(m_u, m_d, m_s)$ is the quark mass matrix, γ_μ ($\mu=0 \dots 3$) are the Dirac matrices and D_μ is the covariant derivative dealing with the coupling between the quark and the gluon fields, $f_{\alpha\beta\gamma}$ is the structure constant of the color gauge group $SU(3)_C$, \mathcal{A} is the gluon field and $g(\kappa)$ is the running coupling constant. The third term of field strength describes the interaction of the gluons with each others, because the gluons carry color charge themselves. This is a fundamental difference between QCD and QED. In QED the photons do not carry electric charge, and thus they do not interact directly with other photons.

If the quark masses are fixed, the only parameter in the Lagrangian is the *running coupling constant*, which is a function of the scale at which it is measured (for example energy or distance, see

Figure 1.3). At low energies (large distances), the coupling constant is large but with increasing energies (small distances) this constant will decrease. This phenomenon is called *asymptotic freedom*. A scale parameter $\Lambda_{qcd} \simeq 200 \text{ MeV}/c$ ($\simeq 1 \text{ fm}^{-1}$) is introduced to describe the scale where the theory becomes non-perturbative.

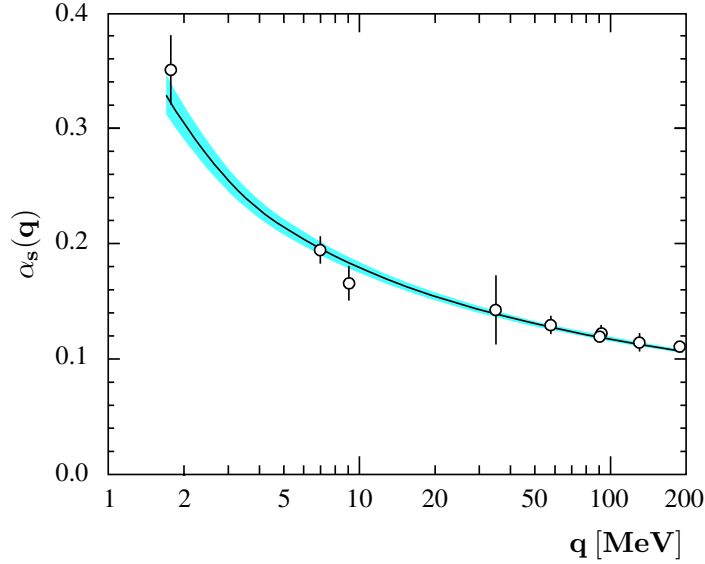


Figure 1.3.: Experimentally measured values of the running coupling constant confirm the theoretically expected behavior [N⁺10].

1.4.1. Chirality

The chirality¹² is a fundamental symmetry of QCD at the limit of vanishing quark masses. It describes the orientation of the spin of the particle relative to the direction of its motion:

$$\chi = \frac{\vec{s} \cdot \vec{p}}{|\vec{s}| \cdot |\vec{p}|}. \quad (1.3)$$

Fermions can be right handed (spin and momentum is pointing to the same direction) or left handed (spin and momentum is pointing to the opposite direction). Gluons do not distinguish between left- and right handed particles, thus they do not change helicity. If the particles are massless, their chirality cannot be changed, it is conserved.

However even the light quarks (u, d, s) have non-zero masses. At small particle masses, the chiral symmetry is an *approximate* symmetry. This means that as long as the masses are small compared to the relevant scale of the theory (the energy scale of the QCD, which is $\Lambda_{QCD} \cong 200 \text{ MeV}$) the prediction under the assumption of the symmetry should be reasonably close to the actual results. The masses of the lightest three quarks fulfill these requirements:

$$\frac{m_u}{\Lambda_{QCD}} \approx 1.5 \cdot 10^{-2}, \quad \frac{m_d}{\Lambda_{QCD}} \approx 2.5 \cdot 10^{-2}, \quad \frac{m_s}{\Lambda_{QCD}} \approx 5 \cdot 10^{-1} \quad (1.4)$$

¹²For massless particles it is also called helicity.

1. Introduction

If the same symmetry was to hold in the hadronic sector in this case the chiral partners should be degenerate in mass: $m_{J^+} = m_{J^-}$ (or - due to the *approximate* behavior - the masses should have small difference). This is not observed in nature (see Figure 1.4).

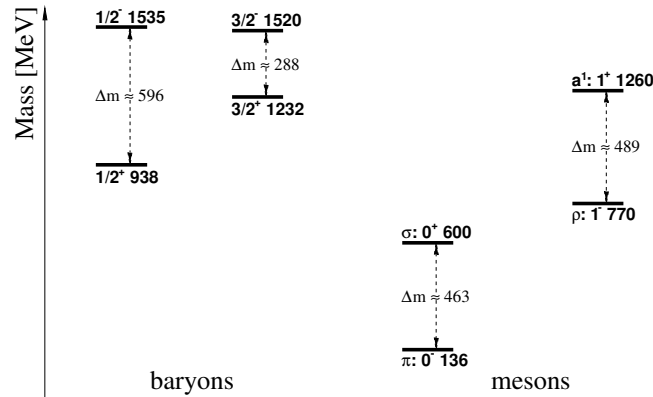


Figure 1.4.: Masses of some hadrons and their chiral partners. The mass-split between the chiral partners are comparable with the mass of the hadrons.

The mass differences between chiral partners in the hadronic sector are not negligible, but even of the same order as the mass of the hadrons. This directly shows that the chiral symmetry is spontaneously broken in the hadronic sector. A symmetry is *spontaneously broken* if the symmetry of the Hamiltonian is not realized in the ground state. In this case, the system is not invariant under any transformation. This feature is illustrated in Figure 1.5:

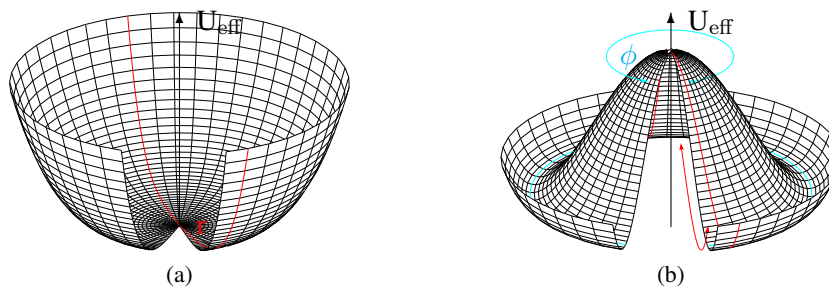


Figure 1.5.: In Figure (a) (restored symmetry), the minimum of the potential is right in the center, therefore the ground state is invariant under rotations (no spontaneous breaking of the symmetry), while in Figure (b) (spontaneously broken symmetry) the ground state is located at a finite distance from the center where actually the potential has a local maximum.

The red lines represent the radial excitation, the cyan line the rotational excitation. (For more details, see text.)

For this type of a potential, the symmetry is spontaneously broken by choosing a certain direction to realize the ground state. However, an effect of the symmetry is still present. Moving around the valley costs no energy (rotational excitation), whereas radial motion does cost energy. An important consequence of the spontaneously broken symmetry is the existence of a massless mode (rotational excitation), the so-called Goldstone boson of the broken symmetry. In QCD - if only

the two lightest quarks (u, d) are considered - the pion-triplet (π^+ , π^- , π^0) is identified as Goldstone bosons. Assume that the QCD-Hamiltonian at zero temperature has a similar form as in Figure 1.5b where the r and ϕ coordinates are replaced by σ (massive) and π (massless) fields. However, the mass of the pions are not zero. The non-zero masses of the quark can lead to non-zero mass of the pions by breaking the chiral symmetry *explicitly*.

In contrast to the spontaneous symmetry breaking where the Lagrangian is symmetric, in the case of explicit symmetry breaking the Lagrangian is not symmetric. It means that the Lagrangian of QCD loses its symmetry if a quark mass term is included ($\delta\mathcal{L} = -m\bar{\phi}_q\phi_q$). Using the example above (see Figure 1.5), the extra mass term tilts the potential. This is visualized by the cross section of the ‘‘Mexican hat’’ potential (see Figure 1.6). In this configuration, the rotational excitations (pion field) also cost energy, hence the Goldstone bosons are massive. As long as the potential is tilted only slightly, rotational excitations are considerably smaller than the radial ones, which is also reflected in the small π masses.

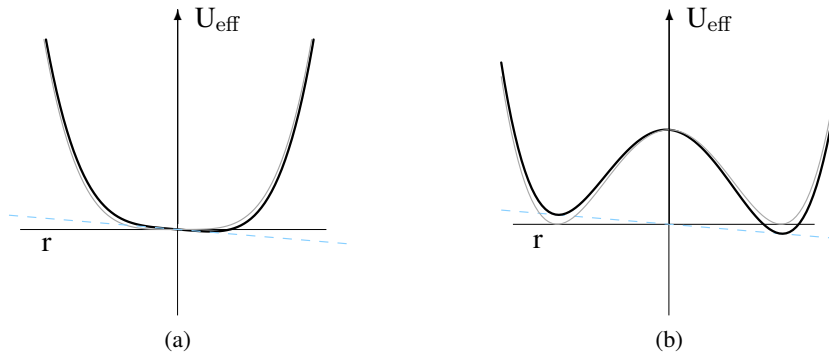


Figure 1.6.: Explicit breaking of the chiral symmetry. The thin gray line represents the symmetric Lagrangian. The thin cyan line shows the explicit symmetry breaking term ($-m\bar{\phi}_q\phi_q$), the black line is the full Lagrangian.

In terms of quark degrees of freedom, one order parameter to measure the violation of symmetry is the chiral condensate that has a value of $\langle q\bar{q} \rangle \approx (-250\text{MeV})^3 \pm 10\%$ in vacuum. An other order parameter is the decay constant of the pion which has a value of $f_{\pi^0} \sim 94\text{MeV}$ in vacuum. The link between the two quantities is built by the Gell-Mann-Oaks-Renner (GOR) expression:

$$m_{\pi^0}^2 = \frac{1}{f_{\pi}^2} \underbrace{\frac{m_u + m_d}{2}}_{\text{explicit symmetry breaking}} \overbrace{(\langle \bar{u}u \rangle + \langle \bar{d}d \rangle)}^{\text{spontaneous symmetry breaking}} + \mathcal{O}(m_{u,d}^2), \quad (1.5)$$

where f_{π} is the pion decay constant of, and $m_{u,d}$ are the quark masses. The right part of the GOR expression carries information on both explicit symmetry breaking through the quark masses and spontaneous breaking of the symmetry through the expression of the chiral condensate $\langle \bar{q}q \rangle$. The order parameters for the symmetry breaking show dependence on temperature and density. A prediction of this dependence is shown in the Figure 1.7.

As can be seen in Figure 1.7, at sufficiently high temperatures ($T > 300\text{MeV}$) or at sufficiently high densities ($\rho \geq 5\rho_0$) the chiral condensate drops significantly, and consequently the chiral symmetry is at least partially restored. This effect is not unique in physics. The phase transition of ferromagnets at the Curie point to paramagnetic material is the same kind of transition. But

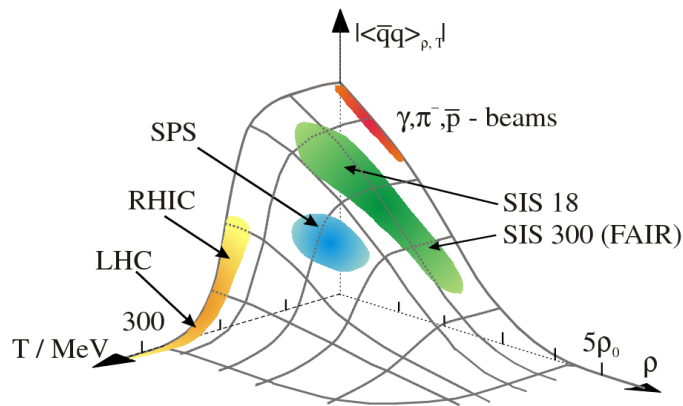


Figure 1.7.: Dependence of the chiral condensate on density and temperature.

contrary to the magnetism (the order parameter of the transition), the chiral condensate and the decay constant of the pion are not observables. The connection between the order parameter (quark condensate) and hadronic observable (excitation function) is given by the QCD Sum Rules which will be described later. While a general consensus exists concerning how the chiral condensate behaves in a thermal bath or in a dense medium, the effect of the the chiral restoration on the observables of hadrons is much less clear.

1.4.2. Hadron properties in the nuclear medium

There are many models predicting medium modifications of the properties of mesons in the nuclear medium. Some models and their predictions will be mentioned here.

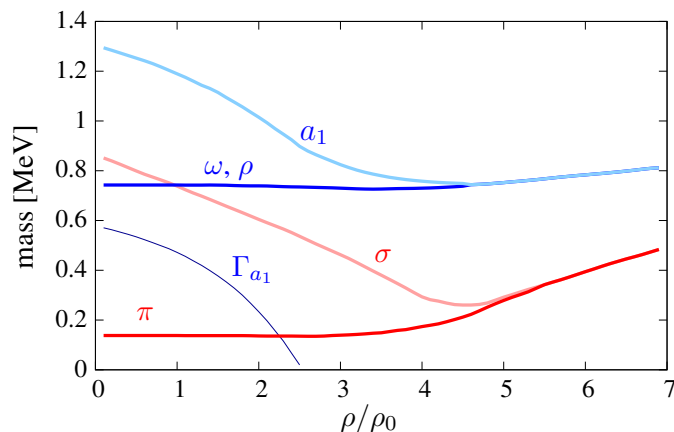


Figure 1.8.: Prediction of the NJL model for meson masses as a function of the density. The decay width $a_1 \rightarrow \bar{q}q$ is also shown. Beyond a critical density the chiral partners (π, σ) and (ρ, a_1) are degenerate in mass. [BM88]

The constituent quark mass m_q originates mainly from the spontaneous breaking of chiral symmetry as proposed by Nambu and Jona-Lasinio (NJL)[NJL61]. If one assumes that the vector meson mass is just given by the additive rule, then it will be of the order of $2m_q$. As chiral symmetry is

restored, the constituent mass drops, therefore one expects a drop in the mass of the vector meson. More elaborate models using the NJL approach at finite temperatures and density were proposed in the late 1980's [BM88] (see Figure 1.8). It is interesting to note that the masses of the pion and the vector mesons are not changing with density. The spectral degeneracy between the σ and the π meson, the ρ and the a_1 meson occurs in dense matter where chiral symmetry is restored ($\rho \sim 5\rho_0$).

The *QCD sum rule method* can relate the QCD condensate to the hadronic spectral functions. QCD sum rules in the medium provide useful constraints evaluating the weighted average of the

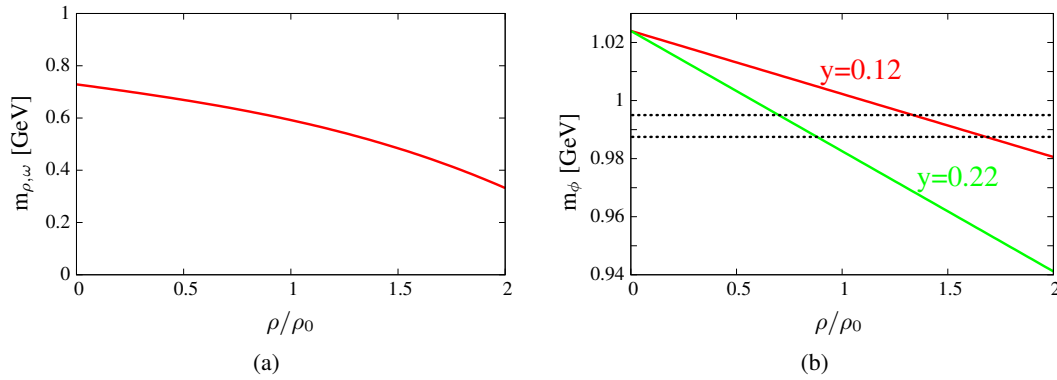


Figure 1.9.: (a) Prediction of the *QCD Sum Rule method* for the $\rho - \omega$ mass as a function of the ρ/ρ_0 .
 (b) The same figure for the ϕ meson with two typical values of y (strangeness content of the meson). Dotted lines indicates the $K^0 K^0$ and the $K^+ K^-$ thresholds which are the main decay modes of the ψ . [HL92]

spectral functions. Hatsuda and Lee [HL92] have predicted that the mass of the vector mesons drops linearly (see Figure 1.9) with the density:

$$\frac{m_V^*}{m_V} = \left(1 - \alpha \frac{\rho}{\rho_0}\right), \quad (1.6)$$

where ρ_0 is the normal nuclear density (0.17 1/fm^3) and $\alpha \simeq 0.18 \pm 0.06$ for $V = \rho, \omega$ and $\alpha \simeq 0.15y$ for $V = \phi$ (y is the nucleon strangeness content)

The *Brown-Rho scaling* [BR91] assumes that the masses of light vector mesons (ρ, ω) scale universally as a function of density and/or temperature:

$$\frac{m^*}{m} \sim \frac{f_{\pi^0}^*}{f_{\pi^0}} \sim 0.8(\rho \sim \rho_0). \quad (1.7)$$

Theoretical foundations for such a scaling were shown using an effective chiral Lagrangian with scaling properties of QCD leading to an approximate in-medium scaling law.

The *Quark-Meson Coupling model* (QMC) is a phenomenological theory in which quarks and gluons are confined in a “bag” inside non-perturbative QCD vacuum. In the medium, baryons composed of three valence quarks feel both scalar and vector potentials with opposite sign, while

the mesons composed of quark and anti-quark only feel the scalar potential and obey a universal scaling law (Figure 1.10). It is interesting to note that at normal nuclear density (ρ_0), the ρ and ω -masses drop by $\sim 15\%$ the nucleon-mass drops by $\sim 20\%$ and the D-meson mass drops by $\sim 3\%$.

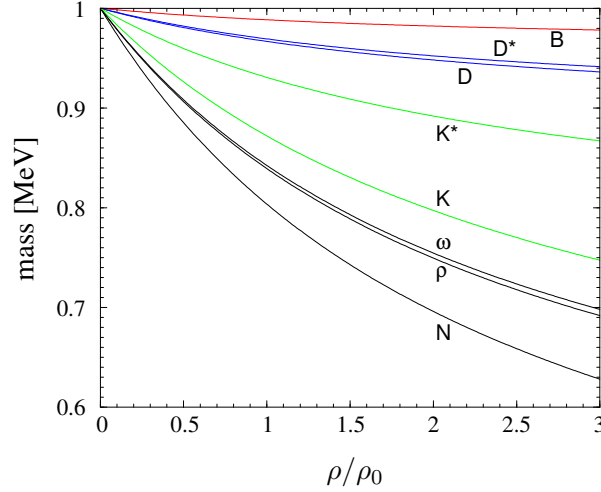


Figure 1.10.: Prediction of the QMC model for the meson masses as a function of the density. [STT07]

Hadronic models use a purely hadronic description of the mesons in the medium. The in-medium self-energy of the meson receives contributions from low-energy particle-hole (p-h) excitations and high energy nucleon-anti nucleon excitations (see Figure 1.11).

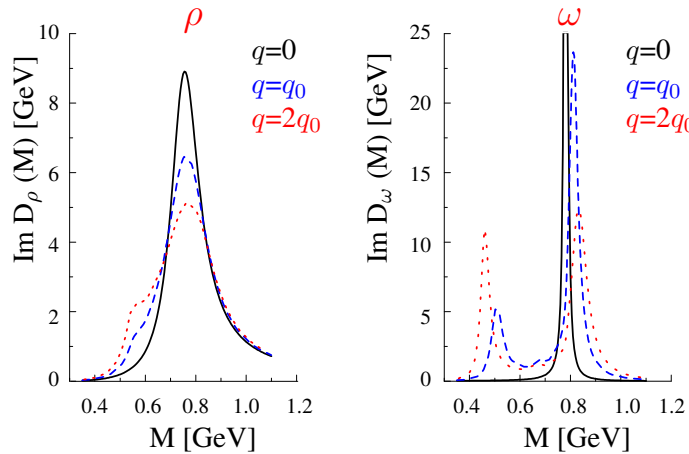


Figure 1.11.: Prediction of the hadronic models for the imaginary part of the ρ - and ω mesons spectral functions in nuclear matter at densities $q = 0$, $q = q_0$ and $q = 2q_0$. [LWF02]

As it propagates in nuclear matter, the vector meson feels not only the nucleon excitation but also resonance excitations such as Δ and N^* . These models provide much “richer” information about the in-medium properties of the mesons. The spectral functions are modified in non-trivial

manners such as spectral shifts, spectral broadening and new spectral peaks. Figure 1.11 shows the predictions of different hadronic models for the ρ and ω mesons [LWF02].

All these models provide measurable predictions even at normal nuclear densities (mass shift, change in interaction, broadening, extra peaks, etc.). For now, these effective theories are the best available models until Lattice QCD calculations produce reliable results at finite density and temperature.

1.4.3. Former experiments

Charged mesons in nuclear medium

Pionic atoms and deeply bound states As it was shown in the previous section the chiral condensate in nuclear is predicted to drop by $\sim 30\text{-}40\%$. The GOR relation (Equation 1.5) links the quark condensate to the mass of the pion and its decay constant. Since the pion is a Goldstone boson, its mass is not expected to change dramatically with increasing nuclear density therefore a drop in the condensate results in a drop of the decay constant.

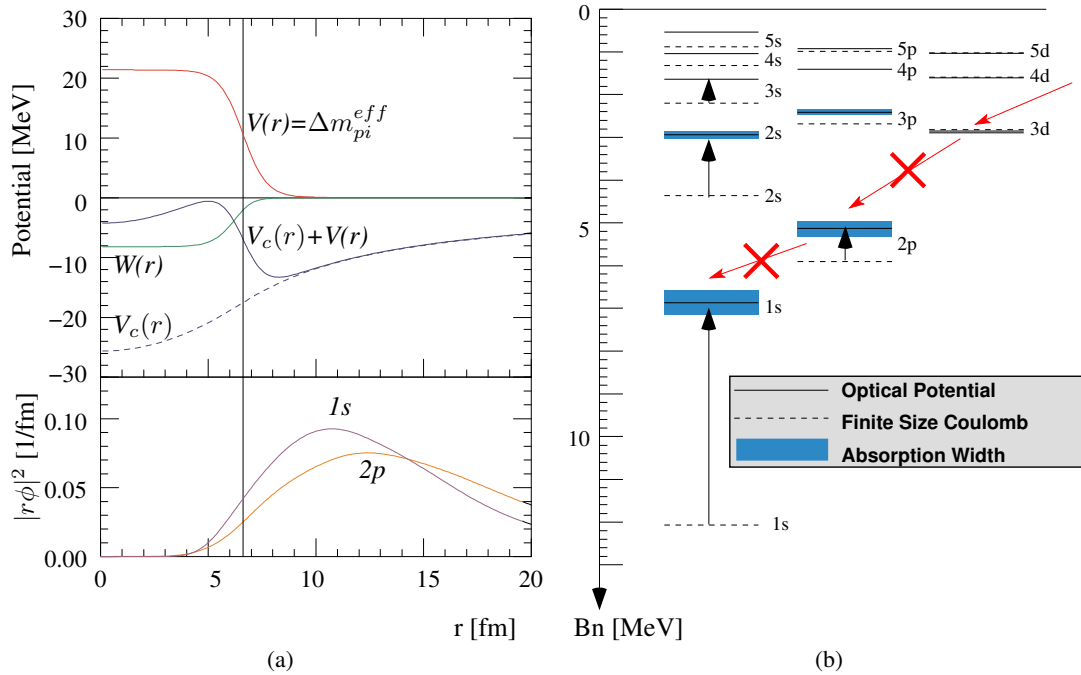


Figure 1.12.: (a), [Upper two panels] Composition of the local pion-nucleus potential for Pb with Coulomb potential (V_c) and the real and imaginary s-wave potential (V and W , respectively). [Lowermost panels] Pionic density distribution for $1s$ and $2p$ states in Pb . [IOH⁺00]

(b), Calculated level scheme of pionic Pb . Level shifts and widths are indicated by the vertical arrows and the shaded areas. The forbidden transitions are labeled with crossed red arrows.

A possible way to look for this reduction is to study the in-medium pion properties through the precision spectroscopy of deeply bound pionic atoms. The superposition of a large repulsive s-wave π^- -nucleus interaction at low pion momenta and an attractive Coulomb interaction leads to

a potential “pocket” at the surface of the nucleus which gives rise to pion-nucleon bound states with halo-like distribution of the pions around the nucleus [Yam90].

The first experiment of this sort was performed by high-precision X-ray spectroscopy of captured π^- in atomic orbits. The effect of the nuclear medium can be expected on the lowest orbits (1s, 2p). However, in Pb this is not possible since the last observed transition is the $4f \rightarrow 3d$ [DLTD⁺85]¹³ (see Figure 1.12). The solution was proposed by Yamazaki and Toki by depositing the pion directly into a deep orbit by a nuclear reaction via recoil-free meson production (see Section 3.5.1). Using missing-mass spectroscopy the binding energy of the deeply bound state¹⁴ was measured.

Kaonic atoms and deeply bound states Studies of kaonic atoms show that the K^- -nucleus potential is attractive. In a more extreme case the potential can be even -600 MeV deep at the center of the nucleus [MYSH⁺10]. If K^- is inserted inside the nucleus then, in this picture, it would lead to a shrinkage of the nucleus, generating a new very compact object with a high central density, which can be 10 times larger than the normal density. This state should be a long-lived state while the strong decay channels of a K^- in this deep potential are highly suppressed. Signatures of such states were reported in several experiments:

- A first claim was made by KEK [SBF⁺04] (see figure 1.13a). This result was retracted after a more careful analysis.
- The FINUDA experiment has reported peaks on the $m_{\Lambda, \text{proton}}$ and on the $m_{\Lambda, \text{deuterium}}$ invariant mass spectra following the absorption of the stopped K^- (see figure 1.13b). These were interpreted in terms of deeply bound K^-pp and K^-ppn clusters [A⁺05, A⁺07].
- Similar results were reported from the OBELIX@CERN experiment from \bar{p} annihilation of ${}^4\text{He}$ [BFL⁺07].
- A recent experiment from the DISTO collaboration also reported a signature of bound kaonic states [Y⁺08].

However, it should be mentioned that the experimental results are not always in agreement with each other and theoretical works can explain these results with conventional mechanisms (like for example final state interactions).

Neutral mesons in nuclear medium

It is of interest to study such meson-nucleus bound systems, where the meson does not carry electric charge and governed by purely strong interaction in contrast to the mesonic atom-states where the potential is created by the interplay of the strong and the electric interactions.

Bound η -mesic states Sokol et al. searched for the existence of η mesic ${}^{11}\text{B}$ in the reaction $\gamma + {}^{12}\text{C} \rightarrow p + {}^{11}\text{B} \rightarrow \pi^+ + n + X$ proceeding via an intermediate $S^{11}(1535)$ resonance which decays into $\pi^+ + n$ [SP01]. The correlated energies and the opening angle between the final state particles were used as a signature for the identification of the decay channel. A peak observed in the kinetic energy distribution below the threshold of the elementary $\pi n \rightarrow \eta n$ reaction was taken as evidence for the formation and decay of a bound η -nucleus system.

¹³However in lighter nuclei even the lowest orbit can be populated and atomic spectroscopy can be used to study the deeply bound states [Got04].

¹⁴The 1s and 2p bound pionic states are called *deeply bound* states.

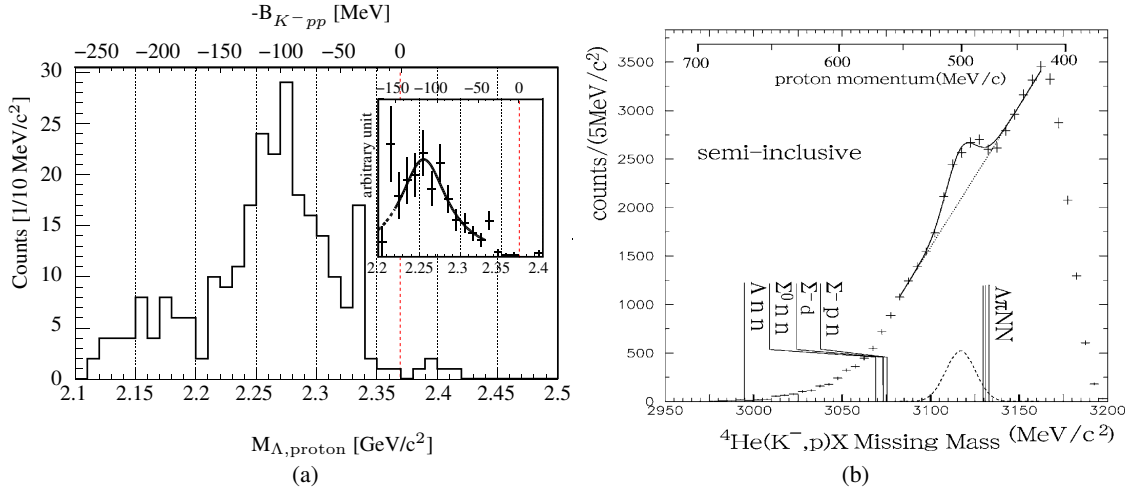


Figure 1.13.: (a), Invariant mass of the back-to-back registered proton- Λ system without acceptance correction (big figure) and with acceptance correction (inlay). The invariant mass, assuming that the process was simply a two-nucleon absorption process, is labeled with red lines. (b), Missing mass spectrum of the semi-inclusive proton events with the proton momentum scale. Possible decay modes are also shown at the corresponding mass thresholds [A^{+05} , A^{+07}].

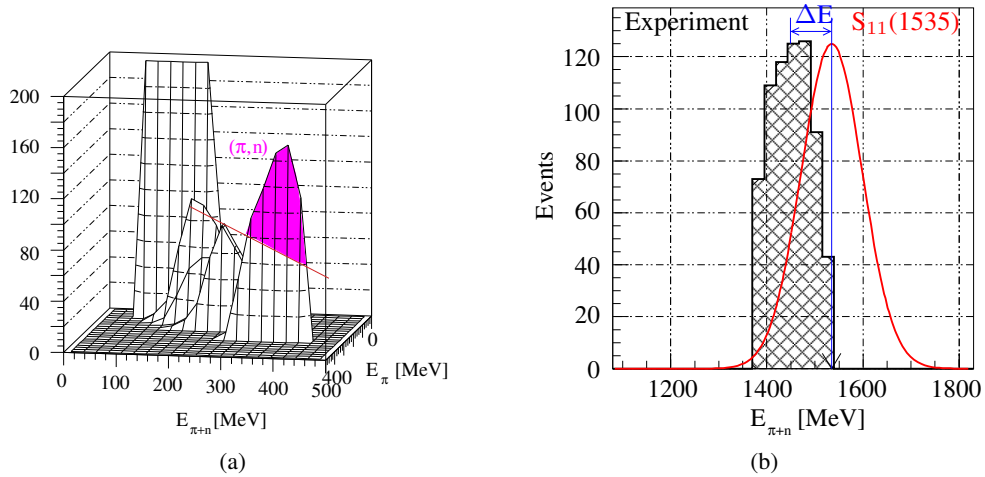


Figure 1.14.: A resonant structure in the 2D energy correlation histogram (a) suggest the presence of a bound η -mesic state. The total energy distribution of the decay products ($E_{\text{total}}=E_{\pi^+}+E_n$) has a width of about 150 MeV and its position is about $\Delta E=90$ MeV below the position of the $S_{11}(1535)$ [SP01] (b).

Coherent photoproduction of η mesons near threshold on ${}^3\text{He}$ was used to form η -mesic states at MAMI in Mainz. The non-vanishing cross sections of the coherent η production at threshold was interpreted as sign of a bound mesic state [PAA⁺04] (see Figure 1.15).

The angular distribution of the produced η s close to threshold confirmed this assumption since the

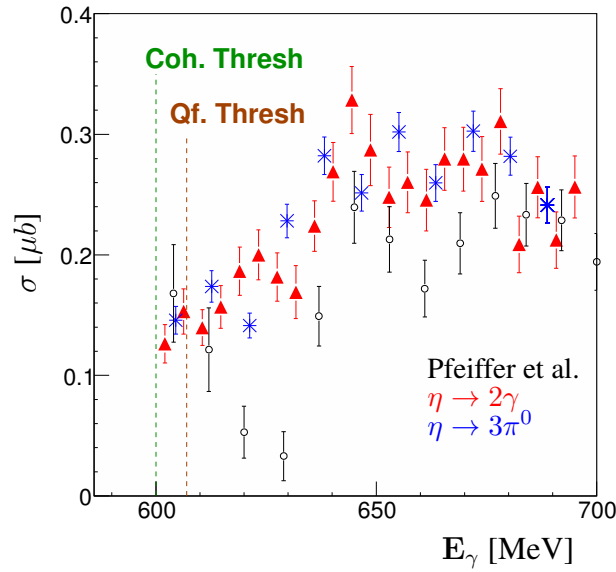


Figure 1.15.: Coherent cross section ($\eta \rightarrow 2\gamma$ in red, $\eta \rightarrow 3\pi^0$ in blue) compared to Pfeiffer et al. (black). The coherent and quasi-free thresholds are also shown. [KPM10]

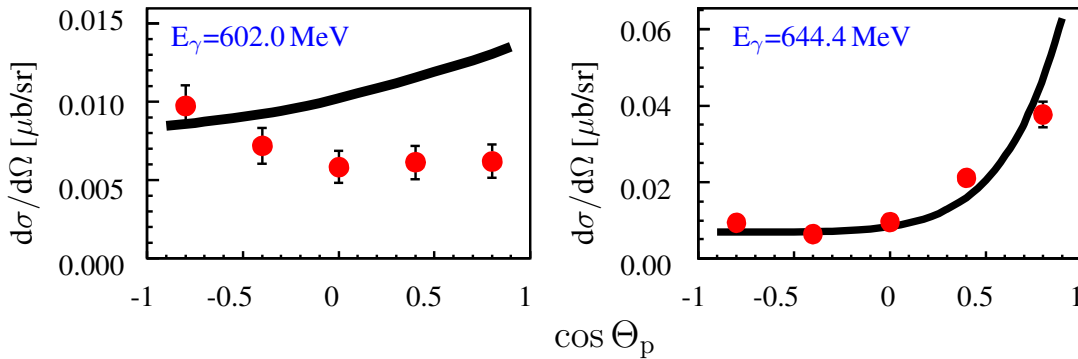


Figure 1.16.: Coherent $\eta \rightarrow 2\gamma$ differential cross section in the $(\gamma, {}^4\text{He})$ center of mass frame and two different beam energies. The black line corresponds to the expected angular distribution from proton data where ${}^3\text{He}$ form factor has been taken into account. At an energy $E_\gamma = 644.4$ MeV the measured data shows a forward peaking behavior which is in agreement with the expected distribution for coherent η -production. At lower energies $E_\gamma = 602.0$ MeV the measured distribution is flat, which is not in agreement with the expected forward peaking distribution. This behavior suggests two different types of reaction mechanisms [Phe10]

angular distribution of the η s close to threshold is also isotropic in the nucleus- γ center-of-mass system in contrast to the expected forward rise for coherent production which was observed at higher incident energies (see Figure 1.16).

Pfeiffer et al. studied the decay channel that was studied also by Sokol et al. (but instead of focusing on the $\pi^+ + n$ final state they studied correlated $\pi^0 + p$ events) [PAA⁺04, KPM10]. Because of the limited phase-space the S^{11} resonance will have low momentum and will therefore

decay into $\pi^0 + p$ where the opening angle between the ejectiles will be almost 180° in the γ -nucleus center-of-mass frame.

Experiments of similar kind with proton beam has been performed at COSY in Jülich [MS10].

1.5. Bound ω -mesic states and the Crystal-ELSA/TAPS experiment

1.5.1. Bound ω -mesic states

Saito and his collaborators made calculations to predict the potential between different light mesons and different nuclei [STT07] (see Figure 1.17). They found that the potential between an ω meson and the nucleus is attractive and approximately 100 MeV deep at the center of the nucleus for a wide range of nuclei (see Figure 1.17). As a consequence, an ω meson with less than 450 MeV/c momentum can be bound in this potential well.

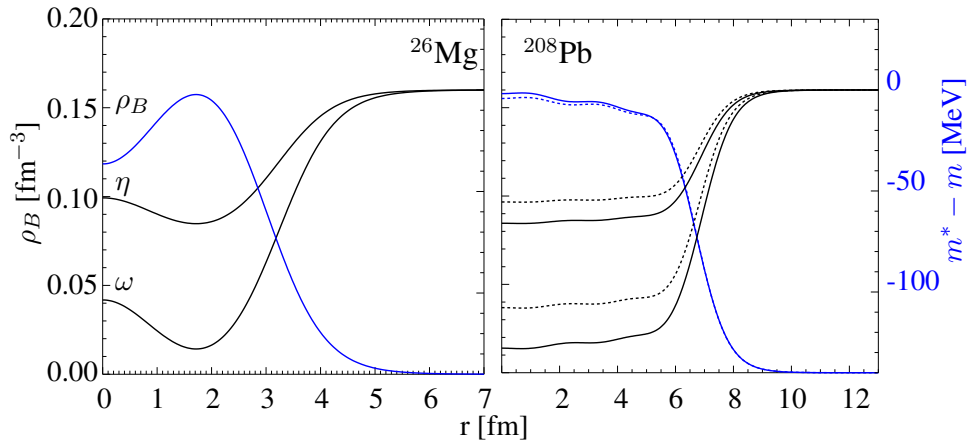


Figure 1.17.: Prediction of the η -nucleus and ω -nucleus potential within the QMC framework for Mg and Pb [STT07]. The blue lines correspond to the density distribution of the nucleus. The black line shows the potential as a function of the radius for ω and η meson. In the right figure two types of QMC predictions are compared.

ω mesic states were predicted by several groups (for example Marco and Weise [MW01], Saito [TLTS98] and Nagahiro [NJH05]).

The calculation of Marco and Weise was performed using an effective Lagrangian based on chiral SU(3) symmetry and vector meson dominance to construct the ω -nucleus potential. A downward mass shift of 15% and in-medium width of 40 MeV at normal nuclear density was assumed in the calculation. The calculation was performed for the case when the ω is produced at rest in the nucleus. The energy of the beam is $E_\gamma=2.75$ GeV and the knocked-out proton is going into the $\Theta_{\text{proton}} = 0^\circ$ direction. The missing energy spectra,

$$E_\gamma + m_p - E_p - m_\omega = E_\omega - m_\omega + |B_p|, \quad (1.8)$$

for carbon and calcium target is shown in Figure 1.18.

For the carbon target a pronounced peak can be seen at ~ -30 MeV while for the calcium target an access at negative energies without pronounced structure can be seen.

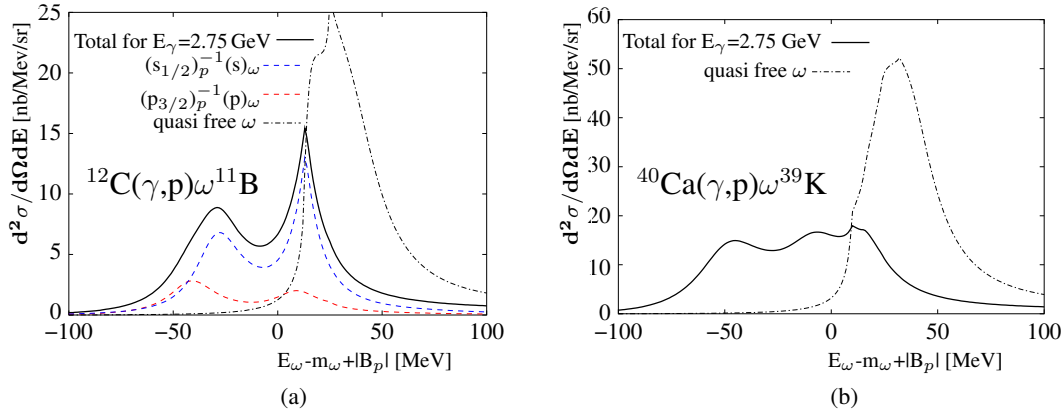


Figure 1.18.: Missing energy spectra at $E_\gamma=2.75$ GeV for the $^{12}\text{C}(\gamma,p)\omega^{11}\text{B}$ (a) and for $^{40}\text{Ca}(\gamma,p)\omega^{39}\text{K}$ (b) reactions. $|B_p|$ is the binding energy of the bound initial proton [MW01].

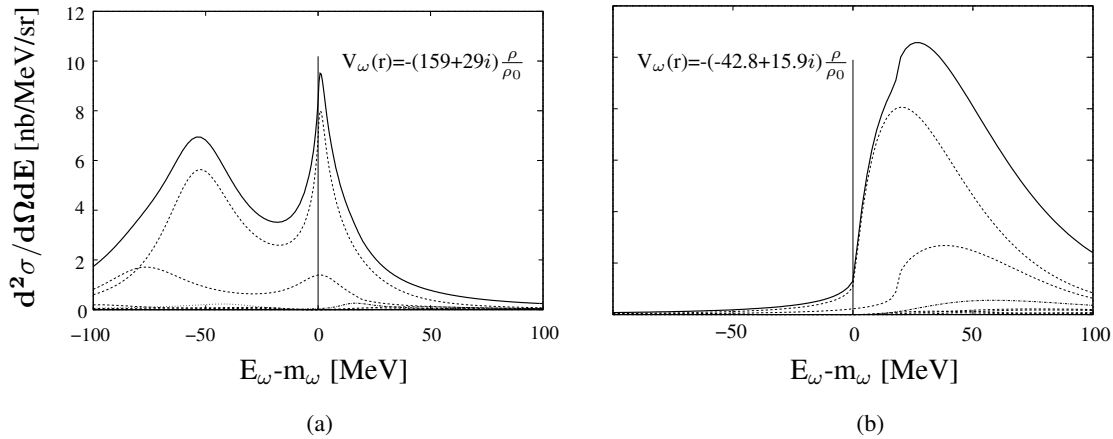


Figure 1.19.: Missing energy spectra of the $^{12}\text{C}(\gamma,p)\omega^{11}\text{B}$ reaction for an attractive (left figure) and a repulsive (right figure) potential [NJH05].

In Nagahiro's work the sensitivity for the chosen potential was studied [NJH05]. Figure 1.19 shows the prediction of the missing energy spectrum using two different potentials:

- an attractive one:

$$V_\omega(r) = -(156 + 29i) \frac{\rho}{\rho_0} \quad (1.9)$$

- and a repulsive one:

$$V_\omega(r) = -(-42.8 + 19.5i) \frac{\rho}{\rho_0}. \quad (1.10)$$

If the potential is attractive a pronounced structure appears at negative energies, while this structure disappears if the the potential is repulsive. The calculations provide a clear and independent statement whether the ω -nucleus potential is attractive or repulsive.

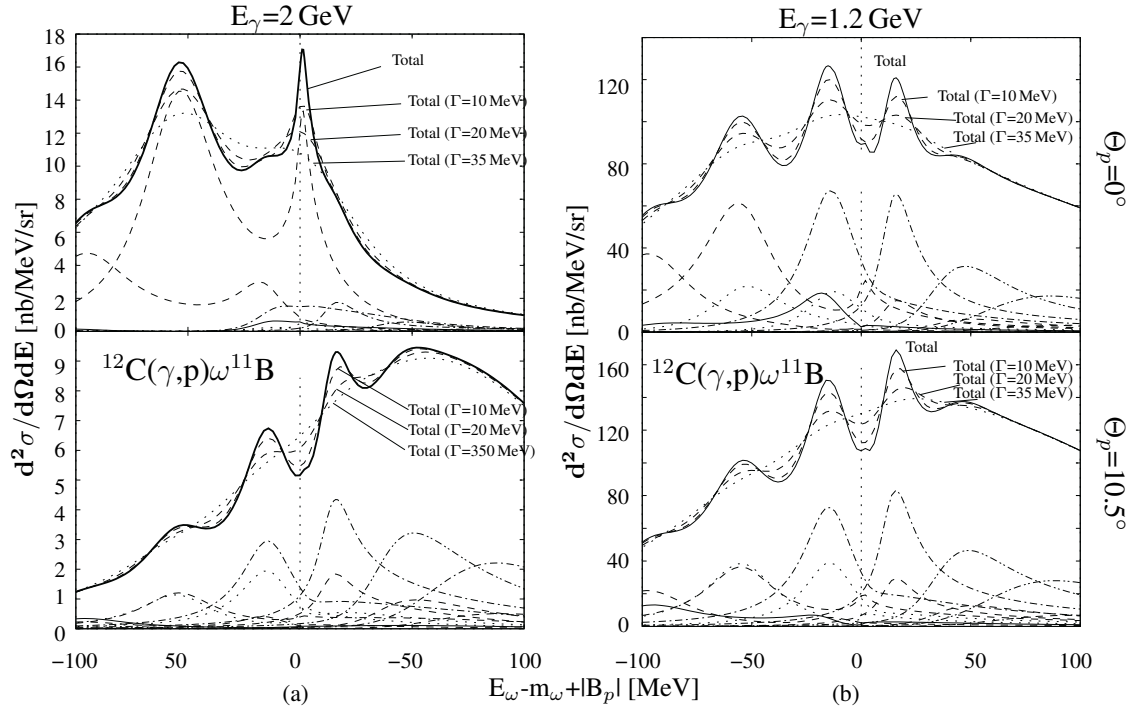


Figure 1.20.: Missing energy spectra of the $^{12}\text{C}(\gamma,p)\omega^{11}\text{B}$ reaction at different beam energies and for different directions of the knocked-out proton. The results are convoluted with different experimental resolutions [KNHO07].

Kaskulov et al. demonstrated the sensitivity of the obtained spectrum for different photon energies, different experimental resolutions and different directions of the knocked-out proton [KNHO07] (see Figure 1.20).

In the same publication Kaskulov et al. pointed out that the main background source are events with four-photons in the final state where one of the photons is not detected. This kind of background produces a peak-like structure close to the predicted peak (see Figure 1.21).

1.5.2. Searching for bound ω -mesic states at the ELSA

Two possible signatures were considered (see Figure 1.23):

- Following the reasoning of Marco and Weise, a non-zero yield should be found on the missing energy spectrum. In the calculation it was assumed that the energy of the forward going proton can be measured precisely (as at the pionic atom case the ejectile was measured), and the missing energy can be reconstructed from the energy of the proton ($E_\omega - m_\omega + |B_p| = E_\gamma + m_p - E_p - m_\omega$).

In the quasi-free reaction the forward going proton has a large momentum and becomes minimum ionizing (see Chapter 3.5.1). Since the BaF_2 crystals of 25 cm length, like in the MiniTAPS detector, stops protons only up to 400 MeV kinetic energy, it is impossible to measure the momentum of the forward going proton.

Because the most forward angles, up to 1° , are not covered by the detectors (see Figure 2.12), protons which are going to this direction cannot be detected at all. As a con-

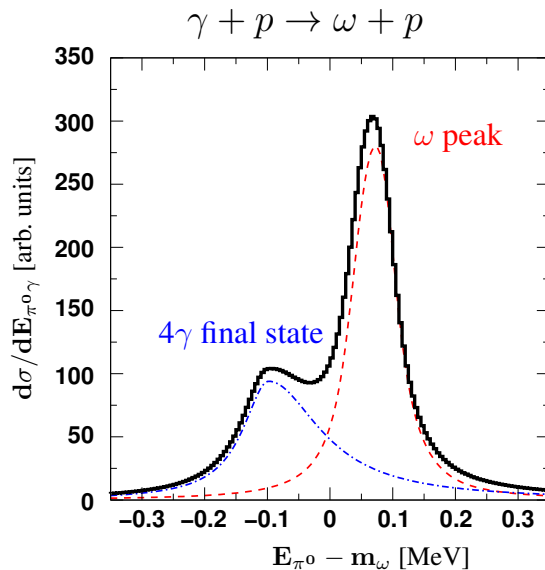


Figure 1.21.: The differential cross section of the reaction $\gamma + p \rightarrow \pi^0\gamma + p$ as a function of the $E_{\pi^0\gamma} - m_\omega$ where $E_{\pi^0\gamma} = E_{\pi^0} + E_\gamma$. The spectrum (black, solid line) is obtained using the reconstructed $\pi^0\gamma$ events from the exclusive $\gamma + p \rightarrow \pi^0\gamma + p$ reaction (red, dashed curve) plus an inclusive $\pi^0\gamma$ background which was obtained from events with 4 photons in the final state ($\pi^0\pi^0 \rightarrow 4\gamma$ and $\pi^0\eta \rightarrow 4\gamma$) when one photon is not detected (blue dashed-dotted line). The following cuts were used on the simulated data: $1.5 \text{ GeV} < E_\gamma < 2.6 \text{ GeV}$, $7^\circ < \Theta_p < 14^\circ$, $|\vec{p}_{\pi^0} + \vec{p}_\gamma| < 400 \text{ MeV}/c$, $|\vec{p}_{\gamma,3}| > 200 \text{ MeV}/c$ and $T_{\pi^0} > 150 \text{ MeV}/c$. The exclusive $\omega \rightarrow \pi^0\gamma$ signal has been convoluted with the experimental resolution of FWHM=50 MeV [KNHO07].

sequence of the problems above, the originally suggested method has to be modified.

If the detector setup can measure the decay products of the ω meson, the original meson can be reconstructed (see Chapter 3.2.5) and the “missing energy”¹⁵ ($E_{\pi^0\gamma} - m_\omega^{\text{PDG}}$) can be calculated directly from the reconstructed ω instead of using the beam energy and the energy of the knocked-out proton as it was suggested in the paper of Marco and Weise.

This method presumes that the bound omega will decay within the nucleus, and the decay products are detected. The Crystal Barrel together with the Forward Plug and the MiniTAPS detectors are suited to detect photons with high accuracy; this is one reason why the neutral decay mode of the ω meson was chosen ($\omega \rightarrow \pi^0\gamma$) to study ω -mesic states.

While the final-state photon can leave the nucleus without distortion, the π^0 may interact with a nucleon via the strong interaction and thus it rescatters inside the nucleus. This distortion effect leads to an inaccurate reconstruction of the meson.

This final state interaction was investigated using BUU transport code [MSC⁺01].

Pions which rescatter in the nuclear medium shift the invariant mass of the $\pi^0\gamma$ to lower values (see Figure 1.22). Only small amounts of distorted events can be seen close to the

¹⁵Measuring the meson directly the “missing energy” is “equivalent” to the kinetic energy of the meson ($T_{\text{meson}} = E_{\text{meson}} - m_{\text{meson}}$) with the restriction that the energy of the meson is the *measured* energy of the reconstructed $\pi^0\gamma$ system, and m_{meson} is the mass of the meson in vacuum which (this is the mass that is listed in the Particle Data Book (m^{PDG})).

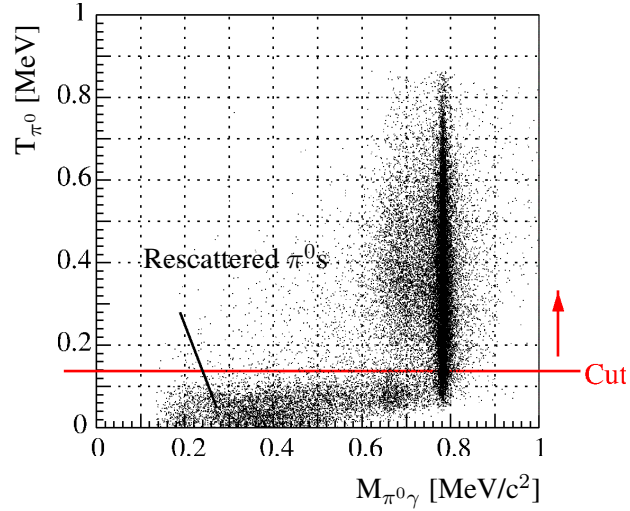


Figure 1.22.: Kinetic energy of the π^0 as a function of the $\pi^0\gamma$ invariant mass. The distorted events via final state interaction are relatively well separated in the $T_{\pi^0} < 150$ MeV region [MSC⁺01].

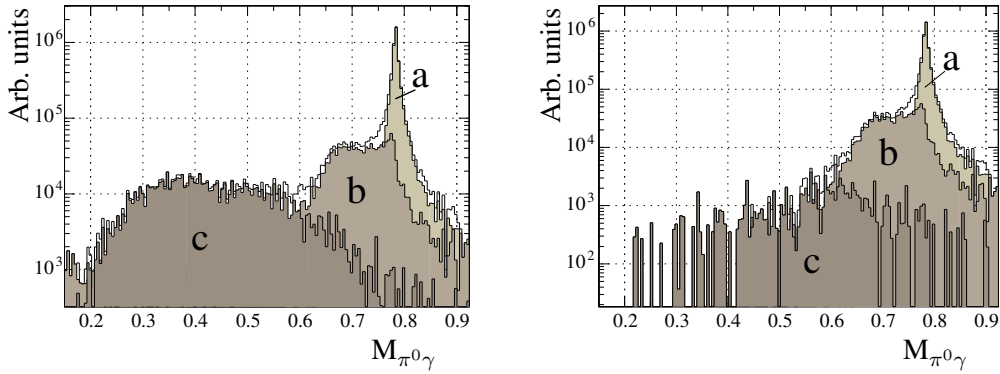


Figure 1.23.: The $\pi^0\gamma$ invariant mass spectrum before- (left figure) and after (right figure) the mentioned cut on the kinetic energy of the π^0 .

- a, fraction of ω mesons decaying outside the nuclear medium,
 - b, fraction of ω mesons decaying inside the nuclear medium into π^0 s and are not distorted by final state interactions,
 - c, fraction of ω mesons decaying inside the nuclear medium into π^0 s which are distorted by final state interactions.
- [MSC⁺01]

mass of the ω meson. With a cut on the kinetic energy of the π^0 s these events can be further suppressed (see Figure 1.23).

- The other way to study whether a bound state of an ω meson was produced is similar to the one that was described by Pfeiffer et al. [PAA⁺04, Phe10]. In this method events have to be found with large relative angles between the decay products of the produced intermediate resonance.

The goal is to produce slow mesons (in the reference frame of the nucleus) which can be absorbed by a nucleon, producing an intermediate baryonic resonance which decays to a

1. Introduction

meson (either π^0 or η) and a proton.

Pfeiffer et al. used coherent meson production¹⁶ close to threshold to reach this goal. In the present thesis a quasi-free reaction¹⁷ is used to produce slow ω mesons.

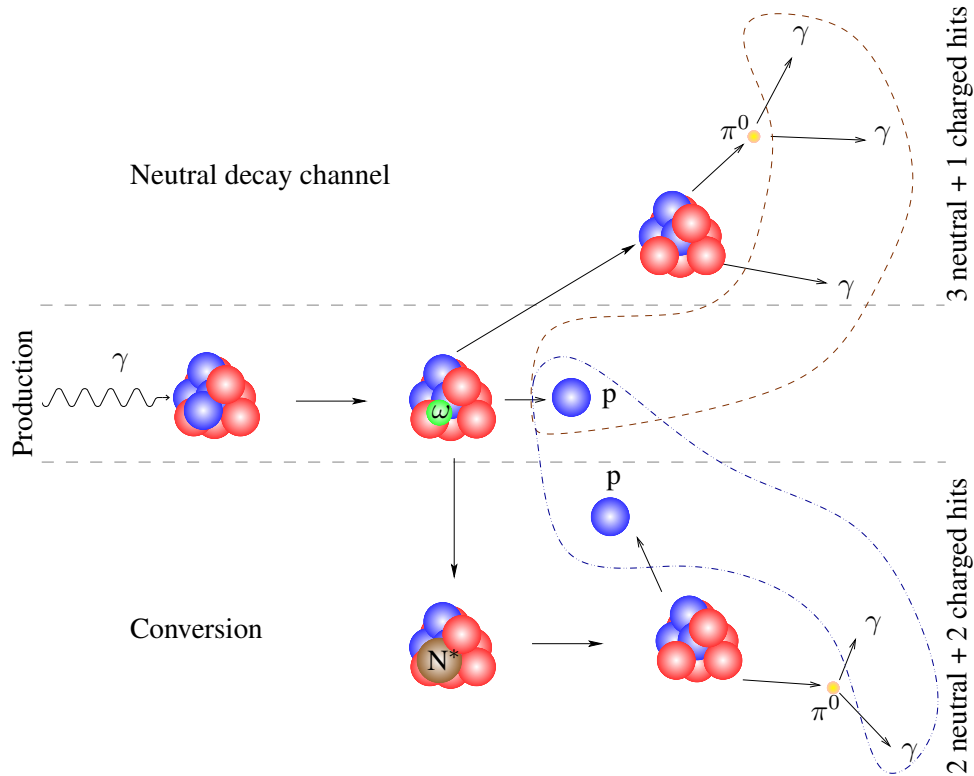


Figure 1.24.: The ω meson, which was produced via recoil-free photoproduction can be bound inside the nucleus. The bound state can be registered either via the decay of the bound ω meson into $\pi^0\gamma$ final state (three photons and one proton are in the final state, brown dashed line) or if a nucleon absorbs the ω meson producing a baryonic excitation which decays into a meson-proton final state where the meson can be either π^0 or η (two photons and two charged hits in the final state, dark blue dashed-dot line).

¹⁶In coherent production the beam interacts with the nucleus, and the nucleus remains in its ground state.

¹⁷In quasi-free reaction the beam interacts with only one nucleon, leaving the rest of the nucleus intact.

2. Experimental setup

Contents

2.1. The accelerator and the beamline	26
2.1.1. The electron beam	26
2.1.2. γ -beam	28
2.1.3. The tagging system	29
2.1.4. Beam dump	30
2.1.5. The target	30
2.1.6. γ intensity monitor	31
2.2. The CB-MiniTAPS experiment	31
2.2.1. The Crystal Barrel detector	32
2.2.2. The Inner Detector	33
2.2.3. Forward Plug	34
2.2.4. The MiniTAPS detector	34
2.3. The aerogel Cherenkov detector	37
2.4. Electronics and data acquisition system	37
2.4.1. The tagger	37
2.4.2. The Crystal Barrel	38
2.4.3. The Inner Detector	38
2.4.4. The MiniTAPS	39
2.5. Trigger	40
2.5.1. First-level trigger	40
2.5.2. Second-level trigger	41
2.5.3. Stand-alone trigger	41
2.6. Parameters during the experiment	41

Chapter summary

The experiment was performed at the accelerator ELSA operating in Bonn at the Rheinische Friedrich-Wilhelms-Universität Bonn. The data presented in this thesis were collected in March of 2007 within the CBELSA/TAPS collaboration. The name of the collaboration is derived from the three major components of the experiment, namely, the **E**lektronen-**S**tretcher-**A**nlage (ELSA) accelerator, the **C**ystal **B**arrel (CB) detector (together with the **F**or**W**ard **P**lug (FWPlug) calorimeter) and the **T**wo **A**rm **P**hoto-**S**pectrometer (MiniTAPS) as a forward wall (see Figure 2.1).

For running of the experiment the following major components are of central importance:

- **Accelerator**, for the production of a mono-energetic quasi-continuous electron beam,

2. Experimental setup

- **Radiator** that generates a photon beam via bremsstrahlung of the electrons and the **Tagging system** to determine the energy of these photons,
- **Target** on which short-lived mesonic states will be produced,
- **Detector system** built around the target to register the final products of the reaction generated by photons,
- **Gamma Intensity Monitor** to measure the number of photons impinging on the target.

These components will be explained in this chapter as well as the readout system and the trigger.

2.1. The accelerator and the beamline

The first accelerator in Bonn, the ancestor of ELSA, started to operate in 1958 as an alternating gradient synchrotron that provided 500 MeV electron bunches. After several years of operation and a major upgrade (a new synchrotron was installed) in 1967, it continued to provide particle bunches with much higher energies (up to 2.5 GeV). In 1982, the operation of the accelerator was paused in order to install a storage ring in addition to the existing accelerator facility and got the name **ELektronen-Stretcher-Anlage** (ELSA). The goal was to provide a quasi-continuous beam with much higher duty factor¹.

2.1.1. The electron beam

The electrons are produced by an electron-gun (with small initial energy) and injected into **LINear ACcelerators** (LINACs). At ELSA there are two LINACs. One of them, the so-called LINAC 1, is used to provide unpolarized electrons, the other one (LINAC 2) is used to provide linearly polarized electrons. As there was no need to use a polarized beam, in the March 2007 run only the LINAC 1 was used.

In the LINACs the electrons are pre-accelerated up to 20 MeV or 26 MeV, respectively. The pre-accelerated electron-beam is sent into the booster synchrotron, accelerating the electrons to 0.5-1.6 GeV and sends the electron-bunches to the stretcher ring. The Synchrotron has a circumference of $\sim 70\text{m}$, and while the electron energy is increasing, the magnetic field of the bending magnets has to be increased synchronously. The acceleration mechanism leads to a pulsed beam with a duty factor of 5 to 10%

Depending on the chosen operation mode, the Stretcher ring can provide electrons from 0.5 GeV up to 1.6 GeV (Stretcher mode – the provided energy is exactly the extraction energy of the synchrotron²) or up to 3.5 GeV (Post-accelerator mode). The result of both operation modes is a quasi-continuous beam with a macroscopic duty factor of up to 95 – 98% with maximum 20 nA external beam-current (Post-accelerator mode) [Cre].

¹The (macroscopic) duty factor is the ratio of the time while beam was delivered to the experiment and the total beam-time

²This operation mode is not used since 1994.

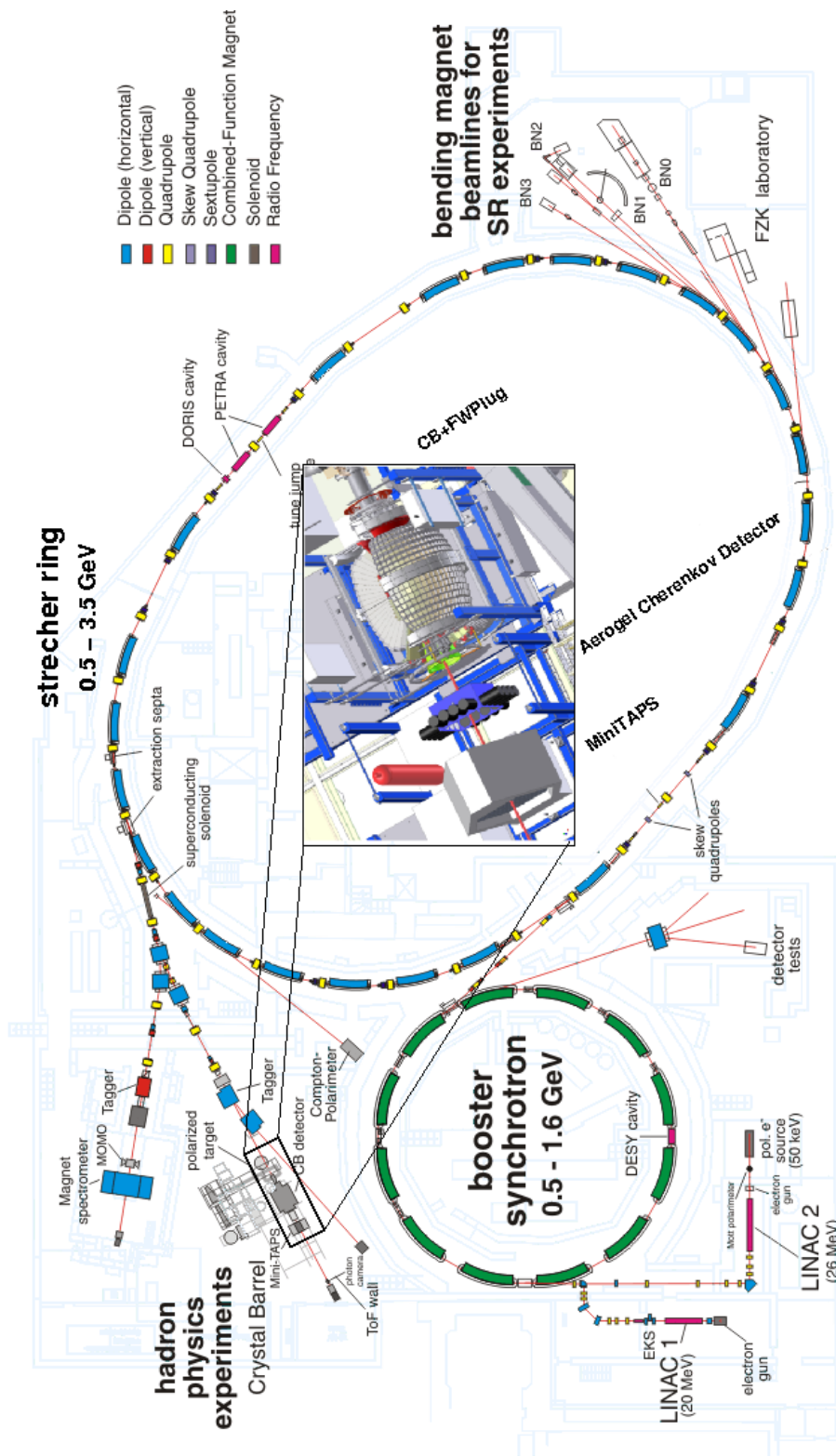


Figure 2.1.: Floor-plan of ELSA

2.1.2. γ -beam

The photon beam is produced by bremsstrahlung of electrons colliding with atomic nuclei in a copper foil. The electrons interact via Coulomb interaction with the nuclei of the foil and emit photons according to the $e(\text{Cu}) \rightarrow e'(\text{Cu})\gamma$ process.

Bremsstrahlung process

The maximum energy of the photons produced in this way is

$$E_{\gamma\max} = E_0 - m_e c^2, \quad (2.1)$$

and the energy distribution can be described reasonably well with the expression

$$N_{E_\gamma} \sim \frac{1}{E_\gamma} \quad (2.2)$$

in the region between

$$0 < E_\gamma < \approx 0.8 \frac{h\nu}{E_{\gamma\max}} \quad (2.3)$$

[OB66] (see Figure 2.2). The average half-angle of the emitted photon can be written as

$$\sqrt{\langle\Theta^2\rangle} \approx \frac{1}{\gamma} = \frac{m_e c^2}{E}. \quad (2.4)$$

This half angle is less than 0.5 mrad at typical ELSA energies. Consequently the generated photon beam points into the direction of the electron beam and is quite well collimated.

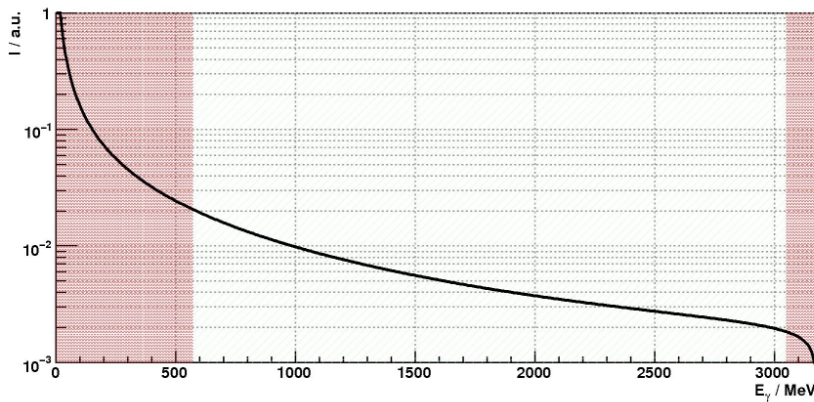


Figure 2.2.: Energy coverage of the tagger. The shaded energy regions are not tagged.

2.1.3. The tagging system

In case of

- the original energy of the electron beam is known,
- the momentum transfer to the nucleus in the foil is small,
- the multiple scattering does not occur in the radiator,

the following equation holds for the energy-momentum conservation for each event:

$$E_{e^-}^{\text{before}} = E_{\gamma} + E_{e^-}^{\text{after}}. \quad (2.5)$$

The energy of the electrons is known with high precision ($\frac{\Delta E}{E} = 0.09\%$ at 3.5 GeV) [Hil06]. Earlier it was shown that the energy transfer to the nuclei is negligible [Kru95] and multiple scattering can be significantly reduced by decreasing the width of the radiator foil. By the choice of a thin radiator foil, the gamma intensity, however, is also reduced. This is the reason why foil thicknesses of 50 μm and 150 μm were chosen: here the intensity remains high enough (tagger rate of ~ 6 MHz) and most of the multiple scattering is eliminated.

Equation (2.5) expresses that the energy of the bremsstrahlung-photon equals the energy loss of the electron. The remaining energy of electron can be measured with a magnetic electron-spectrometer (tagger, see Figure 2.3).

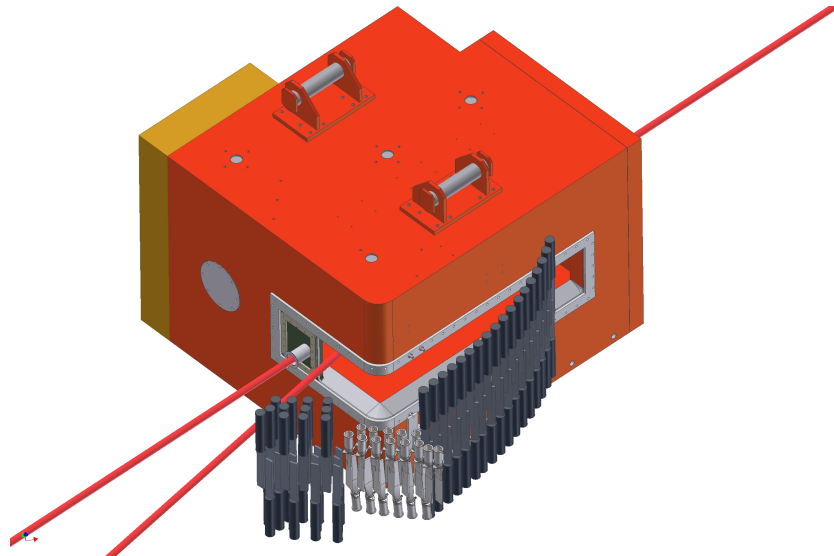


Figure 2.3.: Tagger magnet (red block) and the 96 partly overlapping scintillator taggerbars. The electrons arrive from the upper corner on the right and deflect toward the scintillator bars

In the relativistic case, the energy of the electron is roughly equal to the momentum of the electron

$$E_{e'} = pc = Brcq_{e^-}. \quad (2.6)$$

2. Experimental setup

Knowing the magnetic field (\vec{B}) and the gyro-radius of the electrons (r) the energy of the deflected electron can be extracted. If the initial energy of the electrons is also known, the energy of the generated photon can also be calculated

$$E_\gamma \approx E_{e^-}^{\text{accelerator}} - E_{e^-}^{\text{measured}} \quad (2.7)$$

The deflected electrons are detected by the tagger system consisting of 96 plastic scintillator bars which are read out by **PhotoMultiplier Tubes (PMT)**. The bars overlap each other to reduce the noise and cover the energy between 18% and 96% of the electron-beam energy (see Figure 2.2).

2.1.4. Beam dump

The largest fraction of the electrons, however, passes through the radiator foil without any interaction. In addition, the photon beam also points in the direction of the electron beam, therefore the separation of the photons and electrons is essential. The electrons passing through the radiator foil without interaction will be bent towards the beam dump. The beam dump consists of a beam catcher of a 470 kg heavy iron block that is surrounded by 70 t of steel (see Figure 2.4).

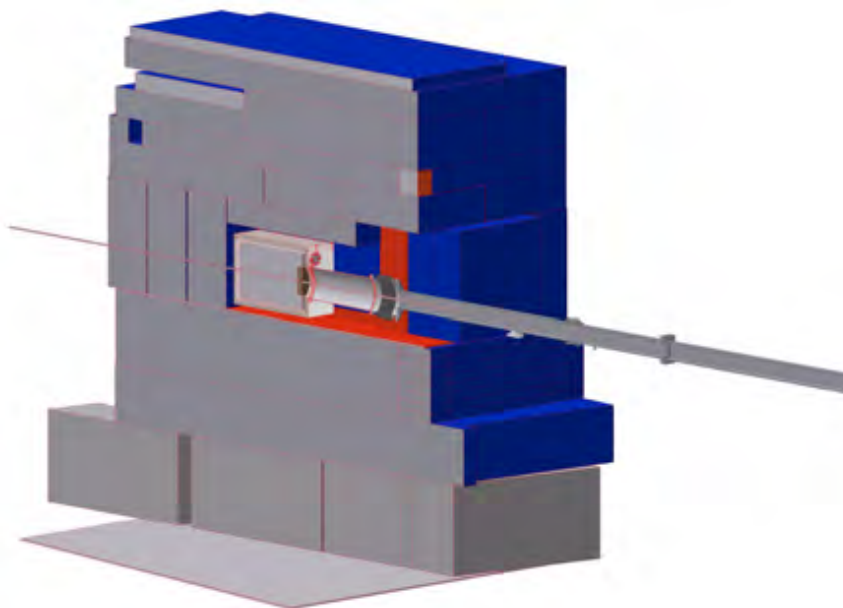


Figure 2.4.: CAD drawing of the beam dump

2.1.5. The target

To place the carbon target in the beam pipe, an aluminum extension was attached to the beam-pipe. The target - a carbon disk with a diameter of 3 cm and a thickness of 2 cm - was held in the center of the CB via a Rohacell frame and was placed inside a carbon-fiber tube. This tube was attached to the aluminum extension.

2.1.6. γ intensity monitor

The **Gamma Intensity Monitor (GIM)** is situated behind the MiniTAPS detector. It was designed to detect photons that did not producing hadronic reactions in the target. The measurement of the photon flux provides an essential information for cross section measurements.

The detector consists of a 4x4 PbF₂ crystal block (see Figure 2.5). The incident particles generate electromagnetic showers³ and the shower particles generate Cherenkov light. This light is read out by PMTs.



Figure 2.5.: CAD drawing of the γ Intensity Monitor.

2.2. The CB-MiniTAPS experiment

The CB, the FWPlug and the MiniTAPS are electromagnetic calorimeters built around the target in order to detect decay products of short-lived hadronic states. These detectors provide spatial and energy information of these decay products. Except for the CB, also time information is provided by these detectors which is used to find coincidences between related hits in the calorimeters and the tagger. It can also be used to measure the **Time-of-Flight (TOF)** of certain particles at forward angles where the distance is sufficiently large to resolve the TOF information. The spatial information, i.e. where a particle hits the detector, together with the energy information can give the four-vectors of the particles.

Particles which have a long enough life time to reach the detectors can interact with the detector material in different ways:

- **Hadrons (p, n, π^\pm):**

The charged hadrons lose energy primarily via elastic and inelastic collisions which is described by the Bethe-Bloch formula. The energetic hadrons ($\beta\gamma \approx 3$), however, become minimum ionizing and the energy deposition in the detector will be independent of the kinetic energy of the hadron.

The neutral hadrons (neutron) interact with the detector material purely by nuclear interactions, thus the deposited energy reflects the emission of the energy from these nuclear

³In High Energy Physics, a shower is a cascade of secondary particles produced as the result of a high-energy particle interacting with dense matter. In an electromagnetic shower electrons and positrons generate photons via bremsstrahlung and photons generate electrons and positrons via pair-production.

2. Experimental setup

reactions and not the kinetic energy of the neutron itself. Charged hadrons also can generate nuclear reactions.

- Electromagnetic particles (e^\pm, γ):
These particles lose energy via generation of electromagnetic showers.

From the measured four-vectors of the decay products, that are typically photons, the decaying particle can be reconstructed by means of an invariant mass analysis. If a decaying particle with mass M and momentum P decays into decay products with mass $m_{0\dots N}$ and momenta $p_{0\dots N}$ then

$$(Mc^2)^2 = \left(\sum_{i=0}^N E_i \right)^2 - \left(\sum_{i=0}^N \vec{p}_i c \right)^2. \quad (2.8)$$

For example, in case of a two-body decay:

$$M = \sqrt{(m_1^2 + m_2^2 + 2 \cdot (E_1 \cdot E_2 - \vec{p}_1 \cdot \vec{p}_2))}. \quad (2.9)$$

If the final state particles are photons ($m_{1,2} = 0$ and thus $p = E$) the expression is simplified to

$$M = \sqrt{(2|p_1| \cdot |p_2|(1 - \cos \alpha))}, \quad (2.10)$$

where α is the angle between the two decay products.

2.2.1. The Crystal Barrel detector

The Crystal Barrel experiment ran at the **Low Energy Antiproton Ring (LEAR)** at the **Conseil Européen pour la Recherche Nucléaire, European Organization for Nuclear Research (CERN)**, from 1989 until the end of 1996 and studied antiproton-proton and antiproton-deuterium annihilations at rest and in flight. The detector is a nearly 4π , high resolution system for charged particles and photons. One of the main goals of the experiment at CERN was to search for gluonic excitations in the meson spectrum. This includes glueballs and hybrid mesons. From 2001 the CB was installed at ELSA and has been primarily used to investigate baryon resonances.

The Crystal Barrel detector was built to detect photons and charged particles with high efficiency, good energy- and spatial resolution over a wide energy range from 20 MeV to 2 GeV. The spatial resolution of the detector is better than 1.5° and the energy resolution is given by

$$\frac{\Delta E}{E} = \frac{2.5\%}{4\sqrt{E}} \quad (2.11)$$

[Wen09]. The CB covers polar angles from 30° to 156° and full 360° in azimuthal angles (see Figure 2.6). It consists of 1230 CsI crystals with Tl doping in order to improve the light output. Each crystal has a length of 30 cm which corresponds to about 16 radiation lengths (see Figure 2.7). The crystals are arranged in 20 rings of 60 crystals per ring and one ring of 30 crystals at the most backward angle. Thallium impurities act as wave length shifter for the emitted scintillation light and due to this effect the light output is “increased” because the reabsorption of the wavelength-shifted light in the crystal is suppressed [Hor05].

Each crystal is mounted in a titanium case for mechanical stability and wrapped in capton foil for electric insulation. The crystals are read out with photodiodes. To match the wavelength of the scintillation light of the crystals to the sensitive area of the photodiode, a wavelength-shifting

plastic of 3 mm is placed between each crystal and the photodiode. Due to the long rise time of the signal ($\sim 2\mu\text{s}$), time information from the CB detector is not used. For ensuring the stability of the gain each crystal is irradiated with a xenon-flashlight based light-pulser system which runs several times per day at dedicated runs.

In order to allow access to the target and the *Inner Detector*, the Crystal Barrel is divided into two independent halves.

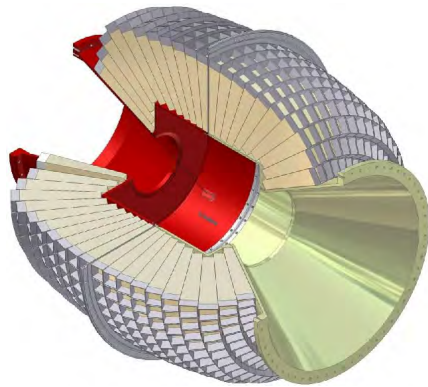


Figure 2.6.: CAD drawing of the Crystal Barrel detector

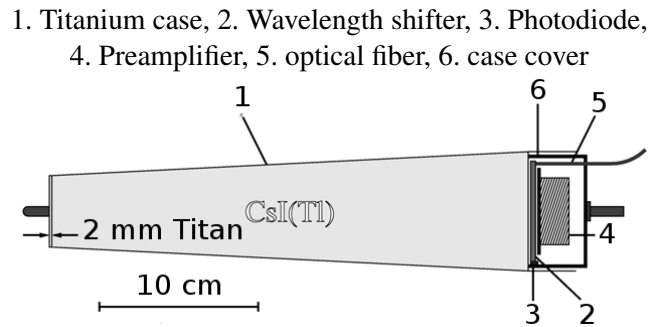


Figure 2.7.: The construction of one module of the Crystal Barrel

2.2.2. The Inner Detector

The Crystal Barrel detector is not suited to distinguish between charged and neutral particles. To make it possible, the Inner Detector is installed inside the CB.

The Inner Detector consists of 513 scintillator fibers with a diameter of 2 mm, which are arranged cylindrically in three layers around an aluminum frame (see Figure 2.9). Two layers of the fibers run with $+25.7^\circ$ and -24.5° declination to the beam direction, while the third one runs parallel to the beam.

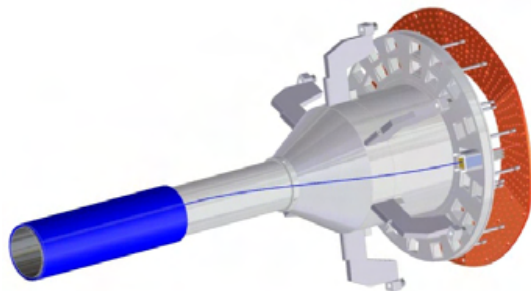


Figure 2.8.: The Inner detector

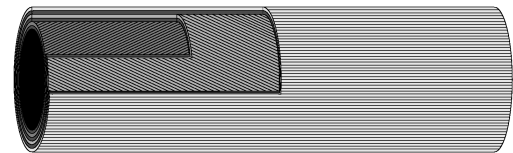


Figure 2.9.: Arrangement of the layers of the Inner Detector

The fibers are read out with 16 channel multi-anode photomultiplier tubes. This detector provides time and - if more than one fiber fires - position information. Energy is not read out.

The detector absorbs the low energetic electromagnetic background and protons with moderate kinetic energy up to 35 MeV [Els07]. In addition protons with smaller kinetic energy than 90 MeV

2. Experimental setup

cannot reach the crystals because they are absorbed in the Inner detector and in the holding frame of the Crystal Barrel.

The detector is 40 cm long and covers the whole 2π azimuth and the polar angles between 16° and 164° [Gru06] (see Figure 2.8).

2.2.3. Forward Plug

In the former beamtimes between 2001 and 2003 the forward region is covered by the MiniTAPS detector. In the setup from 2007 only the central $\pm 10^\circ$ (in polar angles) is covered by MiniTAPS. The acceptance hole between 10° and 30° polar angle is covered by the FWPlug detector.

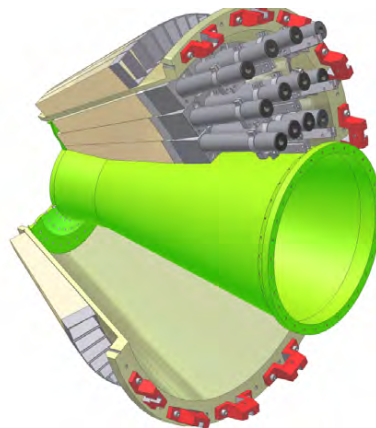


Figure 2.10.: CAD drawing of the FWPlug detector

The detector consists of 90 Tl-doped CsI crystals in 3 rings, covers the 12° - 30° polar angles and 0° - 360° azimuthal angles (see Figure 2.10). In front of the crystals scintillator-plates are installed, in order to enable the discrimination between charged and neutral particles. The scintillation-light is read out with PMTs coupled to the crystals by plastic light-guides. The detector provides spatial-, energy- and time information.

2.2.4. The MiniTAPS detector

The MiniTAPS detector was designed and developed in 1987 by a collaboration of seven institutes. The name originally meant **Two Arm PhotoSpectrometer** referring to the arrangement of the detector-elements at GSI (Gesellschaft für SchwerIonenforschung mbH) in Darmstadt. Since 2006 the available 528 crystals are split into two parts. 216 crystals form the MiniTAPS forward wall in Bonn, the rest of the crystals are used to build a similar kind of forward wall in Mainz.

The MiniTAPS in Bonn

The MiniTAPS detector covers the most forward angles from 1° to 10° - 12° degrees⁴. The detector was originally designed to reach two goals:

- It should be able to detect photons (the decay products of neutral mesons) with great efficiency and good energy- and time-resolution. It also has to detect charged particles.

⁴This value depends on the distance between the detector and the target.

- MiniTAPS was designed to be easily transportable to make the operation possible at different sites.

To fulfill the first requirement MiniTAPS is built of BaF₂ crystals with a plastic scintillator in the front. The BaF₂ has a good energy resolution of

$$\frac{\sigma}{E_\gamma} = \frac{0.59\%}{\sqrt{E_\gamma}} + 1.9\% \quad (2.12)$$

[G⁺94] with a time-resolution of Full Width of Half Maximum (FWHM) $\Delta t = 170$ ps [Nov92]. BaF₂ has two different scintillation components, a fast one and a slow [See table 2.1].

scintillation component	decay constant [ns]	wavelength [nm]	light output
slow	620	320	20%
fast	0.6	220	4%

Table 2.1.: Properties of the slow- and fast component of the BaF₂ scintillation light
The light output is compared to the light output of NaI(Tl)

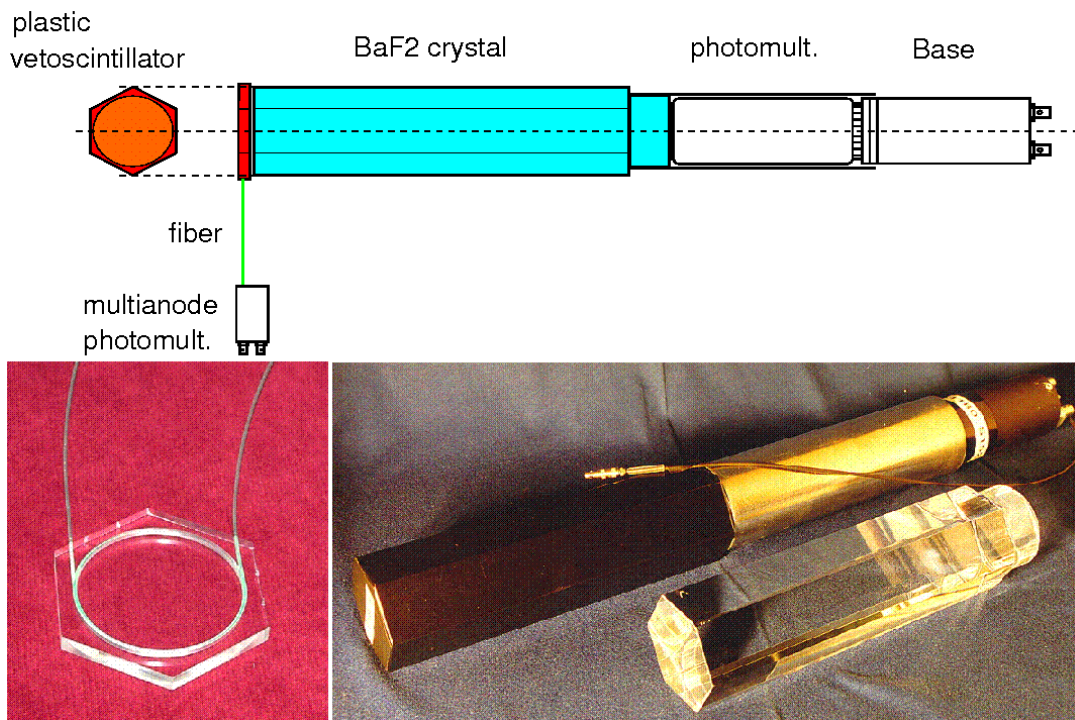


Figure 2.11.: The TAPS module consists of a BAF₂ crystal and a plastic veto.

Because the scintillation light depends on the ionization density and since different particle types populate the luminescence centers with different probability, this behavior allows the use of BaF₂ for particle identification. At ELSA in Bonn the MiniTAPS detector consist of 216 detector modules. Each module are made up of a BaF₂ crystal and a plastic veto. The crystals have two parts:

2. Experimental setup

a cylindrical part with a length of 25 cm and a diameter of 54 mm for the connection to the PMT and the hexagonal part where most of the light-generation happens. The hexagonal part is 225 mm long. The total length is 25 mm, which corresponds to 12 radiation lengths⁵, and its diameter measures 59 mm (see Figure 2.11).

To decrease the loss of photons, all the crystals are wrapped in several layers of Teflon foil (Tetra-tex PTFE 1.5 mil) and one layer of aluminum foil. In order to have a better optical connection between the crystals and the PMTs, optical grease (Baysilone 300000) is used. The crystals and the PMTs are mechanically tied together by heat-shrinking tubes. Altogether there is about 1 mm dead material between the crystals. The PMT is covered with Mu-metal to shield the magnetic fields that can affect the electron collection mechanism of the PMTs.

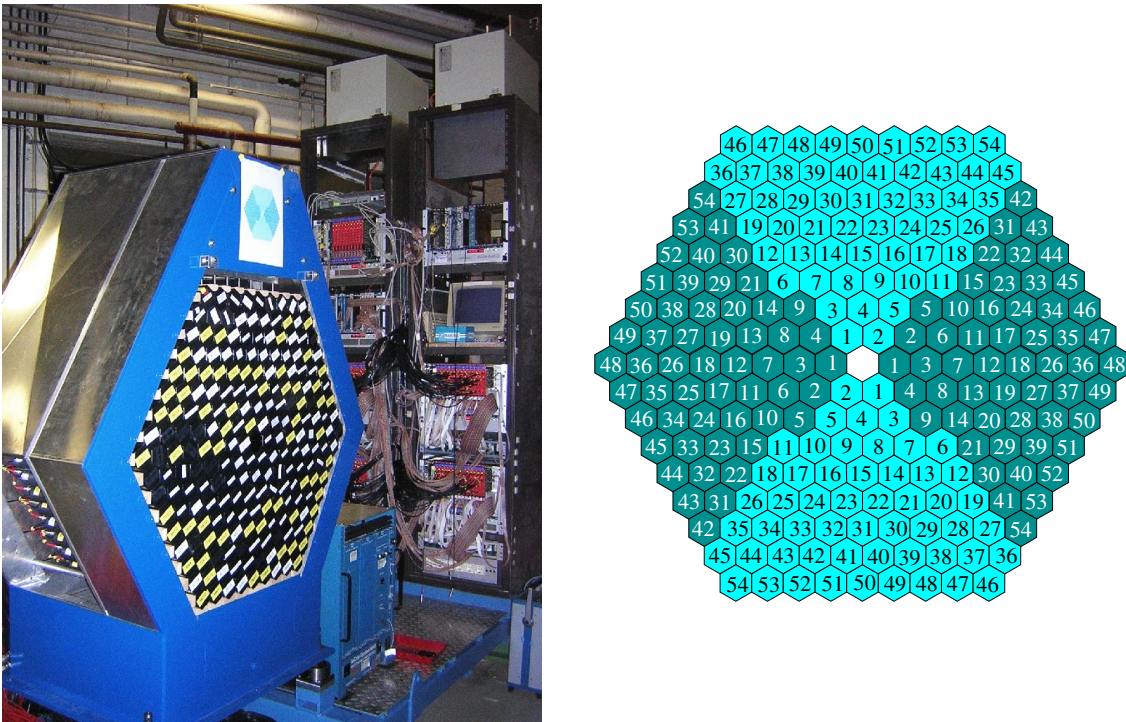


Figure 2.12.: Arrangement of the crystals in the MiniTAPS Wall. One crystal is removed for the center of the setup. Through this hole photons which did not generate hadronic reactions will leave the setup.

The Veto detectors are arranged in a separate wall in front of the crystals and aligned carefully. Each plastic veto consists of a 0.5 cm plastic scintillator (NE 102A) which is read out with 16 channel PMTs. To match the scintillation light to the sensitive range of the PMT, wavelength-shifting fibers (Bichron BFC92) are used to transfer the light of the plastic scintillator to the PMTs. The very forward region has to cope with a very high rate of electromagnetic particles, the middle part of the veto wall is read out with special PMTs designed for standing high particle rates (so called “Booster-base” PMTs).

The 216 detectors are arranged in one big hexagon-shaped wall configuration where the crystals are parallel to each other and to the photon beam (see Figure 2.12). The MiniTAPS detector

⁵The *radiation length* is the average length in a specific material in which an *electron* will lose all but 67% of its energy by bremsstrahlung.

located 233 cm far behind the target.

2.3. The aerogel Cherenkov detector

Because of the forward boost, a large fraction of the particles will be ejected into the forward direction in the lab-system. These ejectiles are electron-positron pairs from the conversion process ($\gamma \rightarrow e^+ + e^-$), energetic knocked-out electrons (δ -electrons) and charged pions. These particles have to be suppressed to make the detection of the forward-going protons more reliable. To distinguish between fast protons and other fast forward-going charged particles, a silica aerogel based Cherenkov detector was inserted between the MiniTAPS detector and the CB (see Figure 2.13).

The used aerogel, which has a density of 0.18 g/cm^3 , and an index of refraction of 1.05, was produced in Japan by the Matsushita Electric Work. 88 aerogel sheets were arranged in 4 layers in a box with dimensions of $60 \times 60 \times 27 \text{ cm}^3$. The inside surface of the box was coated with diffuse reflective paint (Spectrafect) and the generated light was read out with 12 photomultipliers [Kus07, Mat07] (see Figure 2.14).

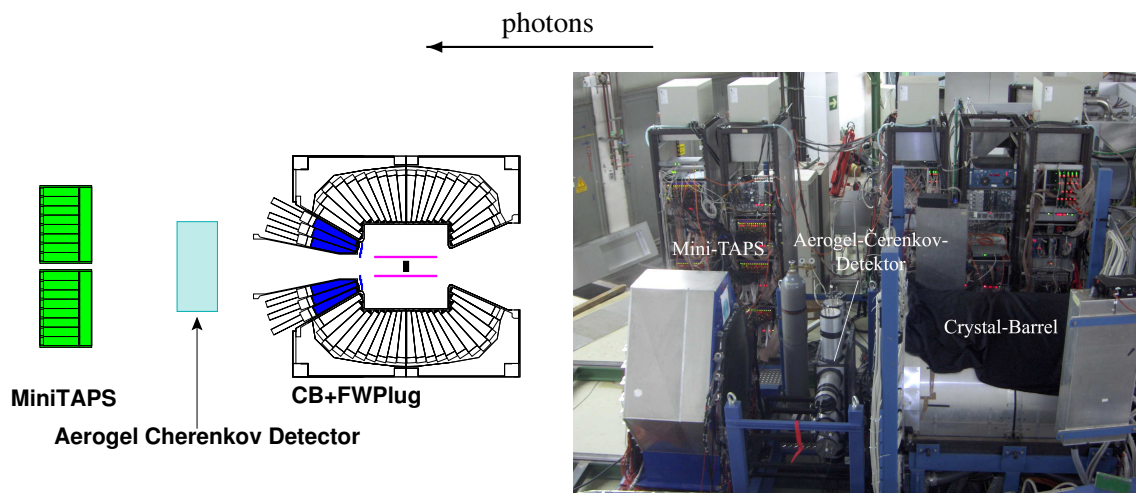


Figure 2.13.: Aerogel Cherenkov detector installed in Bonn

If a charged particle has a velocity larger than $\beta = 1/n \sim 0.95$, it generates light in the detector material. Only a very small portion of the protons can reach this velocity at ELSA energies, while π^\pm s and electrons/positrons even with relatively low momenta fire the detector, so those particles can be discarded (see Figure 3.16). The efficiency of the detector, based on two independent measurements, was larger than 99% [Mat07, Fri07].

2.4. Electronics and data acquisition system

2.4.1. The tagger

All the scintillator bars are connected to **C**onstant **F**raction **D**iscriminators (CFDs) which are located close to the tagger. The resulting digital signal, after passing through a delay line and a



Figure 2.14.: The Aerogel Cherenkov detector. The aerogel tiles and some of the PMTs can be seen.

passive splitter, enters a multi-hit **Time-to-Digital Converter (TDC)** ($64ps/channel$) and a scaler. The TDC is used in *common stop* mode. This means that the TDC gate is opened whenever the trigger is enabled and stopped if a trigger signal is generated. If there is no signal within 300 ns an overflow signal is set.

2.4.2. The Crystal Barrel

The signals coming from the photodiodes pass pre-amplifiers, which are placed at the back of the crystals, and are sent to a **Charge-to-Digital Converter (QDC)**. The total charge is split into two energy ranges. 80% of the signals go to the low-range input covering the energy up to 200 MeV, 10% of it into the high-range input, which covers the energy up to 2 GeV. The rest of the signal is used for internal pedestal correction. The QDCs are read out by a VMIC computer running Linux, on a VME compatible board. Two modules are used: one of them is responsible for the upstream, the other for the downstream half of the Crystal Barrel. Both VMIC computers built their sub-events and sent them via **Transmission Control Protocol/Internet Protocol (TCP/IP)** to a central event builder.

A detailed description of the system can be found in [Sch04].

2.4.3. The Inner Detector

The signals from the Inner Detector are read out using multi-cathode photomultipliers. The PMTs are connected to the trigger electronics being able to determine how many of the layers detected a hit. The signals of every fiber connect to the TDC provided only time, but no energy, information.

2.4.4. The MiniTAPS

The electronics of the MiniTAPS is based on a VME-compatible mother board (CAEN-V874) and on a - so called - piggy-back board which is mounted on top of the mother board. All electronic components for the readout - discriminators (2 Leading Edge Discriminators (LEDs) and one CFD), 4 Charge-to-Analog Converters (QACs), Analog-to-Digital Converter (ADC), Gate Generator and Time-to-Analog Converter (TAC) - are mounted on the piggy board [D⁺03].

The signal coming from the photomultipliers is distributed to the discriminators and four integration circuits. All discriminator signals are connected to the logic unit of the board (PLD).

The PLD generates a bit-pattern to label the event in the data stream and an integration gate. It handles as well the slow control of the discriminator settings, the width and the timing of the signal, the reset functions for the fast clear and the busy signal.

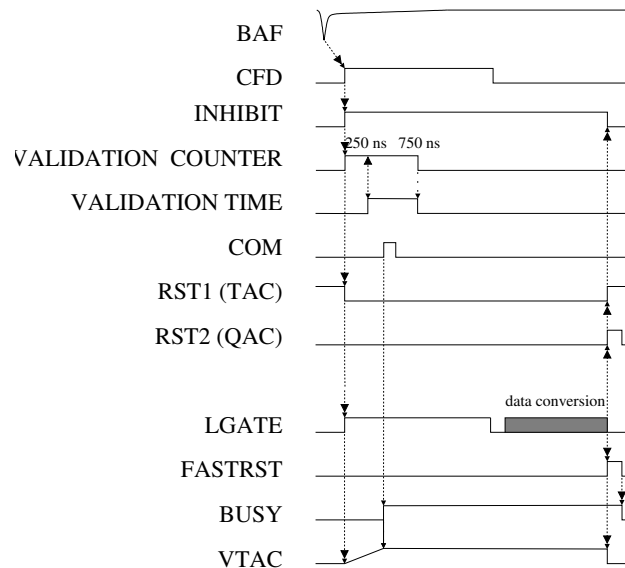


Figure 2.15.: Readout of the MiniTAPS detector

The signal of the CFD initiates the readout. It generates an integration window of $2 \mu\text{s}$ for the digitization of the BaF_2 pulse. Simultaneously, an output signal for the Multi Coincidence Unit (MCU) is generated. If this trigger signal is in coincidence with the first level trigger of the experiment, then a COM signal has to arrive 250 ns later within a 500 ns time window. In case of a positive trigger decision, the detector information of all channels gets digitized and stored. The described read out mode is called *common stop* mode. If a COM signal does not arrive within the time window of 250 ns-750 ns, a fast clear will be executed. The fast clear takes $1.8 \mu\text{s}$. If the readout is triggered by a not physical event then the QACs will integrate no charge. This generates the pedestal.

One board can handle 4 channels. One VME-crate reads out one sector of the MiniTAPS consisting of 54 channels as it is shown in the Figure 2.12. In one crate there are one VME computer, one synchronization module, and 14 readout boards (2 channels of the electronics are reserved as spare). For more details see [D⁺03].

2.5. Trigger

Since the data acquisition system is not fast enough to record all events registered by the detector, and because many events come from background processes like photon conversion, δ -electrons, etc., a dedicated trigger system has to decide on-line whether an event is worth storing on disk. Incorrect definitions cannot be revoked and therefore can cause a drastic reduction of statistics and large acceptance holes.

The main trigger used in the experiment consists of two levels:

First-level trigger: This is the first, fast part of the decision making. Whether the digitization of all values starts, depends on this decision.

Second-level trigger: During the digitization, more time is available for the second-level trigger to decide whether or not to read out the event. The longer time span ensures that the second-level trigger can be more complex.

The reason, why the first-level trigger needs to be fast, is, that a logic decision has to be made before the analog signal reaches the readout electronic passing through a delay line of some hundred ns. The first level trigger is made by the Tagger in coincidence with the FWPlug and/or the MiniTAPS. The CB cannot contribute to the first level trigger because of the slow signal rise-time of the photodiodes. The digitization process needs a certain time of the order of 1 ms and thus more time is available for making the decision. As a consequence, the CB can supply a signal to the second level trigger.

2.5.1. First-level trigger

The FWPlug, the MiniTAPS and the Tagger are the detectors that contribute to the formation of the first level trigger. The FWPlug provides two signals:

FWPlug1: at least one particle hit was registered in the FWPlug

FWPlug2: at least two particle hits were registered in the FWPlug

The MiniTAPS provides three signals:

TAPS1: at least one particle hit was registered in MiniTAPS with an energy higher than the LED_high threshold

TAPS2: at least two particles hits were registered in MiniTAPS with an energy higher than the LED_low threshold

TAPS3: pedestal pulser fired

The first level trigger is generated by the combination of these signals in coincidence with the Tagger.

2.5.2. Second-level trigger

Due to the long rise time of the signal of the photodiode, CB cannot be used in the first level trigger. However, the second level trigger needs more decision time, consequently the information from the CB can also be used for triggering purpose.

The number of the registered hits in the CB is determined by the **FAst Cluster Encoder (FACE)**. The FACE algorithm needs $\sim 10 \mu s$, therefore it is fast enough to contribute to the second level trigger, but too slow for pre-triggering purpose.

Two different types of triggers were applied. The *carbon_omega_prime* was triggering if **at least** 3 particles hit the setup, while in case of **more than** 3 hits *carbon_omega* is generating a trigger. The detailed trigger condition can be found in Table C.1.

2.5.3. Stand-alone trigger

Before the beamtimes, a special trigger condition was used to collect cosmic μ data for calibration purposes. If the read-out energy reached the *LED_low* trigger-threshold in any of the MiniTAPS crystals or the pedestal pulser was firing, then a trigger was generated. This trigger did not involve any other detectors.

2.6. Parameters during the experiment

The experiment took place between 4th and 26th of March 2007. The beam current was about 0.3 nA, the collimator had a diameter of 7 mm and the target was made of carbon with a thickness of 2 cm and a radius of 1.5 cm. The *LED_low* threshold was set to 80 MeV, *LED_high* threshold was set to 120 MeV except for crystals in the innermost ring where no detectors contributed to the trigger. The main parameters of the experiment are summarized in Appendix C.

2. *Experimental setup*

3. Data analysis

Contents

3.1. Calibration	44
3.1.1. Time calibration	44
3.1.2. Energy calibration of the tagger	46
3.1.3. Energy calibration of CB and MiniTAPS	48
3.1.4. LED calibration	56
3.2. Reconstruction of primary particles, mesons and reactions	57
3.2.1. Reconstruction of the energy of primary particles	57
3.2.2. Reconstruction of primary particles	59
3.2.3. Suppressing random time coincidences	64
3.2.4. PEDs and preselection	66
3.2.5. Identification of the reaction	68
3.3. Offline analysis chain	71
3.3.1. Kinematical cuts on the neutral decay channel of the ω meson	71
3.4. Simultaneous fit of the $m_{\pi^0\gamma}$ and the $E_{\pi^0\gamma}$-m_{ω}^{PDG} distributions	74
3.5. Simulation	75
3.5.1. Simulation of the kinematics	76
3.5.2. Particle tracking with GEANT	78
3.5.3. Event generators	80
3.5.4. Background channels of the neutral decay channel of the ω meson	82
3.5.5. Background rejection techniques	86
3.5.6. Simulation of the conversion channels	90
3.6. Detection efficiency	95
3.6.1. Determining the detection efficiency	97

Chapter summary

If a particle interacts with the detector material energy, time, and spatial information can be obtained from the detector, which are to be explained:

- The major part of the setup is an electromagnetic calorimeter based on scintillating materials. Most of the scintillators behave in a nearly linear fashion with respect to the deposited energy.

The Tagger measures energy as well, however, that is supplied by a position information.

- The position of a hit can be determined exploiting the segmentation of the detectors. If a particle is generated at a more or less well defined center-point, the position of the hit can be transformed into the direction of the particle (in spherical coordinate-system: θ and ϕ). The achievable resolution in general depends on the size of the detector elements. However, if the particle generates an *electromagnetic shower* which extends to several adjacent detector elements then a “subpixel” resolution can be reached.
- The timing is always measured relative to a start time-signal, which is given by the trigger. However, the trigger has limitations as a time reference. Making time-differences between the different detector elements, the time uncertainties, given by the trigger, can be eliminated.
- The information of the LED modules is important for the hardware trigger. The precise calibration and the setting of the thresholds of the LED modules are essential for the accurate setting of the trigger conditions.
- Using CB, FWPlug and MiniTAPS in combination with plastic scintillators placed in front of them, allows for the discrimination of charged and neutral particles.

In order to obtain the required information, the raw data of the detector have to be transformed into useful physical units by means of calibrating the detector signal. Combining the calibrated information from different detector elements, short lived particles can also be identified via their decay products.

3.1. Calibration

The purpose of the calibration is to convert raw, digital information delivered by the detectors into physical units (energy, time, etc.). In this chapter it will be described how this conversion routine is carried out by means of time and energy calibration.

3.1.1. Time calibration

The purpose of the time calibration is to convert the digital signal from the TDC into physical time units. In a second step, the time information of the individual detectors have to be aligned in order to ensure that everything happening at the same time is measured at the same time.

To achieve this goal the following parameters have to be determined:

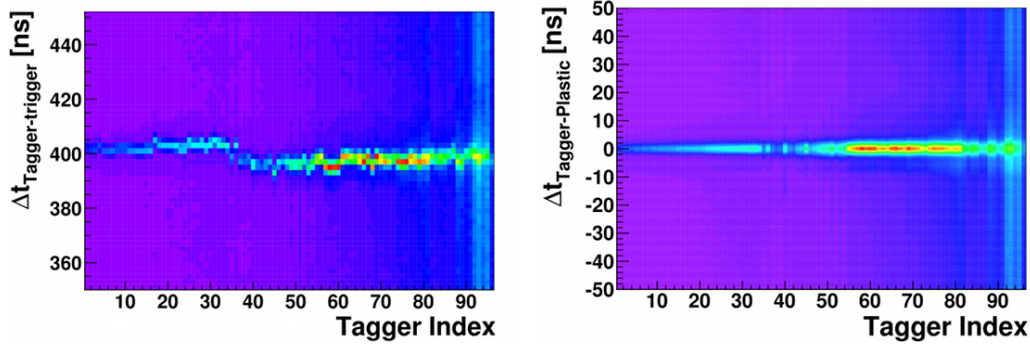
- The conversion factor between the output of the TDC module and the time unit (ns). This factor is defined by the electronics, however higher accuracy can be reached using a fine-tuning of this factor [Har08].
- The calibration offset that compensates the different signal times due to different cable lengths.
- If the TDC information depends on the signal shape and amplitude a time-walk correction has to be applied to compensate it.

Time calibration of the detectors

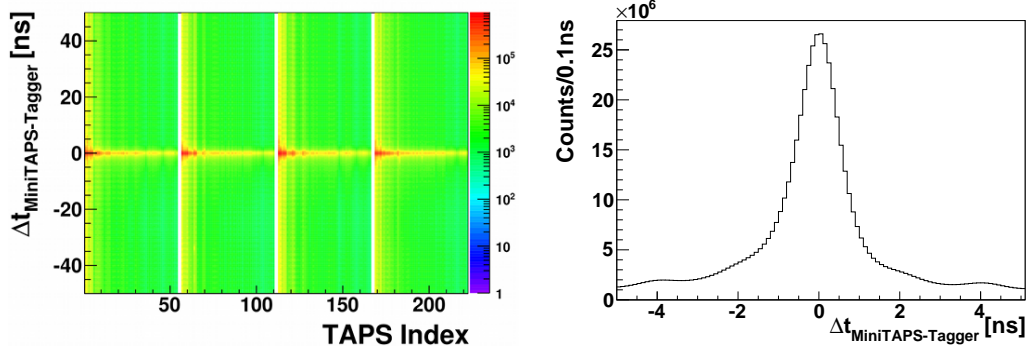
As a first step of the time-calibration, an appropriate time relation to a global time-reference has to be found. Using the trigger as time-reference is insufficient, because different trigger conditions need different decision times¹.

To eliminate the uncertainty in the time measurement caused by the trigger, a reference detector is used and all detector channels have to be aligned to this detector:

$$(t_{\text{detector}_1} - t_{\text{Trigger}}) - (t_{\text{detector}_{\text{Ref}}} - t_{\text{Trigger}}) = (t_{\text{detector}_1} - t_{\text{detector}_{\text{Ref}}}) \quad (3.1)$$



(a) $\Delta t_{\text{Tagger-trigger}}$ time spectrum before the first iteration of the alignment using the trigger (the Z-scale is linear)
 (b) $\Delta t_{\text{Tagger-Plastic}}$ time spectrum after the last iteration of the alignment using the plastic scintillator (the Z-scale is linear)



(c) $\Delta t_{\text{MiniTAPS-Tagger}}$ time spectrum after the last iteration of the alignment using the aligned tagger (the Z-scale is logarithmic)
 (d) Projection showing sharp peak on the $\Delta t_{\text{MiniTAPS-Tagger}}$ spectrum

Figure 3.1.: Time calibration of different detector part before the first iteration of the calibration and after the last iteration.

This detector can be considered an ideal one if it has only one channel and no time-walk (see Section 3.1.1). For this purpose a plastic scintillator was used which was mounted in front of the aerogel detector and was connected to a spare channel of the MiniTAPS electronics.

In course of the elimination of the trigger, at first, all the tagger channels were aligned to the

¹For example the trigger is generated within 300 ns if a particle arrives at MiniTAPS and/or FWPlug which detectors are involved in the generation of the first level trigger. CB cannot provide time information, thus it cannot contribute to the generation of the first level trigger. The second level trigger is generated by FACE within a time up to 6 μs .

plastic scintillator. The time difference between the scintillator and every single detector channel, including the tagger, is set to 0 by varying the offset of the given detector channel (see Figure 3.1). The time resolution of this plastic scintillator is, however, limited because of its relatively large size. To obtain a better time resolution, finally every detector channel is calibrated to the 96 scintillator bars of the tagger. Plotting the time difference between all the channels of the well calibrated tagger and the channels of the detector, the offsets can be determined. This calibration step is carried out for every single detector channel.

Time-Walk correction of FWPlug, γ Intensity Monitor and MiniTAPS-Veto

For certain detectors, for example Forward Plug or the veto detector of the MiniTAPS, the time information depends on the energy of the registered particle.

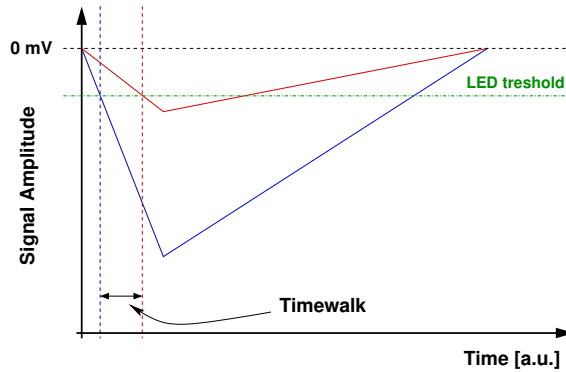


Figure 3.2.: Illustration of the time-walk effect. The red line shows the response signal of a low-energetic event crossing the threshold later than the high energetic blue signal.

This is a typical feature of the LED readout, which can be explained by the energy-dependent rise time of the signals (see Figure 3.2).

To correct for the distortion of the time information, the energy of well-selected² particles are plotted versus their Time-of-Flight ($\Delta t_{\text{detector}-\text{tagger}}$). The selection of fast particles ensures that the real time-of-flight of these particles are about the same. If an energy dependent time shift is observed this is due to the time-walk.

Fitting the projection of every energy slice with the sum of a constant and Gaussian function, the most probable time difference values can be plotted. This data is stored, and in course of the analysis the time-walk is calculated using a spline interpolation between the data points (see Figure 3.3 and Table 3.1). The achieved time resolution of the different detectors are summarized in the table 3.2

3.1.2. Energy calibration of the tagger

The calibration of the tagger is based on the energy measurement of recoiling electrons passing the well mapped magnetic field of the tagger magnet, and bent by the Lorentz force:

$$E_{e^-}^{\text{meas}} = pc = qBRc, \quad \text{for } p_{e^-} \gg m_{e^-} \quad (3.2)$$

²For example in case of the FWPlug, photons from π^0 decays were selected.

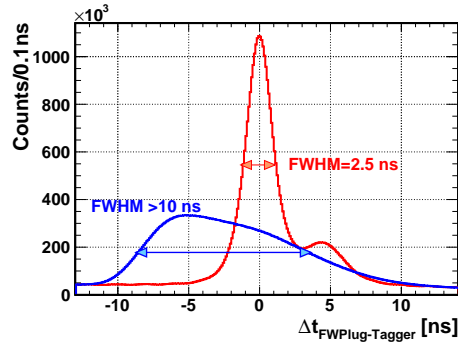
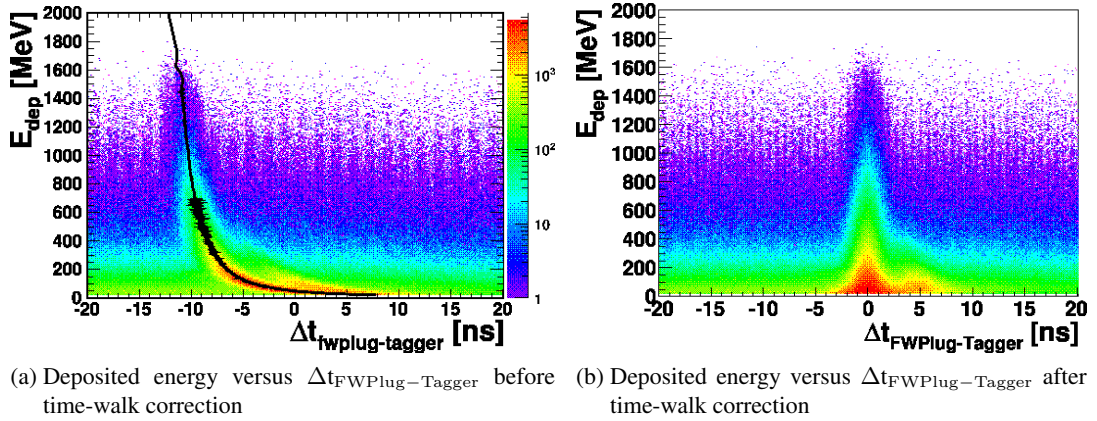


Figure 3.3.: $\Delta t_{\text{FWPlug-Tagger}}$ before and after applying a time-walk correction for γ s from π^0

Energy Range [MeV]	size of the energy-bin [MeV]
20 - 700	1
705 - 1475	10
1475 - 1925	50

Table 3.1.: Three energy ranges with the corresponding width of the energy bins for the time-walk correction.

where q is the charge of the electron, B stands for the magnetic field and R denotes the gyro-radius. Knowing the magnetic field and the gyro-radius (related to the position of impact of the electron) the energy of the electron can be determined. Combining this result with the known energy of the extracted electrons from ELSA, the energy of the generated photons is given by

$$E_{\gamma} = E_{e^{-}}^{\text{ELSA}} - E_{e^{-}}^{\text{meas}}. \quad (3.3)$$

For the calibration of the tagger, a low-intensity electron beam from ELSA was sent directly to the tagger hodoscope with fixed energies of 600 MeV, 650 MeV, 800 MeV, 1270 MeV, 1800 MeV

Detector	$\Delta t_{\text{detector-tagger}}$ FWHM [ns]	
Tagger	1.1	
Aerogel	7.6	
Forward Plug	without time-walk correction	>10
	with time-walk correction	3
Forward Plug veto	4.9	
Inner Detector	2.8	
MiniTAPS	1.4	
MiniTAPS veto	4.2	

Table 3.2.: Achieved time resolutions for the different detector parts.

and 2400 MeV. Varying the magnetic field, the electron beam hits different tagger bars. The tagger bar number is plotted against the energy of the photons and was fitted by a polynomial function. This expression was used to determine the energy of the photons via determining the energy of the scattered electrons (see Figure 3.4)[FP09].

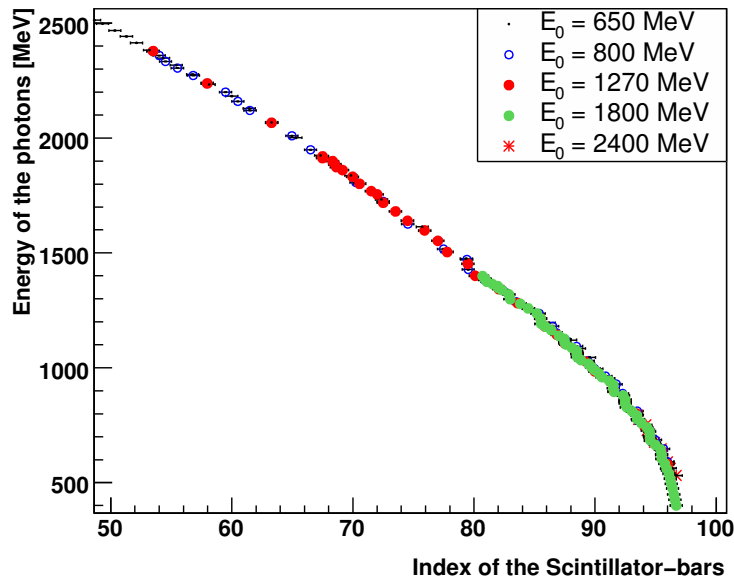


Figure 3.4.: The energy calibration of the tagger. The various data points correspond to the measurements with different beam energies.

3.1.3. Energy calibration of CB and MiniTAPS

Electromagnetic calorimeters measure the amount of scintillation or Cherenkov light which is proportional to the deposited energy and finally coded in digital signal. During the calibration, the uncalibrated digital values are transformed into calibrated physical energy units (MeV).

The calibration consists of four steps:

1. Pedestal determination for measuring the response of the electronics to a 0 MeV signal;
2. Calibration with cosmic muons/preliminary alignment, to provide a rough calibration in course of the data taking, and setting the dynamic range of all channels to approximately the same value.
3. π^0 calibration to have a more accurate (linear) correlation between the QDC channel number and the energy.
4. η calibration or correction function, to compensate energy losses.

Pedestal determination at MiniTAPS

To find the channel number that corresponds to the 0 MeV energy, the so-called pedestal, the detector modules have to be read-out regardless of any real physical event. In this case there is no light generation and the response of the electronics to the 0 MeV energy event can be found (see Section 2.4.4). In order to find events without light generation in the crystals, a trigger was generated periodically by a digital pulser, independently of the detector status. As a consequence, the read out energy most probably was 0 MeV in the majority of the modules. Whenever this artificial trigger happened, a flag was set in the data stream to label this event.

A clear correlation between temperature of the experimental hall and pedestal position was observed as it is shown in Figure 3.5. To be able to measure the pedestal position during the run, the pulser was set to a low frequency (≈ 1 Hz). The low frequency ensures that these pedestal events will not interfere with events generated by physical reactions.

After every run, the pedestal position is determined for all the crystals and the result is used for off-line correction.

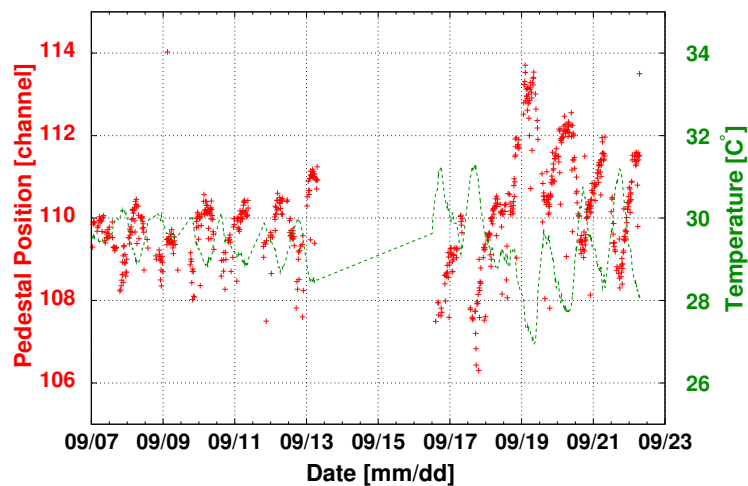


Figure 3.5.: The position of the pedestal peak and the temperature of the hall in a 16-day-period. Both the temperature and the pedestal position show a 24-hours period. The red dots shows the position of the pedestal, the green dashed line corresponds to the temperature.

Cosmic calibration of the MiniTAPS

In the initial raw form, the energy response of the detector modules are unrelated, and they can give very different responses for the same stimulus. The goal of the alignment is to set the detector elements in a way that they respond similarly to the same stimuli. As a result of this procedure, the same dynamic range³ will be set for every detector module and the alignment will serve as a good starting point for a high-precision calibration.

Cosmic muons were used to align the detector modules of the MiniTAPS. Since all crystals of the MiniTAPS are oriented horizontally, the high energy μ^\pm s deposit most probably the same amount of energy⁴ (37.7 MeV) in every crystal [Rob91]. If a dynamic range between 0 MeV and X MeV is needed the cosmic peak has to be set with the help of the expression:

$$\frac{Ch_{\text{cosmic peak}} - Ch_{\text{pedestal}}}{4096 - Ch_{\text{pedestal}}} = \frac{37.7}{X} \quad (3.4)$$

where $Ch_{\text{cosmic peak}}$ means the channel number at the maximum of the cosmic peak while Ch_{pedestal} stands for the position of the pedestal peak expressed by the channel numbers. The linear relation between the deposited energy and the measured QDC channel number allows the conversion of each QDC channel number into energy expressed by the relation:

$$Y = (Ch_Y - Ch_{\text{pedestal}}) \frac{37.7}{Ch_{\text{cosmic peak}} - Ch_{\text{pedestal}}} \quad (3.5)$$

where Ch_Y is the channel number at the unknown energy. The cosmic calibration has to be applied before every beamtime to check the gains of every crystal and, if it is necessary, to adjust them.

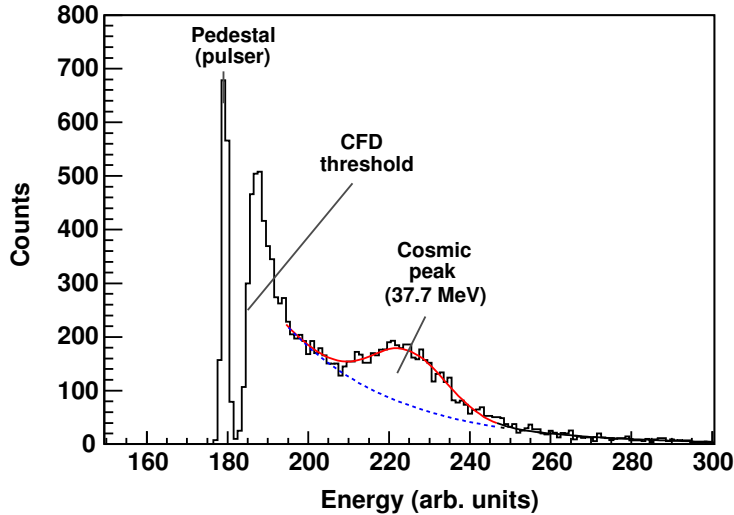


Figure 3.6.: Typical cosmic spectrum from MiniTAPS. The pedestal peak (0 MeV-energy peak), the CFD threshold and the minimum ionizing of cosmic muons are clearly recognizable.

³The dynamic range is the energy range between 0 MeV and the largest energy that the electronics can process.

⁴Cosmic muons are minimum ionizing particles, most probably travel from up to down and deposit energy while passing through the crystals laterally.

The gain, which is set by the cosmic calibration, is not very accurate for the following reasons:

- The position of the peak is determined by fitting the data with the sum of an exponential background and a Gaussian peak-function. This parameterization is not precise enough to use the resulting gain in a high-precision data analysis (see Figure 3.6).
- The described procedure is based on the energy deposition of the minimum ionizing cosmic muons, but the resulting gain has been used for **photons** that are not minimum ionizing particles.
- The linear dependence of the energy on the QDC channels was proven up to 790 MeV photon energy [G⁺94]. At ELSA, photons with much higher energies can be measured. The use of only two low energetic data points (pedestal at 0 MeV and cosmic peak at 37.7 MeV) is not sufficient to cover the whole dynamic range up to 1.8 GeV per crystal.
- Shower losses due to a finite detector volume and non-zero thresholds lead to systematic errors in the measurement of the energy. While shower leakage affects the measurement of high energetic photons, the finite CFD threshold has a larger impact when the deposited energy is smaller. These effects also have to be compensated during the calibration.

π^0 -calibration

The π^0 -calibration uses the precisely known invariant mass of the π^0 meson. By measuring the π^0 invariant mass, the energy of the participant photons can be corrected. The choice of π^0 for this purpose is obvious: it has a large production yield and a high branching ratio for the decay into two photons.

Assuming that the real energy of the photons is linearly depending on the measured energy: $E_{\text{real}} = C \cdot E_{\text{meas}}$. According to the calculation in Appendix D.1, the calibration constant can be determined as:

$$C = \left(\frac{m_{\pi^0}^{\text{PDG}}}{m_{\pi^0}^{\text{measured}}} \right)^2. \quad (3.6)$$

In the case of the CB, events are selected with arbitrary multiplicity and the invariant mass is calculated for every pair of photons where both of them are registered in the CB. The same procedure is followed throughout the calibration of MiniTAPS, but here only events with neutral multiplicity from 2 to 4 are processed (see Table 3.3) and the invariant mass is calculated only for photon pairs where exactly one of the photons is registered in the MiniTAPS.

These values are filled into histograms corresponding to the central crystal of the produced cluster. If one specific module is calibrated the other photon can be detected in any other crystal in the setup. Therefore the effect of this second module cancels out on average.

The invariant mass spectra are fitted in order to determine the position of the π^0 peak. The background of this distribution is fitted by a Chebychev polynomial of the first kind up to the 5th order⁵. Due to the incomplete registration of the shower (finite thresholds, energy leakage, etc.), the peak can be described as a Gaussian with a stronger tail on the low-energy side (see Figure 3.7). This asymmetric peak is fitted by the Novosibirsk function that is usually defined by:

⁵The Chebychev polynomial is defined by $T_n(z) = \frac{1}{4\pi i} \oint \frac{(1-t^2)t^{-n-1}}{(1+tz+t^2)} dt$

3. Data analysis

$$f(m) = A \exp(\tau^2 - 0.5 \cdot \ln^2[1 + \Lambda \tau \cdot (m - m_0)]/\tau^2), \quad (3.7)$$

where

$$\Lambda = \frac{\sinh(\tau\sqrt{\ln 4})}{\sigma\tau\sqrt{\ln 4}}. \quad (3.8)$$

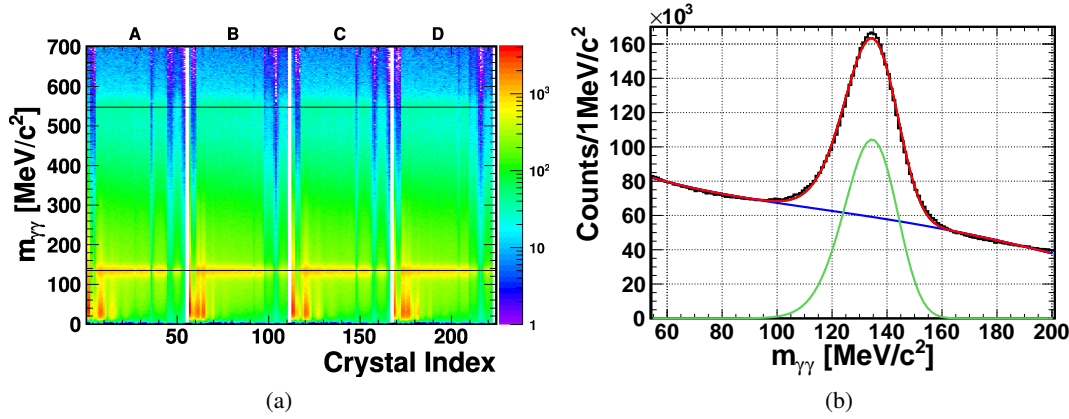


Figure 3.7.: (a) Two-photon invariant mass as function of the crystal index in TAPS. 56 channels belong to one sector, but only 54 are read out. This is the reason why the last two channels of the sectors do not hold any information.

(b) Full projection and fit of the histogram in the Figure 3.7a to the invariant mass axis. The peak appears at 134.5 MeV/c² and its FWHM is 22.7 MeV/c².

In the equation 3.7 m_0 is the position of the peak, the width is denoted by σ , and τ is the tail parameter [Str98, A⁺04]. This calibration step has to be applied iteratively (see Figure 3.8) for each crystal until the mass of the π^0 will appear in the required range between $0.99 \cdot m_{\pi^0}^{PDG} \leq m_{\gamma\gamma} \leq 1.01 \cdot m_{\pi^0}^{PDG}$.

Because of the geometrical arrangement of CB and MiniTAPS, the FWPlug partly covers the outermost crystals belonging to the MiniTAPS (see for example the crystals 46 and 54 in the sectors A and C in Figure 2.12). These crystals cannot be hit by photons directly. In the innermost ring the Signal-to-Noise ratio is very bad because of the high rate of the forward boosted electromagnetic particles. These crystals from the innermost and outermost ring could not be calibrated like the others, only an average gain was set which was deduced from the gain of the calibrated detectors.

η - or polynomial calibration/correction function

Since the ω meson has a larger mass than the π^0 or even the η mesons, it has to be confirmed whether the calibration is correct for photons from the decay of mesons with higher masses.

After the proper π^0 -calibration (see the previous section), a shift of the η mass can be observed (see Figure 3.9). To compensate this mass shift, a correction to the π^0 calibration should be applied. This can be the extension of the linear energy dependence to a second-order polynomial or a correction function can be applied.

Detectors	CB/FWPlug	TAPS
Participating detectors	(CB or FWPlug) - (CB or FWPlug)	(TAPS) - (CB or FWPlug)
number of photons per event	≥ 2	2 - 4
Special requirement for the selected photon-pairs	both photons are in CB or in FWPlug	one photon in MiniTAPS the other one is not in MiniTAPS
number of charged hits per event	no limitation	no limitation
other requirements	neutral hits with multiplicity = 1 are discarded	neutral hits with multiplicity = 1 are discarded ^a
	-	particle hits from $\Theta > 130^\circ$ are discarded ^b
		particles going to MiniTAPS were filtered by the Aerogel Cherenkov detector ^c

^aPotentially misidentified charged particles (identified as neutrals) were discarded.

^bFor the calibration of MiniTAPS, particle hits from the very backward angles in CB were rejected to suppress the electromagnetic background from the beampipe.

^cEvents in which a particle fired the Aerogel Cherenkov detector were ignored to reduce unwanted charged hits in MiniTAPS.

Table 3.3.: Differences between selection criteria for the energy calibration of CB/FWPlug and MiniTAPS

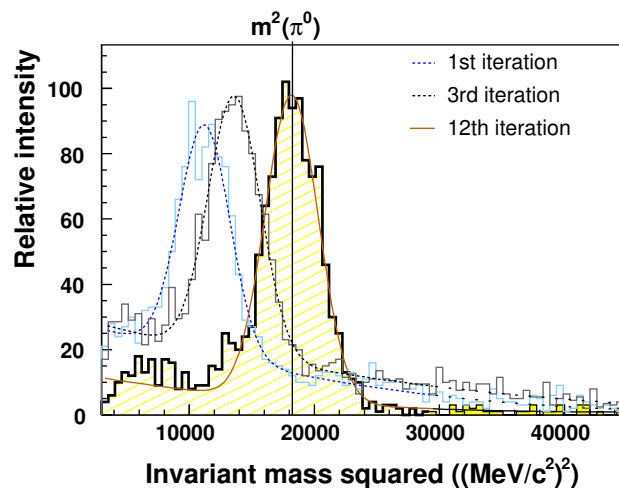


Figure 3.8.: Position of the π^0 peak in the Crystal Barrel after repeated iterations [Jun05]

η - or polynomial calibration The polynomial calibration extends the approximation of the linear energy-dependence to a second order polynomial:

$$E_{\text{real}} = C_1 \cdot E_{\text{meas}} + C_2 \cdot E_{\text{meas}}^2. \quad (3.9)$$

Using the precisely known mass of the π^0 and η mesons, the parameters of the polynomial can be extracted. In case of the calibration of MiniTAPS the calibration constants are (see the Appendix D.2.2)

$$\begin{aligned} C_2 &= \frac{R_\eta^2 - R_{\pi^0}^2}{E_{\eta_1} - E_{\pi_1^0}} \\ C_1 &= \frac{R_{\pi^0}^2 E_{\eta_1} - R_{\eta^0}^2 E_{\pi_1^0}}{E_{\eta_1} - E_{\pi_1^0}} \\ R_{\pi^0} &= \frac{m_{\pi^0 \text{PDG}}}{m_{\pi^0 \text{meas}}} \\ R_\eta &= \frac{m_{\eta \text{PDG}}}{m_{\eta \text{meas}}} \end{aligned}$$

C_1 is close to unity and C_2 is of the order of 10^{-5} - 10^{-4} .

If both photons are measured by the CB, the expressions are slightly different (see Appendix D.2.2). This correction was also used iteratively for each crystal until the invariant mass peaks of both π^0 and η were in the right position (see Figure 3.9).

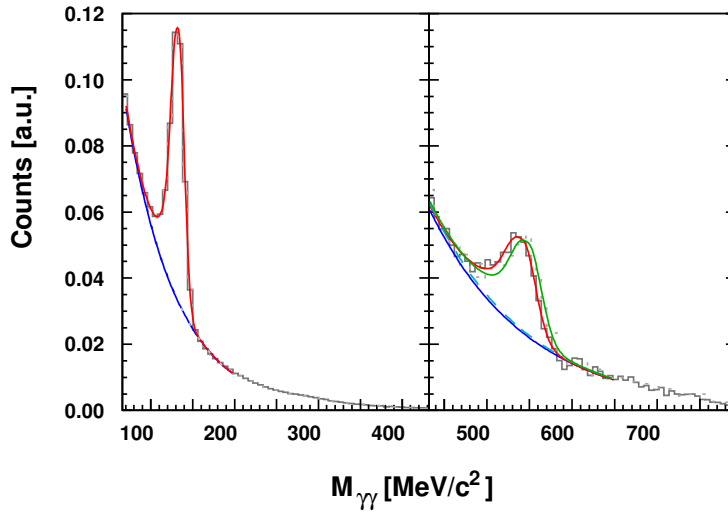


Figure 3.9.: The position of the π^0 (left) and η (right) before (green line) and after (red line) polynomial calibration. The position of the pion is unchanged, while the position of the η is shifted down roughly by 10 MeV to the nominal mass of the η mesons.

The polynomial calibration can be applied globally (one correction for the whole setup), ring-wise (each ring⁶ is calibrated separately) or crystal-wise (each crystal is calibrated separately).

⁶corresponds to a given polar angle range

Correction function Another way of compensating the shower losses is to simulate the energy loss with GEANT (see Section 3.5.2) in order to build a look-up table where the correction factor is expressed as a function of Θ , ϕ and E_{measured} :

$$E_{\text{real}} = E_{\text{measured}} \cdot f(\Theta, \phi, E_{\text{measured}}).$$

This formula is used for every photon hitting the detectors to calculate the real deposited energy from the measured one [Mul07, Dah08].

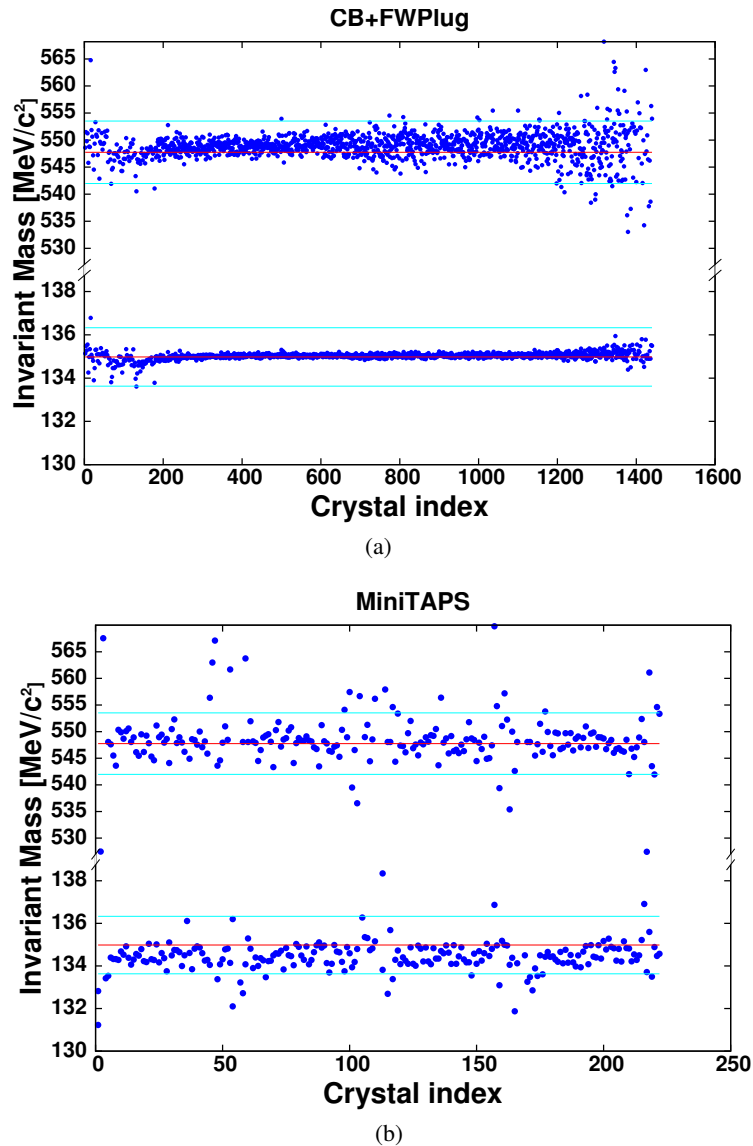


Figure 3.10.: Energy calibration check for each crystal.

The red lines show the position of the nominal masses.

(a) CB + FWPlug: Less than 1% of all crystals are outside the $\pm 1\%$ mass-range. The index range between 1 and 180 refers to the Forward Plug, (b) MiniTAPS: Roughly 10% of all crystals are outside the $\pm 1\%$ mass-range. For them the calibration was not possible (see Paragraph 3.1.3).

To calibrate the CB a correction function was used after the π^0 calibration. The MiniTAPS was calibrated using a polynomial calibration after over a calibration via a correction function.

Final check of the energy calibration

The accurate energy calibration is essential because imprecisely determined energies result in inaccurate invariant masses (see Figure 3.10).

The invariant mass of two photons as a function of the momentum of the two-photon pair is plotted in Figure 3.11. The peak positions of the π^0 and η was determined for 100 MeV/c-wide momentum slices projected on the invariant mass axis. The positions of the mesons masses are within $\pm 2\%$ around the nominal values [N⁺10], for momenta between 100 MeV/c and 1700 MeV/c. The error of the position determination is below 0.1% (see Figure 3.11).

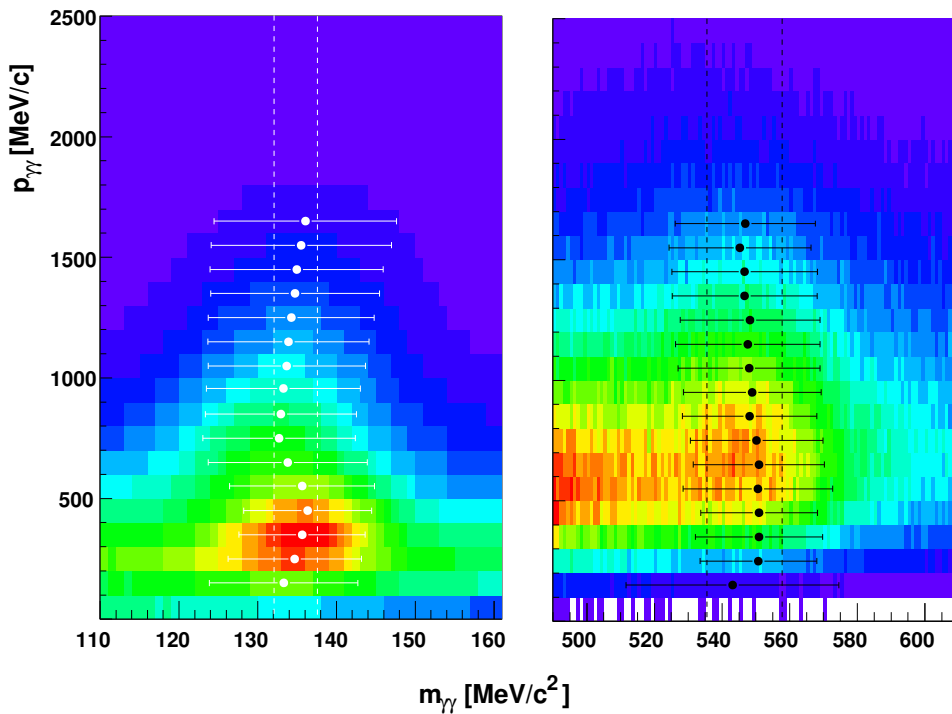


Figure 3.11.: Invariant mass of π^0 s and η s as a function of their momenta. The error bars show **not the fitting error** but the σ of the fitted peak.

The invariant masses are stable within $\pm 2\%$ in the momentum range of $100 \text{ MeV}/c \leq p_{\gamma\gamma} \leq 1700 \text{ MeV}/c$.

3.1.4. LED calibration

In the MiniTAPS electronics LEDs are applied to discriminate events below a certain energy threshold. Events with energy above the LED threshold generate a first level trigger (see Section 2.5).

The LEDs are usually calibrated before taking the data. At least three cosmic ray measurements were taken at different voltage settings on the LED modules⁷. The threshold can be determined

⁷These voltages are usually 30 mV, 50 mV, 70 mV, 100 mV

by dividing the energy spectrum where LED conditions were taken into account with the same quantity with disregarded LED condition. The threshold was set where the ratio spectrum reaches 90% (see Figure 3.12). A linear dependence has to be found between the set voltages (in mV) and the threshold values (in MeV) for every channel. With the help of this dependence the required threshold can be set.

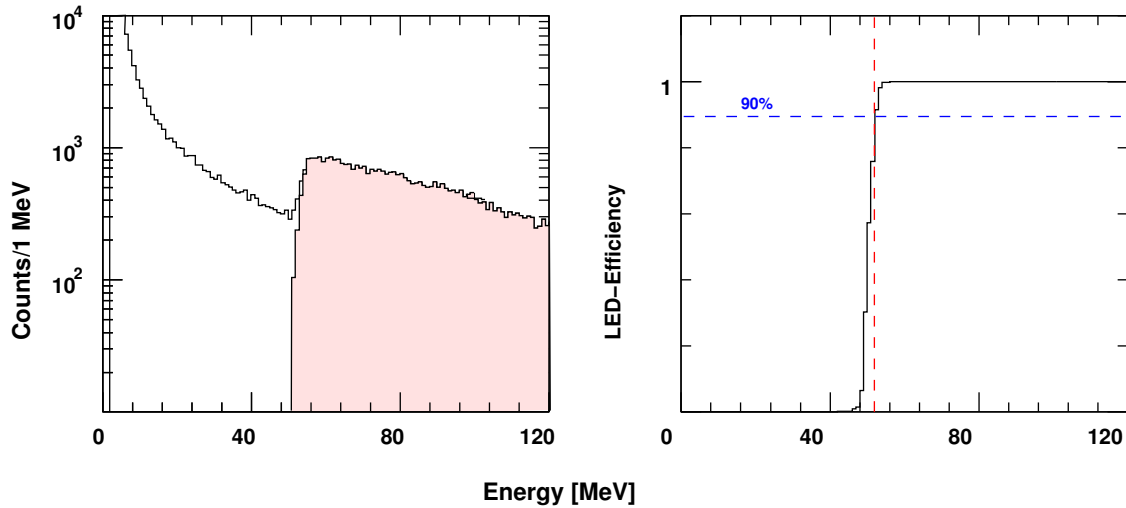


Figure 3.12.: Calibration of the LED threshold. On the left side the solid line illustrates the energy distribution with a very low LED thresholds, the pink area shows the energy distribution with a higher threshold. On the right side the ratio of the two spectra is shown.

3.2. Reconstruction of primary particles, mesons and reactions

After the calibration, the proper energy and/or time information is available for every detector component. The next step is the reconstruction of the four-vectors of the measured particles.

The life-time of neutral mesons (π^0 , η , ω , η' , ...) is so short that they decay before reaching the detector. However, the decay products of these particles will be registered and short-lived mesons can be reconstructed through their decay products. Both the MiniTAPS and the CB (together with the FWPlug) are suitable for measuring photons. This is one of the reasons why the neutral decay channel of the ω meson ($\omega \rightarrow \pi^0\gamma$) was chosen to study the properties of the ω meson in this thesis.

To reconstruct the mesons from the decay photons, the deposited energy and the direction of these photons have to be measured with the greatest possible accuracy.

3.2.1. Reconstruction of the energy of primary particles

When a particle traverses the detector material, it deposits energy in the crystals and thus will give rise to a local maximum in the detector. This group of responding crystals which measures the deposited energy of one single particle is called a **Particle Energy Deposit (PED)**.

In a more general case, several particles can hit the detector close to each other and create a

continuous group of responding crystals. This is a *cluster*. If one cluster is produced by the energy deposit of one single particle, then the names *PED* and *cluster* are interchangeable.

To sum up the energy in a cluster, one element of the cluster has to be found and consecutively all its neighboring elements have to be added to the cluster. Finally, if time information is available then all hits in the cluster should belong together not only in space, but also in time.

Correction for multi-PED clusters

If more than one PEDs are registered in one cluster, then the energy content of the crystals (first of all the crystals being located between two maxima) has to be recalculated because in these detector elements the energy deposition originates from two or more PEDs.

In order to separate them the lateral distribution of the electromagnetic shower is approximated by an exponential function which depends on the energy of the primary particle and the detector material (via its Molière radius R_M ⁸). In this case the deposited energy in the cluster can be determined by varying the positions and the total deposited energies of the contributing PEDs [Sei09] (see figure 3.13).

This method can only be applied if the shower development is symmetric because this is the

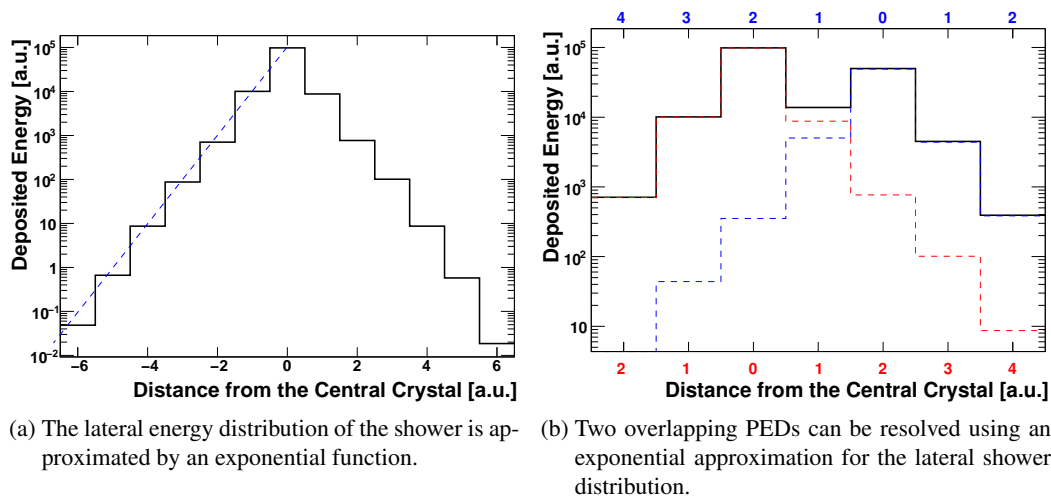


Figure 3.13.: Separation of two PEDs in a multi-PED cluster by using exponential functions to describe the lateral shower distributions [Sei09].

only case when the shape of the shower can be described with only one free parameter (namely the energy of the particle). In the MiniTAPS detector this symmetry requirement is not fulfilled because of the arrangement of the crystals (see Figure 2.12). Consequently this method cannot be used there. Fortunately, in the MiniTAPS only an extremely low number of multi-PED cluster is registered [Sei10], so those events can be safely discarded.

⁸On average only 10% of the energy lies outside the cylinder with radius R_M and 1% outside the cylinder with radius $3.5 R_M$

3.2.2. Reconstruction of primary particles

Reconstruction of the impact position for primary particles

After having the correct energy content of the PEDs, the reconstruction of the impact point of the particle is possible.

Photons, electrons and positrons Energetic photons, electrons and positrons generate electromagnetic showers and produce signals in several adjacent crystals. Using the energy distribution in the shower, the impact point of photons can be reconstructed more precisely than the granularity of the detector would allow for. In order to determine the Cartesian coordinates of the impact point, the coordinates of the given crystals in the PED have to be weighted with the energy deposition within that very crystal:

$$x = \frac{\sum_{i=1}^N W_i x_i}{\sum_{i=1}^N W_i} \quad \text{and} \quad y = \frac{\sum_{i=1}^N W_i y_i}{\sum_{i=1}^N W_i}$$

where $W_i = E_i$ and N is the number of the crystals in one PED.

However it turned out that detectors with low energy are weighted too strongly by this method. Therefore the weighting factor is not the energy but the logarithm of the energy [A⁺92, Mol92]:

$$W_i = \max\left\{0, \left[K + \log \left(\frac{E_i}{\sum_{i=1}^N E_i} \right) \right] \right\} \quad (3.10)$$

The constant K was determined by using a GEANT simulation [Cas06] and it is found to be 4 for BaF₂ and 4.25 for CsI.

This method presumes that the particle arrives perpendicularly to the surface of the detector and produces a symmetric cluster. This approximation gives a false result for clusters in the MiniTAPS, because the crystals are arranged parallel to the beamline thus the incident particles from the target strike the detector askew (see Section 2.2). As a result of this arrangement of the detector elements the developing a shower is tilted compared to the crystals and the reconstructed position reflects the location where the shower deposited the largest amount of energy and not the point of impact. To correct this inconsistency the impact depth⁹ of the shower has to be known:

$$Z = X_0 \left(\ln \frac{E}{E_C} + b \right), \quad (3.11)$$

⁹This quantity is also known as the center of gravity of the longitudinal shower distribution.

3. Data analysis

where E is the energy of the photon in MeV, E_C is the critical energy¹⁰, X_0 denotes the radiation length in the detector material and $b = 1.2$ for photons [Fer87].

The corrections dX and dY can be determined by the following approximation:

$$\frac{X}{X + dX} = \frac{Y}{Y + dY} = \left(\frac{R}{R + Z * \cos(\alpha)} \right), \quad (3.12)$$

where R is the distance between the target and the detector (see Figure 3.14).

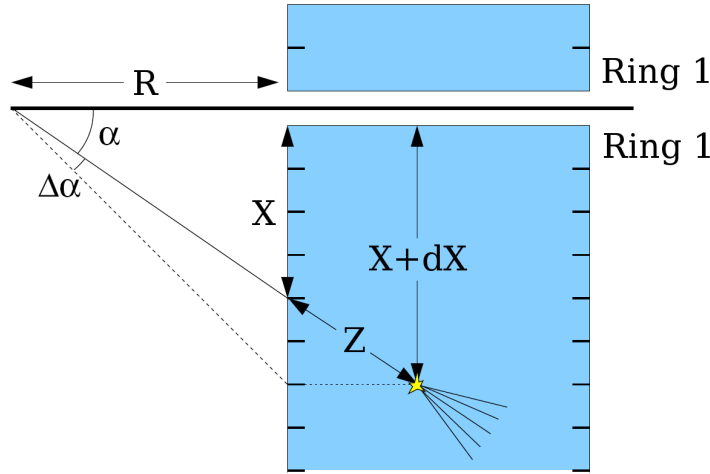


Figure 3.14.: Schematic drawing of the MiniTAPS forward wall located at a distance R behind the target. A systematic error is introduced in the position determination (dashed line) if a photon arrives askew and, due to the tilted shower development, the position appears at $X + dX$ from the beam axis while the real distance is X . The reconstruction routine corrects this effect by approximating the shower maximum in Z which depends on the energy of the photon.

If this method is used alone to reconstruct the impact point of particles in the MiniTAPS, there is a deviation of $\approx \pm 0.2^\circ$ between the original and the reconstructed direction of the photons according to GEANT simulations. This deviation depends on the energy and the impact point of the particle.

In order to make a correct a GEANT simulation was used. After generating and reconstructing photons with different energies and angles (pointing toward the MiniTAPS) a correction function can be constructed. The parameters of this function depend on the the azimuthal angle, the spherical angle and the energy of the photon. The function will show how large correction ($\Delta\theta(E_\gamma, \theta_\gamma, \phi_\gamma)$ and $\Delta\phi(E_\gamma, \theta_\gamma, \phi_\gamma)$) has to be applied to adjust the direction of the registered photon to the real one. Using this procedure an average deviation between the generated and reconstructed directions is reduced below 0.05° for 95% of the crystals was reached (see Figure 3.15).

¹⁰The critical energy is the energy of an electron when the ionization loss per radiation length is equal to the energy of the electron.

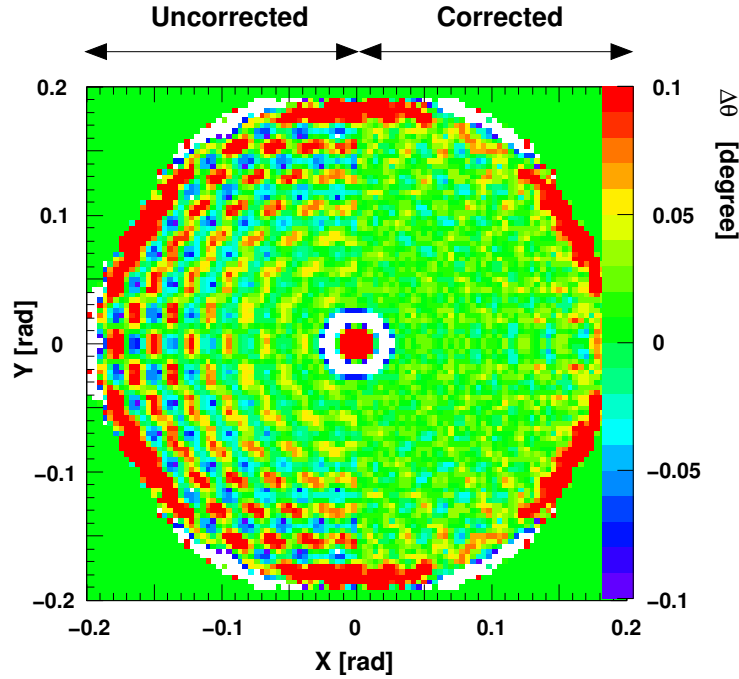


Figure 3.15.: The reconstructed hit position before and after using the correction function in MiniTAPS. The X and Y axes are expressed in radian ($x \approx X * R$, where R is set to 210 cm) and the color code marks the difference between the generated and reconstructed angles (for more details [Sei09]).

Protons and charged pions In most cases, these particles do not develop extended showers which spread over many detector elements. Often only one detector element contains all the deposited energy. In this case the best possible resolution is limited by the granularity of the detector, and the impact point of the particles will be placed in the center of the crystals.

If a charged particle hits the CB, it necessarily passes through the Inner Detector which is designed to detect charged particles efficiently. The fibers of the Inner Detector are arranged in three layers (See Section 2.2.2). If at least two fibers in two different layers respond, the crossing point of the fibers determines the point which corresponds to the particle track.

Each of the FWPlug crystals covers 6° in Θ and 12° in ϕ . This would mean that the granularity of the FWPlug detector is two times worse than the granularity of the CB detector. However, two layers of shifted plastic scintillators with angular coverage of $6^\circ \times 6^\circ$ in front of the FWPlug crystals allow to reach a spatial resolution of 6° in both Θ and ϕ for charged particles¹¹.

Particle classification

The CB, the FWPlug and the MiniTAPS are able to distinguish between charged and neutral particles via separated detector components, so-called charged particle veto detectors. These detector elements generate signals when charged particles are passing through them, while for neutral particles they do not respond (see Section 2.2). Particles are marked as charged, if a time and/or a

¹¹The area of the plastic scintillator is identical to the surface of the crystals, but it is shifted in such a way that a veto from one layer covers half of the surface of the corresponding crystal, the other layer covers the other half.

spatial correlation is found between the signal of the charged veto detectors and the crystals behind them.

Charged particles in the MiniTAPS In the MiniTAPS plastic scintillators are placed in front of the crystals. A simultaneous signal with a well-defined coincidence requirement between the crystal and the plastic-veto is used for the neutral-charged discrimination. Because of the skewed particle tracks, the spatial correlation has a polar angle dependence.

In the final analysis not every charged particle will be processed, only the protons. The MiniTAPS detector combined with the Aerogel Cherenkov detector has an exclusive capability to distinguish between different charged particles in this setup. The Aerogel Cherenkov detector was placed between the MiniTAPS and the target in such a way that all particles arriving from the target into MiniTAPS, necessarily cross the Cherenkov detector (See Section 2.3). Wherever a charged particle traverses the detector material with a velocity $\beta (= v/c)$ larger than $1/n = 0.95$ ($n = 1.05$ is the index of refraction of the detector material) Cherenkov light is generated in the detector material (see Figure 3.16).

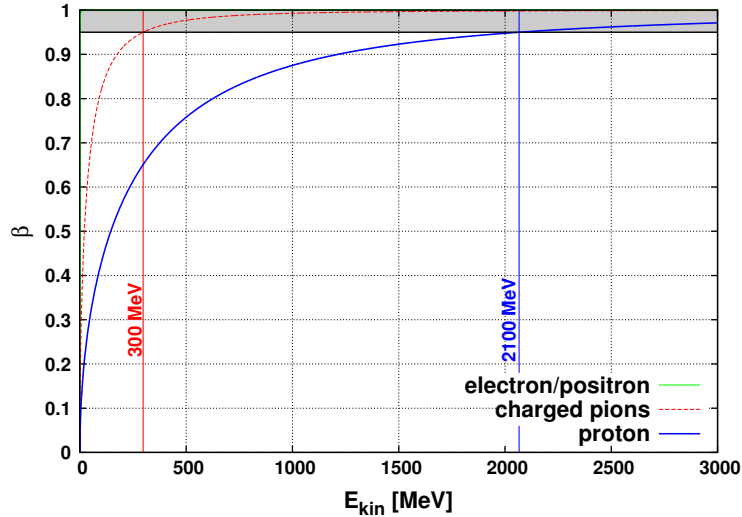


Figure 3.16.: Relativistic $\beta = v/c$ for different particles as a function of the kinetic energy. In the shaded area particles generate signal in the Cherenkov detector.

Protons reach this velocity, if they have a kinetic energy larger than $T_{\text{proton}} \approx 2.1 \text{ GeV}$ ($p_{\text{proton}} \approx 2.8 \text{ GeV}/c$). Charged pions fire the detector if their kinetic energy is larger than $T_{\pi^\pm} \approx 297 \text{ MeV}$ ($p_{\pi^\pm} \approx 400 \text{ MeV}$) and electrons/positron with more than 1 MeV kinetic energy will also generate light in the Cherenkov detector. All electrons/positrons and high energy π^\pm can be filtered out if only those events are accepted, when the Aerogel detector is not firing in coincidence with the MiniTAPS detector¹². Particles also can be distinguished by measuring their time of flight.

The time resolution of the MiniTAPS detector allows to measure the TOF¹³ of particles. Plotting the ToF as a function of the deposited energy of the given charged particle three regions that can be distinguished (see Figure 3.17). Around $E_{\text{deposited}} = 200 \text{ MeV}$ and $\text{ToF} = 0 \text{ ns}$ a strong peak can be seen. This is the *minimum ionizing peak*. Energetic charged particles ($\beta\gamma > 3$) are accumulated here,

¹²This is the so-called anticoincidence mode.

¹³The time difference between MiniTAPS and Tagger with respect to the photons.

because the flight time of these particles is unresolvable and the deposited energy is independent of the original energy. The second region can be found between ≈ 1 ns and ≈ 3 ns in time and between ≈ 200 MeV and ≈ 400 MeV in energy. In this region *protons* are energetic enough to pass through the detector and they will not deposit all their energy in the detector material. The higher the kinetic energy (smaller flight time) the less energy will be deposited. In the third region the pattern created by protons appears as a “banana”-shaped area reflecting the correlation between the flight time and the kinetic energy which is fully deposited in the detector.

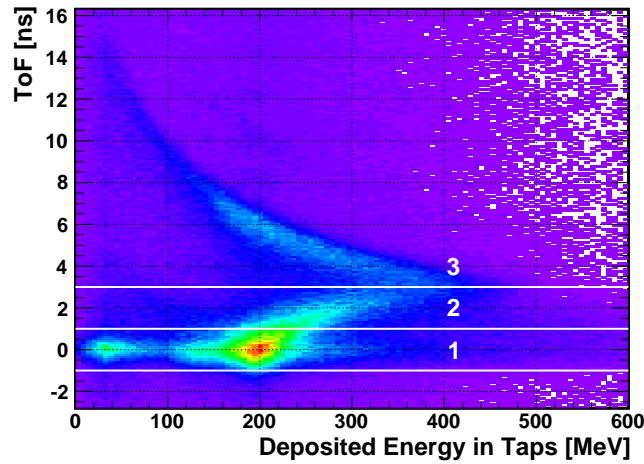


Figure 3.17.: Time-of-Flight of the charged particles is plotted as a function of their deposited energy in the MiniTAPS. The particles, which entered into this plot did not fire the Aerogel Cherenkov detector to ensure that the registered particle is a proton. The three labeled regions are discussed in the text. The fast particles with small energy deposit ($E_{\text{MiniTAPS}} < 100$ MeV and $\text{ToF} \approx 0$ ns) are misidentified electrons/positrons or photons.

Using this method together with the Aerogel Cherenkov detector, electrons, positrons and charged pions can be suppressed efficiently and protons can be positively identified (See Section 2.3 and Figure 3.18).

Charged Particles in the FWPlug and Crystal Barrel As it was discussed before, if a charged particle fires at least two fibers in two different layers in the Inner Detector, the polar- and azimuthal angles of the particle can be determined. If the same particle reaches the Crystal Barrel, these angles also can be reconstructed using information provided only by the CB detector. If the differences between these azimuthal- and polar angles are within $\pm 7^\circ$ in ϕ and $\pm 15^\circ$ in θ , the particle is marked as charged. If there is no correlation found or less than 2 layers are fired the particle is marked as neutral.

In the Forward Plug also plastic scintillators are used to identify charged particles. In case of a time and position correlation between the hits in the FWPlug crystals and the plastic scintillator the particle is marked as charged.

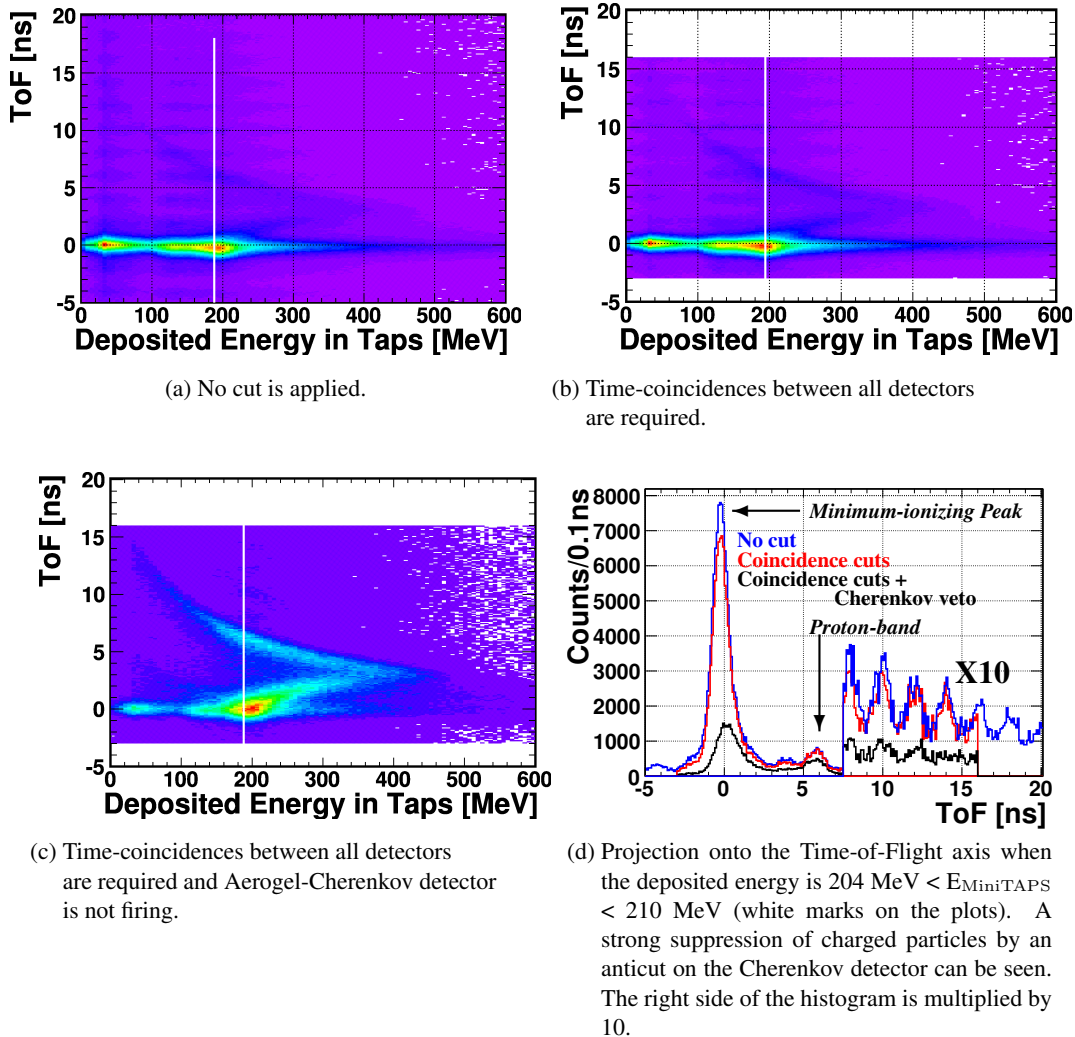


Figure 3.18.: Time-of-Flight versus deposited energy in the MiniTAPS for charged particles with different conditions.

3.2.3. Suppressing random time coincidences

To reconstruct a full reaction, not only the four-vectors of the decay-products are needed to determine with the highest possible accuracy, but also the energy of the photon that induced the reaction. In the tagger, on average, there are more than eight hits belonging to one event (see Figure 3.19). To identify the photon which generated the registered hadronic event is not possible.

One way to reduce the random coincidences between a tagger hit and the reaction is the chance coincidence subtraction technique. This method assumes that the random coincidences are roughly homogeneously distributed over the whole time-difference range between the tagger and the given detector and the chance coincidences under the coincidence peak can be estimated from a sample of background events outside of the coincidence region (see Figure 3.20).

The whole analysis has to be carried out with the events in the coincidence peak only (region “A” + “B” in figure 3.20), to reduce random coincidences. However, cutting strictly around the

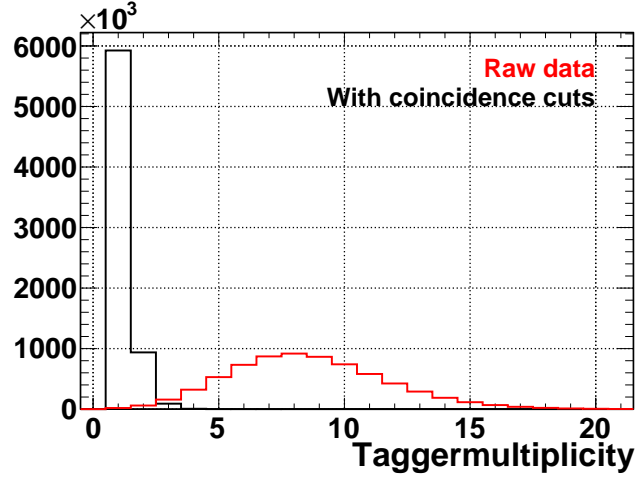


Figure 3.19.: Multiplicity of the Tagger before (red) and after (black) the coincidence timecuts on the detectors.

coincidence peak will not reduce the number of the background events (region “B”) under the real coincidence peak (region “A”). In order to subtract the random coincidences from the true coincidence peak, regions are defined in the $\Delta t_{\text{detector,tagger}}$ histogram where no real coinciding events can be found (region “C” and “D” in Figure 3.20). The whole analysis is performed on the data in the coincidence peak only and on the data in the random coincidence region only.

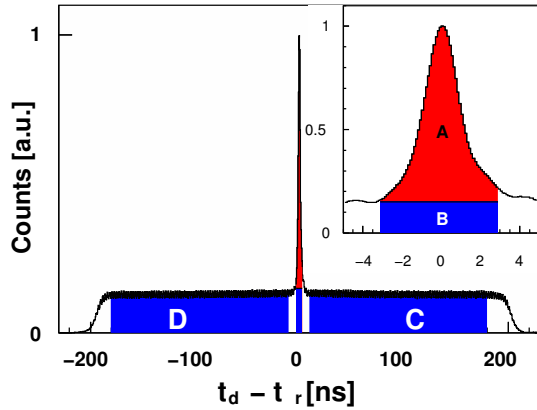


Figure 3.20.: The time difference spectrum between a detector and the tagger spectrum. The blue shaded area shows the random coincidences, the red the real ones.

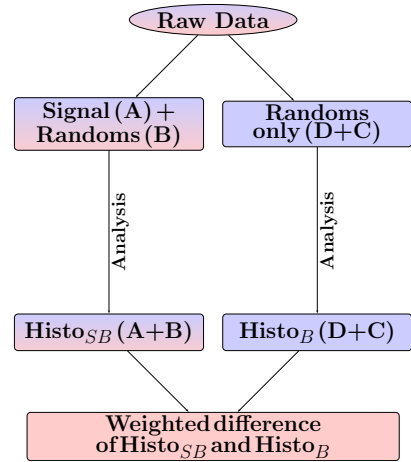


Figure 3.21.: Flow chart of the random subtraction technique.

Taking the different widths of the time windows into account the true signal is given by:

$$\text{Signal} = (\text{Signal} + \text{Background}) - \frac{\Delta B}{\Delta(C + D)} (\text{Background}). \quad (3.13)$$

“Signal + Background” and “Background” refer to the histograms filled with the events in coin-

3. Data analysis

cidence with the $A+B$ and $C+D$ regions, respectively. The “ ΔB ” and the “ $\Delta(C+D)$ ” are the integral of the “B” and the “C+D” regions. The weighted difference of the “Signal + Background” and “Background” histograms results in the “Signal” histogram which contains only true coinciding events (region A in Figure 3.20)¹⁴. (See the flow-chart on the Figure 3.21)

Because the tagger is in the trigger (see Table C.2) another possibility is also given to suppress the effect of the random coincidence hits.

		cut range [ns]	number of hits with time information				average [%]
			1	2	3	4	
detectors ^c	CB	[-5;5]	6.41	9.55	6.16	4.0	6.98
	FWPlug [charged]	[-3;8]	13.4	9.23	5.34	3.81	7.17
	FWPlug [neutral]	[-3;3]	— ^c	6.44	3.58	2.24	4.42
	MiniTAPS [charged] ^b	[-1.5;16]	13.9	11.41	6.11	4.11	8.34
	MiniTAPS [neutral]	[-1;1]	— ^c	1.25	0.69	0.5	0.87
total amount of this type of events [%]			8.8	37.3	32.6	21.3	

^a There are different cut ranges defined for charged particles and neutral ones.

^b The cut is wide enough to include the slow protons.

^c The studied event class is 3 neutral and 1 charged hit. The charged particles always have time information, so if there is only 1 particle with time information in the hit this particle **must be** charged.

Table 3.4.: $\frac{\text{Bckg}}{\text{Signal}+\text{Bckg}}$ ratio (following the convention the Figure 3.20: $\frac{B}{A+B}$) in percentage for different $dt_{\text{detector}-\text{tagger}}$ histograms. There is no cut applied on the prompt peak of the tagger (worst case scenario).

Cutting on the $\Delta t_{\text{tagger,trigger}}$ time-difference spectrum (similarly to the cut made in the previous case) the observed tagger multiplicity is reduced systematically. However, under the coincidence peak of tagger and other detectors ($\Delta t_{\text{detector,tagger}}$) accidentals can remain which have to be removed. To minimize the number of accidentals, cuts are made on the time-difference spectra between detectors and tagger strictly around the coincidence peak. This cut is different for the different detectors. Even within the same detector the response for protons and photons can be different, which influences the cut settings. The applied cuts are summarized in Table 3.4

3.2.4. PEDs and preselection

In one event the number of PEDs should be equal to the number of the final-state particles that can reach the detectors. Consequently, the PED multiplicity can indicate what kind of reaction happened. Unfortunately there are some processes which will lead to differences between the registered number of PEDs and the number of the particles in the final state. The most important effects are:

- particle losses (see Figure 3.22a):
 - explicit particle loss:
 - If the particles are going to an acceptance hole they cannot be detected. In this case

¹⁴In fact this is a more involved procedure because there should be coincidence not only between the tagger and MiniTAPS, but between the tagger and all the other detectors (Inner Detector, FWPlug, veto detectors) too.

the particle and its energy also will be lost, so the energy/momentum balance will not be fulfilled.

– merged particles:

Whenever two or more particles hit the detector so close to each other that the two PEDs cannot be resolved, the resulting cluster will be detected as one PED. In this case the energy/momentum balance will be (approximately) fulfilled.

- Split-offs/electromagnetic fluctuations (see Figure 3.22b): Split-offs are arising from statistical fluctuation during the development of electromagnetic showers and show up as a separated (usually low energetic) PEDs. In case of split-offs - usually - the energy/momentum balance can be approximately fulfilled.

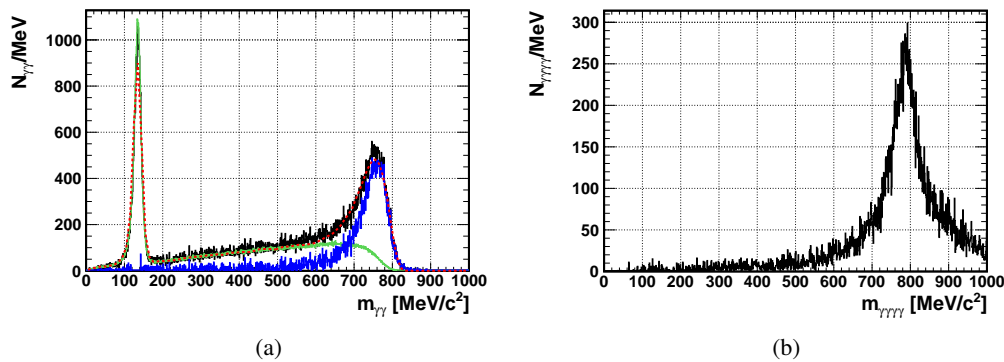


Figure 3.22.: GEANT simulation of quasi-free ω production shows the presence of merged photons (3.22a) and split-offs (3.22b).

3.22a: In the analyzed events-class only 2 neutral and one charged hits were registered. The invariant mass of the two photons shows a peak around the ω -mass. (The black line is the data, the green one is the contribution of the real two-gamma events, the blue one is the difference of the two histograms).

3.22b: In the analyzed events 4 neutral and one charged hits were registered. The invariant mass of four photons shows a peak around the ω -mass.

Roughly 5% of the generated ω events are affected by merged photons, and roughly the same amount of ω events are affected by split-offs (with the threshold values listed in the Table 3.5).

The number of the final-state particles is known in the studied reaction. Because of lost particles, merged events or the presence of split-offs, some of the events will not fall into the category defined by the number of the final-state particles.

The presence of split-offs can be reduced by setting a higher energy threshold on the cluster and also on that crystal in the cluster which detected the largest fraction of the deposited energy (*central crystal*). If these thresholds are not reached the hit will be discarded (see Table 3.5).

A special case of the split-offs occurs when particles are going to the edge of the FWPlug close to the MiniTAPS. In this case, part of the shower will be detected by the MiniTAPS. However, merging a cluster that spreads over the FWPlug and the MiniTAPS is presently not possible and consequently two hits will be detected. One way to get rid off these split-offs is to discard the

3. Data analysis

	TAPS	Forward Plug	Crystal Barrel
Minimum Energy per Crystal [MeV]	13,17	1	0
Minimum Energy per Cluster [MeV]	25	20	20
Minimum Energy in the center of the PED [MeV]	20	20	20
Maximum allowed time-difference crystals within the same cluster [ns]	3	10	-

Table 3.5.: The thresholds in the different detectors. The software-threshold on crystals of the innermost two rings of the MiniTAPS was set to 17 MeV, for the rest of the crystals it was set to 13 MeV. The hardware thresholds are slightly below these values.

particles from the analysis that are registered close to the edge of the FWPlug.

The effect of neither the split-offs nor the particle losses can be avoided totally. As a result the PED number of the effected events will not necessarily reflect the number of the final-state particles of the studied reaction. Of course, not only the studied reactions are affected by particle losses and split-offs and reactions with originally higher or lower multiplicities can appear in the studied channel. These kind of events are the background sources of the studied reactions.

To reconstruct events properly (clustering, determining the energy and the impact point of particles, combining the information between different detector parts) needs lots of processing power, and during the off-line analysis this part of the data processing takes the longest time. In order to reduce the processing time, a preselection can be applied on the data. The preselection tries to store all events which have to be further processed, and tries to reduce the events where the occurrence of the studied reaction has a low probability¹⁵.

While both of the studied reaction channels have 4 particles in the final state (see Section 1.5.2 and Section 3.2.5), an event class with minimum 3 PEDs and maximum 9 PEDs was chosen during the preselection.

3.2.5. Identification of the reaction

At this point the deposited energy and the directions (θ and ϕ) of the photons and protons, are known. Finally, only those events will be processed where the required number of neutral hits (assumed to be photons) and the required number of charged hits (assumed to be protons¹⁶) are registered simultaneously.

Reconstruction of the ω meson via the $\pi^0\gamma$ decay channel

In the processed event exactly 3 neutral hits and one charged hit had to be registered. The ω is reconstructed via the three final state photons and identified by its invariant mass. According to the relation for the total energy

¹⁵For example studying the $\omega \rightarrow \pi^0\gamma$ decay channel, all event with less than 3 PEDs can be safely discarded

¹⁶The distinction between different charged particles is feasible only if the hit was registered in the MiniTAPS via the measurement of the energies and the flight times of the charged particles.

$$E^2 = (mc^2)^2 + (pc)^2 \quad (3.14)$$

the invariant mass is given by

$$(mc^2)^2 = \left(\sum_i E_i \right)^2 - \left(c \sum_i p_i \right)^2 \quad (3.15)$$

In case of ω meson the invariant mass is expressed by

$$(mc^2)^2 = \left(\sum_{i=\gamma_1, \gamma_2, \gamma_3} E_i \right)^2 - \left(\sum_{i=\gamma_1, \gamma_2, \gamma_3} p_i c \right)^2. \quad (3.16)$$

Since the ω decays sequentially into three photons ($\omega \rightarrow \pi^0 \gamma \rightarrow 3\gamma$), the reconstructed particle can only be an ω if two photons out of the three form a π^0 .

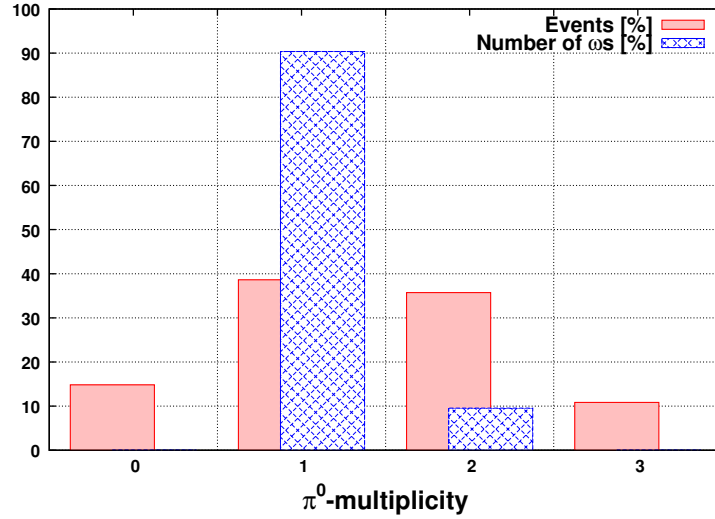


Figure 3.23.: There are 3 possible combinations of two photons out of three. On the X-axis the number of 2 γ combination is shown which falls into the $110 \text{ MeV} < m_{\gamma\gamma} < 160 \text{ MeV}$ mass range. The number of $\pi^0\gamma$ events and ω s as a function of the π^0 multiplicity are also shown.

One can visualize this by plotting the invariant mass of three photons versus the invariant mass of all combinations of two photons. The ω mesons will appear in this plane around the π^0 mass on the axis where the two photon invariant mass is plot and around the ω mass on the axis which belongs to the invariant mass of three photons (see for example Figure G.6a).

There are three different possibilities to combine three photons. In an optimal case only one combination will fulfill the above mentioned mass-constraint for the π^0 and the other two combinations can be discarded. However, in some cases more than one combination will fall into the required mass-range (see Figure 3.23). To handle every combinations, all events will be filled into histograms with a weight of $1/N_{\pi^0}$, where N_{π^0} corresponds to the number of π^0 in the requested mass-range (this is typically $110 \text{ MeV}/c^2 < m_{\gamma\gamma} < 160 \text{ MeV}/c^2$ ¹⁷). In this case there will

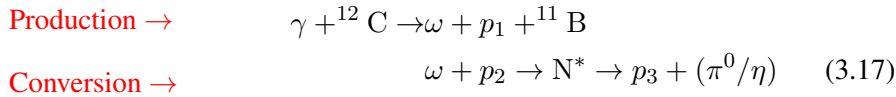
¹⁷This range roughly corresponds to the $\pm 3\sigma$ width of the π^0 peak.

be no difference in the $\pi^0\gamma$ invariant mass-spectra compared to any other method (for example the “best-pion”¹⁸), but all possible π^0 s will be used. This is important because it is not known which π^0 comes from the decay of the ω and which is only an artifact (See Appendix F).

Reconstruction of the bound omega mesic state with conversion

In the final state of this reaction one forward going, high energetic proton is registered in coincidence with two photons which forms a π^0 meson and one other proton. Therefore events were selected with exactly two neutral and two charged hits. The energetic knocked-out proton directly comes from the quasi-free production of the ω meson, and it will be registered in the MiniTAPS (See Figures 3.18).

The reaction channel, in which conversion happens, has two steps. In the first step an ω meson will be produced via quasi-free photoproduction. If the produced meson has a small momentum, then in the second step it can be absorbed by a nucleon and they will form a resonance which will decay to π -nucleon or η -nucleon pairs (in this analysis only protons are considered to participate in the conversion process):



(see also Figure 1.24). Assuming that the produced omega meson had a low momentum (prerequisite for the production of the bound omega) the momentum of the resonance (N^* or Δ) will be also low¹⁹. Thus the momenta of the decay products (proton and π^0 or η) should be roughly equal and they have to go roughly back-to-back in the laboratory frame (see Chapter 3.5.6).

Three kinematical constraints can be considered:

- the correlation between the two momenta,
- the correlation between the ejection angles,
- the expected mass of the resonance (invariant mass of the proton-pion pair) and the expected momentum of this resonance.

The measured quantity in a calorimeter is the kinetic energy of the particle²⁰. To derive the momentum from the measured quantity, the mass of the registered particle also has to be used:

$$p = E_{\text{kin}} \cdot \sqrt{1 + \frac{2m}{E_{\text{kin}}}}$$

While - in a general case - only the charge state and the deposited energy is measured, the mass of the measured particle is not known. Consequently different kinetic energies can give the same momentum depending on the presumption about the type (mass) of the particles (see Section 3.5.6).

¹⁸This method chooses the pions whose mass appears to be the closest in mass to the nominal π^0 mass.

¹⁹the momentum of the resonance can not be derived directly from the momentum of the meson, because the nucleon, which will absorb the ω meson, carries Fermi momentum

²⁰This is true if the particle deposits all its kinetic energy in the detector material. In case of, for example, minimum ionizing particles or particles which generate a nuclear reaction in the detector material there is no correlation between the kinetic energy and the deposited energy (See for example Figure 3.17 or 3.47).

An other uncertainty in this analysis is the mass of the produced resonance. The only known kinematical quantity of this intermediate resonance is the mass that should be in the order of the sum of the masses of the nucleon and the ω meson. A recent publication [K⁺08a] claims that the most dominant contribution to the ω photoproduction is originated from the $P_{13}(1720)$ resonance. This resonance has a large width of 115-275 MeV [N⁺10].

Using the two quantities and assuming that the mass of the bound ω meson is decreased by the binding energy, the mass constraints for the intermediate resonance is set to $1.4 \text{ GeV}/c^2 \leq m_{N^*} \leq 1.8 \text{ GeV}/c^2$.

3.3. Offline analysis chain

At this point the calibrated and preselected data ($3 \leq \text{Number of PEDs per events} \leq 9$) is sorted into containers as four-vectors²¹. Every container holds particles from only one detector. The final goal is to have one container for the charged hits (proton candidates), one for the final-state meson candidates ($\pi^0\gamma$ s or $\gamma\gamma$ depending on the type of the analysis) and a third one for the beam. To reach this goal the following analysis chain was used (see Figure 3.25):

1. The first step is to find the hits which are in time-coincidence with respect to each-other. To suppress the time-accidentals, strict coincidence cuts were applied in all detectors (see Section 3.2.3)
2. It was observed earlier that continuous electromagnetic noise (electron-positron pairs) was registered at the very backward region of the CB. To avoid the influence of these particle showers, all hits in the very backward region of the Crystal Barrel were rejected (see Figure 3.24).
3. In this analysis the protons which are registered in the MiniTAPS detector have a more significant role (see Figure 3.31). To reduce the effect of the background of charged particles (typically charged pions, electrons and positrons) in the forward direction, an aerogel Cherenkov detector was used (see Section 2.3). If the Cherenkov detector fired in coincidence with the MiniTAPS detector, the whole event was rejected (see Figure 3.16).
4. After arranging the hits according to their charge state, only events were selected in which exactly the required number of charged and neutral hits are registered. The neutral hits are treated as photons and the charged hits as protons.

Those events which fulfill all the listed conditions are stored, and the final analysis was performed only on this event-sample. The advantage of this gradual event-selection is that the final analysis runs only on a very small subset of the data, so it is quick²².

3.3.1. Kinematical cuts on the neutral decay channel of the ω meson

The filtered dataset contains 3 neutral hits and one charged hit. In order to reduce the background the following cuts were used:

²¹Technically these four-vectors contain lots of other information too, like the name of the detector where the hit was reconstructed, the size of the cluster, charged state of the hit, time and energy information for every detector element in the cluster, and so on.

²²The disadvantage is that it needs more disk-space.

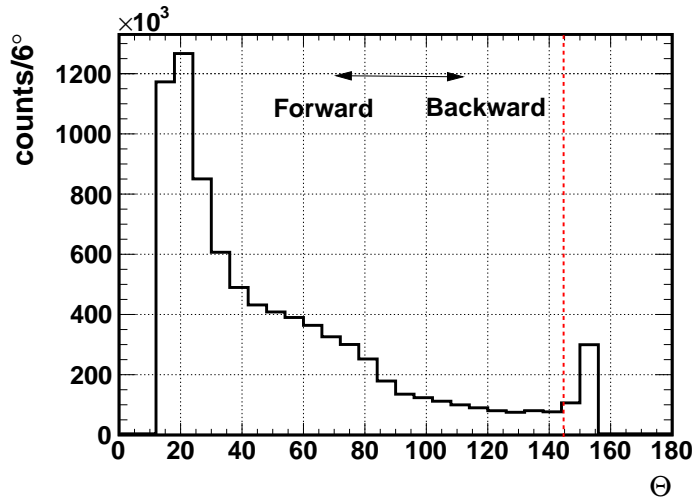


Figure 3.24.: Registered number of particles (both charged and neutral) as a function of the polar angle in the lab system. The increased yield to forward angles (small Θ corresponds to the beam direction) is due to the Lorentz boost. At backward angles electromagnetic noise can be seen from the beampipe. All signals from the most backward angles were discarded.

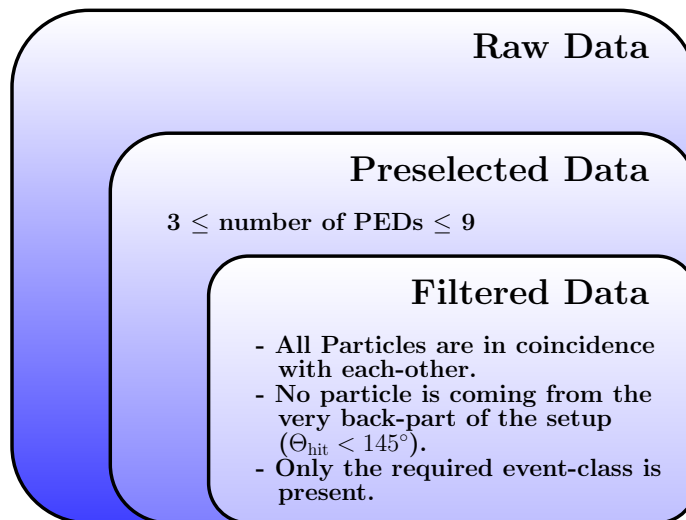


Figure 3.25.: The data are processed sequentially:

First the reconstruction and the preselection are made. After “filtering” the preselected data, only a specialized event class is stored which will be processed further. The final analysis runs more than 50 times faster if only the filtered event class is processed, compared to the processing time of the raw data.

- Cut on the two-gamma invariant mass around the mass of the π^0 is necessary for reconstructing an ω meson (see Chapter 3.2.5).
- The incident beam energy is restricted to $1250 \text{ MeV} < E_\gamma$.

The limit is defined by the tagger: the scalers below this energy were not working reliably, so a cross section measurement would not be impossible.

- The energy of the photon in the final state which did not belong to the π^0 had to be larger than 200 MeV. This cut strongly reduces the background, primarily in the low $\pi^0\gamma$ invariant mass region.
- The kinetic energy of the π^0 in the $\pi^0\gamma$ final state had to be larger than 150 MeV. This cut suppresses the influence of distorted events due to a final state interaction of the π^0 (see Figure 1.23).
- In quasi-free photoproduction of the ω meson the knocked-out proton can have such a high energy that it will be minimum ionizing and its energy-momentum vector cannot be fully reconstructed. However, assuming that the target nucleon was in rest, the four-vector of the knocked out particle can be calculated. This calculated particle is called *missing particle* and its mass is the *missing mass*.

In the reaction $\gamma^{12}C \rightarrow \omega p^{11}B$, the knocked-out particle is the proton, so the missing mass have to be the mass of the proton.

A cut on the missing mass around the proton mass ($m_{\text{proton}} \pm 150 \text{ MeV}/c^2$) was applied to reduce the influence of the events with 4- γ final state (see Figure 3.26).

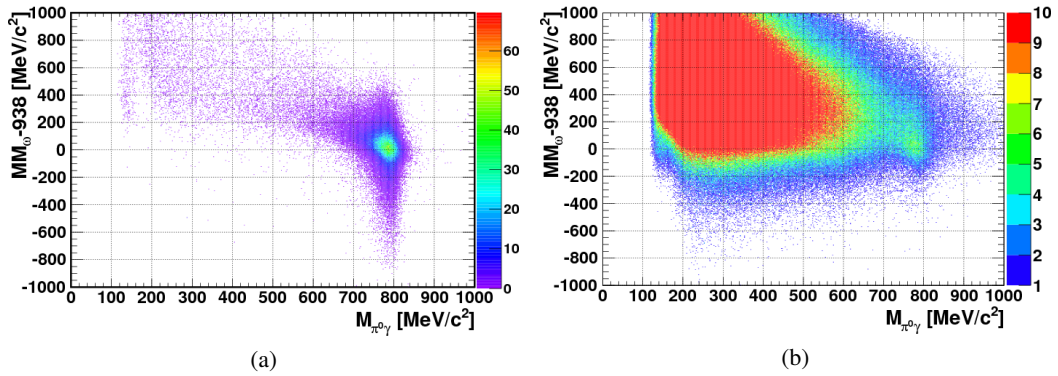


Figure 3.26.: Missing mass as a function of invariant mass of the $\pi^0\gamma$ for simulated ω events (a) and for measured data (b). A strong contribution of the background events can be seen at larger missing masses than the m_{proton} and at smaller invariant masses than m_{ω}^{PDG} .

- Events were accepted if the charged hit was registered in the MiniTAPS. In this setup the MiniTAPS detector is the most suited to identify protons TOF measurement (see Figure 3.17 and Figure 3.18c). The MiniTAPS covers the most forward angles, and if protons go to very forward angles the possibility to produce slow omegas in coincidence is large (see Figure 3.31).
- In order to ensure that the registered charged hit in the MiniTAPS was a proton, a cut around the *proton-band* was applied (as it is described in the Figure 3.17).

The effect of these cuts on the invariant mass spectrum is summarized on the Figure 3.27.

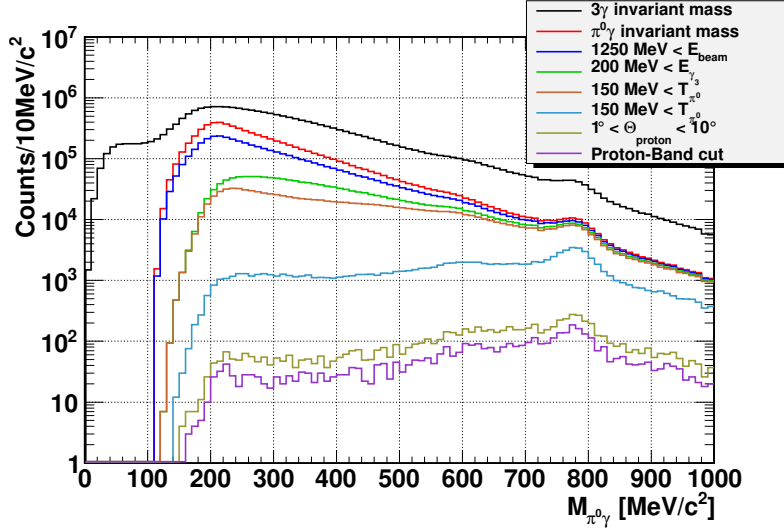


Figure 3.27.: The invariant mass spectrum of the 3-photon events of the measured data after every used cuts.

3.4. Simultaneous fit of the $m_{\pi^0\gamma}$ and the $E_{\pi^0\gamma} - m_{\omega}^{PDG}$ distributions

The signature of a bound mesic state is a non-vanishing yield on the negative side of the kinetic energy ($E_{\text{meson}} - m_{\text{meson}}^{PDG}$) histogram (see Figure 1.18). In the same time the attractive potential that binds the ω meson in the nucleus will shift the mass of the meson downward. This modification of the mass of the ω could be visible in the invariant mass spectrum. Plotting the above mentioned quantities against each other we got a two dimensional representation of the data (see Figure 3.28).

A fit can be used which handles both distributions simultaneously using the fitting functions:

$$f_X = A_X \cdot \text{Bckg}_X + B_X \cdot \text{Novo}(m_0, \sigma, \text{tail}) \quad (3.18)$$

$$f_Y = A_Y \cdot \text{Bckg}_Y + B_Y \cdot \text{Omega}, \quad (3.19)$$

where f_X is the fitting function of $m_{\pi^0\gamma}$ invariant mass distribution (the projection onto the “invariant mass” axis) and f_Y is the fitting function of the $E_{\pi^0\gamma} - m_{\omega}^{PDG}$ kinetic energy distribution (projection onto the “kinetic energy” axis).

The background content of the fit ($\text{Bckg}_{X,Y}$) was derived from events with four registered photons. All the 3-photon combinations were filtered according to section 3.3.1, and finally the invariant mass and the kinetic energy of the reconstructed $\pi^0\gamma$ systems were filled to histograms and normalized to unity. On the invariant mass spectrum the yield of the quasi-free ω s ($\text{Novo}(m_0, \sigma, \text{tail})$) was determined by a Novosibirsk function fit (see Equation 3.7). The kinetic energy distribution in the given momentum bin was simulated by GEANT. This simulated distribution was fitted to the data (Omega). Since both the background and the signal should give the same yield in the two projections (and all the $\text{Bckg}_{X,Y}$, Novo, Omega are normalized) the following equalities should be fulfilled:

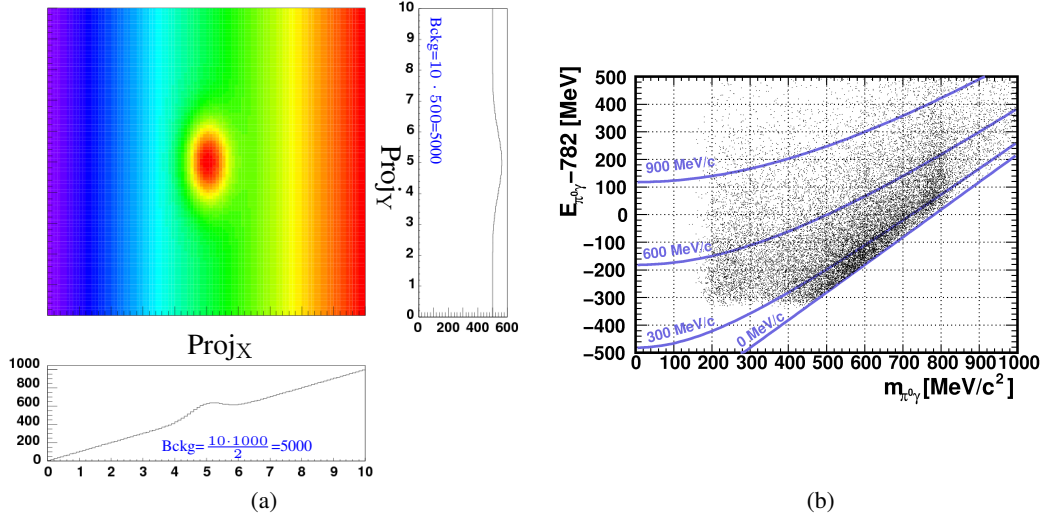


Figure 3.28.: (a): A visualization of the 2D representation of the data. The background yields in the projections are equal. (The signal yields are equal, too.)
 (b): The 2D representation of the data after the mentioned cuts. Finally cuts were made on the momentum of the reconstructed data. The cuts are also shown on the plot.

$$A_X = A_Y = A, \quad (3.20)$$

$$B_X = B_Y = B. \quad (3.21)$$

The χ^2 functions are:

$$\chi_X^2 = \sum_{x_i} \left(\frac{\text{Data}(x_i) - f_X(x_i, A, B, m_0, \sigma, \text{tail})}{\sigma_{x_i}} \right)^2 \quad (3.22)$$

$$\chi_Y^2 = \sum_{y_i} \left(\frac{\text{Data}(y_i) - f_Y(y_i, A, B)}{\sigma_{y_i}} \right)^2, \quad (3.23)$$

where the errors ($\sigma_{x,y}$) contain the statistical fluctuation of the Data, the Bckg and the Omega distributions. Finally a new χ^2 function has to be constructed which will be minimized:

$$\chi^2 = \chi_X^2 + \chi_Y^2. \quad (3.24)$$

3.5. Simulation

An important part of the analysis is to reconstruct events that are generated by *only* one type of reaction (in contrast to reality, where other reactions also contribute, as it was discussed earlier

(Section 3.2.4))

Using Monte Carlo (MC) simulations is a common method in the middle and high energy physics to model reaction kinematics (event generators) and track the generated particles through the detector (particle tracking). While the type of the event generators can be different, depending on the type of the studied physics, energy range and so on, the GEANT²³ software package became ‘de facto’ standard in the medium and high energy physics for particle tracking.

Two different types of MC simulation were used to study the bound mesic states. In the first step only a rough simulation was performed with certain simplifications (see Section 3.5.1). This is called *kinematic simulation* here.

A dedicated code, the *RelKineCal* (see the Appendix E)²⁴, was developed to solve the two-body kinematics problem. The production of ω meson in quasi-free reaction was studied with this code. To generate phase-space decays the *GENBOD* [Jam68] and its descendant the *TGenPhaseSpace* routines were applied. The *RelKineCal* together with the *TGenPhaseSpace* gives possibility to simulate complicated reaction chains quickly.

The other type of MC simulations - so called *full simulation* - includes not only the kinematics but the full particle propagation in the detector material (see Chapter 3.5.2).

3.5.1. Simulation of the kinematics

First, the results of the simulations will be shown where only the kinematical equations are solved for the “2-body kinematics” problem (see Appendix E) and no particle tracking is applied. This type of simulation is much faster than the GEANT simulation, but introduces a set of simplifications:

- the beam energy is equally distributed between 800 and 3000 MeV,
- the cross section of the photoproduction of the ω does not depend on its direction,
- every generated particle can be reconstructed with 100% efficiency,
- the detectors have infinitely good energy resolution.

Originally Toki and Yamazaki suggested to use recoilless meson-production to find bound mesic states [TY88]. The recoilless kinematics is a special case of the quasi-free kinematics. If the knocked-out particle (on which the meson was produced) takes the full momentum of the beam-particle, the meson will be produced at rest in the laboratory system (see Figure 3.29). The full momentum of the beam-particle will be transferred to the nucleon at one given beam-energy which depends on the mass of the created meson, the beam-particle and the knocked-out particle. In this case, when the full momentum is transferred to the knocked-out proton, it must propagate into the direction of the beam ($\Theta_{\text{proton}}=0^\circ$). The importance of the recoil-free dynamics was demonstrated by the discovery of the deeply bound pionic states in heavy nuclei in (d, ^3He) reaction [SFG⁺04]. The momentum-transfer to the produced mesons is shown as a function of the photon-beam energy in Figure 3.29. In this calculation the target nucleon is assumed to be at rest. This approximation is not correct for nuclear targets like ^{12}C where all nucleons carry Fermi momentum. In a realistic simulation this effect has to be taken into account. For nuclei heavier than deuterium, the Fermi momentum distribution of the nucleons can practically be described with the same function

²³GEometry ANd Tracking. In this thesis the GEANT 3.21 (2004.11.04) version was used.

²⁴It can be downloaded from <http://relkinecalc.sourceforge.net/>

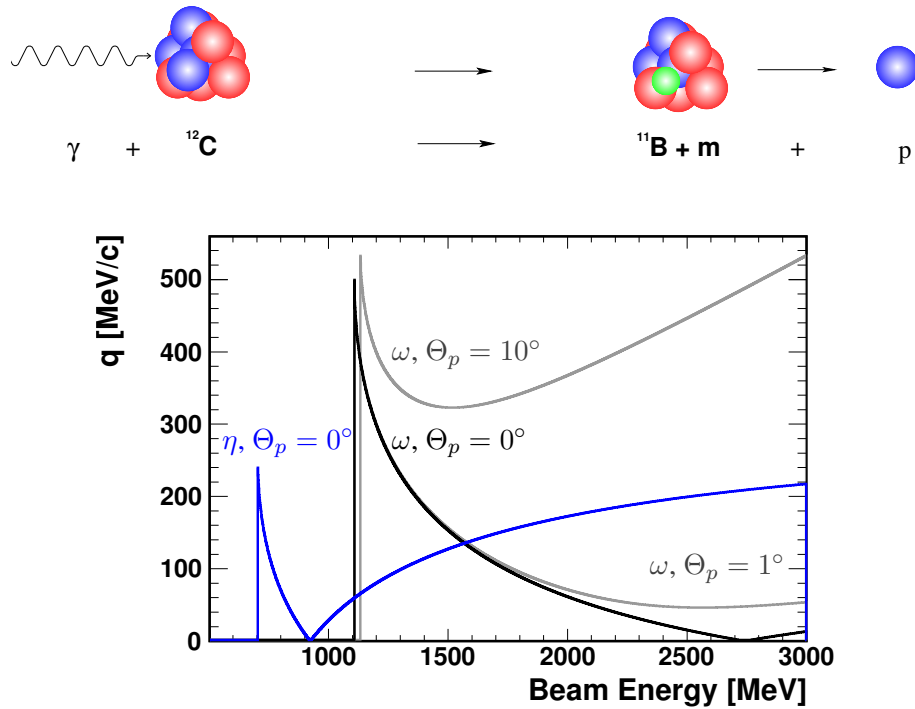


Figure 3.29.: Recoilless photoproduction of mesons on ^{12}C .

Calculation of the momentum transfer as a function of the photon beam energy is shown for the η and ω mesons. Different ejection angles of the proton in ω meson production is also taken into account.

[Lug07] (the used momentum distribution is illustrated in Figure 3.33a). As a consequence of the smearing effect by the Fermi momentum of the nucleons, the momentum of the produced meson will not have a sharp minimum at 2.75 GeV anymore, but slow ω s can be produced by almost the whole used energy range of the beam. This is demonstrated by Figure 3.30.

With the present setup, protons can not be registered for $\Theta_{\text{proton}} < 1^\circ$, because in this direction a hole is left in the MiniTAPS detector where the photons leave the setup that did not generate reactions (see Figure 2.12). If a proton goes into this direction it will not be registered, thus the reaction cannot be identified. If a proton is registered, this implies that not the full momentum of the beam was transferred to the knocked-out proton, but some momentum was transferred to the produced meson, too. This would imply that the average momentum of the produced mesons is somewhat higher compared to the mesons which were produced in coincidence with a proton going in beam direction ($\Theta_{\text{proton}} = 0^\circ$). Due to the smearing effect of the Fermi momenta this does not affect the momentum distribution of the ω s (Figure 3.30, 3.31d).

The energy of the knocked-out proton will correspondingly larger with smaller ω momenta in laboratory system. Larger energy corresponds to a smaller TOF. The energy of protons cannot be measured properly in a calorimeter, because they become a minimum ionizing particle in case they have large enough energy. However, due to the relatively large distance between the target and the MiniTAPS detector, the TOF can be measured. This is illustrated on the Figure 3.32.

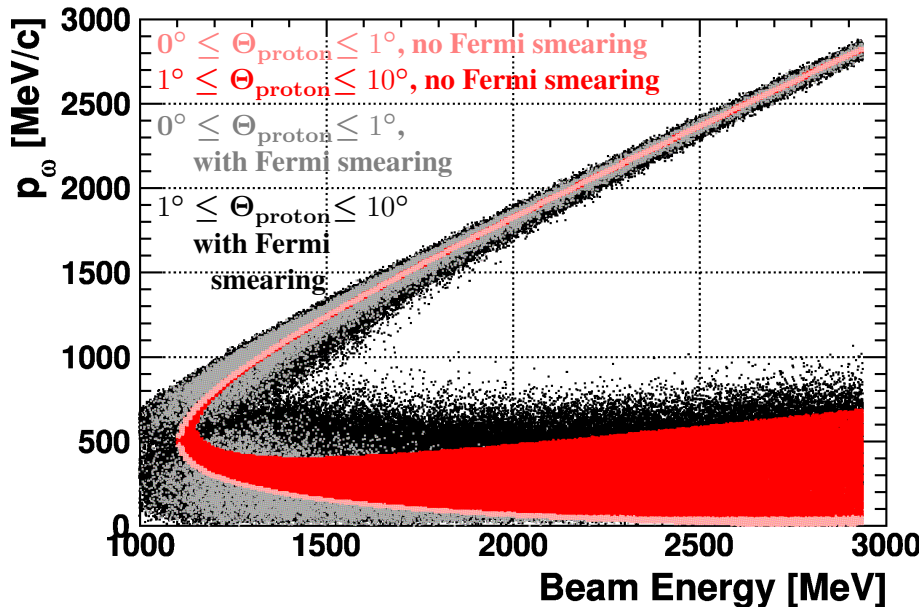


Figure 3.30.: The effect of the Fermi momentum on the $p_\omega - E_{\text{beam}}$ correlation.

The pink plot shows the result of the calculation without Fermi-smearing. The proton is knocked out to the $\Theta_p < 1^\circ$ direction.

The red distribution shows the result also without Fermi smearing but the proton goes into the $1^\circ < \Theta_p < 10^\circ$ direction (this is the Θ -range covered by the MiniTAPS). The gray plot shows the same situation as the pink one, but the target nucleon carries Fermi momentum.

The black plot shows a calculation with Fermi-distribution and the proton going into the $1^\circ < \Theta_p < 10^\circ$ direction.

The plot shows two different branches of the produced mesons with a separation around $p_\omega = 500$ MeV/c. The two branches correspond to the mesons which are going “forward” (into the direction of the beam) and “backward” (opposite to the beam direction) in the Center of Mass (CM)-system.

3.5.2. Particle tracking with GEANT

In the real measurement the earlier mentioned constraints do not hold because

- beam energy has a $N \sim E^{-1}$ dependence (see Chapter 2.1.2),
- the cross section of the ω photoproduction does depend on the direction of the ejected ω (see Figure 3.33b),
- the detector setup has finite acceptance and detection efficiency (see Chapter 3.6),
- the detectors have finite energy resolution (see Equations 2.11 and 2.12),

The full simulation with GEANT takes these effects into account. In GEANT the correct geometry of the experimental setup is implemented with dimensions, relative locations and detector materials identical to the real setup. The GEANT code calculates the interactions between the

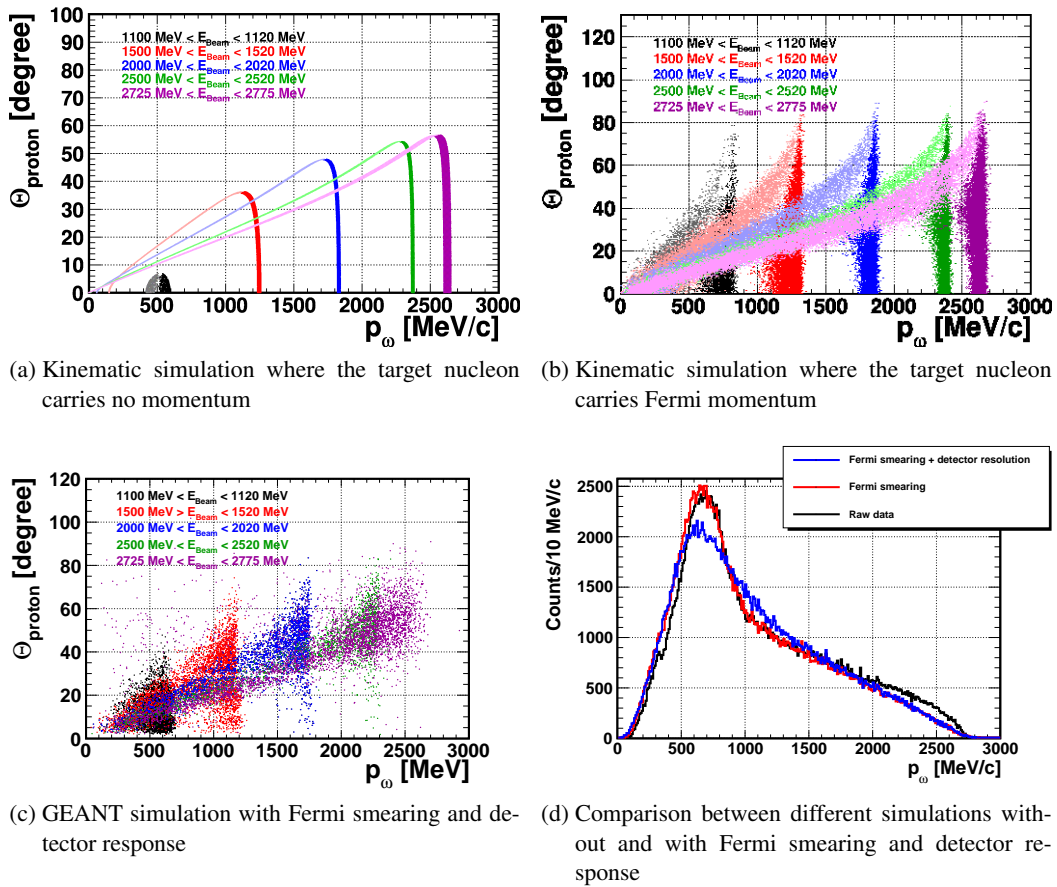


Figure 3.31.: The correlation between the momentum of the ω and the Θ angle of the knocked-out proton for given beam energy ranges.

The upper two figures show kinematical simulations. The light-colored part of the plot shows the solution of the equations when the proton is going forward in the CM system.

The detector resolution plays only a minor role.

generated particles and the detector materials (including “dead materials²⁵”) It is also possible to simulate the read-out chain (digitization, read-out noise, etc.). Finally the output is stored in the same format (list-mode data) as the measured data and they can be processed by the same analysis code, but in the simulated one it is exactly known which reactions were contributing.

The most general use of the GEANT is to determine the acceptance of the setup and the detection efficiency (see Section 3.6) of the given reaction for cross-section measurement, but it is also used to tune reconstruction algorithms (see for example chapters 3.2.1 or 3.2.2), and can be used to determine better kinematical cuts.

²⁵The deposited energy cannot be read out from every part of the detector (for example beam-pipe, holding structure, ...). These parts of the setup are called as *dead materials*.

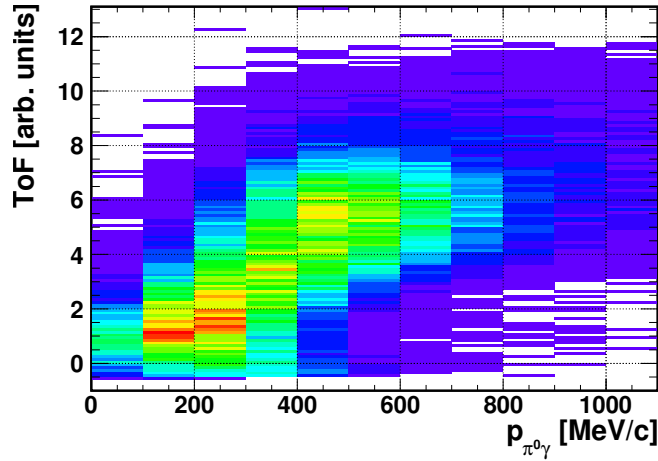


Figure 3.32.: The *Time of Flight* of the forward going proton as a function of the momentum of the produced ω meson. The simulation shows that the majority of the produced ω mesons are in coincidence with a fast proton with small ToF (large kinetic energy).

3.5.3. Event generators

The N-body phase-space integral is defined by

$$R_n = \int^{4n} \delta^4 \left(P - \sum_{j=1}^n p_j \right) \prod_{i=1}^n \delta(p_i^2 - m_i^2) dp_i^4 \quad (3.25)$$

where P denotes the total four-vector of the n-body system, p_i are the four-vectors of the individual particles and m_i are the masses of the particles [N⁺10]. The spectrum of any kinematic parameter is given by

$$f(\alpha) = \frac{d}{d\alpha} (|\mathcal{M}|^2 R_n) \quad (3.26)$$

where \mathcal{M} is the matrix element describing the reaction between the particles. If there is no interaction between the outgoing particles then $|\mathcal{M}|^2 = 1$, and all the spectra are given by the phase-space alone [Jam68]. In GEANT only one event generator is available, where $|\mathcal{M}|^2 = 1$. This type of event generator is called *Phase-Space generator*.

A phase-space generator is not sufficient to reproduce the photoproduction of ω mesons on a nuclear target, because it does not include the

- angular distribution of ω mesons in the quasi-free photo production and
- Fermi motion of the target nucleons (the Fermi momentum distribution is taken from [RL95]).

The angular distribution of the produced ω meson which was used in the simulation follows a Θ -distribution derived from an analysis of the differential cross-section measured for deuterium [Hje09].

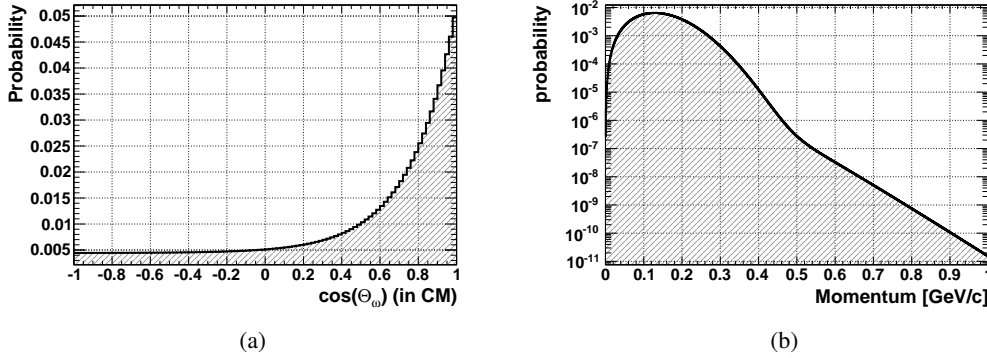


Figure 3.33.: The angular distribution of the ω (a) and the Fermi momentum distribution of the target-proton (b) which was used in the simulation

In the calculation of the reaction kinematics it is assumed that the production of the meson takes place on one of the nucleons (this nucleon is called *participant nucleon*), whereas the others are treated as *spectators* and stay intact during the interaction (impulse approximation [PZ02]). The participant nucleon (labeled by “n”) carries Fermi momentum, so its energy is

$$E_n = \sqrt{(m_n)^2 + (p_f)^2} \quad (3.27)$$

and the available energy in the center-of-momentum frame (CM) can be calculated:

$$\sqrt{s} = \sqrt{(P_\gamma + P_n)^2} = \sqrt{(E_\gamma + E_n)^2 - (E_\gamma \hat{\mathbf{e}}_z + \vec{p}_f)^2} \quad (3.28)$$

where, P_γ and P_n are the four-vectors of the incoming photon and the participant nucleon, respectively. In the initial state the nucleus is in rest, so its energy is given by its mass, m_{12C} . The participant nucleus carries momentum \vec{p}_f and the spectators carries negative momentum $-\vec{p}_f$. Assuming the reaction takes place on a proton. In this case the energy-balance can be written as

$$m_{12C} = \sqrt{(m_p)^2 + (\vec{p}_f)^2} + \sqrt{(m_{11B})^2 + (\vec{p}_f)^2}, \quad (3.29)$$

where m_p is the mass of the proton and m_{11B} denotes the mass of the spectator, respectively. It can be seen that the balance is fulfilled with $\vec{p}_f = 0$ only (the binding energy is ignored here). Energy can, however, be conserved via putting the mass of the proton off-shell [Bug75]. This consequently modifies the energy of the participant nucleon:

$$E'_n = m_{12C} - \sqrt{(m_{11B})^2 + (\vec{p}_f)^2} \quad (3.30)$$

The available energy is also modified:

$$\sqrt{s'} = \sqrt{(P_\gamma + P_n)^2} = \sqrt{(E_\gamma + E'_n)^2 - (E_\gamma \hat{\mathbf{e}}_z + \vec{p}_f)^2}. \quad (3.31)$$

3.5.4. Background channels of the neutral decay channel of the ω meson

Three types of background are considered:

- Due to particle losses and merged events (see Section 3.2.4), events with originally higher particle multiplicities can appear in the studied channel (for example $\gamma A \rightarrow \pi^0 \pi^0 p(A-1)$, $\gamma A \rightarrow \pi^0 \eta p(A-1)$). Excited hadronic states can decay into 4γ final states via $\pi^0 \pi^0$ or $\pi^0 \eta$ with high branching ratios. The largest fraction of the background of the studied reaction channels stems from this kind of sources.
- Due to split-offs (see Section 3.2.4), events with originally lower particle multiplicities can appear in the studied channel (for example $\gamma A \rightarrow \pi^0 p(A-1)$, $\gamma A \rightarrow \eta p(A-1)$). In these channels not only photons can generate split-offs (with low energy, which could be removed by a higher threshold setting), but a proton also can generate additional hits.
- If a neutron will be identified as a photon (it will not fire the veto detectors, but deposits energy in the crystals) and a π^+ will be identified as a proton (will fire the veto detector and deposits energy in the crystals), in this case the final state of the $\gamma A \rightarrow \pi^+ \pi^0 n$ channel also can be misidentified as $\gamma\gamma\gamma + p$ in the final state.

These possible background channels were studied using GEANT simulations. To visualize the result, a two-dimensional representation of the invariant masses is shown, where on the X -axis the invariant mass of the three-photon combination, on the Y -axis all two-photon invariant masses²⁶ are plotted, respectively.

	Fermi Motion	Θ_ω distribution
Signal	X	X
Background	X	-

Table 3.6.: The $\omega \rightarrow \pi^0 \gamma$ channel was simulated with the Fermi motion of the target nucleon, the Θ dependence of the photo-production of the ω was taken into account.

In the case of the background channels only the Fermi momentum distribution of the target nucleons was modeled.

The projection onto the three-photon invariant mass axis is shown in the region where the two-photon invariant mass falls to the pion-mass range ($110 \text{ MeV}/c^2 \leq m_{\gamma\gamma} \leq 160 \text{ MeV}/c^2$). Without using any cuts all the background channels, except the $\gamma A \rightarrow \pi^0 \eta p(A-1)$, channels show smooth distributions without structures (see the Figure 3.34.). These background contributions can be parameterized and be removed. The $\pi^0 \eta$ channel behaves differently. If it was known which two photons come from the decay of the π^0 and which from the η then the produced background distribution would be structureless (see Figure 3.35), smooth, which also can be fitted and removed. In reality this is not always the case.

The combinations where the two photons originate from different mesons can be identified as a real π^0 by their invariant mass (see Appendix F). This wrong combination leads to a structure in the “two-gamma versus three-gamma” plane (see Figure G.3a), and appears as a distinct peak in the projection on the 3-photon invariant mass axis if a cut is made around the π^0 mass on the two-gamma invariant mass axis (see Figure G.3c).

²⁶This means 3 combinations per events.

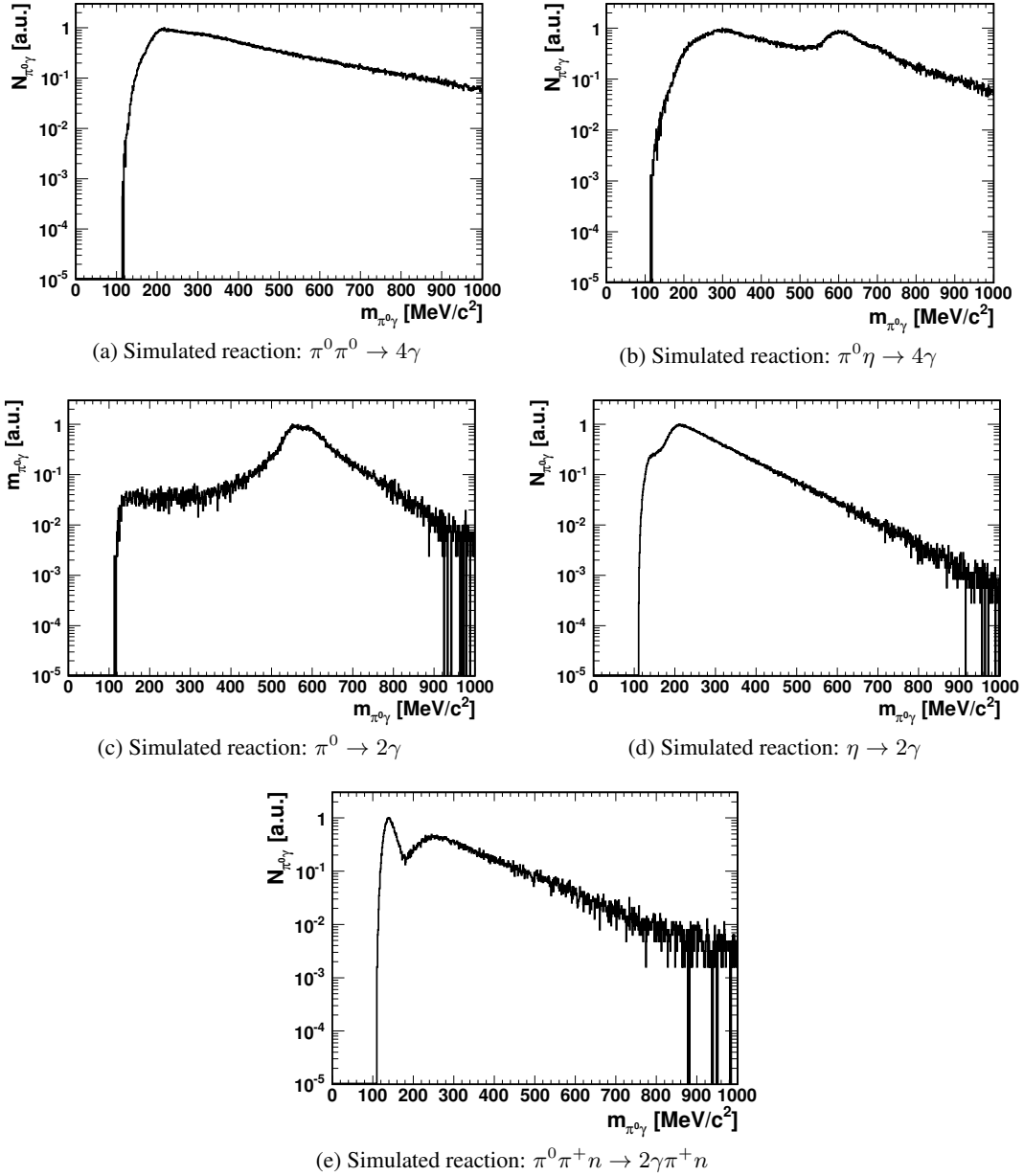


Figure 3.34.: The plot illustrates the simulated background channels where 3 neutral hits were registered in the final state. The figures show the invariant masses of the registered three neutral hits (treated as photons), where the invariant mass of two neutral hits gives the mass of the π^0 meson. (See the text for details.)

After the used analysis cuts (including the momentum cut $p_{\pi^0\gamma} < 300 \text{ MeV}/c$) the $\gamma A \rightarrow \pi^0\pi^0 p(A-1)$ and $\gamma A \rightarrow \pi^0\eta p(A-1)$ channels give broad distributions which reaches its maximum on the negative side of the kinetic energy distribution (see Figure H.3, H.4) where the signal of the bound ω -mesic nucleus is expected (see Figure 1.21). During the fitting procedure, these distributions are derived from events with four photons (see Section 3.4).

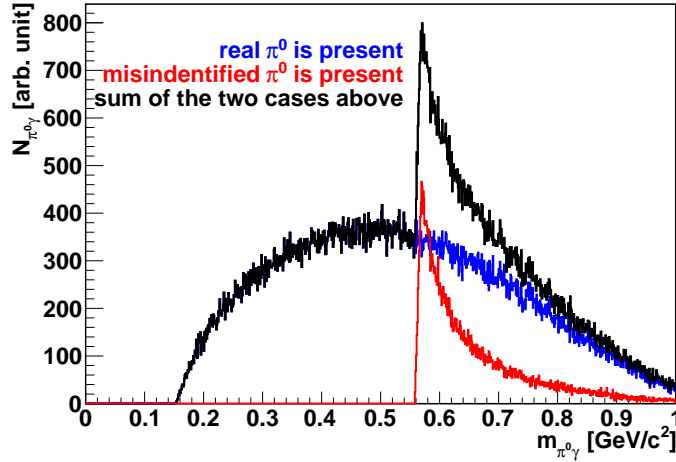


Figure 3.35.: Kinematical simulation (no detector acceptance or detector resolution was taken into account) to illustrate the problem of the reconstruction of the $\pi^0\eta$ background channel. If the gammas which were identified as the decay products of the π^0 come from a “real” π^0 , then the resulting background is smooth (blue line). If those gammas are not coming from a “real” π^0 , then the resulting background is sharply peaking (red line). In reality we always observe the sum of the two distributions (black line). (For more details see the text and the Appendix F).

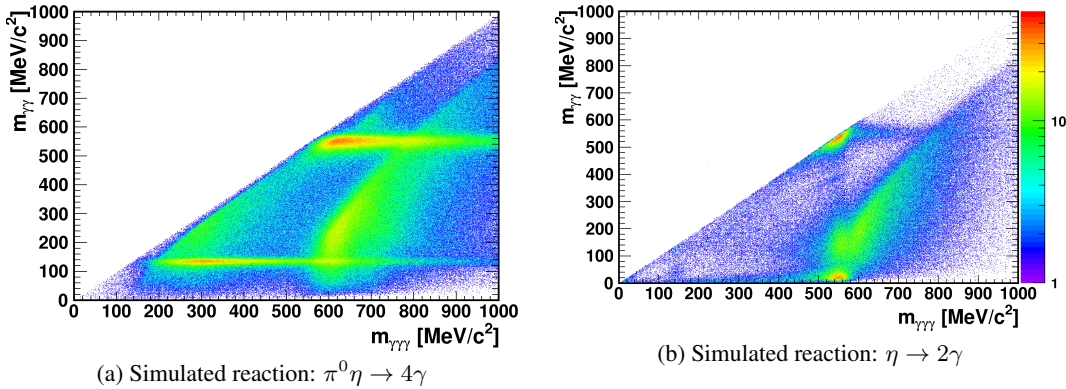


Figure 3.36.: Both the $\pi^0\eta \rightarrow 4\gamma$ and the $\eta \rightarrow 2\gamma$ channels show a band-like structure on the two-gamma invariant mass vs. three-gamma invariant mass histogram. This structure appears as a peak on the three-gamma invariant mass spectrum.

The single π^0 production shows a smooth $m_{\pi^0\gamma}$ distribution on the Figure 3.34e. However, applying the earlier listed cuts (see Section 3.3.1) an increased yield appears at around $600 \text{ MeV}/c^2$ which yield can interfere with the expected signal (see Figure 3.38a).

The single η production does not shows a π^0 peak on the $m_{\gamma\gamma}$ spectrum and the $m_{\pi^0\gamma}$ projection also shows an increased yield at around $600 \text{ MeV}/c^2$ (see Figure 3.38b).

The simulations above show only the shape of the different background channels which contribute to the $\pi^0\gamma$ invariant mass spectrum. The strength of the mentioned channels were studied using GiBUU simulations as an event generator and the generated particles were tracked by GEANT.

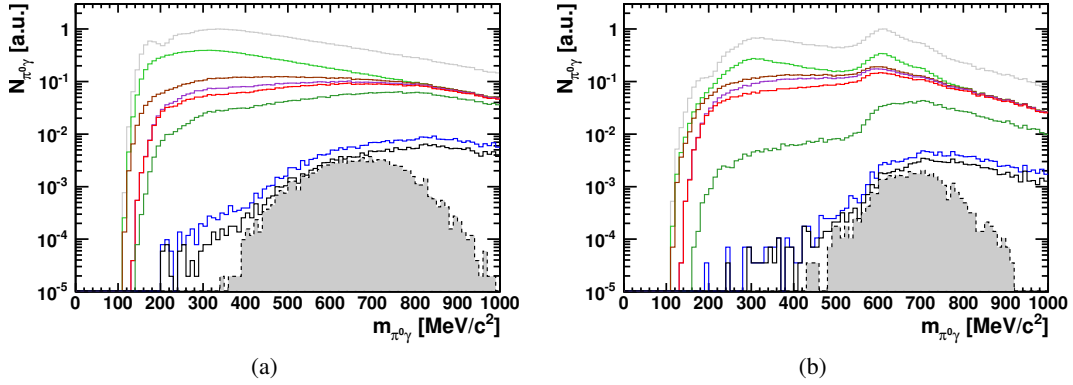


Figure 3.37.: Invariant mass distributions of the $\pi^0\gamma$ events coming from $\pi^0\pi^0$ (a) and $\pi^0\eta$ (b) events after losing one photon. The filled gray distribution shows the distribution after applying all the analysis cuts (see Section 3.3.1) included the momentum cut $p_{\pi^0\gamma} \leq 300 \text{ MeV}/c$. The color code is described in the Appendix H.

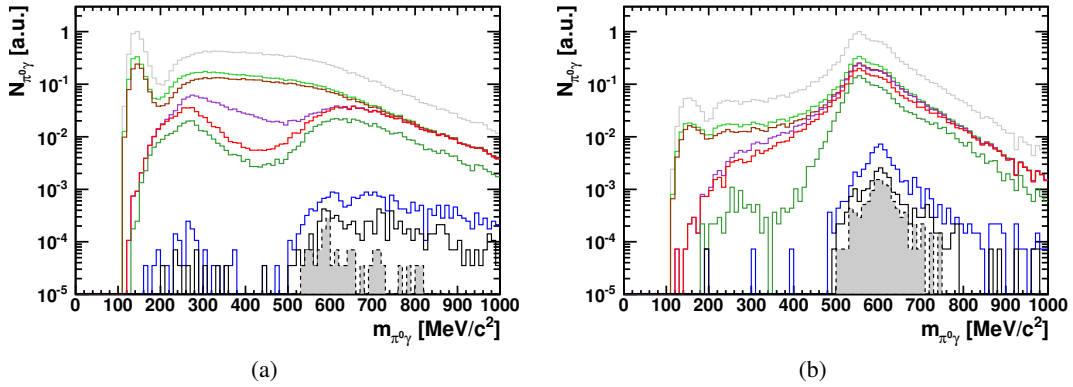


Figure 3.38.: Invariant mass distributions of the $\pi^0\gamma$ events coming from π^0 (a) and η (b) events after a split-off. The filled gray distribution shows the distribution after applying all the analysis cuts (see Section 3.3.1) included the momentum cut $p_{\pi^0\gamma} \leq 300 \text{ MeV}/c$. The color code is described in the Appendix H.

The GiBUU is an unified transport framework in the MeV and GeV energy regimes for

- elementary reactions like
 - electron + A
 - photon + A,
 - neutrino + A ,
 - hadron + A (especially pion + A and proton + A)
- and for heavy-ion collisions.

The time-propagation of particles is modeled within a Boltzmann-Uehling-Uhlenbeck (BUU) framework. Mesons and baryons propagate in mean fields and scatter according to cross sections which are tuned to the energy range of 10 MeV to more than 10 GeV. The omega signal

and the contribution of the discussed channels is shown in the Figure 3.39. In addition, the same structures can be seen in the analyzed data (see Figure G.7)

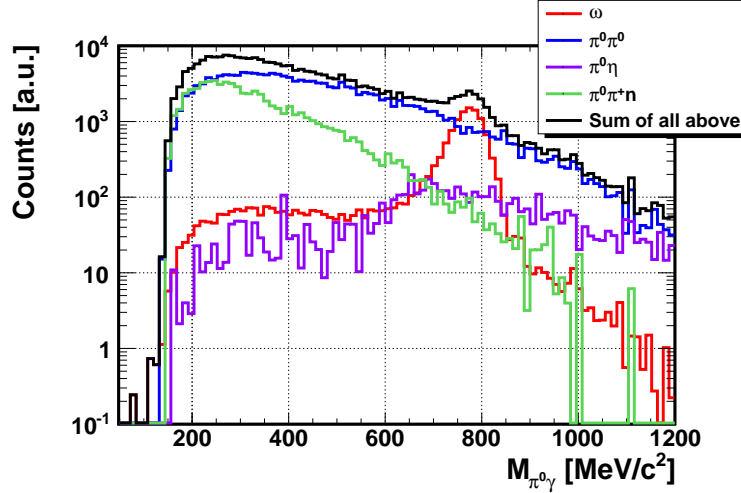


Figure 3.39.: $m_{\pi^0\gamma}$ invariant mass spectra for different reaction after registering only 3 photons in the final state simulated with the GiBUU event generator and reconstructed by GEANT3 [Fri10, Nan10]

3.5.5. Background rejection techniques

As it was be discussed earlier (See Chapter 3.5.4), there are several background channels contributing to the studied reaction channel of $\omega \rightarrow \pi^0\gamma \rightarrow 3\gamma$.

- The majority of the background events comes from reactions with 4 photons in the final state.
 - A large fraction of this type of background originates from double neutral pion production where one photon is lost. This contribution is taken into account by the fitting method (See Chapter 3.4).
 - The $\pi^0\eta$ channel is removed by using a *sideband subtraction* technique.
- Single meson production (π^0 and η) can partly removed by using a sideband subtraction technique (the η channel) or using additional kinematical cuts (primarily the π^0 channel).

Sideband subtraction

If an η meson is involved in the detected reaction (single η production or $\pi^0\eta$ channels) it can occur that one additional neutral hit will be detected besides the photons from the decay of the η . This can happen in the $\pi^0\eta$ channel when one photon from the decay of the π^0 is paired to the η and the other photon from the π^0 is not registered (See the Appendix F for details) or one of the final state photons or the proton splits off in case of single η production. This type of artifacts show up as a continuous diagonal band (See Figure 3.36) on the two-photon invariant mass versus three-photon invariant mass plane. To reduce this structure and to suppress the combinatorial background, a

sideband subtraction technique was applied²⁷.

This method based on the assumption that the background contribution under the *Signal* can be derived from the regions outside of the *Signal* using an interpolation between the side-bands.

The procedure is the following:

A projection is made onto the $m_{\gamma\gamma}$ -axis in the range $500 \text{ MeV}/c^2 < m_{\gamma\gamma} < 700 \text{ MeV}/c^2$. The *Signal*- and the *Sideband* regions are set in this projection according to Figure 3.40. The region of the *Signal* is set on the π^0 mass ($110 \text{ MeV}/c^2 < m_{\gamma\gamma} < 110 \text{ MeV}/c^2$) and the *Sideband* regions is set close to the π^0 peak on both sides ($40 \text{ MeV}/c^2 < m_{\gamma\gamma} < 90 \text{ MeV}/c^2$ and $170 \text{ MeV}/c^2 < m_{\gamma\gamma} < 220 \text{ MeV}/c^2$). The background contribution under the π^0 peak is estimated by fitting the whole spectrum with a Novosibirsk peak function (See Equation 3.7) and a $\exp(a + bx + cx^2)$ background function between $30 \text{ MeV}/c^2$ and $250 \text{ MeV}/c^2$.

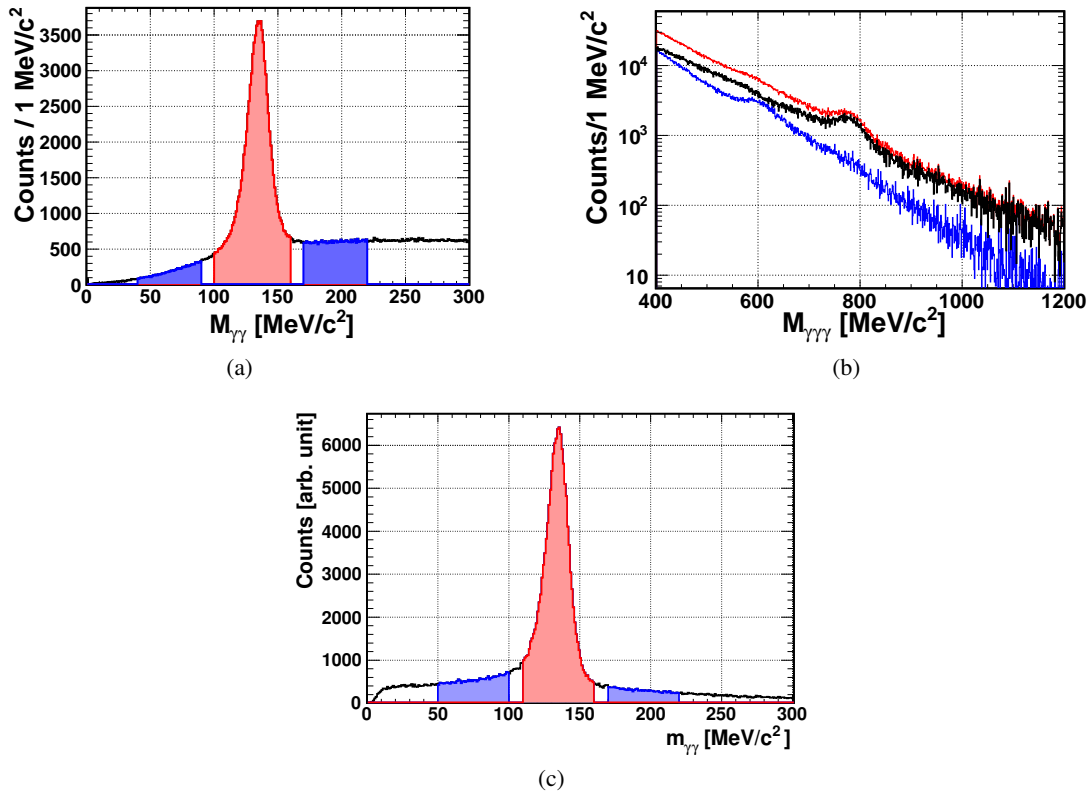


Figure 3.40.: (a) In the two-photon invariant mass spectrum the π^0 -peak ($110 \text{ MeV}/c^2 < m_{\gamma\gamma} < 110 \text{ MeV}/c^2$, red shaded area) and the sideband ($40 \text{ MeV}/c^2 < m_{\gamma\gamma} < 90 \text{ MeV}/c^2$ and $170 \text{ MeV}/c^2 < m_{\gamma\gamma} < 220 \text{ MeV}/c^2$, blue shaded area) is shown.

(b) The 3-gamma invariant mass spectra for the π^0 -peak (red curve) and the sideband (blue curve) and the difference between them (black curve).

The sideband subtraction technique was used in the analysis of the neutral decay channel ((a), (b)) and also in the analysis of the conversion channel (c).

²⁷The used technique is similar to the technique which was used to suppress random coincidences from the tagger spectrum (See Section 3.2.3)

3. Data analysis

After filling the spectra under the condition that the invariant mass of the two photons falls into the *Signal* region and a different one when the invariant mass of the two photons falls into the *Sideband* region, the two spectra can be subtracted from each other following equation 3.13.

In the difference spectrum the structure due to the $\pi^0\eta$ channels cannot be seen, while the ω signal remains unaffected (see Figure 3.40b).

The invariant mass spectrum of the two gammas in the conversion channels also has background which have to be removed (See Figure 3.40c).

The procedure is similar to the previously detailed method:

- events are separated according to the invariant mass of the two photons,
- both groups (*Sideband* and *Peak*) of the events will go through the analysis chain,
- the final histograms are filled in coincidence with the *Peak* and the *Sideband* region respectively,
- the weighted histograms are subtracted.

Kinematical cuts

Probably the most “dangerous” channel is the $\gamma + p \rightarrow \pi^0 + p$ channel where the third neutral particle is produced as an artifact. This channel has a very low production threshold (far below the tagged energy range), it has large cross section (See Figure 3.41) and the π^0 decays into two-photon final state with a branching ratio of 98.798% [N⁺10]. Because only those events are studied where three neutral hits and a charged hit was registered, only roughly 5% of the neutral pion-events will be processed further. The $\gamma + p \rightarrow \pi^0 + p \rightarrow 2\gamma + p$ reaction can satisfy this multiplicity constraint if one photon generates a split-off or the proton generates an additional neutral hit.

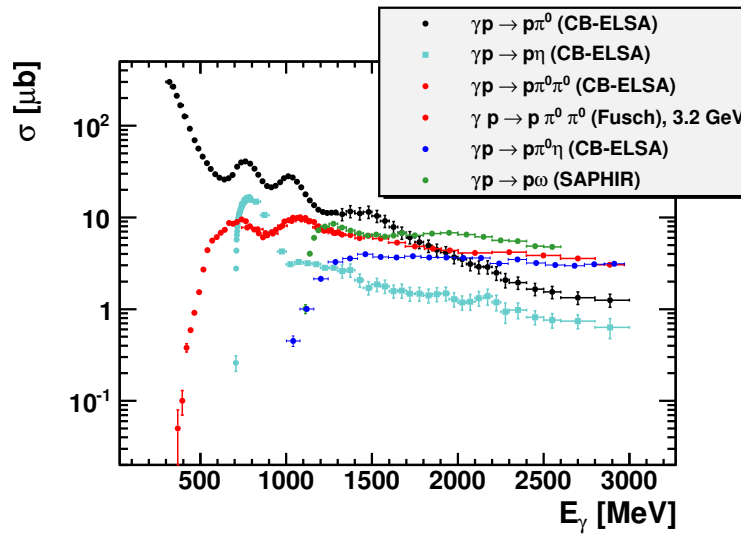


Figure 3.41.: Integrated cross section of the contributing background channels and the signal channel in photoproduction on the proton ($\gamma + p \rightarrow X + p$) [Tho10].

After the cuts which were applied during the data analysis (See Section 3.3.1) a pronounced structure appears which reaches its maximum slightly above $600 \text{ MeV}/c^2$ (See Figure 3.38). This contribution can not be removed by using the sideband subtraction technique, because this artifact emerges from the decay of a pion so the mass constraint for the pion mass will always be fulfilled and in the sidebands no additional structures will appear.

First, a study was performed to find the origin of this structure around $600 \text{ MeV}/c^2$. Plotting the energy of each photon as a function of the invariant mass of the three registered neutral hits (treated as photons) there are two structures visible (See Figure 3.42).

The events where one photon splits off and produces a low-energetic “hit” will lead to a vertical band around the invariant mass of the pion (the invariant mass of this structure is slightly higher than the mass of the π^0 ($141 \text{ MeV}/c^2$) and also its width is slightly larger than the width of the π^0 in this detector ($14 \text{ MeV}/c^2$).

The other pronounced structure is a diagonal band which starts around the invariant mass of the earlier discussed structure and with increasing energy of the photon produces larger and larger invariant masses. If the lower part of this 2 dimensional distribution is removed (cut on the energy of the bachelor photon), the remaining part of this diagonal band will produce the enhanced yield at around $600 \text{ MeV}/c^2$ (See Figure 3.42).

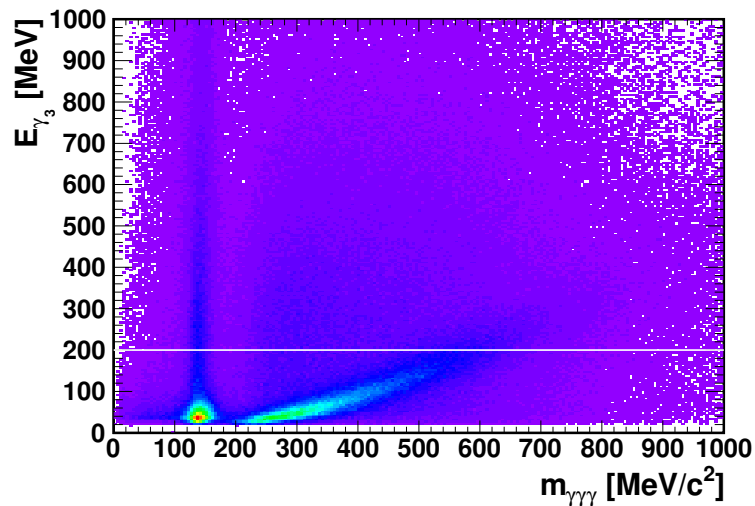


Figure 3.42.: The correlation between the invariant mass of three photons and the energy of each photons. A vertical structure is visible due to photon split-offs (see the text for details). A diagonal structure can also be seen. If the lower part of the distribution is removed, as indicated by the white line, a peak-like structure will be produced via the remaining part of the diagonal structure.

An effort was made to remove this structure via additional kinematical cuts. This is necessary, because the contribution of this channel is not removed neither by sideband subtraction (see the discussion above) nor by the fitting method (where background is derived from 4-photon final states).

To reject these events the following cuts were applied:

- A standard procedure to reduce the influence of photon generated split-offs is to increase the detection threshold. This was applied in this analysis, too: whenever a *neutral particle* (*photon*) deposited less than 50 MeV energy, the whole event was rejected.

- If a split-off of a gamma happens, the hit which was generated by the split-off, should be close to the place of the original energy deposit of the (real) particle. This can be measured by the “opening angle”²⁸ between the hits. All events were rejected where the opening angle between two photons (neutral hits) was less than 20° and one of these photons had smaller energy than 100 MeV (see Figure 3.43).

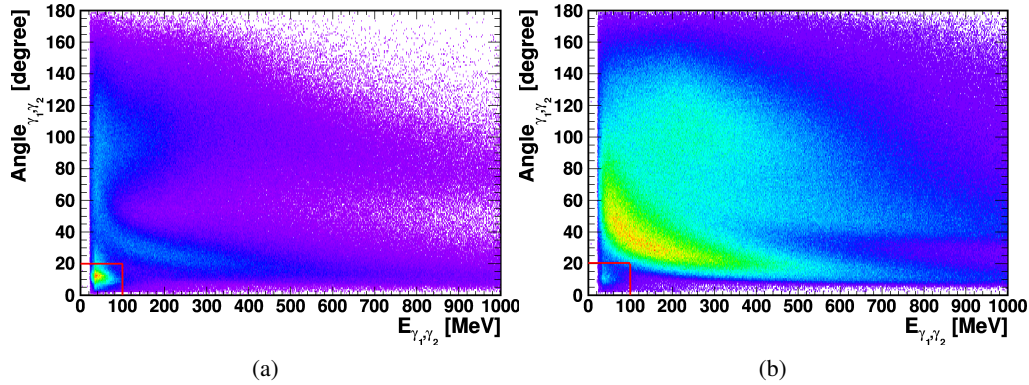


Figure 3.43.: GEANT simulation shows the correlation between the relative angle between neutral hit-pairs and the energy of the contributing photons in $\gamma + p \rightarrow \pi^0 + p$ (a) reaction when three neutral- and a charged hit were registered. As a comparison the same correlation is shown for $\gamma + p \rightarrow \omega + p$ (b).

- If a split-off happens (either split-off of a photon or a proton) the correlations between opening angle between pair of photons and the opening angle between the “third photon” (which was not used to produced the photon-pair) and the charged hit will show a maximum where both of these angles are small. This is a characteristic difference between real ω decay and π^0 decay and this region should be removed (see Figure 3.44).
- Proton-generated split-offs frequently occur when the proton hits the Forward Plug and the neutral hit from this split-off is registered in the MiniTAPS. To avoid the influence of these artifacts, all events where a photon is registered at less than 20° were rejected.
- In addition, the originally proposed cuts on the energy of the bachelor photon and on the kinetic energy of the π^0 (see Section 3.3.1) are not used in order not to produce an artificial structure at invariant mass of roughly $600 \text{ MeV}/c^2$.

3.5.6. Simulation of the conversion channels

As it has been mentioned, this reaction consists of two steps. In the first step a slow ω meson will be produced in quasi-free photoproduction. In the second step this meson will form a resonance

²⁸The opening angle is defined as $\Theta = \frac{\vec{a} \cdot \vec{b}}{||\vec{a}|| \cdot ||\vec{b}||}$, where $||\vec{a}||$ denotes the magnitude of \vec{a} .

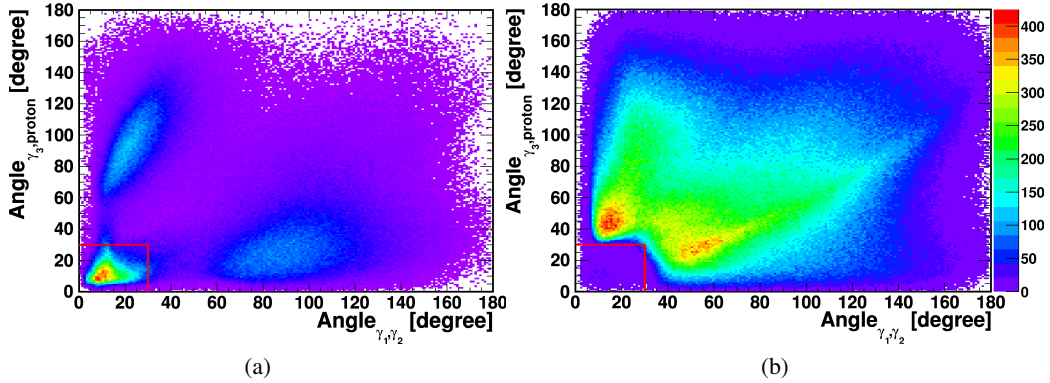


Figure 3.44.: GEANT simulation shows the correlation between the relative angle between neutral hit-pairs and the opening angle between the third neutral hit and the charged hit. Characteristic difference can be seen between these planes in case of $\gamma + p \rightarrow \pi^0 + p$ (a) and $\gamma + p \rightarrow \omega + p$ (b) events. (The simulation of the ω meson production includes a realistic angular distribution.)

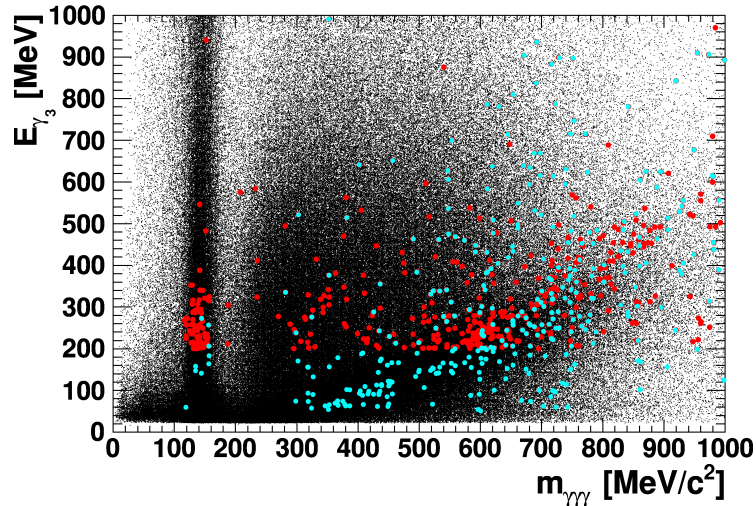


Figure 3.45.: Simulation shows the effect of the kinematical cuts on the π^0 spectrum where an additional neutral hit was registered. The black histogram is the E_γ vs. $m_{\gamma\gamma}$ distribution without any cut applied. The red dots shows the remaining distribution after the kinematical cuts applied in the analysis (See Section 3.3.1). The cyan dots show the distribution of the events after using the additional cuts listed above. The overall yield of this type of events did not change dramatically, but the bump-like structure around $600 \text{ MeV}/c^2$ was removed. For more comparison, see the Appendix H.

with a nucleon. Finally the produced resonance will decay to π^0 -proton or η -proton pairs (see Figure 1.24).

This reaction chain was simulated with GEANT using the following constraints:

- If the produced ω meson has momentum less than $500 \text{ MeV}/c$, then the conversion is simu-

3. Data analysis

lated, otherwise a new event is generated.

- All participating nucleons carry Fermi momentum.
- The mass of the produced resonance (N^* or Δ) is between $1.4 \text{ GeV}/c^2$ and $1.8 \text{ GeV}/c^2$ (see Section 3.2.5).
- The resonance is produced only if it is allowed (the invariant mass of the proton- ω system is larger than the minimum allowed mass of the resonance).
- If there is enough energy to produce the resonance then the mass of the produced resonance will be randomly chosen within the mentioned range (flat distribution).

If the mentioned constraints are fulfilled, the final state particles (two protons and two photons) will be tracked.

The main goal of this simulation is a detailed study to clarify:

- What are the kinematical constraints for the reaction? Which cuts can be used?
- What is the effect of the holding structure of the CB detector on the detection of the proton?
- What is the effect of the misidentified charged particles on the identification of the reaction?

Kinematical constraints and cuts

As it was described in the Section 3.2.5 three kinematical constraints have to be fulfilled to accept an event:

- there are two assumptions for the produced resonance:
 - its mass should be between 1.4 GeV and 1.8 GeV ,
 - it was produced by the absorption of a slow ω meson ($p_\omega < 500 \text{ MeV}/c$) and a proton which carries Fermi momentum (see Figure 3.33a),
- the correlation between the ejection angles,
- the correlation between the momenta of the decay products of the resonance.

The later two constraints explicitly depend on the first assumptions: a larger mass of the resonance would imply that the opening angle between the meson and the proton is closer to 180° (second constraint) and their momenta are larger (third constraint).

A simple kinematical simulation will not necessarily give enough information about the correlated momenta of the proton and the meson (see the Section 3.5.6), but the opening angle distribution between them can be calculated (see Figure 3.46).

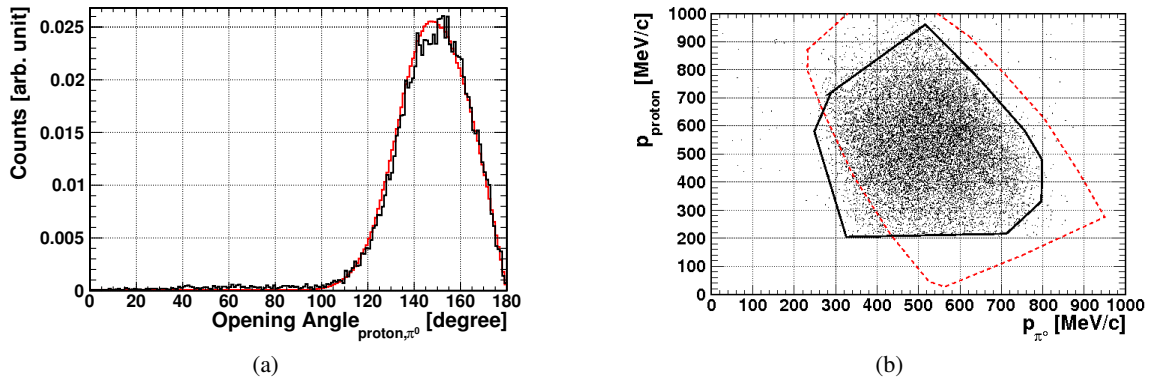


Figure 3.46.: Simulation of the conversion channel. The figure (a) shows the opening angle distribution between the proton and the π^0 under the conditions listed at the beginning of this chapter. The red line shows the result of the kinematical simulation, the black one represents a full particle tracking with GEANT. The figure (b) shows the correlation of momenta between the proton and the neutral pion. The scatter plot and the black line show the result of a full particle tracking using GEANT. In comparison, the red dashed line dashed line represents the contour of the correlated momenta using a kinematical simulation, where the effect of the holding structure cannot be seen.

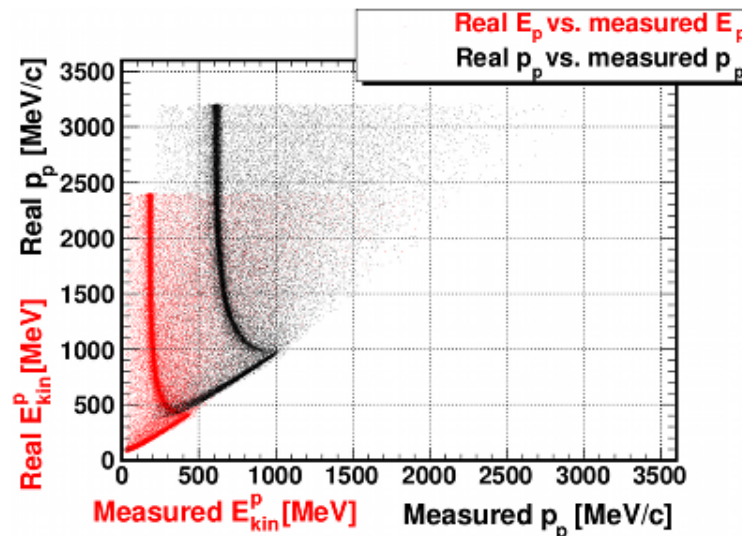


Figure 3.47.: GEANT simulation to demonstrate the effect of the holding structure on the reconstruction of the momentum of the protons. The red scatter plot shows the correlation between the real kinetic energy and the measured one (this is the measured quantity). The black one shows the correlation between the real momentum of the proton and its reconstructed momentum. Protons with small energy ($\lesssim 90$ MeV) will be absorbed in the holding structure of the detector, and will not reach the crystals. A proton with high energy ($\gtrsim 400$ MeV) will become a minimum ionizing particle and will not deposit all its kinetic energy in the detector material.

Effect of the holding structure of the CB on the proton detection

It is a known effect that the Inner detector and the holding structure of the CB detector absorb low energetic electromagnetic background and also protons (see Section 2.2.2). As a consequence, charged particles either can not reach the crystals or their measured energy will be less than the original energy. This effect can be studied only with a full GEANT simulation (see Figure 3.47).

Protons with low momentum ($p_{\text{generated}} < 400 \text{ MeV}/c$) will be fully absorbed. With higher momenta ($400 \text{ MeV}/c < p_{\text{generated}} < 1000 \text{ MeV}/c$) there is an approximately linear correlation between the generated and the measured momenta. With even higher momenta ($p_{\text{generated}} > 1000 \text{ MeV}/c$) the protons become minimum ionizing and the measured momentum will be smaller and smaller with increasing momentum of the proton, finally the measured momentum will be independent from the real momentum. It is worth to mention that protons (and also pions) generate nuclear reaction and the energy deposition by this secondary reaction gives a background to the correlation picture which was described above.

One of the cuts for identifying the conversion channel is the correlation between the momenta of the meson (π^0 or η) and the proton from the decay of the intermediate resonance. A GEANT simulation was performed to study the momentum distribution of the proton and the π^0 from the decay of a resonance which was produced by the absorption of a slow ω meson by a proton which carries Fermi momentum.

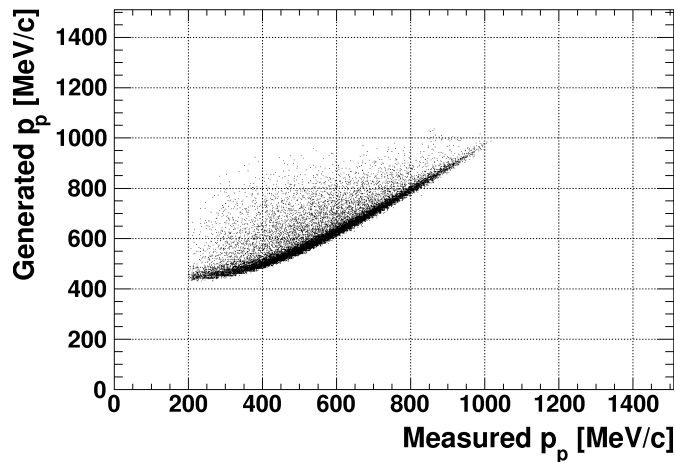


Figure 3.48.: The correlation between the generated (real) and reconstructed proton momenta when the proton is produced by a conversion of the ω meson to a π^0 -proton pair via resonance excitation and decay (see Section 3.2.5).

The simulation shows that the momenta of the protons for both studied decay channels (π^0 -proton and η -proton) are quite low, they do not reach the $1 \text{ GeV}/c$ momentum (see Figures 3.48 and 3.49). In this momentum range the real momentum of the proton can be determined from its measured value.

On the other hand the momentum distribution of the proton in the η -proton decay channel has too low values, so significant part of the protons will be absorbed in the holding structure, and the event can not be reconstructed (see Figure 3.49).

Therefore in the final analysis only those events will be used where the produced resonance decays into π^0 and proton.

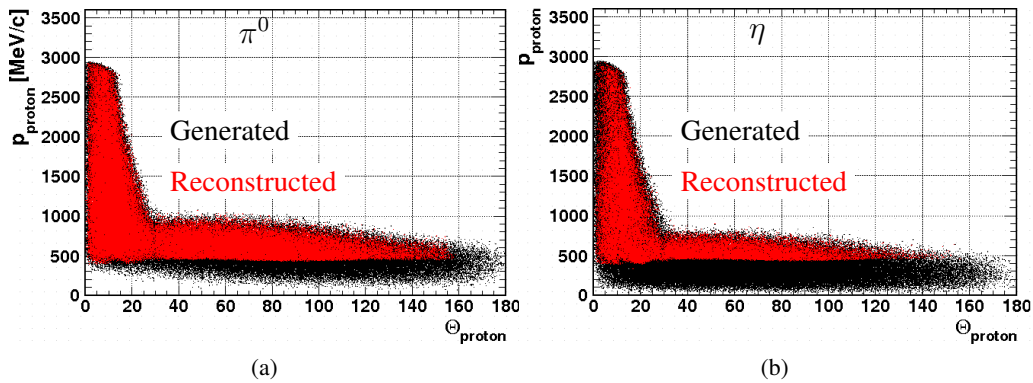


Figure 3.49.: The simulation shows the effect of the holding structure of the CB. The real polar angles and momenta of all generated particles is shown by the black scattered plots. The red scattered plot shows them if they are registered (energy was deposited by them in the detectors).

If the excited resonance decays into η and proton, most of the produced protons will not reach the detector, they will not be registered (b). In case of the resonance decays to π^0 and proton, the proton will have a larger average momentum and most of the protons will be detected (a).

Effect of the misidentification of the charged particles

The capability of the experiment is quite limited to distinguish between different type of charged particles. If a charged particle arrives in the MiniTAPS then the charged particle can be identified via the correlation of its flight-time and its energy. The rest of the detectors are too close to the target for a time-of-flight measurement. As a result, if a single charged particle hits the setup, in a general case it cannot be known what type of particle it was.

This behavior produces lots of unavoidable background to this reaction channel. In the final state it is assumed to measure two photons (from a π^0) and one proton (in addition one more proton which goes forward and can be precisely identified). Because the experimental setup cannot identify which kind of charged particle hits the setup, also π^\pm s and e^\pm s will be selected as possible final state particles. Using the kinematical constraints - the correlation between the momenta of the registered π^0 and the charged particle - do not lead to a reliable identification of the charged particles either.

The measured quantity in a calorimeter is the kinetic energy: $E_{\text{kin}} = E - m$. The cuts are made on the momentum of the particles. To derive the momentum from the kinetic energy, the mass of the particle has to be explicitly known in the calculation: $p = E_{\text{kin}} \sqrt{1 + \frac{2m}{E_{\text{kin}}}}$. This misidentification leads to “fake” momenta for charged particles with the incorrect masses (see Figures 3.50 and 3.51).

3.6. Detection efficiency

The *detection efficiency* describes the probability for reconstructing a certain reaction from the final state particles. The detection efficiency can be constructed out of three more basic efficien-

3. Data analysis

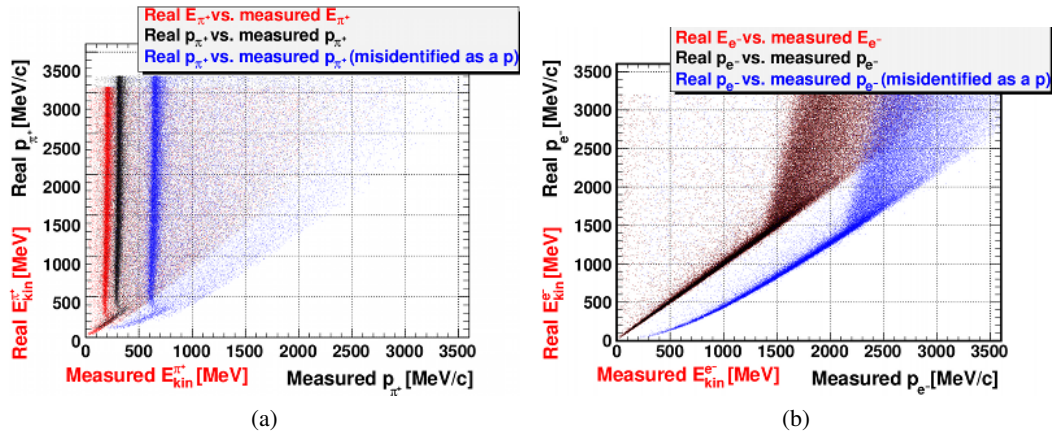


Figure 3.50.: Simulation to demonstrate the effect of a misidentified charged particle in the proton detection. In the figure (a) π^+ s were simulated and reconstructed. It can be seen that depending on the assumed mass the measured momentum is changing (black line: the mass of the particle is its nominal mass, blue line: the momentum distribution of the π^+ assuming that the particle is a proton). For more details, see text. In the figure (b) electrons were simulated and reconstructed. The color code is the same as in the other plot. Electrons are not contributing to the minimum ionizing peak.

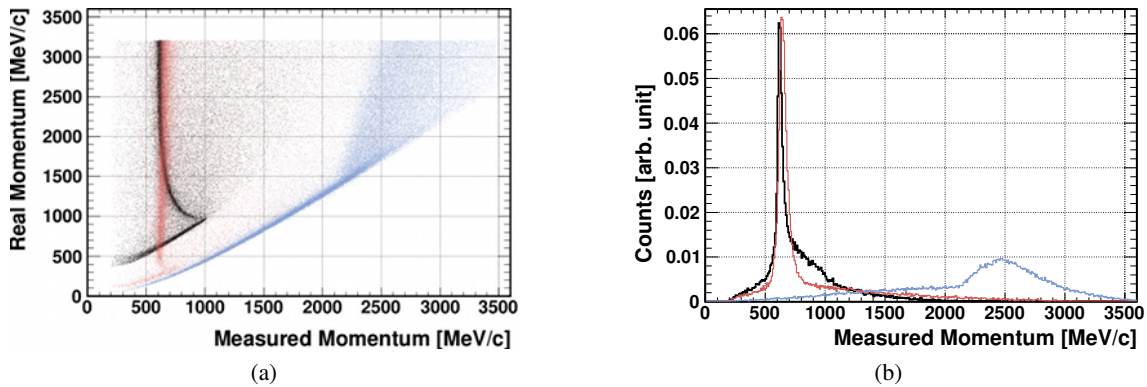


Figure 3.51.: (a) Momenta of different charged particles (black: proton, brown: π^+ , light blue: electron) when they are reconstructed as a proton. (b) The measured distribution shows a minimum ionizing peak in case of the proton and the π^+ . Electron do not contribute to the minimum ionizing peak, they produce a stronger yield at higher momenta. Besides the minimum ionizing peak scattered events can be seen due to nuclear reactions.

cies:

- **Detector acceptance:** This quantity can be deduced from the geometrical setup of the detector. The *detector acceptance* gives the probability for detecting of a particle with certain properties (momentum, direction, type of particle, ...) in a given detector setup. For ex-

ample an ω meson potentially can be detected even if it goes towards an acceptance hole²⁹, because the emission angle of decay products of the meson (three photons) are independent of the direction of the meson³⁰.

- **Detector efficiency:** There are some properties of the detector that influence the detection efficiency. For example the finite CFD and LED thresholds cut off hits with low energies. This implies that particles which decay into at least one low energy particle cannot be reconstructed.
- **Analysis efficiency:** During the analysis of the data, it is necessary to set certain cuts which not only reduce the background channels, but also reduce the signal. When these cuts are used they always have to be set in such a way that the cuts should reduce the largest amount of background events while keeping the signal untouched as much as possible.

3.6.1. Determining the detection efficiency

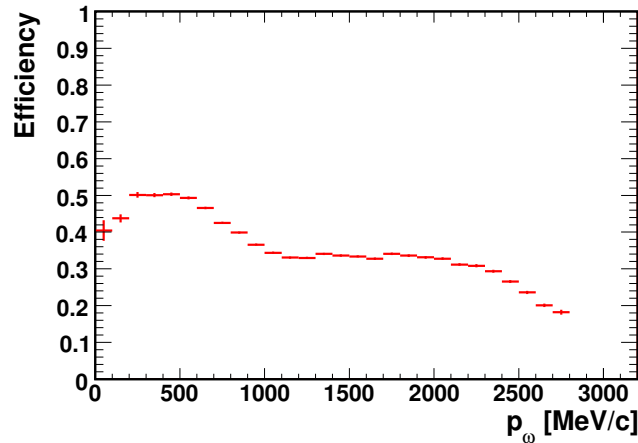


Figure 3.52.: Efficiency of the reconstruction of the $\gamma + p \rightarrow \omega + p$ reaction as a function of the momentum of the ω meson. Only the neutral decay channel of the ω meson is considered, where it decays into the 3γ final state.

To determine the detector efficiency a GEANT simulation was used. Since the detector geometry, the properties of the detector materials and the physical processes are included in the simulation package, the same behavior is expected in the simulation as in the real data. The detection efficiency of the ω meson via 3 photons in coincidence with a proton ($\epsilon_{\omega,p}$) is given by the ratio of the reconstructed events and the generated events (see Figure 3.52).

$$\epsilon_{\omega,p} = \frac{N_{\omega,p}^{\text{reconstructed}}}{N_{\omega,p}^{\text{generated}}} \quad (3.32)$$

²⁹Acceptance hole usually is a direction where no detector is placed.

³⁰This statement is true in the center of mass system if the decay is defined by the phase-space only. If the reference frame is not the CM or the decay is not a phase-space decay, the direction of the decay products are not absolutely independent of the direction of the meson.

3. *Data analysis*

The efficiency generally depends on some kinematical value (momentum of the meson, beam energy, ejection angles of the knocked-out proton, and so on).

4. Results and discussion

Contents

4.1. Momentum distribution of the photo-produced ω mesons	100
4.2. Searching for bound ω-mesic states	101
4.2.1. Back-to-back analysis	101
4.2.2. Study of the kinetic energy distribution (Marco-Weise analysis)	103
4.2.3. Conclusion	110

Chapter summary

In this chapter the obtained results are presented.

First, the momentum distribution of the ω mesons produced via quasi-free photoproduction will be discussed. This result confirms the assumption that a slow ω meson can be produced in coincidence with a forward going proton (see Section 3.5.1).

After that the study of ω -mesic states will be presented. A simultaneous fit of the kinetic energy ($E_{\pi^0\gamma} - m_{\omega}^{\text{PDG}}$) and the invariant mass histograms in different momentum bins gives the opportunity to clarify whether there is any non-zero yield above the background in the region $E_{\pi^0\gamma} - m_{\omega}^{\text{PDG}} < 0$ MeV, as it was predicted theoretically (for example see Figure 1.18).

Finally, the analysis of those events will be presented where the ω meson is absorbed by a nucleon and the produced excited nucleon decays into proton- π^0 final state with a large relative angle between them. This channel gives an alternative tool to study the ω -mesic nuclear state.

4.1. Momentum distribution of the photo-produced ω mesons

Theoretical considerations predict a binding energy between ω and a ^{11}B nucleus (^{12}C with one proton removed) of about 80 MeV [STT07]. This implies that a slow ω meson with a momentum smaller than $\approx 360\text{ MeV}/c$ can be bound. The prerequisite for the production of a bound mesic nucleus is that the momentum difference between the produced meson and the nucleus is less than this value.

In order to determine the momentum distribution of the ω meson the invariant mass spectrum of the reconstructed $\pi^0\gamma$ system was plotted for different momentum bins, and fitted by a skewed Gaussian (Novosibirsk function, see equation 3.7) on an $\exp(\text{pol4})$ background, where the “*pol4*” denotes an ordinary polynomial of the fourth degree. The uncertainty of the fits were decreased by fixing the width and the skewness parameters of the Novosibirsk function ($\sigma=29.5\text{ MeV}/c^2$, skewness=-0.18). The same procedure was repeated in different cases where the charged particle was registered in different parts of the setup. Because the Crystal Barrel, the Forward Plug and the MiniTAPS cover different polar ranges, the momentum distribution of the produced ω mesons can be mapped as a function of the Θ_{charged} (see Figure 4.1).

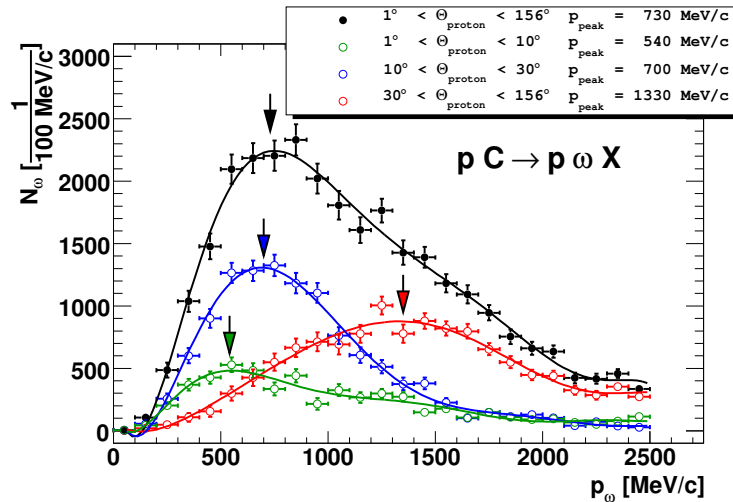


Figure 4.1.: Momentum distribution of ω mesons produced in quasi-free photoproduction. The different colors show the momentum distribution of the ω mesons when the knocked out protons are registered in different parts of the setup. The most probable value of the momentum distribution shows correlation with the polar angle of the knocked-out particle.

The kinematic calculations show that a very forward going proton can be an indication for an ω meson produced with low momentum (see Section 3.5.1). This assumption is proven here.

The positions of the most probable values of the distributions correlate with the covered polar angular range of the knocked-out protons and the smallest value is given by an ω meson in coincidence with a proton registered in the MiniTAPS ($1^\circ \leq \Theta_p \leq 10^\circ$).

The rest of the analysis will use only the slow ω mesons registered in coincidence with a proton in the MiniTAPS.

The measured momentum distribution gives an interesting aspect to compare it to GiBUU simula-

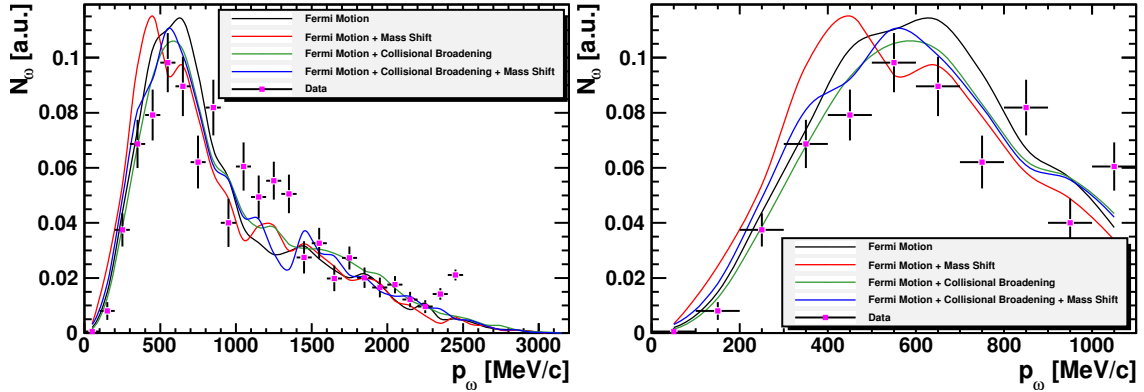


Figure 4.2.: Momentum distribution of the ω mesons compared to GiBUU simulation. The simulated data was tracked through the setup using GEANT. The results of the measured momentum distribution and the GEANT-tracked GiBUU data can be compared directly. All histograms are normalized to the same area.

tions where different in-medium scenarios are simulated (see Figure 4.2).

In vacuum the mesons must have their nominal vacuum mass. If in the nuclear medium the mass of the meson is lowered compared its vacuum value then this mass difference have to be compensated from its kinetic energy if it goes from the nucleus to the vacuum. As a result, the momentum of the mesons have to be smaller than the momentum with which it was produced. Comparing the measured momentum distribution with GiBUU simulations, where different in-medium effects are simulated (Fermi motion, collisional broadening, mass shift and combination of these scenarios) information can be gained about the type of the interaction inside the nucleus.

Due to the poor statistics, no conclusion can be drawn about the in-medium behavior of the ω mesons using this analysis method.

4.2. Searching for bound ω -mesic states

4.2.1. Back-to-back analysis

Monte Carlo simulation shows that charged particles which are misidentified as a proton (primarily π^\pm) produce a peak in the momentum distribution (minimum ionizing peak, see Figure 3.51). To avoid the effect of these misidentified particles the analysis is performed only for events where p_{measured} is smaller than $500 \text{ MeV}/c$, i.e. only particles will be processed which are not minimum ionizing.

After cutting on the reconstructed momenta of the π^0 and the charged particles (see Figure 3.46), the events will be sorted according to the opening angle between π^0 and the charged particles. One histogram is filled with events having opening angle larger than 120 degree (signal), the other one is filled when the opening angle is between 90 and 120 degree (background, see Figure 3.46).

In order to avoid the effect of the different efficiencies of the tagger channels, the resulting histograms are normalized to the original tagger distribution. To observe the difference between the two distributions the two histograms were divided by each other. At higher energies (above 2.5 GeV) the resulting ratio histogram has a big statistical uncertainty¹. Between 1.5 GeV and

¹The tagger bars have an equal size, but they cover energy ranges with different size. At higher energies, where the

4. Results and discussion

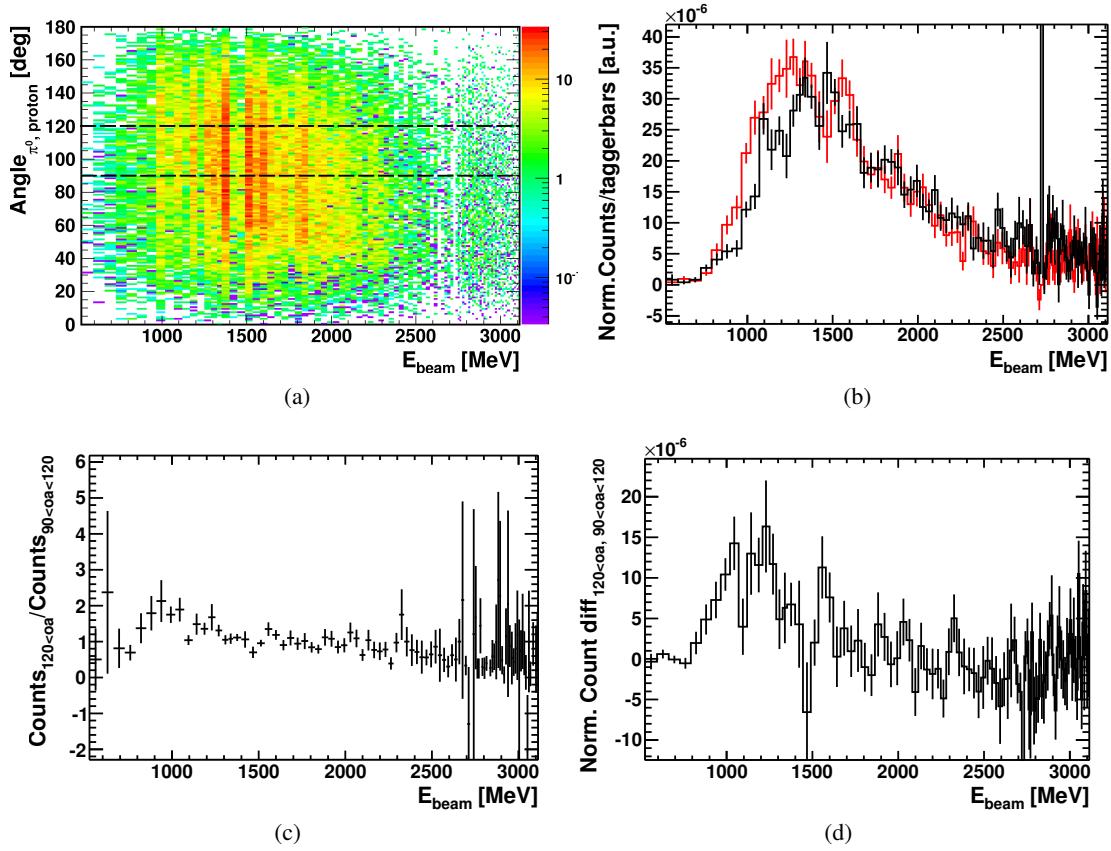


Figure 4.3.: One proton was registered in the MiniTAPS (identified by a cut around the *proton-band*) in coincidence with two photons which form a π^0 meson and one additional charged hit. The relative angle between the charged hit and the π^0 is plotted as a function of the beam energy (a). The two horizontal lines show the borders of the *signal region* ($120^\circ \leq \text{Angle}_{\pi^0, \text{proton}} \leq 180^\circ$) and the *background region* ($90^\circ \leq \text{Angle}_{\pi^0, \text{proton}} \leq 120^\circ$). The projected spectra were normalized by the original tagger spectrum (b). The ratio (c) and the difference (d) of the normalized spectra are also shown.

2.5 GeV the distribution is flat which gives the opportunity to normalize the two spectra to this energy range. The normalized spectra can be subtracted from each other.

In the ratio-distribution there is an increased yield in coincidence with opening angles larger than 120 degree at lower beam-energies ($E_{\text{beam}} < 1.5 \text{ GeV}$). The same structure is visible in the difference spectrum, too.

However, the difficulties to distinguish between different charged particles in the setup make the identification of the reaction problematic. A baryonic resonance produced via the reaction $\gamma + n \rightarrow (N^*/\Delta) \rightarrow p + \pi^- + \pi^0$ leads to also two neutral hits and two charged hits in the final state just as the possible bound state via a conversion would do. This channel can have a lower

number of the Bremsstrahlung photons is low ($N \sim \frac{1}{E}$), the tagger bars cover a smaller energy range. These two effects (smaller number of photons and smaller energy coverage per tagger channels) result in poorer statistics in the higher energy bins.

production threshold than the quasi-free ω production and may have a higher branching than the studied channel.

4.2.2. Study of the kinetic energy distribution (Marco-Weise analysis)

If an ω meson decays inside the nucleus where an attractive potential is assumed between the nucleus and the meson, there will be a non-zero yield appearing on the negative side of the kinetic energy spectrum ($E_{\pi^0\gamma} - m_{\omega}^{\text{PDG}}$). Simultaneously, the mass of the ω meson will be lowered.

In order to get these spectra, certain kinematical cuts (see also Section 3.3.1) were made on the selected events with 3 neutral hits and one charged hit.

- Since the ω meson decays into $\pi^0\gamma$, the invariant mass of two neutral particles out (treated as a photons) of the detected three, should fall into the invariant mass-range of the π^0 .
- The incident beam energy is restricted to $1250 \text{ MeV} < E_{\gamma}$.
- The energy of the final state photon, which does not belong to the π^0 , has to be larger than 200 MeV.
- The kinetic energy of the π^0 in the final state must be larger than 150 MeV.
- There was a cut applied on the missing mass ($m_{\text{proton}} \pm 150 \text{ MeV}/c^2$) to reduce the influence of the events with $4\text{-}\gamma$ final state.
- Events are accepted, if a charged hit is registered in the MiniTAPS.
- In order to ensure that the registered charged hit in the MiniTAPS is a proton, there was a cut applied around the *proton-band* (see Figure 4.7).

The reconstructed invariant mass and the kinetic energy of the surviving $\pi^0\gamma$ events were filled into histograms for different $p_{\pi^0\gamma}$ ranges (see Figure 4.4).

The main background contribution is due to events with - originally - four photons in the final state (see Section 3.2.4). These kind of events can be reproduced from the data, selecting events with exactly four photons (and one charged hit) in the final state, making all three-photon combinations and analyzing them in the same way as the data was analyzed.

The kinetic energy and invariant mass distributions were fitted simultaneously with a background term and a quasi-free ω signal. The background was extracted from events with four neutral hits in the final state, the invariant mass distribution of the ω signal was modelled by a Novosibirsk function (see equation 3.7) while the kinetic energy distribution of the ω s was simulated (see Section 3.4). Because of the poor statistics that remained after the kinematical cuts, the momentum bins had to be chosen as wide as $300 \text{ MeV}/c$ (see Figure 4.5) and the binning of the resulting histograms was chosen to 40 MeV in the kinetic energy histogram and $40 \text{ MeV}/c^2$ in the invariant mass histogram.

In the higher momentum bins ($300 \text{ MeV}/c \leq p_{\pi^0\gamma}$, where bound states are not expected), the distributions can be described with the signal of the quasi-free ω meson and the background from the events with four γ s in the final state (see Section 3.4, Figures 4.5a and 4.5b). In the lowest momentum bin ($0 \text{ MeV}/c \leq p_{\pi^0\gamma} \leq 300 \text{ MeV}/c$) an extra yield appears above the background between $600 \text{ MeV}/c^2 < m_{\pi^0\gamma} < 700 \text{ MeV}/c^2$ in the invariant mass spectrum and around -100 MeV in

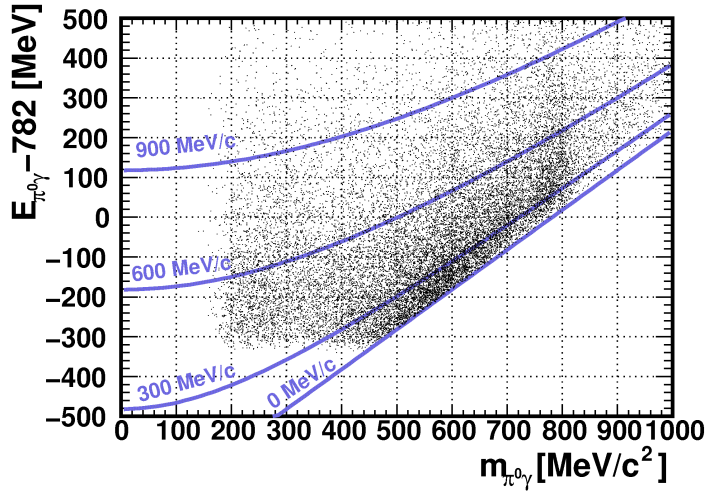


Figure 4.4.: The 2D representation of the data after all kinematic cuts. The cuts on the momentum are also visualized. Projections onto the X and Y axes gives the invariant mass and kinetic energy distribution, respectively.

the $E_{\pi^0\gamma} - m_{\omega}^{\text{DPG}}$ spectrum. This structure is visible, even if the fitting routine overestimates the background (see Figure 4.5c).

To quantify the structure, another Gaussian term was added to the fitting functions. The new Gaussian term, that fits the extra yield above the background, measures 83 ± 32 counts (see Table 4.1).

	$0 \text{ MeV}/c \leq p_{\pi^0\gamma} \leq 300 \text{ MeV}/c$	$300 \text{ MeV}/c \leq p_{\pi^0\gamma} \leq 600 \text{ MeV}/c$	$600 \text{ MeV}/c \leq p_{\pi^0\gamma} \leq 900 \text{ MeV}/c$
Omega Yield	92 ± 12	226 ± 21	152 ± 17
Omega Position	766 ± 6	781 ± 4	785 ± 5
Omega Width	25 [fixed]	25 [fixed]	25 [fixed]
Omega tail	-0.02 [fixed]	-0.02 [fixed]	-0.02 [fixed]
Background yield	387 ± 38	1300 ± 35	819 ± 28
Signal yield	83 ± 32	-	-
Signal position (E_{kin})	-101 ± 24	-	-
Signal position ($m_{\pi^0\gamma}$)	646 ± 13	-	-
Signal width (E_{kin})	60 ± 28	-	-
Signal width ($m_{\pi^0\gamma}$)	39 ± 14	-	-

Table 4.1.: Parameters of the fit of the data after applying the cuts listed in Section 3.3.1.

In order to compare this result to theoretical models the expected number of the hits is calculated using the theoretical prediction made by Nagahiro et al. [NJH05].

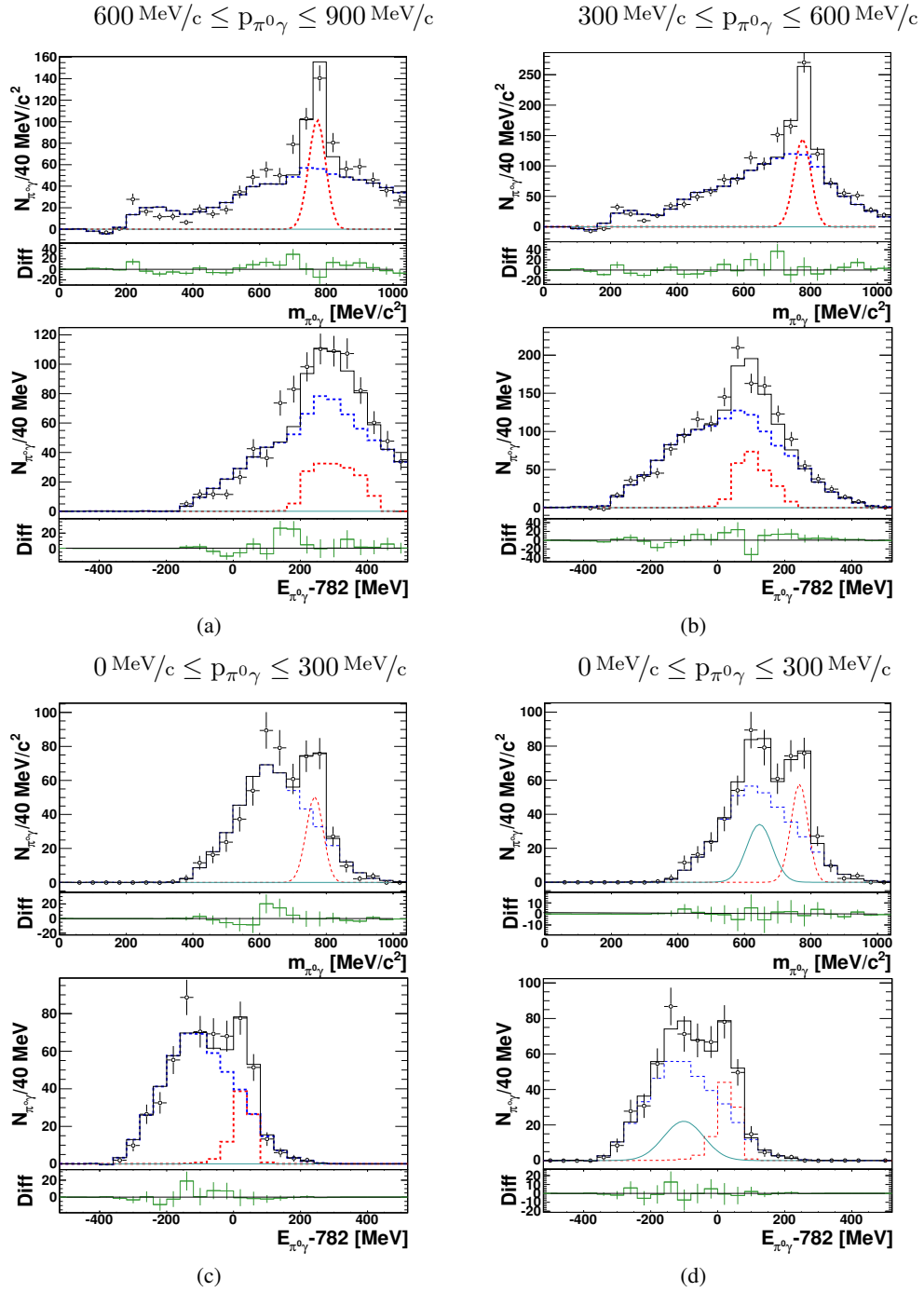


Figure 4.5.: Simultaneous fit of the invariant mass and the kinetic energy spectra in different momentum bins. The blue distribution is the background derived from events with four photons in the final state. The red lines denote the quasi-free ω signals (see Section 3.4). The azure line is the fit of the yield above the background in the lowest momentum bin. The green line is the difference between the data points and the sum of the background and the signal(s) (black line). The measured data in the lowest momentum bin cannot be described only with the four-photon background and ω signal.

Count rate estimate

The number of registered counts is calculated using the expression:

$$N_{\text{events}} = \frac{d\sigma}{d\Omega} \Delta\Omega \epsilon_p \epsilon_{\pi^0\gamma} B_{\pi^0\gamma} N_t N_\gamma \quad (4.1)$$

where $\frac{d\sigma}{d\Omega}$ is the differential cross section, $\Delta\Omega$ is the covered solid angle, ϵ_p and $\epsilon_{\pi^0\gamma}$ are the detection efficiencies of a proton and a $\pi^0\gamma$ event, respectively, $B_{\pi^0\gamma}$ denotes the branching ratio of the neutral decay channel of the ω meson and finally N_t and N_γ mean the number of the target atoms and the number of the beam photons.

The differential cross section between $-100 \text{ MeV} \leq E_\omega - m_\omega \leq -23 \text{ MeV}$ (see Figure 4.6) is

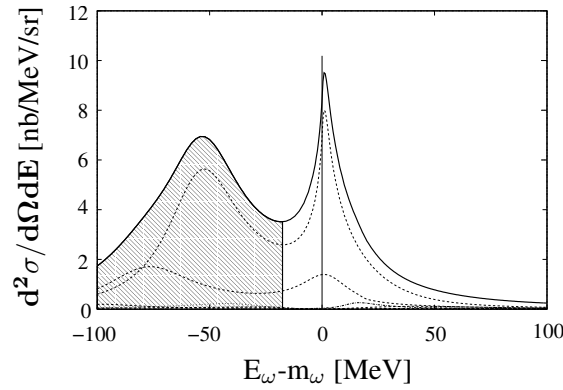


Figure 4.6.: Missing energy spectra of the $^{12}\text{C}(\gamma,p)\omega^{11}\text{B}$ for an attractive potential (see section 1.5.2).

$$\frac{d\sigma}{d\Omega} \approx 360 \text{ nb/sr}. \quad (4.2)$$

Covered solid angle: MiniTAPS covers the polar range between 1° and 10° and the full spherical angular range between 0 and 2π radian. The covered solid angle is

$$\begin{aligned} \Delta\Omega &= \frac{1}{2} ((1 - \cos(10^\circ)) - (1 - \cos(1^\circ))) \cdot 4\pi \\ &= 7.53 \cdot 10^{-3} 4\pi = 9.45 \cdot 10^{-2} \text{ sr} \end{aligned}$$

Proton detection efficiency: Single protons were distributed homogeneously in the setup by means of Monte Carlo simulation. The ratio of the number of the reconstructed events² and the generated ones gives a first approximation of the reconstruction efficiency of a proton in the MiniTAPS (see Section 3.6). In order to achieve a better proton identification only those events are processed further where the proton did not generate a nuclear reaction, consequently the correlation between the (deposited) energy and the flight time of the protons is well defined (See Figure 3.17). Since only $\approx 60\%$ of the protons lie in the proton band, this cut will further reduce the detection efficiency of the proton to

²The reconstruction required that the detected hit is coming from a charged particle (veto detector was fired) and the relative angle between the generated and hits is smaller than 10°

$$\epsilon_p \approx 40\%$$

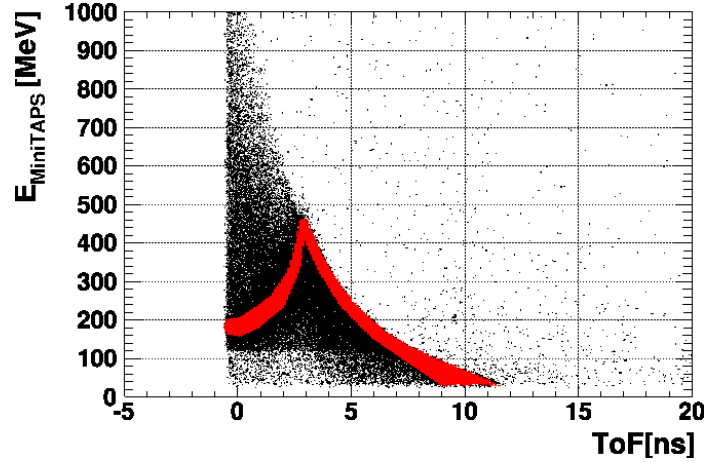


Figure 4.7.: Energy deposition of charged particles in MiniTAPS as a function of the flight time. The effect of a strict cut on the proton band is illustrated. The black scatter plot shows all proton events in the $\gamma + p \rightarrow \omega + p$ reaction that arrive in the MiniTAPS detector. The red scatter plot shows the identified events in the proton-band. In the proton-band only $\approx 60\%$ of all protons are registered, the rest induces nuclear reactions.

Detection efficiency of the ω meson via $\pi^0\gamma$ decay channel: ω mesons were isotropically distributed over 4π solid angle via a GEANT simulation. Every simulated ω mesons decayed into the three-photon final state. The ratio of the generated and reconstructed events gives the detection efficiency for the ω events:

$$\epsilon_\omega \approx 50\%$$

Branching ratio of the ω to $\pi^0\gamma$: This quantity gives the probability that the ω meson will decay into $\pi^0\gamma$. According to the Particle Data Group [N⁺10], this value is:

$$B_{\omega \rightarrow \pi^0\gamma} \approx 8.2\%.$$

However, the branching ratio necessarily has to decrease, because a fraction of the produced ω mesons will be absorbed in the nuclear medium ([K⁺08b]).

The width of the observed additional signal is $\Gamma_{\text{observed}} \approx 80$ MeV, the vacuum width of the ω meson is approximately $\Gamma_\omega^{\text{Vac}} \approx 8.4$ MeV and the measured width of the ω signal value $\Gamma_{\omega, \text{vacuum}} \approx 50$ MeV. Approximating the shape of the distributions by Gaussians the total width of the signal not folded by the experimental resolution is

$$\Gamma_{\text{tot}} \approx 60 \text{ MeV}$$

The branching ratio $B_{\omega \rightarrow \pi^0\gamma}$ into the $\pi^0\gamma$ channel is given by.

4. Results and discussion

$$B_{\omega \rightarrow \pi^0 \gamma} = \frac{\Gamma_{\pi^0 \gamma}}{\Gamma_{\text{tot}}} = \frac{0.082 \Gamma_{\omega}^{\text{Vac}}}{\Gamma_{\text{tot}}} \approx \frac{0.09 \cdot 8.4 \text{ MeV}}{60 \text{ MeV}} \approx 1.3 \cdot 10^{-2}$$

Number of target atoms: The number of atoms in a carbon cylinder of 2 cm length is:

$$N_t \approx \frac{6.0 \cdot 10^{23}}{12 \text{ g}} 1.67 \text{ g/cm}^3 * 2 \text{ cm} = 1.67 \cdot 10^{23} \text{ cm}^{-2}.$$

Number of beam photons: Measuring the number of produced ω^0 s (via three photons in the final state [Nan10]) and η s (via six photons in the final state [M⁺08]) on a carbon target and using the measured cross sections of these reactions ($\langle \sigma_{\omega} \rangle \approx 8.6296^{-30} \mu\text{b}$ and $\langle \sigma_{\eta} \rangle \approx 3.33^{-29} \mu\text{b}$ for the energy range $E_{\gamma} = 1250 - 2150 \text{ MeV}$), the number of the beam photons in the 1250-3113 MeV energy range is estimated to be

$$N_{\gamma} \approx 10^{12}$$

Expected number of counts: Using equation 4.1 the expected number of counts from the prediction of Nagahiro et al. is: [NJH05] (see Figure 4.6)

$$N_{\text{events}} = \frac{d\sigma}{d\Omega} \Delta\Omega \epsilon_p \epsilon_{\pi^0 \gamma} B_{\pi^0 \gamma} N_{\gamma} N_t \approx 16 \text{ counts.} \quad (4.3)$$

In order to exclude that the analysis method produces artifacts that can accumulate and appear as a peak in the studied histograms, a check was performed.

Data was simulated by GiBUU which contains the

$$\gamma + {}^{12}\text{C} \rightarrow \begin{cases} p + \omega + N + X \\ p + \omega + \Delta + X \\ p + \rho + N + X \\ p + \rho + \Delta + X \\ p + \pi^{0,\pm} \pi^{0,\pm} + X \\ p + \pi^0 \eta + X \\ \dots \end{cases}$$

reaction channels. No mass-shift of the ω meson was simulated. The generated particles were tracked through the setup by GEANT and finally the data was analyzed in the same manner as the measured data.

The result shows that the GiBUU data, where neither bound states nor mass shift were simulated, produces distributions that can be fitted by only a background distribution and an ω signal (see Figure 4.8 and Table 4.2).

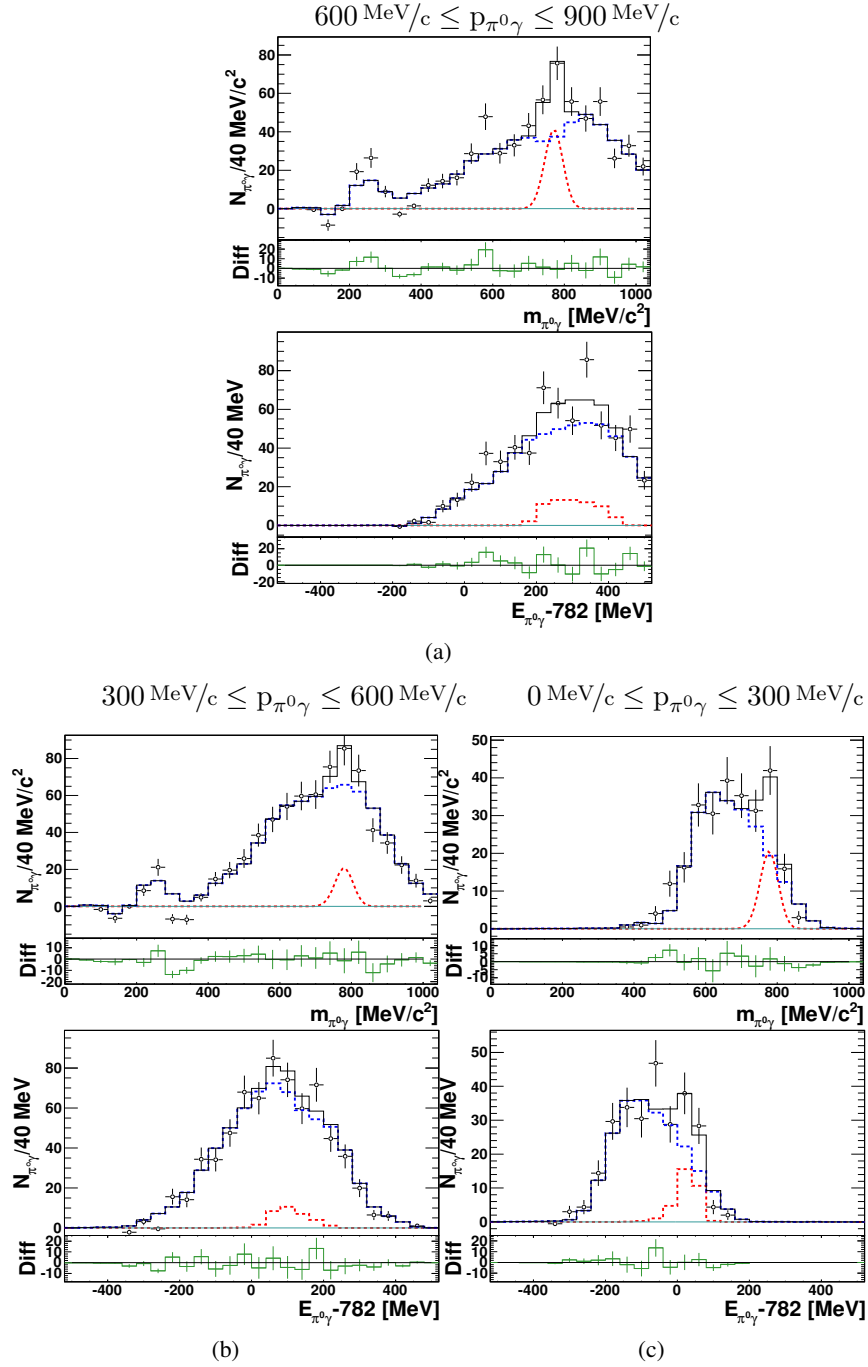


Figure 4.8.: Simultaneous fit of the invariant mass and the kinetic energy spectra in different momentum bins. Data from GiBUU simulation can be reproduced with 4 photon background and ω signal in every momentum bin. (Color code is described in the caption of the Figure 4.5)

Single $\pi^0 \rightarrow \gamma\gamma$ and $\eta \rightarrow \gamma\gamma$ channels can produce non-smooth background distributions in the $E_{\pi^0\gamma} - m_\omega$ and in the $m_{\pi^0\gamma}$ distributions after a split-off (see Figures H.5 and H.6). These yields are not taken into account during the construction of the background of the fit. The single η contribution can be removed by sideband subtraction (together with the contribution from the

4. Results and discussion

	$0 \text{ MeV}/c \leq$ $p_{\pi^0\gamma}$ $\leq 300 \text{ MeV}/c$	$300 \text{ MeV}/c \leq$ $p_{\pi^0\gamma}$ $\leq 600 \text{ MeV}/c$	$600 \text{ MeV}/c \leq$ $p_{\pi^0\gamma}$ $\leq 900 \text{ MeV}/c$
Omega Yield	35 ± 7	48 ± 14	64 ± 13
Omega Position	783.8 ± 7.7	793.1 ± 9.2	777.9 ± 14.6
Omega Width	25 [fixed]	25 [fixed]	25 [fixed]
Omega tail	-0.21 [fixed]	-0.21 [fixed]	-0.21 [fixed]
Background yield	227 ± 13	658 ± 25	595 ± 23

Table 4.2.: Parameters of the fit of the data after applying the cuts listed in Section 3.3.1.

$\pi^0\eta$ channel). The background coming from single π^0 channel cannot be removed by sideband subtraction, since in the sidebands no intensity can be found from this channel. A peak-like structure appears in the $m_{\pi^0\gamma}$ invariant mass spectrum in this channel after placing a threshold on the “third” neutral hit (which does not belong to the π^0). This cut has only a minor impact on the yield of the ω and the shape of the background. In order to avoid this artifact, the cut $E_{\gamma_3} > 200 \text{ MeV}$ is removed (on both the “signal” and “background” dataset).

An attempt was made to further decrease this background yield via additional kinematical cuts:

- The energy threshold on the clusters was also increased to 50 MeV to reduce the impact of the split-offs (every cluster with a smaller energy deposit than 50 MeV was rejected).
- Every event was removed where two neutral particles were registered with small relative angle between them *and* if one of them had relatively small energy. This cuts effectively removes the photon induced split-offs.
- A characteristic difference was found between the ω -channel and the π^0 channel if the opening angle between photon-pairs are plotted against the opening angle between the charged hit and the photon which does not belong to the earlier mentioned pair of photons (see Figure 3.44).
- A typical source of the split-offs is the Forward Plug detector. If a split-off is generated in this detector the produced “neutral hit” will be detected in the MiniTAPS or in the Forward Plug itself. To decrease the influence of these distorted events, all events were discarded where one neutral is detected in polar angles less than 20° .

After these modification the simultaneous fit was performed on this data (see Figure 4.9).

This test shows that - due to the poor statistics - it is not easy to estimate the background anymore, but a remaining yield above the background cannot be excluded (49 ± 20 counts, see Table 4.3).

4.2.3. Conclusion

If there is an attractive potential between the nucleus and an ω meson and if the momentum of the ω is small enough a bound state of the ω -nucleus system, so-called ω -mesic nucleus, might exist. The goal of this experiment was to study the existence and the properties of the ω -mesic nucleus.

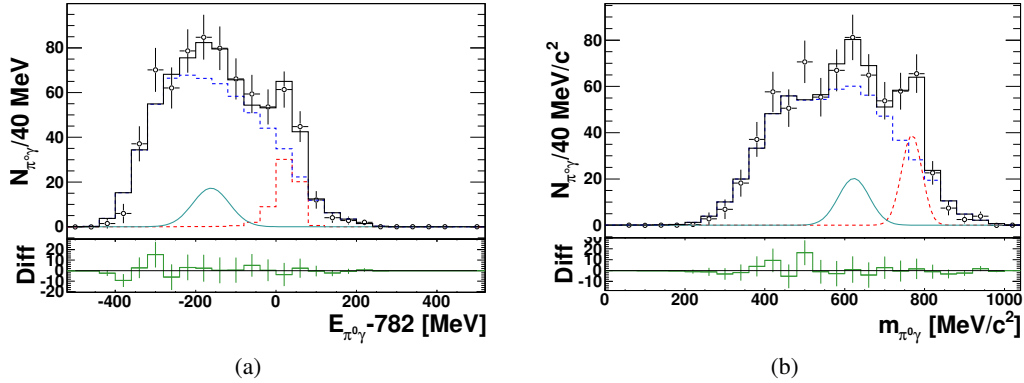


Figure 4.9.: Simultaneous fit of the invariant mass and the kinetic energy spectra in the lowest ($p_{\pi^0\gamma} < 300 \text{ MeV}/c$) momentum bins after using cuts to remove single π^0 and η contribution to the studied reaction channel, a simultaneous fit was performed on the invariant mass and kinetic energy spectra. (Color code is described in the caption of the Figure 4.5)

Omega Yield	62 ± 9	1.479 ± 0.305
Omega Position	768 ± 6	
Omega Width	25 [fixed]	
Omega tail	-0.02 [fixed]	
Background yield	606 ± 31	0.638 ± 0.0712
Signal yield	49 ± 20	1.685 ± 0.702
Signal position (E_{kin})	-162 ± 26	
Signal position ($m_{\pi^0\gamma}$)	623 ± 19	
Signal width (E_{kin})	46 ± 19	
Signal width ($m_{\pi^0\gamma}$)	38.8 [at limit]	

Table 4.3.: Parameters of the fit of the data for $0 \text{ MeV}/c \leq p_{\pi^0\gamma} \leq 300 \text{ MeV}/c$ after applying the cuts to reduce the contribution of the background channels (see Section 3.5.5). The third column the gives the ratio of the fitted values without and with applying the extra cuts to remove the background contribution.

The ω was produced by quasi-free photoproduction (see Section 3.5.1) directly inside the nucleus. Two different decay modes were studied.

- If the bound ω meson is absorbed by a nucleon, then this meson will not appear in the neutral decay channel anymore. The produced baryonic excitations, however, can decay into a proton-meson (where the meson can be either π^0 or η) system and a correlation between the momenta of the proton and the meson, together with a large opening angle between them, can indicate the presence of a bound ω mesic state.

Unfortunately, a strong background contribution is present from the $\gamma + n \rightarrow p + \pi^- + \pi^0$ reaction channel where the charged pion is misidentified as a proton. This background

overwhelms the possible signals.

- If a bound ω meson decays inside the nucleus, its invariant mass and the kinetic energy can be studied via its decay products. The analysis of the neutral decay channel of the ω ($\omega \rightarrow \pi^0\gamma \rightarrow 3\gamma$) was chosen because of the relatively large branching ratio ($\sim 9\%$) and because the detector setup is suited to detect photons (see Sections 2.2.1, 2.2.3 and 2.2.4). After kinematical cuts (see Section 3.3.1), a simultaneous fit of the kinetic energy and the invariant mass histograms in different momentum bins was performed (see Section 3.4).

This analysis shows that the distributions in the higher momentum bins can be described with an ω signal and a background distribution obtained from events with four neutral hits in the final state. However, in the lowest momentum bin an extra yield appears at ~ -100 MeV in the kinetic energy distribution and simultaneously at ~ 650 MeV/ c^2 in the invariant mass distribution (see Figure 4.5). The excess yield was fitted with a Gaussian function and the integral of the Gaussian measures 83 ± 32 counts which yield corresponds to a differential cross section of 1.87 ± 0.72 $\mu\text{b}/\text{sr}$.

Three scenarios can be considered to explain this structure:

1. *The fitting method produces an artifact, that is interpreted as a signal yield.*
Simulated data, where several contributing reaction channel were simulated but neither mass shift nor bound state was present, can be fitted with a background distribution (obtained from events with four neutral hits in the final state) and with a free ω meson signal.
2. *There is another source of background that does not relate to the four photon final state.*

The major background sources of this reaction are events with four neutral hits in the final state (like $\gamma + p \rightarrow \pi^0\pi^0 + p$ or $\gamma + p \rightarrow \pi^0\eta + p$ channels) with one photon lost (see Section 3.5.4). This type of background is taken into account in the simultaneous fit (see Section 3.4). However it is shown that other channels can also contribute to the $\pi^0\gamma$ final states (for example single π^0 or η production with a split-off or the $\gamma + p \rightarrow \pi^0\pi^+n$ channel with mis-identified charged pion and neutron). The reaction channel where the charged pion in the final state is misinterpreted as proton and the neutron is misinterpreted as photon ($\gamma + p \rightarrow \pi^0\pi^+n$) is effectively removed by the kinematical cuts used in the analysis (see Figure H.2). In order to remove the effect of the single π^0 and η channels, additional kinematical cuts were used (see Section 3.5.5).

These cuts have relatively small influence on the events with four photons in the final state, but they reduce the number of the registered quasi-free ω mesons (compare the Figure 4.5d to the Figure 4.9). At the same time these cuts remove or smooth in the originally peaking distributions in the region of the signal (see Figure H.9). As a result, it is very difficult to fit the remaining distribution, but the presence of the remaining signal cannot be excluded (see Figure 4.9).

3. *The measured yield is a signature of an ω -nucleus bound state.*

Although the sensitivity level to test the theoretical predictions has been reached, in this experiment no surplus intensity has been observed at ≈ -60 MeV in the kinetic energy spectrum where excess yield is anticipated according to theoretical calculations. However,

an extra intensity is observed in a mass and energy range where structures from background reactions may be expected although cuts to suppress those have been applied. Because the statistical and systematic uncertainties this excess yield is considered an upper limit for the existence of an ω mesic state. The observed 83 ± 31 counts correspond to a 3σ upper limit of 180 counts. Using the countrate estimate given above this 3σ upper limit corresponds to $\approx 4 \mu\text{b}/\text{sr}$ for the incident photon energy range of $E_\gamma = 1250 - 3113 \text{ MeV}$.

To test whether the observed structures can also be attributed to background effects which are not fully under control, a reference measurement on LH_2 target has been performed, which is presently being analyzed within another PhD-thesis [Fri11].

4. *Results and discussion*

Frequently Used Abbreviations

CB	Crystal B arrel.
ELSA	Elektronen- S tretcher- A nlage.
FWPlug	For W ard P lug.
MC	Monte C arlo.
MiniTAPS	Two A rm P hoto- S pectrometer.
PED	Particle E nergy D eposit.
QCD	Quantum Chromo D ynamics.
QED	Quantum E lectro D ynamics.
SM	Standard M odel of Particle Physics.
SPS	Super P roton S ynchrotron.
TOF	Time- o f- F light.

A. Quantum numbers

The ordering scheme invented by M. Gell-Mann et al. classifies the particles according to their quantum numbers. In this chapter a quick overview of the QCD quantum numbers of the will be presented.

- **Spin, Orbital angular momentum and Total angular momentum**

- **Spin**

- Spin (quantum number S) is a vector quantity that represents the "intrinsic" angular momentum of a particle. It comes in increments of $1/2\hbar$. Fermions (for example quarks, electrons, neutrinos, baryons, ...) carry "half integer" spin ($N \cdot \pm 1/2$) while bosons (for example gluons, photon, mesons, ...) carry "integer" spin (0, 1, 2, ...). According to quantum mechanics, the spin of two particles can be aligned in which case the two spin vectors couple to a vector of length $S = 1$ and three spin projections ($S_z = +1, 0, -1$) called the *spin-1 triplet*. If they are antialigned then the length of the vector is $S = 0$ and has only one projection ($S_z = 0$) called the *spin-0 singlet*. Since mesons are made of one quark and one antiquark, they can be found in triplets and singlet states.

- **Orbital angular momentum**

- The orbital angular momentum (quantum number L) represents the relative angular momentum with which two particles can couple.

- **Total angular momentum**

- The intrinsic- and the orbital angular momenta couple to the total angular momentum of the states (quantum number J). The possible states are $|L - S| \leq J \leq |L + S|$ in increments of 1.

- **Parity**

- Parity (quantum number P) transformation is a simultaneous flip in the sign of all three spatial coordinates and can be either positive ($P = +1$ or simply $P = +$) or negative ($P = -1$ or simply $P = -$). The total parity of mesonic states are given by: $P = (-1)^{L+1}$, where L is the orbital angular momentum.

- **Isospin** Isospin (quantum number I) was introduced by Heisenberg to describe the similarities of neutrons and protons concerning strong interaction. According to the isospin formalism the u and d quarks can be treated as the same particle with different isospin. Isospin is handled in the same way as the spin and its third component I_3 distinguishes the two states of u and d .

- **Flavor quantum numbers** Since only the u and d quarks have similar masses only these two quarks can be handled with the same quantum number (isospin). As new type of quarks were discovered new quantum numbers were introduced to describe the quark-content of the particles (quantum number S -strangeness, C - charmness, B - bottomness, T - topness). Quarks carry quantum number +1 antiquarks -1.

A. Quantum numbers

Types of mesons	S	L	J	P	JP	example
Pseudoscalar	0	0	0	-	0-	$\pi^{0,\pm}$
Pseudovector	0	1	1	+	1+	$a_1(1260)$
Vector	1	0	1	-	1-	ω
Scalar	1	1	0	+	0+	$a_0(980)$

B. Trigger-scheme of the MiniTAPS

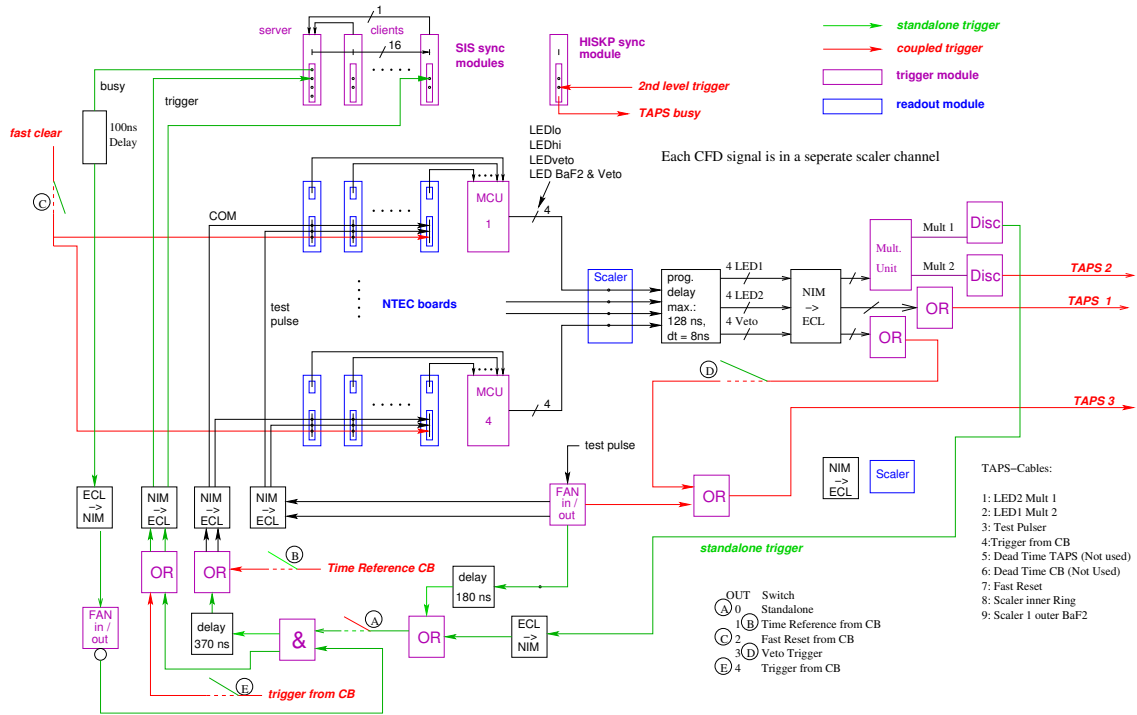


Figure B.1.: Trigger-scheme of the TAPS

B. Trigger-scheme of the MiniTAPS

C. Parameters during the experiment

trigger	carbon_omega_prime
radiator	Cu-50
current	0.138 nA
tagger	5.3 MHz
GIM	4.4 MHz
Tagger && GIM	3.2 MHz
Inner	186 kHz
FP1	8 kHz
FP2	760 Hz
FP veto	275 kHz
Taps1	33 kHz
Taps2	15 kHz
Taps3	3 Hz
FastReset	5 kHz
Event	425 Hz
Lifetime	310 kHz
Tagger (upper32ch coinc)	1.3 MHz

Figure C.1.: Typical rates

Radiator	Tagger rate	Trigger	event rate	LED1 rate	LED2 rate	total		
						files	time	events
Cu50	6 MHz	carbon_omega_prime	400 Hz	33 kHz	16 kHz	1055	8:15:56:56	204581999
Cu150	10 MHz	carbon_omega_prime	650 Hz	65 kHz	55 kHz	71	13:32:45	13838187
Cu150	10 MHz	carbon_omega	320 Hz	65 kHz	55 kHz	22	6:28:10	4810522
Cu50	6 MHz	carbon_omega	280 Hz	30 kHz	20 kHz	301	3:08:00:55	57450535
total						1449	12:19:58:46	280681243

(a)

Table C.1.: Main parameters during the March 2007 beamtime.

carbon_omega		FACE
1st level	Taps1	>=3
Tagger +	FWPlug2 & Taps1	>=1
	FWPlug1 & Taps1	>=2
	FWPlug2	>=2
	FWPlug1	>=3

(a)

Taps1	at least 1 particle in the TAPS, E > LED_high
Taps2	at least 2 particles in the TAPS, E > LED_low
FWPlug1	at least 1 particle in the Forward Plug
FWPlug2	at least 2 particles in the Forward Plug

(b)

Table C.2.: (a) Four-particle trigger, (b) Meaning of the used abbreviations, (c) Three-particle trigger

carbon_omega_prime		FACE
1st level	Taps1	>=2
Tagger +	FWPlug2 & Taps1	>=0
	FWPlug1 & Taps1	>=1
	FWPlug2	>=1
	FWPlug1	>=2

(c)

D. Calibration

D.1. π^0 -calibration

The π^0 calibration is performed off-line using the collected data of the beamtime. During the calibration it is always assumed, that

- the measured and the real energy of the γ s are linearly correlated to each other ($E_{\text{real}} = C * E_{\text{measured}}$),
- the energy of one of the measured γ s is known precisely (Two photons are registered. While the correction factor for one of them is calculated, the energy of the other one is treated as if its energy were precisely known.).

Using the assumptions above the invariant mass of the π^0 can be expressed like (See Equation 2.8):

$$\begin{aligned}(M_{\pi^0}^{\text{PDG}})^2 &= 2E_{\gamma_1}E_{\gamma_2}(1 - \cos(\alpha)) \\ &= 2CE_1^{\text{meas}}E_2^{\text{real}}(1 - \cos(\alpha)) \\ &= CM_{\text{meas}}^2\end{aligned}$$

where α is the angle between the two photons and E_{γ_1} and E_{γ_2} are the energies of clusters and these energies are associated to the crystals where the largest fraction of the energies were deposited.

From the expression above the calibration constant can be derived like:

$$C = \left(\frac{M_{\pi^0}^{\text{PDG}}}{M_{\pi^0}^{\text{measured}}} \right)^2$$

D.2. η -calibration

It is assumed that the real deposited energy of the γ s depends on the measured energy not only linearly but a quadratic term is also involved:

$$E_{\text{real}} = C_1 * E_{\text{measured}} + C_2 * E_{\text{measured}}^2$$

D.2.1. η calibration in the Crystal Barrel/Forward Plug detectors

Both photons are measured in the CB or in the FWPlug and both have been calibrated assuming a linear correlation between the measured and the real energy (see Section D.1). Using the known mass of the π^0 and η mesons the following equations can be written:

$$\begin{aligned}
 M_{\pi^0}^2 &= 2 * (C_1 * E_{\gamma_{\pi^0_1}} + C_2 * E_{\gamma_{\pi^0_1}}^2) * (C_1 * E_{\gamma_{\pi^0_2}} + C_2 * E_{\gamma_{\pi^0_2}}^2) * (1 - \cos\alpha_{\pi^0}) \\
 M_{\eta}^2 &= 2 * (C_1 * E_{\gamma_{\eta_1}} + C_2 * E_{\gamma_{\eta_1}}^2) * (C_1 * E_{\gamma_{\eta_2}} + C_2 * E_{\gamma_{\eta_2}}^2) * (1 - \cos\alpha_{\eta})
 \end{aligned}$$

where $E_{\gamma_{\pi^0_{1,2}}}$ are the energies of the photons coming from the π^0 decay, $E_{\gamma_{\eta_{1,2}}}$ are the ones from the η decay, and $\cos\alpha_{\pi^0,\eta}$ are the angles between the two photons. However, this set of equation contains too many unknown variables!

An approximation can be used, namely that the energy of the two γ s are roughly equal ($E_{\gamma_{\pi^0_1}} \sim E_{\gamma_{\pi^0_2}} = E_{\pi^0}^{\text{meas}} (= \sqrt{E_{\gamma_{\pi^0_1}} E_{\gamma_{\pi^0_2}}})$) and the same for η : $E_{\gamma_{\eta_1}} \sim E_{\gamma_{\eta_2}} = E_{\eta}^{\text{meas}} (= \sqrt{E_{\gamma_{\eta_1}} E_{\gamma_{\eta_2}}})$. Using this approximation the set of equations will be simplified as:

$$\begin{aligned}
 M_{\pi^0}^2 &= 2(C_1 E_{\pi^0}^{\text{meas}} + C_2 (E_{\pi^0}^{\text{meas}})^2)^2 (1 - \cos\alpha_{\pi^0}) \\
 &= 2(E_{\pi^0}^{\text{meas}})^2 (1 - \cos\alpha_{\pi^0}) * (C_1 + C_2 E_{\pi^0}^{\text{meas}})^2 \\
 M_{\pi^0} &= M_{\pi^0}^{\text{meas}} * (C_1 + C_2 E_{\pi^0}^{\text{meas}}) \\
 M_{\eta} &= M_{\eta}^{\text{meas}} * (C_1 + C_2 E_{\eta}^{\text{meas}})
 \end{aligned}$$

The calibration constants can be expressed as:

$$\begin{aligned}
 C_2 &= \frac{R_{\eta} - R_{\pi^0}}{E_{\text{meas}_{\eta}} - E_{\text{meas}_{\pi^0}}} \\
 C_1 &= R_{\pi^0} - C_2 * E_{\text{meas}_{\pi^0}} \\
 R_{\pi^0} &= \frac{m_{\pi^0}^{PDG}}{m_{\pi^0}^{\text{meas}}} \\
 R_{\eta} &= \frac{m_{\eta}^{PDG}}{m_{\eta}^{\text{meas}}}
 \end{aligned}$$

D.2.2. η calibration in MiniTAPS

After the calibration of the CB and FWPlug the energy of the photons in the CB or in the FWPlug is precisely known. The next step is to calibrate the MiniTAPS. Events are selected where one photon goes to the (well calibrated) CB or FWPlug, the other goes to the MiniTAPS.

$$\begin{aligned}
 M_{\pi^0}^2 &= 2 * (C_1 * E_{\gamma_{\pi^0_1}} + C_2 * E_{\gamma_{\pi^0_1}}^2) * E_{\gamma_{\pi^0_2}} * (1 - \cos\alpha_{\pi^0}) \\
 M_{\eta}^2 &= 2 * (C_1 * E_{\gamma_{\eta_1}} + C_2 * E_{\gamma_{\eta_1}}^2) * E_{\gamma_{\eta_2}} * (1 - \cos\alpha_{\eta})
 \end{aligned}$$

Solving these equations we can express the calibration constants:

$$\begin{aligned}
 C_2 &= \frac{R_\eta^2 - R_{\pi^0}^2}{E_{\eta_1} - E_{\pi_1^0}} \\
 C_1 &= \frac{R_{\pi^0}^2 E_{\eta_1} - R_{\eta^0}^2 E_{\pi_1^0}}{E_{\eta_1} - E_{\pi_1^0}} \\
 R_{\pi^0} &= \frac{m_{\pi^0}^{PDG}}{m_{\pi^0}^{\text{meas}}} \\
 R_\eta &= \frac{m_\eta^{PDG}}{m_\eta^{\text{meas}}}
 \end{aligned}$$

D.3. Fine-tuning of the π^0 calibration

The calibration of the energy is an iterative process. One reason is that the energy of the “second” photon is always assumed to be precisely known. But there is at least one other reason.

The calibration constants are determined by using the energy which was deposited in the whole cluster. However, the calculated calibration constants are associated always with the central crystal of the cluster, only. This means that the energy which is used for the calculation is larger than the energy which was deposited in the actual crystal and consequently the calculated calibration constants will be lower than the real calibration constant should be.

To avoid the effect of the “surrounding” crystals (every crystal in the cluster, but the center one) on the calibration procedure, they have to be removed.

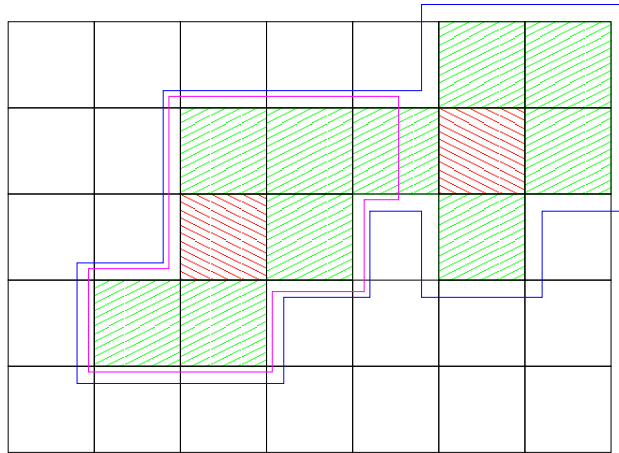


Figure D.1.: Visualization of a cluster:

White boxes denote the crystals where the energy deposit did not exceed the threshold. The striped boxes symbolize all the crystals which are firing. The red striped boxes are the *central crystals* of the PEDs, where most of the energy is deposited, the area with magenta border is one PED. The area with blue border is one cluster (with two PEDs).

During the π^0 calibration a linear correlation is assumed between the deposited energy by one photon and the real energy of this photon.

D. Calibration

$$E_{\text{real}} = C * E_{\text{measured}},$$

where the

$$E_{\text{measured}} = \sum_i E_{i_{\text{measured}}} = E_{\text{central}} + E_{\text{surrounding}}.$$

E_{central} is the deposited energy in the central crystal of the given PED (red box on the Fig.D.1) and $E_{\text{surrounding}}$ is the energy deposited in the surrounding crystals of the same PED (green boxes on the Figure D.1) Since only the central crystal is calibrated (the calibration constant is associated to the central crystal only and not to the whole cluster!) the result should not change if only the central crystal is recalibrated while the others (surrounding crystals) are left untouched:

$$E_{\text{real}} = C * E_{\text{measured}} = C_{\text{central}} * E_{\text{central}} + E_{\text{surrounding}}$$

After rearranging the equation we can express the new calibration constant (C_{central}) by the old constant (C):

$$C_{\text{central}} = C \left(1 + \frac{E_{\text{surrounding}}}{E_{\text{central}}} \right) - 1$$

E. The kinematics of two-body reactions

In quasi-free meson production it is assumed that the beam-particle interacts only with one nucleon, while the rest of the nucleus stays intact. This remaining part of the nucleus is called spectator.

Kinematically the problem can be described with the following equation:

$$\mathbf{P}_{\text{beam}} + \mathbf{P}_{\text{nucleus}} = \mathbf{P}_{\text{meson}} + \mathbf{P}_{\text{nucleon}} + \mathbf{P}_{\text{spectator}},$$

where all the components are Lorentz-vectors. As the beam always moves to “Z” direction and the nucleus in the lab-system is at rest, the equation can be written in the following way:

$$\begin{pmatrix} 0 \\ 0 \\ p_{\text{beam}} \\ E_{\text{beam}} \end{pmatrix} + \begin{pmatrix} 0 \\ 0 \\ 0 \\ M_{\text{nucleus}} \end{pmatrix} = \begin{pmatrix} p_{\text{meson}_x} \\ p_{\text{meson}_y} \\ p_{\text{meson}_z} \\ E_{\text{meson}} \end{pmatrix} + \begin{pmatrix} p_{\text{nucleon}_x} \\ p_{\text{nucleon}_y} \\ p_{\text{nucleon}_z} \\ E_{\text{nucleon}} \end{pmatrix} + \begin{pmatrix} p_{\text{spectator}_x} \\ p_{\text{spectator}_y} \\ p_{\text{spectator}_z} \\ E_{\text{spectator}} \end{pmatrix}$$

The beam energy, the mass of the nucleus, the spectator, the nucleon and the meson are known. In a general case the energy of the knocked-out nucleon is not known, because it can be too large and the particle becomes minimum ionizing or generates nuclear reactions, and the deposited energy will be independent of the kinetic energy of the nucleon. However, it is registered where the nucleon hits the setup, so its direction is registered properly. Altogether there are four equations with seven unknowns (p_{nucleon} , $p_{\text{spectator}}$, $\theta_{\text{spectator}}$, $\phi_{\text{spectator}}$, p_{meson} , θ_{meson} , ϕ_{meson}), so without any additional information the system of equation cannot be solved.

The knowledge of the properties of the *spectator* particle is important, because it holds information about the Fermi momentum of the knocked-out nucleon in the nucleus (see the description of the *impulse approximation* in the Chapter 3.5.3 and in [PZ02]).

The target nucleus is at rest, but all the nucleons carry Fermi momenta: $0 = \sum_{i=0 \dots N} \bar{p}_i$. This

summation can be divided into two arbitrary parts, for example $0 = \sum_{i=1 \dots N} \bar{p}_i + \bar{p}_0$ where the

0th nucleon is the *participating* nucleon, the rest is the *spectator* nucleus. After rearranging the equation: $\bar{p}_{\text{spectator}} = -\bar{p}_{\text{nucleon}}$.

E.1. Solution I.

If a Monte Carlo simulation is performed to understand the reaction kinematics better, the momentum of the participating nucleon is known in every event and consequently the momentum of the spectator nucleus is also known. In this case the unknown quantities are the momentum vector of the produced meson and the absolute value of the momentum of the registered nucleon

(in practice a random momentum vector is generated for the participating nucleon, and a direction for the knocked-out nucleon, so its momentum has to be calculated). This implies four unknown variables and four equations and the set of equations can be solved.

E.1.1. Calculation of $\mathbf{p}_{\text{nucleon}}$

The momentum of the nucleon has to be calculated. The components of the unknown momentum of the meson are:

$$\begin{aligned} p_{\text{meson}_x} &= -(p_{\text{nucleon}_x} + p_{\text{spectator}_x}) \\ p_{\text{meson}_y} &= -(p_{\text{nucleon}_y} + p_{\text{spectator}_y}) \\ p_{\text{meson}_z} &= p_{\text{beam}} - (p_{\text{nucleon}_x} + p_{\text{spectator}_x}) \\ E_{\text{meson}} &= (E_{\text{beam}} + M_{\text{nucleus}} - E_{\text{spectator}}) - E_{\text{nucleon}} \end{aligned}$$

Because $p_x^2 + p_y^2 + p_z^2 = p^2$, p_{meson} can be expressed using its components:

$$\begin{aligned} p_{\text{meson}}^2 &= (-(p_{\text{nucleon}_x} + p_{\text{spectator}_x}))^2 \\ &\quad + (-(p_{\text{nucleon}_y} + p_{\text{spectator}_y}))^2 \\ &\quad + (p_{\text{beam}} - (p_{\text{nucleon}_x} + p_{\text{spectator}_x}))^2 \\ &= p_{\text{beam}}^2 + p_{\text{nucleon}}^2 + p_{\text{spectator}}^2 - \\ &\quad 2\vec{p}_{\text{beam}} \cdot \vec{p}_{\text{nucleon}} - 2\vec{p}_{\text{beam}} \cdot \vec{p}_{\text{spectator}} + 2\vec{p}_{\text{nucleon}} \cdot \vec{p}_{\text{spectator}} \end{aligned}$$

where $\vec{p}_A \cdot \vec{p}_B$ means the dot-product of the two vectors.

Putting these results into the expression of the energy conservation leads to:

$$\begin{aligned} E_{\text{meson}} + E_{\text{nucleon}} + E_{\text{spectator}} &= (E_{\text{beam}} + M_{\text{nucleus}}) \\ \sqrt{m_{\text{meson}}^2 + p_{\text{meson}}^2} + \sqrt{m_{\text{nucleon}}^2 + p_{\text{nucleon}}^2} &= (E_{\text{beam}} + M_{\text{nucleus}} - E_{\text{spectator}}), \end{aligned}$$

where

$$p_{\text{meson}}^2 = p_{\text{beam}}^2 + p_{\text{nucleon}}^2 + p_{\text{spectator}}^2 + 2(\vec{p}_{\text{nucleon}} \cdot \vec{p}_{\text{spectator}} - \vec{p}_{\text{beam}} \cdot \vec{p}_{\text{nucleon}} - \vec{p}_{\text{beam}} \cdot \vec{p}_{\text{spectator}}).$$

The only unknown in the expression is the p_{nucleon}^2 .

E.1.2. Calculation of the momentum vector of the meson

If the momentum of the knocked-out nucleon is known, the momentum components of the meson can be calculated (the direction of the proton is known!):

$$\begin{aligned} p_{\text{meson}_x} &= -(p_{\text{nucleon}_x} + p_{\text{spectator}_x}) \\ p_{\text{meson}_y} &= -(p_{\text{nucleon}_y} + p_{\text{spectator}_y}) \\ p_{\text{meson}_z} &= p_{\text{beam}} - (p_{\text{nucleon}_x} + p_{\text{spectator}_x}). \end{aligned}$$

And finally the full momentum of the meson is:

$$p_{\text{meson}}^2 = p_{\text{meson}_x}^2 + p_{\text{meson}_y}^2 + p_{\text{meson}_z}^2 \quad (\text{E.1})$$

E.2. Solution II.

When a measurement is performed, the momentum of the meson is reconstructed from its decay products, but the momentum of the spectator nucleus is not measured. The unknown quantities are the momentum vector of the spectator and the absolute value of the momentum of the proton. The equation can be solved in a similar way as in chapter E.1, so only the final results will be quoted: The momentum of the nucleon can be calculated by solving the following equation:

$$\begin{aligned}
 p_{\text{spectator}}^2 &= (-(p_{\text{nucleon}_x} + p_{\text{meson}_x}))^2 \\
 &\quad (-(p_{\text{nucleon}_y} + p_{\text{meson}_y}))^2 \\
 &\quad (p_{\text{beam}} - (p_{\text{nucleon}_x} + p_{\text{meson}_x}))^2 \\
 &= p_{\text{beam}}^2 + p_{\text{nucleon}}^2 + p_{\text{meson}}^2 - \\
 &\quad 2\vec{p}_{\text{beam}} \cdot \vec{p}_{\text{nucleon}} - 2\vec{p}_{\text{beam}} \cdot \vec{p}_{\text{meson}} + 2\vec{p}_{\text{nucleon}} \cdot \vec{p}_{\text{meson}}
 \end{aligned}$$

where $\vec{p}_A \cdot \vec{p}_B$ means the dot-product of the two vectors.

$$\begin{aligned}
 E_{\text{meson}} + E_{\text{nucleon}} + E_{\text{spectator}} &= (E_{\text{beam}} + M_{\text{nucleus}}) \\
 \sqrt{m_{\text{spectator}}^2 + p_{\text{meson}}^2} + \sqrt{m_{\text{nucleon}}^2 + p_{\text{nucleon}}^2} &= (E_{\text{beam}} + M_{\text{nucleus}} - E_{\text{meson}}),
 \end{aligned}$$

The momentum of the spectator (and also the Fermi momentum of the participating nucleon) can be calculated:

$$\begin{aligned}
 p_{\text{spectator}_x} &= -(p_{\text{nucleon}_x} + p_{\text{meson}_x}) \\
 p_{\text{spectator}_y} &= -(p_{\text{nucleon}_y} + p_{\text{meson}_y}) \\
 p_{\text{spectator}_z} &= p_{\text{beam}} - (p_{\text{nucleon}_x} + p_{\text{meson}_x}),
 \end{aligned}$$

and $p_{\text{spectator}}^2 = p_{\text{spectator}_x}^2 + p_{\text{spectator}_y}^2 + p_{\text{spectator}_z}^2$.

F. An explanation for the structures on the 3-gamma invariant mass spectrum of the $\pi^0\eta$ channel

One of the main backgrounds of the $\omega \rightarrow \pi^0\gamma \rightarrow 3\gamma$ decay channel is the $\pi^0\eta \rightarrow 4\gamma$ channel. If one of the four final state photons is lost the same number of particles will be registered in the final state like in the decay of the ω meson.

Both the π^0 and the η decay into two photons $[\gamma_{1,\pi^0}, \gamma_{2,\pi^0}, \gamma_{1,\eta}, \gamma_{2,\eta}]$. If one photons is lost the following combinations can be formed:

$$\begin{aligned} &\gamma_{1,\pi^0}, \gamma_{2,\pi^0}, \gamma_{1,\eta}, \\ &\gamma_{1,\pi^0}, \gamma_{2,\pi^0}, \gamma_{2,\eta}, \\ &\gamma_{1,\pi^0}, \gamma_{1,\eta}, \gamma_{2,\eta}, \\ &\gamma_{2,\pi^0}, \gamma_{1,\eta}, \gamma_{2,\eta}. \end{aligned}$$

If one photon is lost from the π^0 -decay photons then a real π^0 cannot be reconstructed. However, accidentally it can happen that the invariant mass of a photon from the decay of the π^0 and another from the decay of the η will fall into the mass range of the π^0 and result in a “fake” π^0 :

This wrong combination can occur if one photon from the η decay is lost. For example:

$$\begin{aligned} &\gamma_{1,\pi^0}, [\gamma_{2,\pi^0}, \gamma_{1,\eta}], \\ &\gamma_{1,\pi^0}, [\gamma_{2,\pi^0}, \gamma_{2,\eta}], \\ &\gamma_{2,\pi^0}, [\gamma_{1,\pi^0}, \gamma_{1,\eta}], \\ &\gamma_{2,\pi^0}, [\gamma_{1,\pi^0}, \gamma_{2,\eta}], \end{aligned}$$

where there are in squared bracket the wrong combinations which can result in a “fake” π^0 .

Nevertheless, if a “fake” π^0 is found it should be possible to reconstruct another “real” meson from one combination of two photons out of the three registered ones:

real π^0	fake π^0	real η	fake π^0
$\{\gamma_{1,\pi^0}, [\gamma_{2,\pi^0}], \gamma_{1,\eta}\}$,	$\{\gamma_{1,\eta}, [\gamma_{2,\eta}], \gamma_{1,\pi^0}\}$,	
$\{\gamma_{1,\pi^0}, [\gamma_{2,\pi^0}], \gamma_{2,\eta}\}$,	$\{\gamma_{1,\eta}, [\gamma_{2,\eta}], \gamma_{2,\pi^0}\}$,	
$\{\gamma_{2,\pi^0}, [\gamma_{1,\pi^0}], \gamma_{1,\eta}\}$,	$\{\gamma_{2,\eta}, [\gamma_{1,\eta}], \gamma_{1,\pi^0}\}$,	
$\{\gamma_{2,\pi^0}, [\gamma_{1,\pi^0}], \gamma_{2,\eta}\}$,	$\{\gamma_{2,\eta}, [\gamma_{1,\eta}], \gamma_{2,\pi^0}\}$,	

In squared brackets are the combinations for which the invariant mass of the photons corresponds to the nominal mass of the mesons but the photons originate from the decay of two different

F. An explanation for the structures on the 3-gamma invariant mass spectrum of the $\pi^0\eta$ channel

mesons (“fake” meson), in curly brackets are the photons which come from the decay of the same meson (“real” mesons).

The invariant mass of 3 photons is

$$m^2 = \left(\sum_{i=\gamma_1, \gamma_2, \gamma_3} E_i \right)^2 - \left(\sum_{i=\gamma_1, \gamma_2, \gamma_3} p_i \right)^2 \quad (\text{F.1})$$

This expression can be expanded:

$$\begin{aligned} m^2 &= \left(\sum_{i=\gamma_1, \gamma_2, \gamma_3} E_i \right)^2 - \left(\sum_{i=\gamma_1, \gamma_2, \gamma_3} p_i \right)^2 \\ &= E_{\gamma_1}^2 + E_{\gamma_2}^2 + E_{\gamma_3}^2 + \\ &\quad 2E_{\gamma_1}E_{\gamma_2} + 2E_{\gamma_1}E_{\gamma_3} + 2E_{\gamma_2}E_{\gamma_3} - \\ &\quad (P_{\gamma_1}^2 + P_{\gamma_2}^2 + P_{\gamma_3}^2 + \\ &\quad 2P_{\gamma_1}P_{\gamma_2} \cos(\Theta_{1,2}) + \\ &\quad 2P_{\gamma_1}P_{\gamma_3} \cos(\Theta_{1,3}) + \\ &\quad 2P_{\gamma_2}P_{\gamma_3} \cos(\Theta_{2,3})) \\ &= (E_{\gamma_1}^2 - P_{\gamma_1}^2) + (E_{\gamma_2}^2 - P_{\gamma_2}^2) + (E_{\gamma_3}^2 - P_{\gamma_3}^2) + \\ &\quad 2E_{\gamma_1}E_{\gamma_2} - 2P_{\gamma_1}P_{\gamma_2} \cos(\Theta_{1,2}) + \\ &\quad 2E_{\gamma_1}E_{\gamma_3} - 2P_{\gamma_1}P_{\gamma_3} \cos(\Theta_{1,3}) + \\ &\quad 2E_{\gamma_2}E_{\gamma_3} - 2P_{\gamma_2}P_{\gamma_3} \cos(\Theta_{2,3}). \end{aligned}$$

The photons are massless ($m_{\gamma_{1,2,3}} = 0$), and their momenta are equal to their energy ($E_{\gamma_{1,2,3}}^2 = P_{\gamma_{1,2,3}}^2 + m_{\gamma_{1,2,3}}^2 = P_{\gamma_{1,2,3}}^2$). The formula for the invariant mass of three photons can be written

$$\begin{aligned} m^2 &= (E_{\gamma_1}^2 - P_{\gamma_1}^2) + (E_{\gamma_2}^2 - P_{\gamma_2}^2) + (E_{\gamma_3}^2 - P_{\gamma_3}^2) + \\ &\quad 2E_{\gamma_1}E_{\gamma_2} - 2P_{\gamma_1}P_{\gamma_2} \cos(\Theta_{1,2}) + \\ &\quad 2E_{\gamma_1}E_{\gamma_3} - 2P_{\gamma_1}P_{\gamma_3} \cos(\Theta_{1,3}) + \\ &\quad 2E_{\gamma_2}E_{\gamma_3} - 2P_{\gamma_2}P_{\gamma_3} \cos(\Theta_{2,3}) \\ &= 2E_{\gamma_1}E_{\gamma_2}(1 - \cos(\Theta_{1,2})) + 2E_{\gamma_1}E_{\gamma_3}(1 - \cos(\Theta_{1,3})) + 2E_{\gamma_2}E_{\gamma_3}(1 - \cos(\Theta_{2,3})) \\ &= m_{\gamma_1\gamma_2}^2 + m_{\gamma_1\gamma_3}^2 + m_{\gamma_2\gamma_3}^2 \\ &= \sum_{i,j=1\dots 3(i \neq j)} m_{\gamma_i\gamma_j}^2 \end{aligned}$$

This means that the invariant mass of three photons can be calculated from the invariant mass of all possible two photon invariant masses.

Wherever a “fake” and a “real” meson are registered in the two-photon combinations, it has to be assumed that the particles does not come from the decay of an ω meson, but were produced by one of the background channels with four photons in the final state.

Fixing the invariant masses of the “real” and the “fake” mesons and varying the invariant mass of the third two-photon combination (shown on the y-axis) the correlation between the invariant

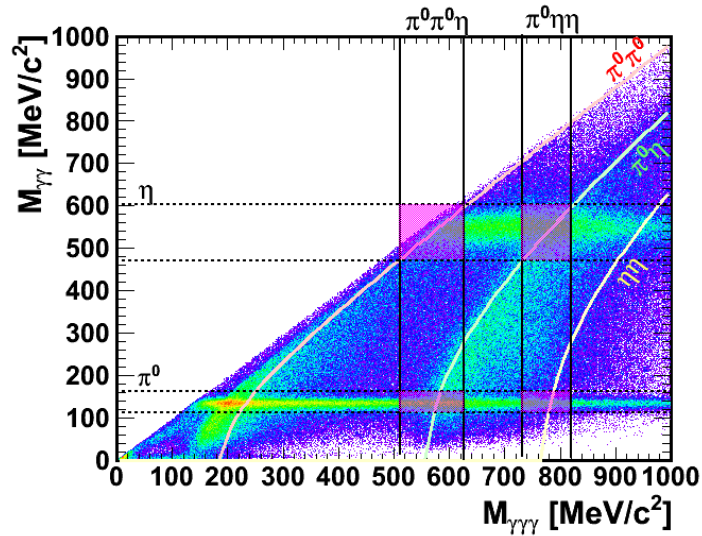


Figure F.1.: Simulations of $\pi^0\eta$ events, with only three photons detected in the final state. The invariant mass of three photons vs. all the three two-photon invariant masses is plotted. The light pink line illustrates the location of the events where one photon from the decay of the η is lost, but the invariant mass of two combinations, out of the remaining three photons, corresponds to the nominal mass of a π^0 meson. The light green line shows the same but the photon from the decay of the π^0 was lost.

masses of the “third” two-photon combination can be plotted as a function of the invariant mass of the three-photon combination (see Figure F.1).

The rainbow colored plot displays the three-photon invariant mass versus the invariant masses of all two-photon combinations in $\pi^0\eta \rightarrow 4\gamma$ simulation. The solid curves represent the correlation between the two-photon and the three-photon invariant masses, where the invariant masses of two two-photon combinations of the three photons are fixed and the invariant mass of the third two-photon combination is varied.

This calculation shows that the bump which appears in the $\pi^0\gamma$ invariant mass spectrum at around 550-600 MeV/c^2 is in correlation with wrongly paired photons.

F. An explanation for the structures on the 3-gamma invariant mass spectrum of the $\pi^0\eta$ channel

G. Simulated background channels

$$\pi^+ + \pi^0 + n$$

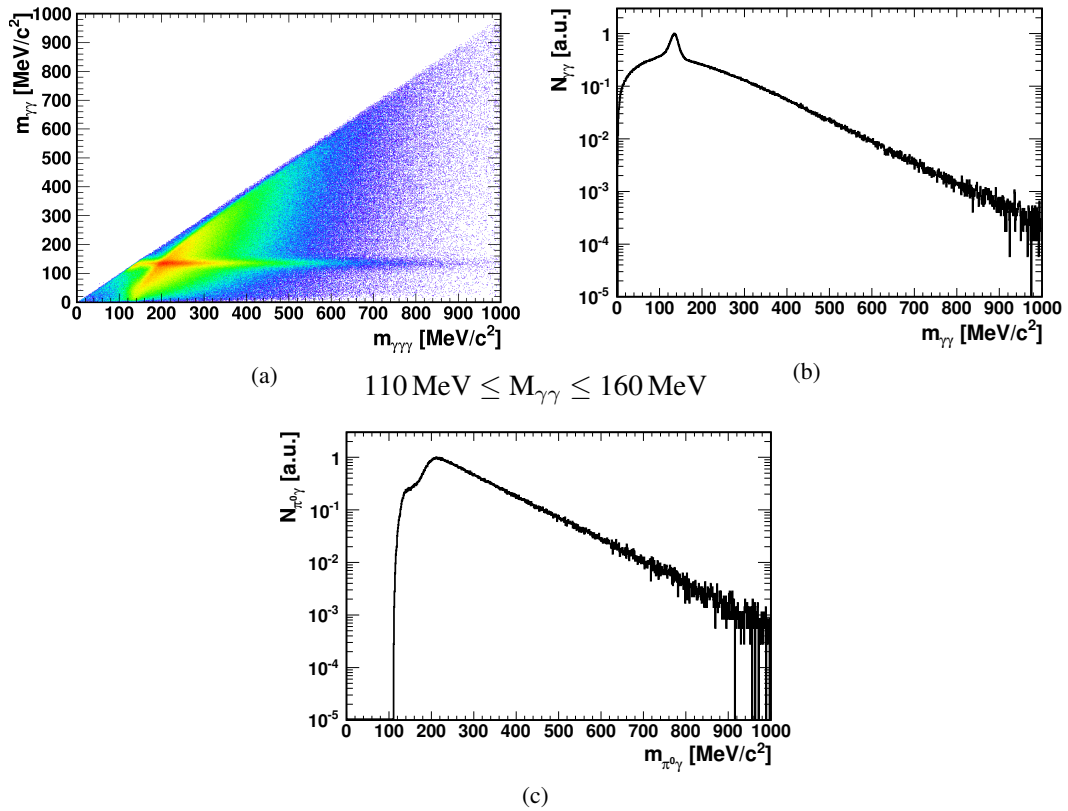


Figure G.1.: Two-photon invariant mass versus three-photon invariant mass plot for the simulated $\pi^+ + \pi^0 + n \rightarrow \pi^+ + n + 2\gamma$ final state (Fig. (a)) where the π^+ is misidentified as a proton and the n is misidentified as a photon.. Projection on the two-gamma (Fig. (b)) axis shows a peak at the mass of the mass of the π^0 . The projection on the three-gamma (Fig. (c)) axis shows a smooth distribution.

$$\pi^0 + \pi^0$$

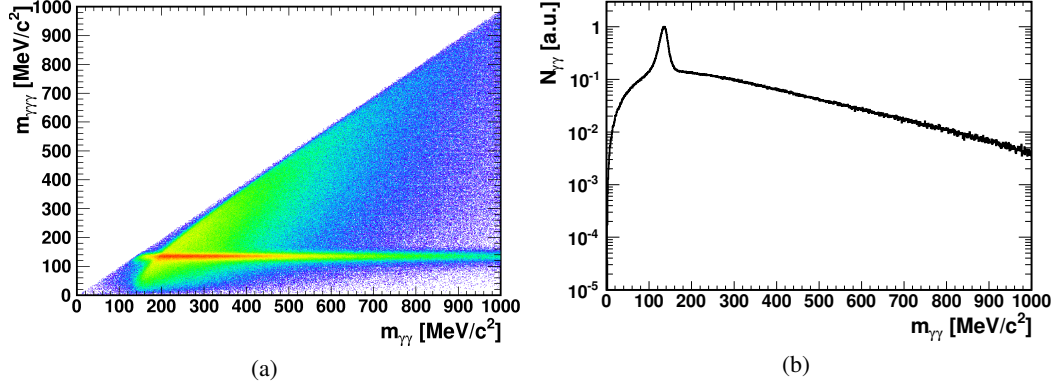


Figure G.2.: Two-photon invariant mass versus three-photon photon invariant mass plot for the simulated $\pi^0 + \pi^0 \rightarrow 4\gamma$ final state (Fig. (a)). Projection on the two-gamma (Fig. (b)) axis shows a peak at the mass of the mass of the π^0 . The projection on the three-gamma (Fig. (c)) axis shows a smooth distribution.

$$\pi^0 + \eta$$

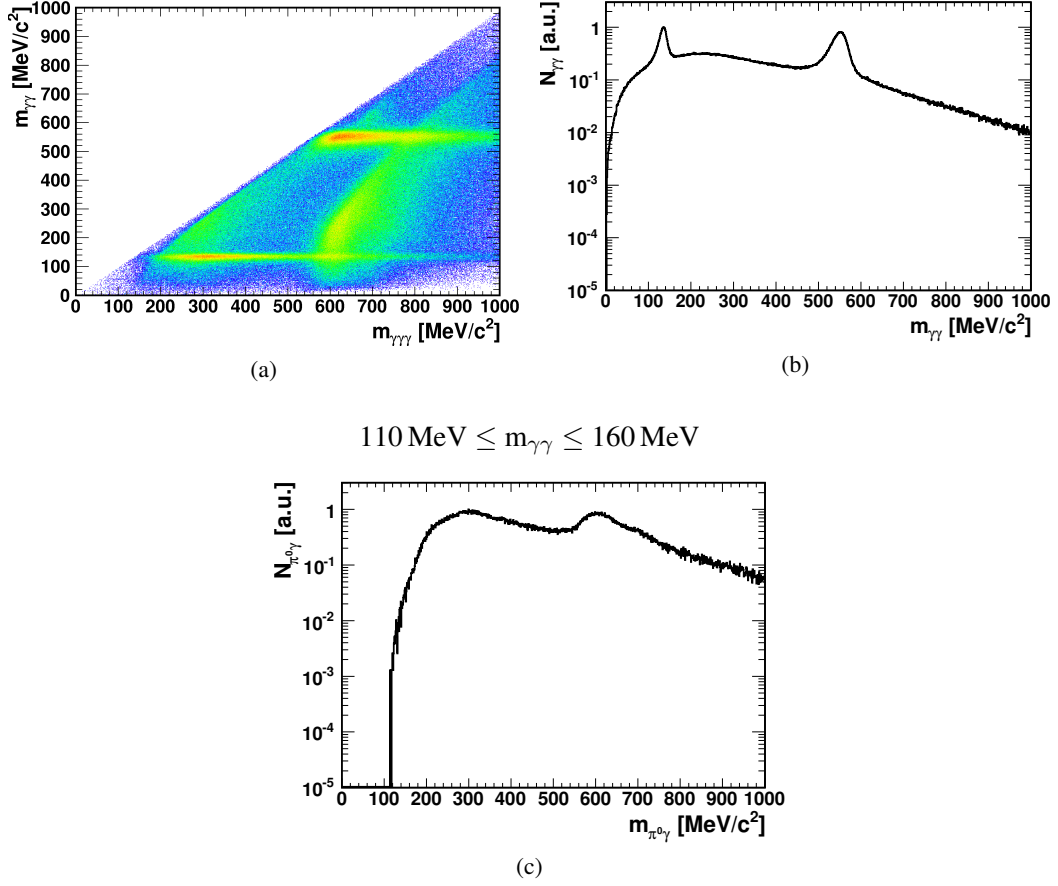


Figure G.3.: Two-photon invariant mass versus three-photon photon invariant mass for the simulated $\pi^0 + \eta \rightarrow 4\gamma$ final state (Fig. (a)). Projection on the two-gamma (Fig. (b)) axis shows a peak at the mass of the mass of the π^0 . The projection on the three-gamma (Fig. (c)) axis shows a pronounced structure at roughly $600 \text{ MeV}/c^2$ which can be removed by a side-band subtraction technique (see Section 3.5.5).

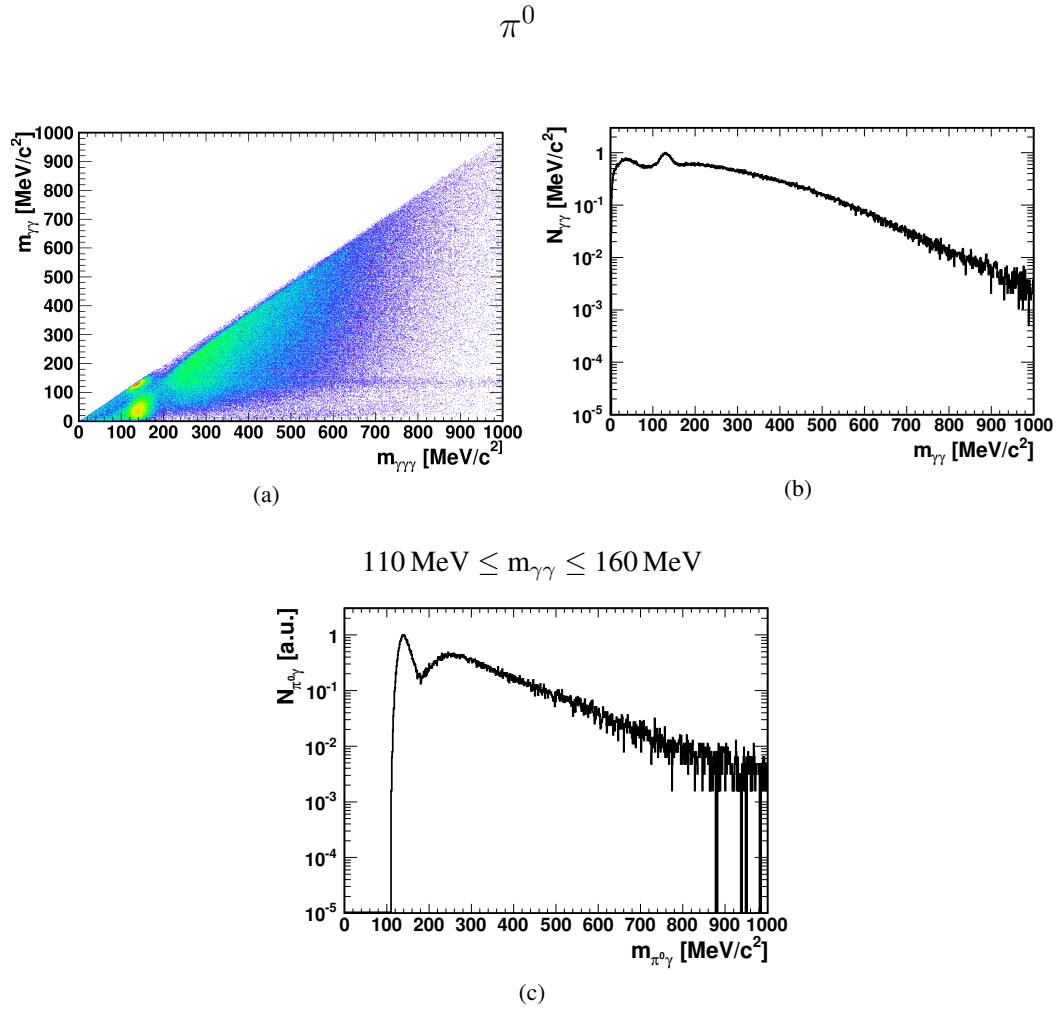
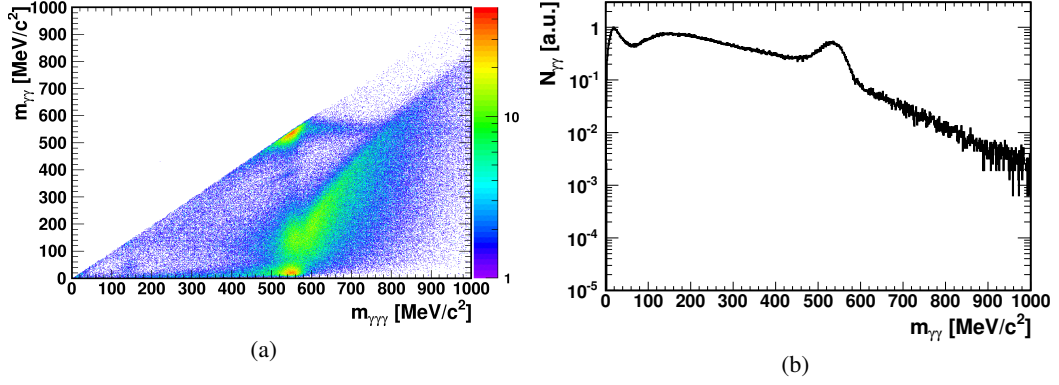


Figure G.4.: Two-photon invariant mass versus three-photon photon invariant mass plot for the simulated $\pi^0 \rightarrow 2\gamma$ final state (Fig. (a)) where one additional neutral hit was generated. Projection on the two-photon (Fig. (b)) axis shows a peak at the mass of the mass of the π^0 . The projection on the three-photon (Fig. (c)) axis shows a smooth distribution.

η



$$110 \text{ MeV} \leq m_{\gamma\gamma} \leq 160 \text{ MeV}$$

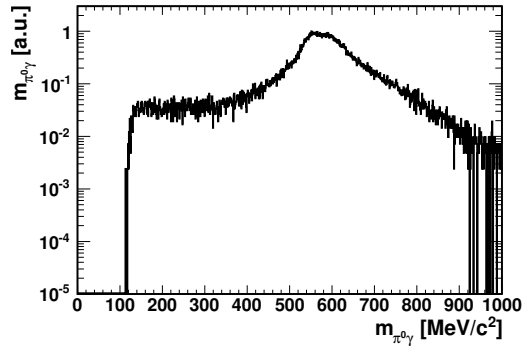


Figure G.5.: Two-photon invariant mass versus three-photon photon invariant mass plot for the simulated $\eta \rightarrow 2\gamma$ final state (Fig. (a)) where one additional neutral hit was generated. Projection on the two-gamma (Fig. (b)) axis shows a peak at the mass of the mass of the π^0 . The projection on the three-gamma (Fig. (c)) axis shows a pronounced structure at roughly $600 \text{ MeV}/c^2$ which can be removed by a side-band subtraction technique and by kinematical cuts (see Section 3.5.5).

ω

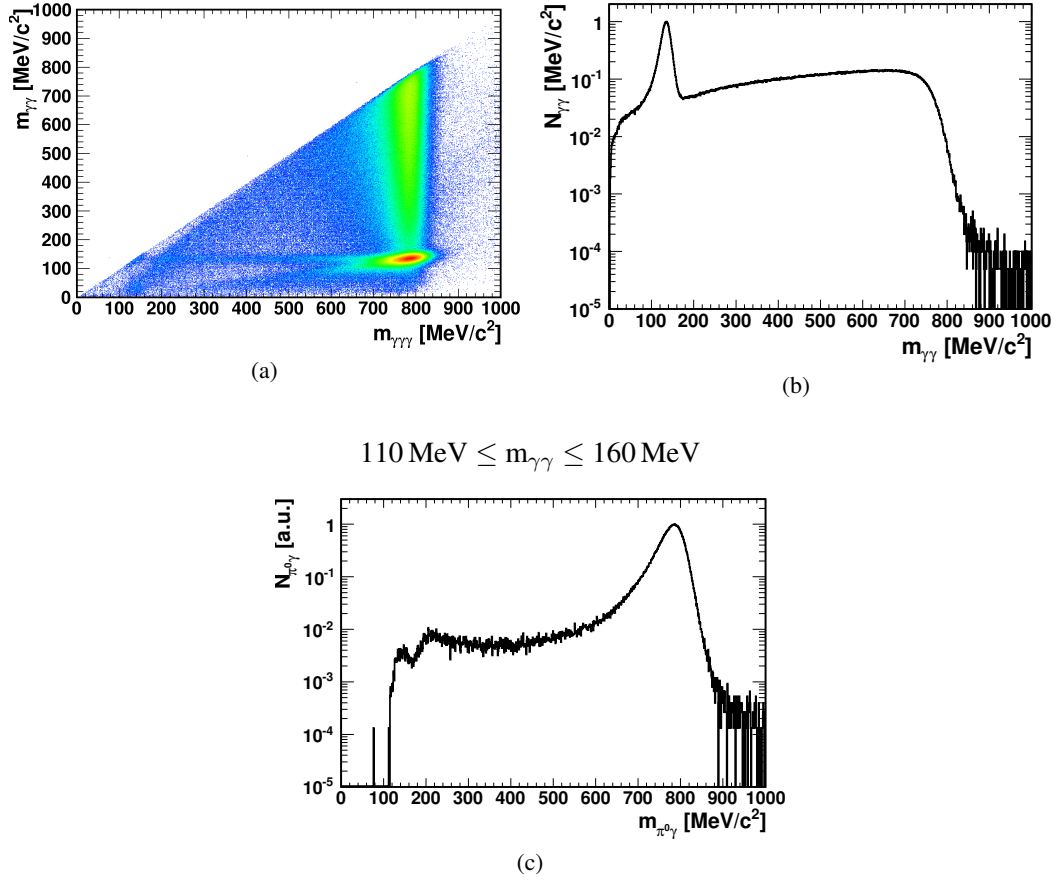


Figure G.6.: Two-photon invariant mass versus three-photon photon invariant mass plot for the simulated $\omega \rightarrow \pi^0\gamma \rightarrow 3\gamma$ final state (Fig. (a)). Projection on the two-gamma (Fig. (b)) axis shows a peak at the mass of the mass of the π^0 . The projection on the three-gamma (Fig. (c)) axis shows the ω -peak.

Data

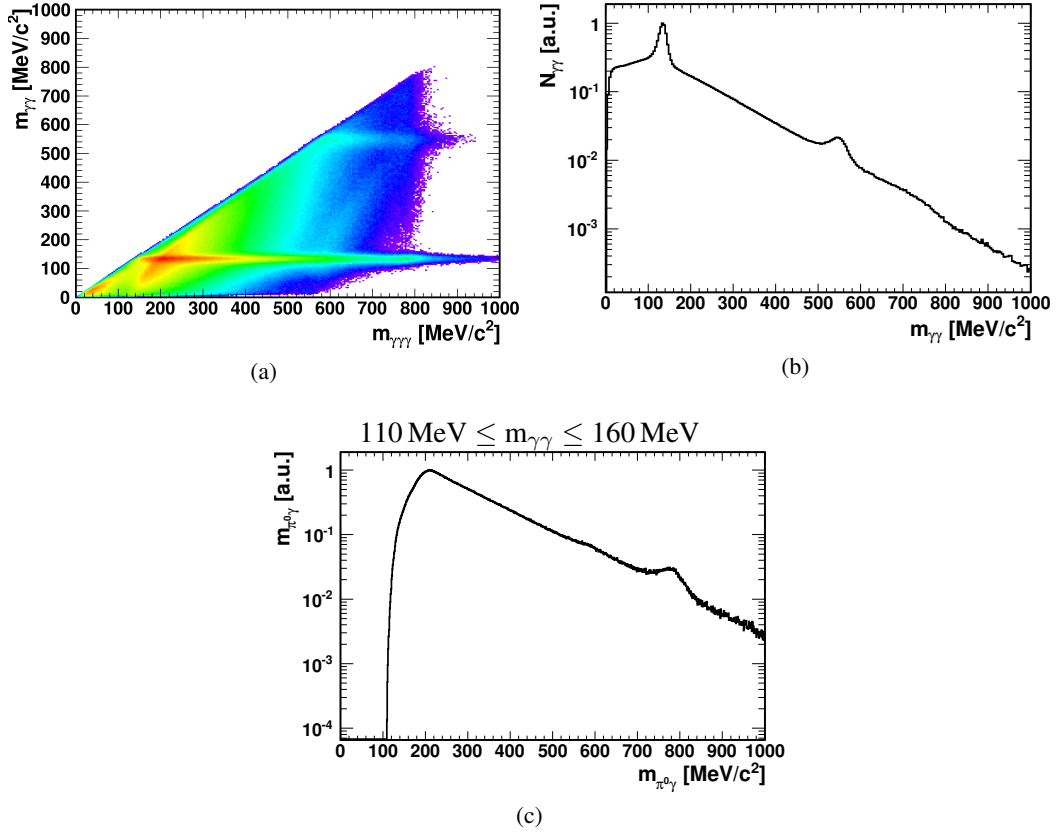


Figure G.7.: Two photon invariant mass versus 3 photon photon invariant mass (Figure (a)), and its projection to the two-gamma (Figure (c)), and to the three-gamma invariant mass axis (Fig. (b)) for data.

H. Kinematical Cuts and Background Rejection

	<input type="checkbox"/>								
$110 \text{ MeV}/c^2 < m_{\gamma\gamma} < 160 \text{ MeV}/c^2$	-	+	+	+	+	+	+	+	+
$E_{\text{beam}} < 1250 \text{ MeV}$	-	-	+	+	+	+	+	+	+
$E_{\gamma_3} < 200 \text{ MeV}$	-	-	-	+	+	+	+	+	+
$T_{\pi^0} < 150 \text{ MeV}$	-	-	-	-	+	+	+	+	+
$110 \text{ MeV}/c^2 < MM_{\omega} - m_{\text{proton}} < 110 \text{ MeV}/c^2$	-	-	-	-	-	+	+	+	+
$\Theta_{\text{proton}} < 10^\circ$	-	-	-	-	-	-	+	+	+
cut on the p -band	-	-	-	-	-	-	-	+	+
$p_{\pi^0\gamma} < 300 \text{ MeV}/c$	-	-	-	-	-	-	-	-	+

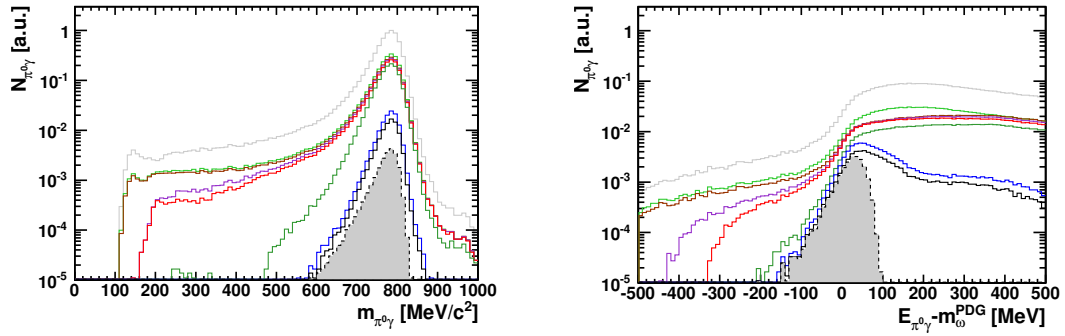


Figure H.1.: Simulation of the $\gamma + {}^{12}\text{C} \rightarrow \omega + p + {}^{11}\text{B}$ channel. The three-gamma invariant mass (left figure) and the “kinetic energy” (right figure) distributions are shown after every cut which is listed in Section 3.3.1. The gray shaded area shows the $m_{\pi^0\gamma}$ invariant mass distribution in the lowest studied momentum bin $p_{\pi^0\gamma} < 300 \text{ MeV}/c$.

H. Kinematical Cuts and Background Rejection

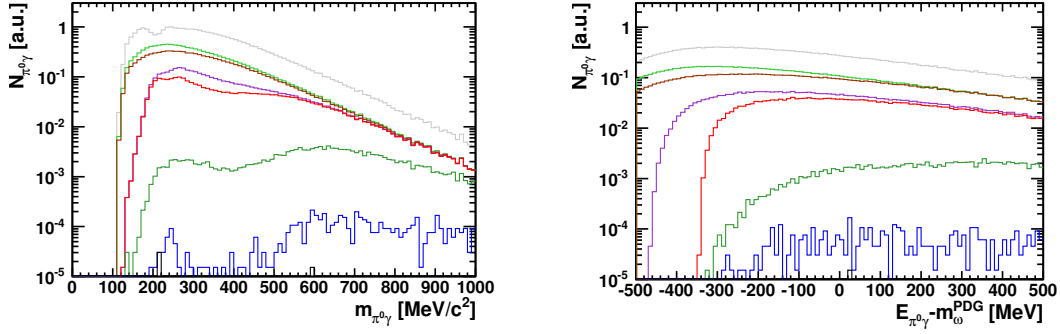


Figure H.2.: Simulation of the $\gamma + {}^{12}\text{C} \rightarrow \pi^0 + \pi^+ + n + {}^{11}\text{B}$ background channel where the π^+ is misidentified as a proton, and the neutron is misidentified as a photon (See the Section 3.5.4). Simulation shows the three-gamma invariant mass (left figure) and the “kinetic energy” (right figure) distributions after every cut which is listed in Section 3.3.1. After requiring that the proton should be identified by the cut on the *proton-band* (See Section 3.2.2) practically there is no intensity remains.

	□	■	□	■	□	■	□	■
$110 \text{ MeV}/c^2 < m_{\gamma\gamma} < 160 \text{ MeV}/c^2$	-	+	+	+	+	+	+	+
$E_{\text{beam}} < 1250 \text{ MeV}$	-	-	+	+	+	+	+	+
$E_{\gamma_3} < 200 \text{ MeV}$	-	-	-	+	+	+	+	+
$T_{\pi^0} < 150 \text{ MeV}$	-	-	-	-	+	+	+	+
$110 \text{ MeV}/c^2 < MM_{\omega} - m_{\text{proton}} < 110 \text{ MeV}/c^2$	-	-	-	-	-	+	+	+
$\Theta_{\text{proton}} < 10^\circ$	-	-	-	-	-	-	+	+
cut on the <i>p-band</i>	-	-	-	-	-	-	-	+
$p_{\pi^0\gamma} < 300 \text{ MeV}/c$	-	-	-	-	-	-	-	+

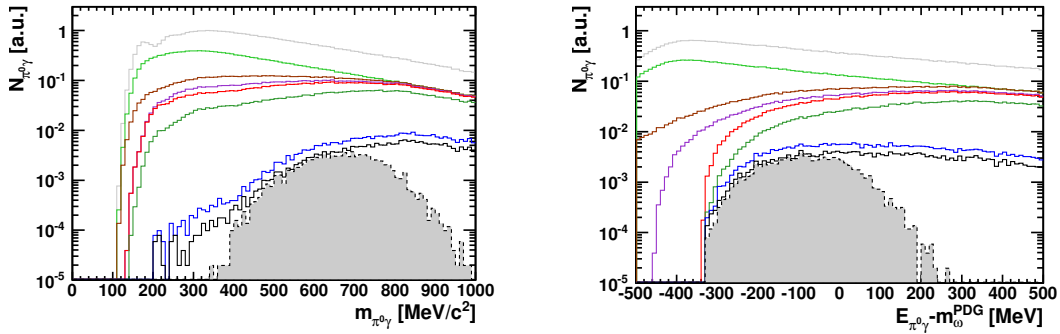


Figure H.3.: Simulation of the $\gamma + {}^{12}\text{C} \rightarrow \pi^0 + \pi^0 + p + {}^{11}\text{B}$ channel where one photon from the decay of the π^0 s is lost (See the Section 3.5.4). The three-gamma invariant mass (left figure) and the “kinetic energy” (right figure) distributions are shown after every cut which is listed in Section 3.3.1. The gray shaded area shows the $m_{\pi^0\gamma}$ invariant mass distribution in the lowest studied momentum bin $p_{\pi^0\gamma} < 300 \text{ MeV}/c$.

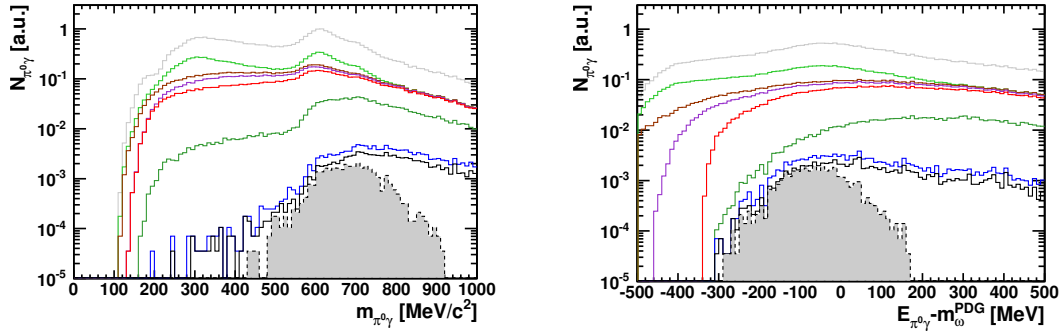


Figure H.4.: Simulation of the $\gamma + {}^{12}\text{C} \rightarrow \pi^0 + \eta + p + {}^{11}\text{B}$ channel where one photon from the decay of the π^0 or the η is lost (see the Section 3.5.4). The three-gamma invariant mass (left figure) and the “kinetic energy” (right figure) distributions are shown after every cut which is listed in Section 3.3.1. The gray shaded area shows the $m_{\pi^0\gamma}$ invariant mass distribution in the lowest studied momentum bin $p_{\pi^0\gamma} < 300 \text{ MeV}/c$.

	□	□	□	□	□	□	□	□	■
$110 \text{ MeV}/c^2 < m_{\gamma\gamma} < 160 \text{ MeV}/c^2$	-	+	+	+	+	+	+	+	+
$E_{\text{beam}} < 1250 \text{ MeV}$	-	-	+	+	+	+	+	+	+
$E_{\gamma_3} < 200 \text{ MeV}$	-	-	-	+	+	+	+	+	+
$T_{\pi^0} < 150 \text{ MeV}$	-	-	-	-	+	+	+	+	+
$110 \text{ MeV}/c^2 < MM_\omega - m_{\text{proton}} < 110 \text{ MeV}/c^2$	-	-	-	-	-	+	+	+	+
$\Theta_{\text{proton}} < 10^\circ$	-	-	-	-	-	-	+	+	+
cut on the p -band	-	-	-	-	-	-	-	+	+
$p_{\pi^0\gamma} < 300 \text{ MeV}/c$	-	-	-	-	-	-	-	-	+

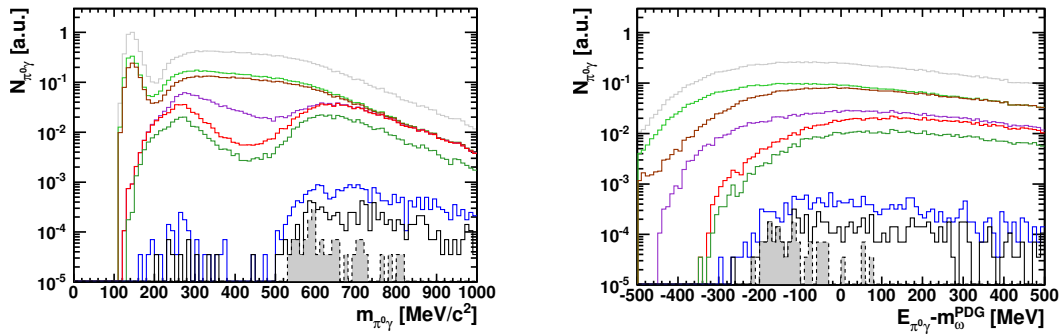


Figure H.5.: Simulation of the $\gamma + {}^{12}\text{C} \rightarrow \pi^0 + p + {}^{11}\text{B}$ channel where one additional neutral hit was produced (See the Section 3.5.4). The three-gamma invariant mass (left figure) and the “kinetic energy” (right figure) distributions are shown after every cut which is listed in Section 3.3.1. An artificial structure is produced by the cut on the energy of the bachelor photon. The gray shaded area shows the $m_{\pi^0\gamma}$ invariant mass distribution in the lowest studied momentum bin $p_{\pi^0\gamma} < 300 \text{ MeV}/c$.

H. Kinematical Cuts and Background Rejection

	□	□	□	□	□	□	□	□
$110 \text{ MeV}/c^2 < m_{\gamma\gamma} < 160 \text{ MeV}/c^2$	-	+	+	+	+	+	+	+
$E_{\text{beam}} < 1250 \text{ MeV}$	-	-	+	+	+	+	+	+
$E_{\gamma_3} < 200 \text{ MeV}$	-	-	-	+	+	+	+	+
$T_{\pi^0} < 150 \text{ MeV}$	-	-	-	-	+	+	+	+
$110 \text{ MeV}/c^2 < MM_{\omega} - m_{\text{proton}} < 110 \text{ MeV}/c^2$	-	-	-	-	-	+	+	+
$\Theta_{\text{proton}} < 10^\circ$	-	-	-	-	-	-	+	+
cut on the p -band	-	-	-	-	-	-	-	+
$p_{\pi^0\gamma} < 300 \text{ MeV}/c$	-	-	-	-	-	-	-	+

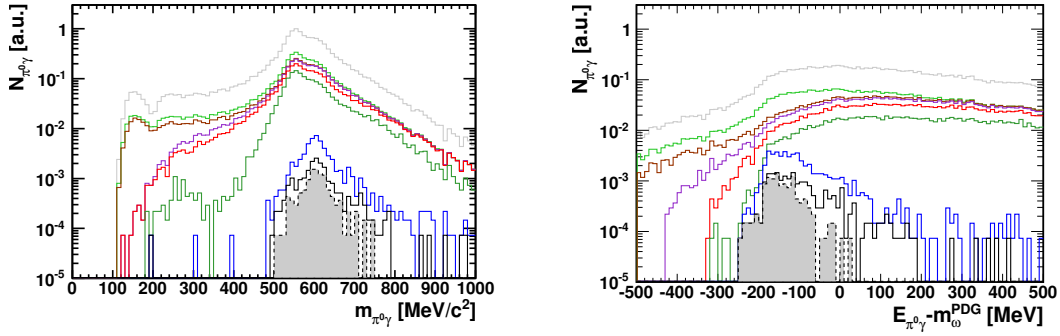


Figure H.6.: Simulation of the $\gamma + {}^{12}\text{C} \rightarrow \eta + p + {}^{11}\text{B}$ channel where one additional neutral hit was produced (See the Section 3.5.4). The three-gamma invariant mass (left figure) and the “kinetic energy” (right figure) distributions are shown after every cut which is listed in Section 3.3.1. An artificial structure appear which peaks sharply around $600 \text{ MeV}/c^2$ on the invariant mass and under -100 MeV on the kinetic energy histograms. The gray shaded area shows the $m_{\pi^0\gamma}$ invariant mass distribution in the lowest studied momentum bin $p_{\pi^0\gamma} < 300 \text{ MeV}/c$.

	□	□	□	□	□	□
$110 \text{ MeV}/c^2 < m_{\gamma\gamma} < 160 \text{ MeV}/c^2$	-	+	+	+	+	+
$E_{\text{beam}} < 1250 \text{ MeV}$	-	-	+	-	+	+
$E_{\gamma_3} < 200 \text{ MeV}$	-	-	+	-	-	-
$T_{\pi^0} < 150 \text{ MeV}$	-	-	+	-	-	-
$110 \text{ MeV}/c^2 < MM_\omega - m_{\text{proton}} < 110 \text{ MeV}/c^2$	-	-	+	-	+	+
$\Theta_{\text{proton}} < 10^\circ$	-	-	+	-	+	+
cut on the <i>proton-band</i>	-	-	+	-	+	+
$E_\gamma < 50 \text{ MeV}$	-	-	-	+	+	+
angular correlations between particles	-	-	-	+	+	+
$\Theta_\gamma > 20^\circ$	-	-	-	+	+	+
$p_{\pi^0\gamma} < 300 \text{ MeV}/c$	-	-	-	-	-	+

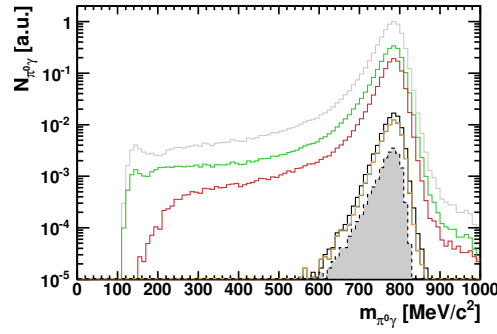


Figure H.7.: Effect of different cuts on simulated ω events.
After small changes ...

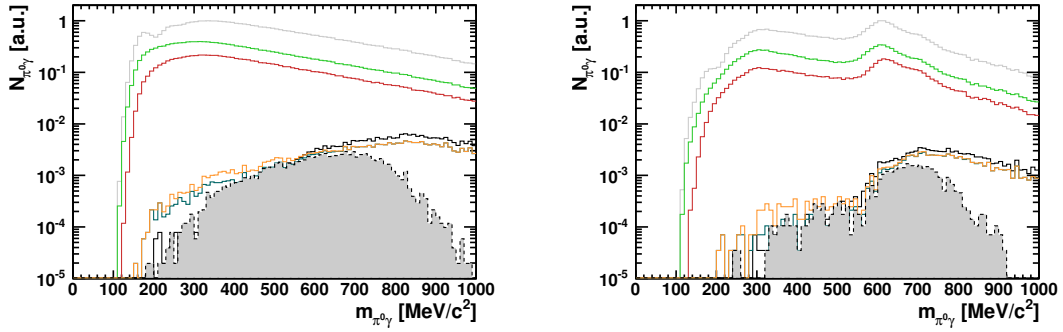


Figure H.8.: Effect of different cuts on simulated $\pi^0\pi^0$ events (left plot).

After cuts a wide, but smooth distribution remains which is taken into account in the fitting procedure (See Section 3.4).

Effect of different cuts on simulated $\pi^0\eta$ events (right plot).

After cuts a wide, but smooth distribution remains which is reduced using a side-band subtraction technique (See Section 3.5.5) and also taken into account in the fitting procedure (See Section 3.4).

H. Kinematical Cuts and Background Rejection

	□	□	□	□	□	□
$110 \text{ MeV}/c^2 < m_{\gamma\gamma} < 160 \text{ MeV}/c^2$	-	+	+	+	+	+
$E_{\text{beam}} < 1250 \text{ MeV}$	-	-	+	-	+	+
$E_{\gamma 3} < 200 \text{ MeV}$	-	-	+	-	-	-
$T_{\pi^0} < 150 \text{ MeV}$	-	-	+	-	-	-
$110 \text{ MeV}/c^2 < M M_{\omega} - m_{\text{proton}} < 110 \text{ MeV}/c^2$	-	-	+	-	+	+
$\Theta_{\text{proton}} < 10^\circ$	-	-	+	-	+	+
cut on the <i>proton-band</i>	-	-	+	-	+	+
$E_{\gamma} < 50 \text{ MeV}$	-	-	-	+	+	+
angular correlations between particles	-	-	-	+	+	+
$\Theta_{\gamma} > 20^\circ$	-	-	-	+	+	+
$p_{\pi^0\gamma} < 300 \text{ MeV}/c$	-	-	-	-	-	+

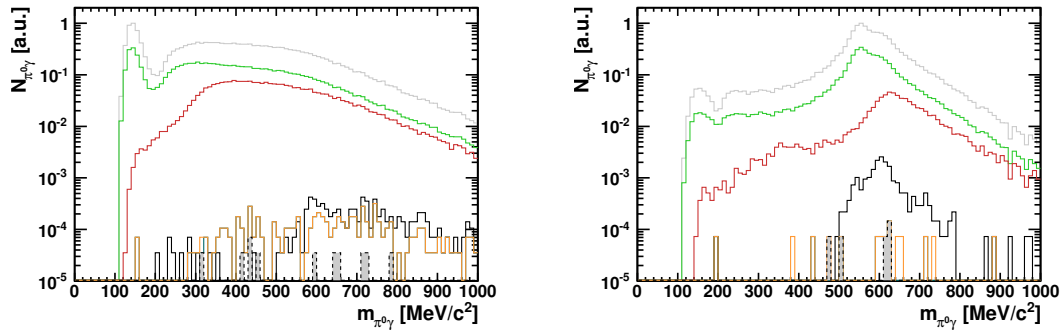


Figure H.9.: Effect of different cuts on simulated π^0 events (left plot).

After the cuts only a small amount of events remains which are distributed smoothly over a wide range of invariant masses.

Effect of different cuts on simulated η events (right plot).

After cuts the sharp peak-like structure disappears.

Bibliography

- [A⁺81] G. Arnison et al. Some Observations on the First Events Seen at the CERN Proton - anti-Proton Collider. *Phys.Lett.*, B107:320–324, 1981.
- [A⁺83a] G. Arnison et al. Experimental observation of isolated large transverse energy electrons with associated missing energy at $\sqrt{s} = 540$ GeV. *Phys.Lett.*, B122:103–116, 1983.
- [A⁺83b] G. Arnison et al. Experimental observation of lepton pairs of invariant mass around 95 GeV/c² at the CERN SPS collider. *Phys.Lett.*, B126:398–410, 1983.
- [A⁺92] T. C. Awes et al. A simple method of shower localization and identification in laterally segmented calorimeters. *NIM A*, 311:130–138, January 1992.
- [A⁺95] S. Abachi et al. Search for High Mass Top Quark Production in \overline{pp} Collisions at $\sqrt{s} = 1.8$ TeV. *Phys. Rev. Lett.*, 74(13):2422–2426, Mar 1995.
- [A⁺04] Bernard Aubert et al. Measurement of branching fractions, and CP and isospin asymmetries, for $B \rightarrow K^*\gamma$. *Phys. Rev.*, D70:112006, 2004.
- [A⁺05] M. Agnello et al. Evidence for a kaon-bound state $K^- p p$ produced in K^- absorption reactions at rest. *Phys.Rev.Lett.*, 94:212303, 2005.
- [A⁺07] M. Agnello et al. Correlated Λd pairs from the $K_{stop}^- A \rightarrow \Lambda d A'$ reaction. *Phys. Lett.*, B654:80–86, 2007.
- [AHA10] Ahmed Ali, Christian Hambrock, and M. Jamil Aslam. Tetraquark Interpretation of the BELLE Data on the Anomalous $\Upsilon(1S)\pi^+\pi^-$ and $\Upsilon(2S)\pi^+\pi^-$ Production near the $\Upsilon(5S)$ Resonance. *Phys. Rev. Lett.*, 104(16):162001, Apr 2010.
- [BFL⁺07] G. Bendiscioli, A. Fontana, L. Lavezzi, A. Panzarasa, A. Rotondi, et al. Search for signals of bound anti-K nuclear states in antiproton He-4 annihilations at rest. *Nucl.Phys.*, A789:222–242, 2007.
- [BM88] Veronique Bernard and Ulf G. Meissner. Properties of Vector and Axial Vector Mesons from a Generalized Nambu-Jona-Lasinio Model. *Nucl.Phys.*, A489:647, 1988.
- [BR91] G.E. Brown and Mannque Rho. Scaling effective lagrangians in a dense medium. *Phys.Rev.Lett.*, 66:2720–2723, 1991.
- [Bry04] Bill Bryson. *A Short History of Nearly Everything*. Black Swan edition, 2004.
- [Bug75] D. V. Bugg. Collision broadening in particle physics. *Nuclear Physics B*, 88:381–410, April 1975.
- [C⁺03] S.K. Choi et al. Observation of a narrow charmonium - like state in exclusive $B^\pm \rightarrow K^\pm \pi^+ \pi^- J/\Psi$ decays. *Phys.Rev.Lett.*, 91:262001, 2003.

- [Cas06] Ralph Castelijns. *Photoproduction of strange mesons and hyperons on the proton*. PhD thesis, Groningen, 2006.
- [CP98] F. E. Close and P. R. Page. Glueballs. *Sci. Am.*, 279:52–57, 1998.
- [Cre] Elsa Crew. Technical overview of ELSA. ELSA web-page.
- [Cre09] Volker Crede. The experimental status of glueballs. *AIP Conf. Proc.*, 1182:471–474, 2009.
- [D⁺03] P. Drexler et al. The new readout electronics for the $ba.f_2$ calorimeter taps. *IEEE Trans. Nucl. Sci.*, 50:969–973, 2003.
- [Dah08] Thomas Dahlke. Bestimmung einer winkelabhangigen Energiekorrekturfunktion fur das TAPS-Kalorimeter des Crystal-Barrel/TAPS-Experimentes an ELSA. Master’s thesis, Bonn, 2008.
- [DLTD⁺85] C.T.A.M. De Laat, A. Taal, W. Duinker, A.H. Wapstra, J. Konijn, et al. Strong Interaction Effects In Pionic Pb-208. *Phys.Lett.*, B162:81–86, 1985.
- [Els07] Daniel Elsner. *Untersuchung kleiner Partialwellenbeitrage in der Nhe dominierenden Resonanzzustande des Protons mit linear polarisierten Photonen*. PhD thesis, Bonn, 2007.
- [Fer87] Thomas Ferbel. *Experimental techniques in High Energy Physics*. Addison-Wesley Publishing, 1987.
- [FP09] Kathrin Fornet-Ponse. *Die Photonenmarkierungsanlage fur das Crystal-Barrel/TAPS-Experiment an ELSA*. PhD thesis, Bonn, PI, 2009.
- [Fri07] Stefan Friedrich. Teilchenidentifikation mittels cerenkov- und szintillationsdetektoren. diploma thesis, Giessen, 2007.
- [Fri10] Stefan Friedrich. Private Communication, 2010.
- [Fri11] Stefan Friedrich. Private Communication, 2011.
- [G⁺94] A. R. Gabler et al. Response of taps to monochromatic photons with energies between 45-mev and 790-mev. *Nucl. Instrum. Meth.*, A346:168–176, 1994.
- [Got04] D. Gotta. Precision spectroscopy of light exotic atoms. *Prog.Part.Nucl.Phys.*, 52:133–195, 2004.
- [Gru06] Marcus Gruner. Modifikation und test des innendetektors fur das crystal barrel experiment. diploma thesis, Bonn, 2006.
- [H⁺77] S. W. Herb et al. Observation of a dimuon resonance at 9.5 gev in 400-gev proton-nucleus collisions. *Phys. Rev. Lett.*, 39(5):252–255, Aug 1977.
- [Har08] Jan Hartmann. Zeitkalibrierung und photonenflussbestimmung fur das crystal-barrel-experiment an elsa. diploma thesis, Bonn, 2008.
- [HFK⁺73] F.J. Hasert, H. Faissner, W. Krenz, J. Von Krogh, D. Lanske, et al. Search for elastic muon-neutrino electron scattering. *Phys.Lett.*, B46:121–124, 1973.

- [Hic05] Ken Hicks. An experimental review of the θ^+ pentaquark. *J.Phys.Conf.Ser.*, 9:183–191, 2005.
- [Hil06] W. Hillert. The bonn electron stretcher accelerator elsa: Past and future. *Eur. Phys. J.*, A28S1:139–148, 2006.
- [Hje09] Frida Hjelm. Private Communication, 2009.
- [HL92] Tetsuo Hatsuda and Su Hounng Lee. Qcd sum rules for vector mesons in nuclear medium. *Phys.Rev.*, C46:34–38, 1992.
- [Hor05] Igor Horn. *The decay of the γp system into the $p\pi^0\eta$ final state*. PhD thesis, Bonn, 2005.
- [IOH⁺00] K. Itahashi, K. Oyama, R.S. Hayano, H. Gilg, A. Gillitzer, et al. Deeply bound pi- states in pb-207 formed in the pb-208(d, he-3) reaction part ii: Deduced binding energies and widths and the pion-nucleus interaction. *Phys.Rev.*, C62:025202, 2000.
- [Jam68] Frederick James. Monte carlo phase space. Technical report, CERN, 1968. CERN-68-15.
- [Jun05] Jorg Junkersfeld. *Photoproduktion von $\pi^0\omega$ am Proton bei Energien bis zu 3 GeV*. PhD thesis, Bonn, HISKP, 2005.
- [K⁺01] K. Kodama et al. Observation of tau neutrino interactions. *Phys.Lett.*, B504:218–224, 2001.
- [K⁺08a] Frank Klein et al. Beam asymmetry in near threshold ω photoproduction off the proton. *Phys.Rev.*, D78:117101, 2008.
- [K⁺08b] M. Kotulla et al. Modification of the omega-meson lifetime in nuclear matter. *Phys.Rev.Lett.*, 100:192302, 2008.
- [KNHO07] M. Kaskulov, H. Nagahiro, S. Hirenzaki, and E. Oset. Study of possible omega bound states in nuclei with the (gamma,p) reaction. *Phys.Rev.*, C75:064616, 2007.
- [KPM10] B. Krusche, F. Pheron, and Y. Magrbhi. Photoproduction of mesons off light nuclei – the search for η -mesic nuclei. *Acta Phys.Polon.*, B41:2249–2260, 2010. * Temporary entry *.
- [Kru95] B. Krusche. Photoproduction of π^0 and η mesons from nucleons and nuclei in the second resonance region. Habilitation, 1995.
- [Kus07] Till Kuske. Private Communication, 2007.
- [Lug07] Stefan Lugert. *In Medium Modification of pion-pairs on deuterium*. PhD thesis, Giessen, 2007.
- [LWF02] M.F.M. Lutz, G. Wolf, and B. Friman. Scattering of vector mesons off nucleons. *Nucl.Phys.*, A706:431–496, 2002.
- [M⁺08] T. Mertens et al. Photoproduction of eta-mesons off nuclei for $e(\gamma) < 2.2$ -gev. *Eur.Phys.J.*, A38:195–207, 2008.
- [Mat07] Stefan Materne. Ein aerogel-cerenkov-detektor fur das cbelsa/taps-experiment. diploma thesis, Bonn, PI, 2007.

- [Mol92] Kees Molenaar. Performance of taps in the tagged photon beam of mami. diploma thesis, Groningen, 1992.
- [MS10] P. Moskal and J. Smyrski. Search for the eta-mesic nuclei by means of cosy-11, wasa-at-cosy and cosy-tof detector systems. *Acta Phys.Polon.*, B41:2281–2292, 2010.
- [MSC⁺01] J.G. Messchendorp, A. Sibirtsev, W. Cassing, V. Metag, and S. Schadmand. Studying the ω mass in-medium in $\gamma + a \rightarrow \pi^0\gamma + x$ reactions. *Eur.Phys.J.*, A11:95–103, 2001.
- [Mul07] Jonas Muller. Bestimmung einer energiekorrekturfunktion für das kalorimeter des crystal-barrel-experiments an elsa. diploma thesis, Bonn, 2007.
- [MW01] E. Marco and W. Weise. Photoproduction of quasibound omega mesons in nuclei. *Phys.Lett.*, B502:59–62, 2001.
- [MYSH⁺10] V.K. Magas, J. Yamagata-Sekihara, S. Hirenzaki, E. Oset, and A. Ramos. Experimental status of deeply bound kaonic states in nuclei. *AIP Conf.Proc.*, 1322:334–338, 2010.
- [N⁺10] K Nakamura et al. Review of particle physics. *J.Phys.G*, G37:075021, 2010.
- [Nan10] Mariana Nanova. Private Communication, 2010.
- [NJH05] H. Nagahiro, D. Jido, and S. Hirenzaki. Formation of mesic nuclei by (gamma,p) reactions. *Nucl.Phys.*, A761:92–119, 2005.
- [NJL61] Y. Nambu and G. Jona-Lasinio. Dynamical model of elementary particles based on an analogy with superconductivity. i. *Phys. Rev.*, 122(1):345–358, Apr 1961.
- [Nov92] R. Novotny. The baf-2 photon spectrometer taps, 1992. Prepared for International Workshop on Heavy Scintillators for Scientific and Industrial Applications: Crystal 2000, Chamonix, France, 22-26 Sep 1992.
- [OB66] F.A. Nikolaev O.V. Bogdankevich. *Methods in Bremsstrahlung Research*. Academic Press, 1966.
- [PAA⁺04] M. Pfeiffer, J. Ahrens, J.R.M. Annand, R. Beck, G. Caselotti, et al. Photoproduction of eta mesic he-3. *Phys.Rev.Lett.*, 92:252001, 2004.
- [Phe10] Francis Pheron. η photoproduction off ^3He ; Search for η mesic nuclei. PhD thesis, Basel, 2010.
- [PZ02] Scholz Povh, Rith and Zetsche. *Particles and Nuclei*. Springer, 2002.
- [RL95] Matthias E. Rößig-Landau. *Photoproduktion von η -Mesonen an komplexen Kernen*. PhD thesis, Universität Giessen, 1995.
- [Rob91] Mathias E. Robig. Eichung des taps-detektorsystems mit hochenstrahlung. diploma thesis, Giessen, 1991.
- [SBF⁺04] T. Suzuki, H. Bhang, G. Franklin, K. Gomikawa, R.S. Hayano, et al. Discovery of a strange tribaryon $s_0(3115)$ in he-4(stopped k-, p) reaction. *Phys.Lett.*, B597:263–269, 2004.

- [Sch04] Christoph Schmidt. *Entwicklung eines neuen Datenakquisitionssystems für das CB-ELSA-Experiment*. PhD thesis, Bonn, 2004.
- [Sei09] Tobias Seifen. Verbesserung der rekonstruktion und entwicklung eines first-level-trigger schemas für das crystal-barrel-kalorimeter. Master's thesis, Bonn, 2009.
- [Sei10] Tobias Seifen. Private Communication, 2010.
- [SFG⁺04] K. Suzuki, M. Fujita, H. Geissel, H. Gilg, A. Gillitzer, et al. Precision spectroscopy of pionic 1s states of sn nuclei and evidence for partial restoration of chiral symmetry in the nuclear medium. *Phys.Rev.Lett.*, 92:072302, 2004.
- [SP01] G.A. Sokol and L.N. Pavlyuchenko. Discovery of eta-mesic nuclei. *arxiv*, 2001.
- [Str98] Philip David Strother. *Design and application of the reconstruction software for the BaBar calorimeter*. PhD thesis, London, 1998.
- [STT07] K. Saito, K. Tsushima, and A.W. Thomas. Nucleon and hadron structure changes in the nuclear medium and the impact on observables. *Progress in Particle and Nuclear Physics*, Volume 58:1–167, 2007.
- [Tho10] Ulrika Thoma. Private Communication, 2010.
- [TLTS98] Kazuo Tsushima, Ding-Hui Lu, Anthony William Thomas, and K. Saito. Are eta and omega nuclear states bound? *Phys.Lett.*, B443:26–32, 1998.
- [TY88] H. Toki and T. Yamazaki. Deeply bound pionic states of heavy nuclei. *Phys. Lett.*, B213:129, 1988.
- [Wen09] Christoph Wendel. The crystal-barrel/taps experiment at elsa: Current status of the csi(tl) calorimeters. *J. Phys. Conf. Ser.*, 160:012006, 2009.
- [Y⁺08] T. Yamazaki et al. First exclusive measurements of the k^-pp state populated in the $pp \rightarrow k^+ \lambda p$ reaction at 2.85-gev. *arXive*, 2008.
- [Yam90] Yamazaki, T. and Hayano, R.S. and Toki, H. and Kienle, P. Pion transfer reaction spectroscopy of inverse kinematics for studies of deeply bound pionic atoms in heavy nuclei. *Nucl.Instrum.Meth.*, A292:619–628, 1990.

List of Figures

1.1.	The lightest pseudoscalar (a) and vector mesons (b) are listed, classified according to their isospin I_3 , strangeness S and electric charge.	7
1.2.	The lightest baryon octet (a) and decuplet (b) are listed, classified according to their isospin I_3 , strangeness S and electric charge.	8
1.3.	Experimentally measured values of the running coupling constant confirm the theoretically expected behavior [N ⁺ 10].	9
1.4.	Masses of some hadrons and their chiral partners. The mass-split between the chiral partners are comparable with the mass of the hadrons.	10
1.5.	In Figure (a) (restored symmetry), the minimum of the potential is right in the center, therefore the ground state is invariant under rotations (no spontaneous breaking of the symmetry), while in Figure (b) (spontaneously broken symmetry) the ground state is located at a finite distance from the center where actually the potential has a local maximum. The red lines represent the radial excitation, the cyan line the rotational excitation. (For more details, see text.)	10
1.6.	Explicit breaking of the chiral symmetry. The thin gray line represents the symmetric Lagrangian. The thin cyan line shows the explicit symmetry breaking term $(-m\bar{\phi}_q\phi_q)$, the black line is the full Lagrangian.	11
1.7.	Dependence of the chiral condensate on density and temperature.	12
1.8.	Prediction of the NJL model for meson masses as a function of the density. The decay width $a_1 \rightarrow \bar{q}q$ is also shown. Beyond a critical density the chiral partners (π, σ) and (ρ, a_1) are degenerate in mass. [BM88]	12
1.9.	(a) Prediction of the <i>QCD Sum Rule method</i> for the $\rho - \omega$ mass as a function of the ρ/ρ_0 . (b) The same figure for the ϕ meson with two typical values of y (strangeness content of the meson). Dotted lines indicates the $K^0 K^0$ and the $K^+ K^-$ thresholds which are the main decay modes of the ψ . [HL92]	13
1.10.	Prediction of the QMC model for the meson masses as a function of the density. [STT07]	14
1.11.	Prediction of the hadronic models for the imaginary part of the ρ - and ω mesons spectral functions in nuclear matter at densities $q = 0$, $q = q_0$ and $q = 2q_0$. [LWF02]	14
1.12.	(a), [Upper two panels] Composition of the local pion-nucleus potential for Pb with Coulomb potential (V_c) and the real and imaginary s-wave potential (V and W , respectively). [Lowermost panels] Pionic density distribution for $1s$ and $2p$ states in Pb . [IOH ⁺ 00] (b), Calculated level scheme of pionic Pb . Level shifts and widths are indicated by the vertical arrows and the shaded areas. The forbidden transitions are labeled with crossed red arrows.	15

1.13. (a), Invariant mass of the back-to-back registered proton- Λ system without acceptance correction (big figure) and with acceptance correction (inlay). The invariant mass, assuming that the process was simply a two-nucleon absorption process, is labeled with red lines.	
(b), Missing mass spectrum of the semi-inclusive proton events with the proton momentum scale. Possible decay modes are also shown at the corresponding mass thresholds [A ⁺ 05, A ⁺ 07].	17
1.14. A resonant structure in the 2D energy correlation histogram (a) suggest the presence of a bound η -mesic state. The total energy distribution of the decay products ($E_{\text{total}}=E_{\pi^+}+E_n$) has a width of about 150 MeV and its position is about $\Delta E=90$ MeV below the position of the $S_{11}(1535)$ [SP01] (b).	17
1.15. Coherent cross section ($\eta \rightarrow 2\gamma$ in red, $\eta \rightarrow 3\pi^0$ in blue) compared to Pfeiffer et al. (black). The coherent and quasi-free thresholds are also shown. [KPM10] . .	18
1.16. Coherent $\eta \rightarrow 2\gamma$ differential cross section in the $(\gamma, {}^4\text{He})$ center of mass frame and two different beam energies. The black line corresponds to the expected angular distribution from proton data where ${}^3\text{He}$ form factor has been taken into account the.	
At an energy $E_\gamma = 644.4$ MeV the measured data shows a forward peaking behavior which is in agreement with the expected distribution for coherent η -production. At lower energies $E_\gamma=602.0$ MeV the measured distribution is flat, which is not in agreement with the expected forward peaking distribution. This behavior suggests two different types of reaction mechanisms [Phe10]	18
1.17. Prediction of the η -nucleus and ω -nucleus potential within the QMC framework for Mg and Pb [STT07]. The blue lines correspond to the density distribution of the nucleus. The black line shows the potential as a function of the radius for ω and η meson. In the right figure two types of QMC predictions are compared. . .	19
1.18. Missing energy spectra at $E_\gamma=2.75$ GeV for the ${}^{12}\text{C}(\gamma, p)\omega^{11}\text{B}$ (a) and for ${}^{40}\text{Ca}(\gamma, p)\omega^{39}\text{K}$ (b) reactions. $ B_p $ is the binding energy of the bound initial proton [MW01]. . .	20
1.19. Missing energy spectra of the ${}^{12}\text{C}(\gamma, p)\omega^{11}\text{B}$ reaction for an attractive (left figure) and a repulsive (right figure) potential [NJH05].	20
1.20. Missing energy spectra of the ${}^{12}\text{C}(\gamma, p)\omega^{11}\text{B}$ reaction at different beam energies and for different directions of the knocked-out proton. The results are convoluted with different experimental resolutions [KNHO07].	21
1.21. The differential cross section of the reaction $\gamma + p \rightarrow \pi^0\gamma + p$ as a function of the $E_{\pi^0\gamma} - m_\omega$ where $E_{\pi^0\gamma} = E_{\pi^0} + E_\gamma$. The spectrum (black, solid line) is obtained using the reconstructed $\pi^0\gamma$ events from the exclusive $\gamma + p \rightarrow \pi^0\gamma + p$ reaction (red, dashed curve) plus an inclusive $\pi^0\gamma$ background which was obtained from events with 4 photons in the final state ($\pi^0\pi^0 \rightarrow 4\gamma$ and $\pi^0\eta \rightarrow 4\gamma$) when one photon is not detected (blue dashed-dotted line). The following cuts were used on the simulated data: $1.5 \text{ GeV} < E_\gamma < 2.6 \text{ GeV}$, $7^\circ < \Theta_p < 14^\circ$, $ \vec{p}_{\pi^0} + \vec{p}_\gamma < 400 \text{ MeV}/c$, $ \vec{p}_{\gamma,3} > 200 \text{ MeV}/c$ and $T_{\pi^0} > 150 \text{ MeV}/c$. The exclusive $\omega \rightarrow \pi^0\gamma$ signal has been convoluted with the experimental resolution of FWHM=50 MeV [KNHO07].	22
1.22. Kinetic energy of the π^0 as a function of the $\pi^0\gamma$ invariant mass. The distorted events via final state interaction are relatively well separated in the $T_{\pi^0} < 150$ MeV region [MSC ⁺ 01].	23

1.23. The $\pi^0\gamma$ invariant mass spectrum before- (left figure) and after (right figure) the mentioned cut on the kinetic energy of the π^0 .	
a, fraction of ω mesons decaying outside the nuclear medium,	
b, fraction of ω mesons decaying inside the nuclear medium into π^0 s and are not distorted by final state interactions,	
c, fraction of ω mesons decaying inside the nuclear medium into π^0 s which are distorted by final state interactions.	
[MSC ⁺ 01]	23
1.24. The ω meson, which was produced via recoil-free photoproduction can be bound inside the nucleus. The bound state can be registered either via the decay of the bound ω meson into $\pi^0\gamma$ final state (three photons and one proton are in the final state, brown dashed line) or if a nucleon absorbs the ω meson producing a baryonic excitation which decays into a meson-proton final state where the meson can be either π^0 or η (two photons and two charged hits in the final state, dark blue dashed-dot line).	24
2.1. Floor-plan of ELSA	27
2.2. Energy coverage of the tagger. The shaded energy regions are not tagged.	28
2.3. Tagger magnet (red block) and the 96 partly overlapping scintillator taggerbars. The electrons arrive from the upper corner on the right and deflect toward the scintillator bars	29
2.4. CAD drawing of the beam dump	30
2.5. CAD drawing of the γ Intensity Monitor.	31
2.6. CAD drawing of the Crystal Barrel detector	33
2.7. The construction of one module of the Crystal Barrel	33
2.8. The Inner detector	33
2.9. Arrangement of the layers of the Inner Detector	33
2.10. CAD drawing of the FWPlug detector	34
2.11. The TAPS module consists of a BAF ₂ crystal and a plastic veto.	35
2.12. Arrangement of the crystals in the MiniTAPS Wall. One crystal is removed for the center of the setup. Through this hole photons which did not generate hadronic reactions will leave the setup.	36
2.13. Aerogel Cherenkov detector installed in Bonn	37
2.14. The Aerogel Cherenkov detector. The aerogel tiles and some of the PMTs can be seen.	38
2.15. Readout of the MiniTAPS detector	39
3.1. Time calibration Demo	45
3.2. Illustration of the time-walk effect. The red line shows the response signal of a low-energetic event crossing the threshold later than the high energetic blue signal.	46
3.3. $\Delta t_{FWPlug-Tagger}$ before and after applying a time-walk correction for γ s from π^0	47
3.4. The energy calibration of the tagger. The various data points correspond to the measurements with different beam energies.	48
3.5. The position of the pedestal peak and the temperature of the hall in a 16-day-period. Both the temperature and the pedestal position show a 24-hours period. The red dots shows the position of the pedestal, the green dashed line corresponds to the temperature.	49

3.6. Typical cosmic spectrum from MiniTAPS. The pedestal peak (0 MeV-energy peak), the CFD threshold and the minimum ionizing of cosmic muons are clearly recognizable.	50
3.7. Time calibration Demo	52
3.8. Position of the π^0 peak in the Crystal Barrel after repeated iterations [Jun05] . . .	53
3.9. The position of the π^0 (left) and η (right) before (green line)and after (red line) polynomial calibration. The position of the pion is unchanged, while the position of the η is shifted down roughly by 10 MeV to the nominal mass of the η mesons.	54
3.10. Final check of the energy calibration	55
3.11. Invariant mass of π^0 s and η s as a function of their momenta. The error bars show not the fitting error but the σ of the fitted peak. The invariant masses are stable within $\pm 2\%$ in the momentum range of $100 \text{ MeV}/c \leq p_{\gamma\gamma} \leq 1700 \text{ MeV}/c$	56
3.12. Calibration of the LED threshold. On the left side the solid line illustrates the energy distribution with a very low LED thresholds, the pink area shows the energy distribution with a higher threshold. On the right side the ratio of the two spectra is shown.	57
3.13. Separation of two PEDs in a multi-PED cluster by using exponential functions to describe the lateral shower distributions [Sei09].	58
3.14. Schematic drawing of the MiniTAPS forward wall located at a distance R behind the target. A systematic error is introduced in the position determination (dashed line) if a photon arrives askew and, due to the tilted shower development, the position appears at $X + dX$ from the beam axis while the real distance is X . The reconstruction routine corrects this effect by approximating the shower maximum in Z which depends on the energy of the photon.	60
3.15. The reconstructed hit position before and after using the correction function in MiniTAPS. The X and Y axes are expressed in radian ($x \approx X * R$, where R is set to 210 cm) and the color code marks the difference between the generated and reconstructed angles (for more details [Sei09]).	61
3.16. Relativistic $\beta = v/c$ for different particles as a function of the kinetic energy. In the shaded area particles generate signal in the Cherenkov detector.	62
3.17. Time-of-Flight of the charged particles is plotted as a function of their deposited energy in the MiniTAPS. The particles, which entered into this plot did not fire the Aerogel Cherenkov detector to ensure that the registered particle is a proton. The three labeled regions are discussed in the text. The fast particles with small energy deposit ($E_{\text{MiniTAPS}} < 100 \text{ MeV}$ and $\text{ToF} \approx 0 \text{ ns}$) are misidentified electrons/positrons or photons.	63
3.18. Time-of-Flight versus deposited energy in the MiniTAPS for charged particles with different conditions.	64
3.19. Multiplicity of the Tagger before (red) and after (black) the coincidence timecuts on the detectors.	65
3.20. The time difference spectrum between a detector and the tagger spectrum. The blue shaded area shows the random coincidences, the red the real ones.	65
3.21. Flow chart of the random subtraction technique.	65

3.22. GEANT simulation of quasi-free ω production shows the presence of merged photons (3.22a) and split-offs (3.22b). 3.22a: In the analyzed events-class only 2 neutral and one charged hits were registered. The invariant mass of the two photons shows a peak around the ω -mass. (The black line is the data, the green one is the contribution of the real two-gamma events, the blue one is the difference of the two histograms). 3.22b: In the analyzed events 4 neutral and one charged hits were registered. The invariant mass of four photons shows a peak around the ω -mass. Roughly 5% of the generated ω events are affected by merged photons, and roughly the same amount of ω events are affected by split-offs (with the threshold values listed in the Table 3.5).	67
3.23. There are 3 possible combinations of two photons out of three. On the X-axis the number of 2γ combination is shown which falls into the $110 \text{ MeV} < m_{\gamma\gamma} < 160 \text{ MeV}$ mass range. The number of $\pi^0\gamma$ events and ω s as a function of the π^0 multiplicity are also shown.	69
3.24. Registered number of particles (both charged and neutral) as a function of the polar angle in the lab system. The increased yield to forward angles (small Θ corresponds to the beam direction) is due to the Lorentz boost. At backward angles electromagnetic noise can be seen from the beampipe. All signals from the most backward angles were discarded.	72
3.25. The data are processed sequentially: First the reconstruction and the preselection are made. After “filtering” the preselected data, only a specialized event class is stored which will be processed further. The final analysis runs more than 50 times faster if only the filtered event class is processed, compared to the processing time of the raw data.	72
3.26. Missing mass as a function of invariant mass of the $\pi^0\gamma$ for simulated ω events (a) and for measured data (b). A strong contribution of the background events can be seen at larger missing masses than the m_{proton} and at smaller invariant masses than m_{ω}^{PDG}	73
3.27. The invariant mass spectrum of the 3-photon events of the measured data after every used cuts.	74
3.28. (a): A visualization of the 2D representation of the data. The background yields in the projections are equal. (The signal yields are equal, too.) (b): The 2D representation of the data after the mentioned cuts. Finally cuts were made on the momentum of the reconstructed data. The cuts are also shown on the plot.	75
3.29. Recoilless photoproduction of mesons on ^{12}C . Calculation of the momentum transfer as a function of the photon beam energy is shown for the η and ω mesons. Different ejection angles of the proton in ω meson production is also taken into account.	77

3.30.	The effect of the Fermi momentum on the $p_\omega - E_{\text{beam}}$ correlation. The pink plot shows the result of the calculation without Fermi-smearing. The proton is knocked out to the $\Theta_p < 1^\circ$ direction. The red distribution shows the result also without Fermi smearing but the proton goes into the $1^\circ < \Theta_p < 10^\circ$ direction (this is the Θ -range covered by the Mini-TAPS) The gray plot shows the same situation as the pink one, but the target nucleon carries Fermi momentum. The black plot shows a calculation with Fermi-distribution and the proton going into the $1^\circ < \Theta_p < 10^\circ$ direction. The plot shows two different branches of the produced mesons with a separation around $p_\omega = 500 \text{ MeV}/c$. The two branches correspond to the mesons which are going “forward” (into the direction of the beam) and “backward” (opposite to the beam direction) in the Center of Mass (CM)-system.	78
3.31.	The correlation between the momentum of the ω and the Θ angle of the knocked-out proton for given beam energy ranges. The upper two figures show kinematical simulations. The light-colored part of the plot shows the solution of the equations when the proton is going forward in the CM system. The detector resolution plays only a minor role.	79
3.32.	The <i>Time of Flight</i> of the forward going proton as a function of the momentum of the produced ω meson. The simulation shows that the majority of the produced ω mesons are in coincidence with a fast proton with small ToF (large kinetic energy).	80
3.33.	Used angular distribution and Θ_ω distribution	81
3.34.	The plot illustrates the simulates background channels where 3 neutral hits were registered in the final state. The figures shown the invariant masses of the registered three neutral hits (treated as photons), where the invariant mass of two neutral hits gives the mass of the π^0 meson. (See the text for details.)	83
3.36.	Both the $\pi^0\eta \rightarrow 4\gamma$ and the $\eta \rightarrow 2\gamma$ channels show a band-like structure on the two-gamma invariant mass vs. three-gamma invariant mass histogram. This structure appears as a peak on the three-gamma invariant mass spectrum.	84
3.37.	Invariant mass distributions of the $\pi^0\gamma$ events coming from $\pi^0\pi^0$ (a) and $\pi^0\eta$ (b) events after loosing one photon. The filled gray distribution shows the distribution after applying all the analysis cuts (see Section 3.3.1) included the momentum cut $p_{\pi^0\gamma} \leq 300 \text{ MeV}/c$. The color code is described in the Appendix H.	85
3.38.	Invariant mass distributions of the $\pi^0\gamma$ events coming from π^0 (a) and η (b) events after a split-off. The filled gray distribution shows the distribution after applying all the analysis cuts (see Section 3.3.1) included the momentum cut $p_{\pi^0\gamma} \leq 300 \text{ MeV}/c$. The color code is described in the Appendix H.	85
3.39.	$m_{\pi^0\gamma}$ invariant mass spectra for different reaction after registering only 3 photons in the final state simulated with the GiBUU event generator and reconstructed by GEANT3 [Fri10, Nan10]	86

3.40. (a) In the two-photon invariant mass spectrum the π^0 -peak ($110 \text{ MeV}/c^2 < m_{\gamma\gamma} < 110 \text{ MeV}/c^2$, red shaded area) and the sideband ($40 \text{ MeV}/c^2 < m_{\gamma\gamma} < 90 \text{ MeV}/c^2$ and $170 \text{ MeV}/c^2 < m_{\gamma\gamma} < 220 \text{ MeV}/c^2$, blue shaded area) is shown. (b) The 3-gamma invariant mass spectra for the π^0 -peak (red curve) and the sideband (blue curve) and the difference between them (black curve). The sideband subtraction technique was used in the analysis of the neutral decay channel ((a), (b)) and also in the analysis of the conversion channel (c).	87
3.41. Integrated cross section of the contributing background channels and the signal channel in photoproduction on the proton ($\gamma + p \rightarrow X + p$) [Tho10].	88
3.42. The correlation between the invariant mass of three photons and the energy of each photons. A vertical structure is visible due to photon split-offs (see the text for details). A diagonal structure can also be seen. If the lower part of the distribution is removed, as indicated by the white line, a peak-like structure will be produced via the remaining part of the diagonal structure.	89
3.43. GEANT simulation shows the correlation between the relative angle between neutral hit-pairs and the energy of the contributing photons in $\gamma + p \rightarrow \pi^0 + p$ (a) reaction when three neutral- and a charged hit were registered. As a comparison the same correlation is shown for $\gamma + p \rightarrow \omega + p$ (b).	90
3.44. GEANT simulation shows the correlation between the relative angle between neutral hit-pairs and the opening angle between the third neutral hit and the charged hit. Characteristic difference can be seen between these planes in case of $\gamma + p \rightarrow \pi^0 + p$ (a) and $\gamma + p \rightarrow \omega + p$ (b) events. (The simulation of the ω meson production includes a realistic angular distribution.)	91
3.45. Simulation shows the effect of the kinematical cuts on the π^0 spectrum where an additional neutral hit was registered. The black histogram is the E_γ vs. $m_{\gamma\gamma}$ distribution without any cut applied. The red dots shows the remaining distribution after the kinematical cuts applied in the analysis (See Section 3.3.1). The cyan dots show the distribution of the events after using the additional cuts listed above. The overall yield of this type of events did not change dramatically, but the bump-like structure around $600 \text{ MeV}/c^2$ was removed. For more comparison, see the Appendix H.	91
3.46. Simulation of the conversion channel. The figure (a) shows the opening angle distribution between the proton and the π^0 under the conditions listed at the beginning of this chapter. The red line shows the result of the kinematical simulation, the black one represents a full particle tracking with GEANT. The figure (b) shows the correlation of momenta between the proton and the neutral pion. The scatter plot and the black line show the result of a full particle tracking using GEANT. In comparison, the red dashed line dashed line represents the contour of the correlated momenta using a kinematical simulation, where the effect of the holding structure cannot be seen.	93

3.47. GEANT simulation to demonstrate the effect of the holding structure on the reconstruction of the momentum of the protons. The red scatter plot shows the correlation between the real kinetic energy and the measured one (this is the measured quantity). The black one shows the correlation between the real momentum of the proton and its reconstructed momentum. Protons with small energy ($\lesssim 90$ MeV) will be absorbed in the holding structure of the detector, and will not reach the crystals. A proton with high energy ($\gtrsim 400$ MeV) will become a minimum ionizing particle and will not deposit all its kinetic energy in the detector material.	93
3.48. The correlation between the generated (real) and reconstructed proton momenta when the proton is produced by a conversion of the ω meson to a π^0 -proton pair via resonance excitation and decay (see Section 3.2.5).	94
3.49. The simulation shows the effect of the holding structure of the CB. The real polar angles and momenta of all generated particles is shown by the black scattered plots. The red scattered plot shows them if they are registered (energy was deposited by them in the detectors). If the excited resonance decays into η and proton, most of the produced protons will not reach the detector, they will not be registered (b). In case of the resonance decays to π^0 and proton, the proton will have a larger average momentum and most of the protons will be detected (a).	95
3.50. Simulation to demonstrate the effect of a misidentified charged particle in the proton detection. In the figure (a) π^+ s were simulated and reconstructed. It can be seen that depending on the assumed mass the measured momentum is changing (black line: the mass of the particle is its nominal mass, blue line: the momentum distribution of the π^+ assuming that the particle is a proton). For more details, see text. In the figure (b) electrons were simulated and reconstructed. The color code is the same as in the other plot. Electrons are not contributing to the minimum ionizing peak.	96
3.51. (a) Momenta of different charged particles (black: proton, brown: π^+ , light blue: electron) when they are reconstructed as a proton. (b) The measured distribution shows a minimum ionizing peak in case of the proton and the π^+ . Electron do not contribute to the minimum ionizing peak, they produce a stronger yield at higher momenta. Besides the minimum ionizing peak scattered events can be seen due to nuclear reactions.	96
3.52. Efficiency of the reconstruction of the $\gamma + p \rightarrow \omega + p$ reaction as a function of the momentum of the ω meson. Only the neutral decay channel of the ω meson is considered, where it decays into the 3γ final state.	97
4.3. One proton was registered in the MiniTAPS (identified by a cut around the <i>proton-band</i>) in coincidence with two photons which form a π^0 meson and one additional charged hit. The relative angle between the charged hit and the π^0 is plotted as a function of the beam energy (a). The two horizontal lines show the borders of the <i>signal</i> region ($120^\circ \leq \text{Angle}_{\pi^0, \text{proton}} \leq 180^\circ$) and the <i>background</i> region ($90^\circ \leq \text{Angle}_{\pi^0, \text{proton}} \leq 120^\circ$). The projected spectra were normalized by the original tagger spectrum (b). The ratio (c) and the difference (d) of the normalized spectra are also shown.	102

4.4.	The 2D representation of the data after all kinematic cuts. The cuts on the momentum are also visualized. Projections onto the X and Y axes gives the invariant mass and kinetic energy distribution, respectively.	104
4.5.	Simultaneous fit of the invariant mass and the kinetic energy spectra in different momentum bins. The blue distribution is the background derived from events with four photons in the final state. The red lines denote the quasi-free ω signals (see Section 3.4). The azure line is the fit of the yield above the background in the lowest momentum bin. The green line is the difference between the data points and the sum of the background and the signal(s) (black line). The measured data in the lowest momentum bin cannot be described only with the four-photon background and ω signal.	105
4.6.	Missing energy spectra of the $^{12}\text{C}(\gamma,p)\omega^{11}\text{B}$ for an attractive potential (see section 1.5.2).	106
4.7.	Energy deposition of charged particles in MiniTAPS as a function of the flight time. The effect of a strict cut on the proton band is illustrated. The black scatter plot shows all proton events in the $\gamma + p \rightarrow \omega + p$ reaction that arrive in the MiniTAPS detector. The red scatter plot shows the identified events in the proton-band. In the proton-band only $\approx 60\%$ of all protons are registered, the rest induces nuclear reactions.	107
4.8.	Simultaneous fit of the invariant mass and the kinetic energy spectra in different momentum bins. Data from GiBUU simulation can be reproduced with 4 photon background and ω signal in every momentum bin. (Color code is described in the caption of the Figure 4.5)	109
B.1.	Trigger-scheme of the TAPS	119
C.1.	Typical rates	121
D.1.	Visualization of a cluster: White boxes denotes the crystals where the energy deposit did not exceed the threshold. The stripped boxes symbolize all the crystals which are firing. The red stripped boxes are the <i>central crystals</i> of the PEDs, where most of the energy is deposited, the area with magenta border is one PED. The area with blue border is one cluster (with two PEDs).	125
G.1.	Two-photon invariant mass versus three-photon invariant mass plot for the simulated $\pi^+ + \pi^0 + n \rightarrow \pi^+ + n + 2\gamma$ final state (Fig. (a)) where the π^+ is misidentified as a proton and the n is misidentified as a photon.. Projection on the two-gamma (Fig. (b)) axis shows a peak at the mass of the mass of the π^0 . The projection on the three-gamma (Fig. (c)) axis shows a smooth distribution.	135
G.2.	Two-photon invariant mass versus three-photon photon invariant mass plot for the simulated $\pi^0 + \pi^0 \rightarrow 4\gamma$ final state (Fig. (a)). Projection on the two-gamma (Fig. (b)) axis shows a peak at the mass of the mass of the π^0 . The projection on the three-gamma (Fig. (c)) axis shows a smooth distribution.	136

G.3.	Two-photon invariant mass versus three-photon photon invariant mass for the simulated $\pi^0 + \eta \rightarrow 4\gamma$ final state (Fig. (a)). Projection on the two-gamma (Fig. (b)) axis shows a peak at the mass of the mass of the π^0 . The projection on the three-gamma (Fig. (c)) axis shows a pronounced structure at roughly $600 \text{ MeV}/c^2$ which can be removed by a side-band subtraction technique (see Section 3.5.5).	137
G.4.	Two-photon invariant mass versus three-photon photon invariant mass plot for the simulated $\pi^0 \rightarrow 2\gamma$ final state (Fig. (a)) where one additional neutral hit was generated. Projection on the two-gamma (Fig. (b)) axis shows a peak at the mass of the mass of the π^0 . The projection on the three-gamma (Fig. (c)) axis shows a smooth distribution.	138
G.5.	Two-photon invariant mass versus three-photon photon invariant mass plot for the simulated $\eta \rightarrow 2\gamma$ final state (Fig. (a)) where one additional neutral hit was generated. Projection on the two-gamma (Fig. (b)) axis shows a peak at the mass of the mass of the π^0 . The projection on the three-gamma (Fig. (c)) axis shows a pronounced structure at roughly $600 \text{ MeV}/c^2$ which can be removed by a side-band subtraction technique and by kinematical cuts (see Section 3.5.5).	139
G.6.	Two-photon invariant mass versus three-photon photon invariant mass plot for the simulated $\omega \rightarrow \pi^0\gamma \rightarrow 3\gamma$ final state (Fig. (a)). Projection on the two-gamma (Fig. (b)) axis shows a peak at the mass of the mass of the π^0 . The projection on the three-gamma (Fig. (c)) axis shows the ω -peak.	140
G.7.	Two photon invariant mass versus 3 photon photon invariant mass (Figure (a)), and its projection to the two-gamma (Figure (c)), and to the three-gamma invariant mass axis (Fig. (b)) for data.	141
H.1.	Simulation of the $\gamma + {}^{12}\text{C} \rightarrow \omega + p + {}^{11}\text{B}$ channel. The three-gamma invariant mass (left figure) and the “kinetic energy” (right figure) distributions are shown after every cut which is listed in Section 3.3.1. The gray shaded area shows the $m_{\pi^0\gamma}$ invariant mass distribution in the lowest studied momentum bin $p_{\pi^0\gamma} < 300 \text{ MeV}/c$	143
H.2.	Simulation of the $\gamma + {}^{12}\text{C} \rightarrow \pi^0 + \pi^+ + n + {}^{11}\text{B}$ background channel where the π^+ is misidentified as a proton, and the neutron is misidentified as a photon (See the Section 3.5.4). Simulation shows the three-gamma invariant mass (left figure) and the “kinetic energy” (right figure) distributions after every cut which is listed in Section 3.3.1. After requiring that the proton should be identified by the cut on the <i>proton-band</i> (See Section 3.2.2) practically there is no intensity remains.	144
H.3.	Simulation of the $\gamma + {}^{12}\text{C} \rightarrow \pi^0 + \pi^0 + p + {}^{11}\text{B}$ channel where one photon from the decay of the π^0 s is lost (See the Section 3.5.4). The three-gamma invariant mass (left figure) and the “kinetic energy” (right figure) distributions are shown after every cut which is listed in Section 3.3.1. The gray shaded area shows the $m_{\pi^0\gamma}$ invariant mass distribution in the lowest studied momentum bin $p_{\pi^0\gamma} < 300 \text{ MeV}/c$	144
H.4.	Simulation of the $\gamma + {}^{12}\text{C} \rightarrow \pi^0 + \eta + p + {}^{11}\text{B}$ channel where one photon from the decay of the π^0 or the η is lost (see the Section 3.5.4). The three-gamma invariant mass (left figure) and the “kinetic energy” (right figure) distributions are shown after every cut which is listed in Section 3.3.1. The gray shaded area shows the $m_{\pi^0\gamma}$ invariant mass distribution in the lowest studied momentum bin $p_{\pi^0\gamma} < 300 \text{ MeV}/c$	145

H.5.	Simulation of the $\gamma + {}^{12}\text{C} \rightarrow \pi^0 + p + {}^{11}\text{B}$ channel where one additional neutral hit was produced (See the Section 3.5.4). The three-gamma invariant mass (left figure) and the “kinetic energy” (right figure) distributions are shown after every cut which is listed in Section 3.3.1. An artificial structure is produced by the cut on the energy of the bachelor photon. The gray shaded area shows the $m_{\pi^0\gamma}$ invariant mass distribution in the lowest studied momentum bin $p_{\pi^0\gamma} < 300 \text{ MeV}/c$	145
H.6.	Simulation of the $\gamma + {}^{12}\text{C} \rightarrow \eta + p + {}^{11}\text{B}$ channel where one additional neutral hit was produced (See the Section 3.5.4). The three-gamma invariant mass (left figure) and the “kinetic energy” (right figure) distributions are shown after every cut which is listed in Section 3.3.1. An artificial structure appear which peaks sharply around $600 \text{ MeV}/c^2$ on the invariant mass and under -100 MeV on the kinetic energy histograms. The gray shaded area shows the $m_{\pi^0\gamma}$ invariant mass distribution in the lowest studied momentum bin $p_{\pi^0\gamma} < 300 \text{ MeV}/c$	146
H.7.	Effect of different cuts on simulated ω events. After small changes	147
H.8.	Effect of different cuts on simulated $\pi^0\pi^0$ events (left plot). After cuts a wide, but smooth distribution remains which is taken into account in the fitting procedure (See Section 3.4). Effect of different cuts on simulated $\pi^0\eta$ events (right plot). After cuts a wide, but smooth distribution remains which is reduced using a side-band subtraction technique (See Section 3.5.5) and also taken into account in the fitting procedure (See Section 3.4).	147
H.9.	Effect of different cuts on simulated π^0 events (left plot). After the cuts only a small amount of events remains which are distributed smoothly over a wide range of invariant masses. Effect of different cuts on simulated η events (right plot). After cuts the sharp peak-like structure disappears.	148

List of Tables

1.1.	An overview of particles and antiparticles. Here, b is the baryon number and l the lepton number. There are three different lepton numbers, one for e , μ and τ , which are separately conserved. I is the isospin, with I_Z the projection of the isospin on the third axis, S the strangeness, C the charmness and B the bottomness. The antiparticles have an opposite charge. The existence of all elementary particles, but the Higgs-boson, has been demonstrated experimentally.	6
2.1.	Properties of the slow- and fast component of the BaF ₂ scintillation light The light output is compared to the light output of NaI(Tl)	35
3.1.	Three energy ranges with the corresponding width of the energy bins for the time-walk correction.	47
3.2.	Achieved time resolutions for the different detector parts.	48
3.3.	Differences between selection criteria for the energy calibration of CB/FWPlug and MiniTAPS	53
3.4.	Timecuts	66
3.5.	The thresholds in the different detectors. The software-threshold on crystals of the innermost two rings of the MiniTAPS was set to 17 MeV, for the rest of the crystals it was set to 13 MeV. The hardware thresholds are slightly below these values. . .	68
3.6.	The $\omega \rightarrow \pi^0\gamma$ channel was simulated with the Fermi motion of the target nucleon, the Θ dependence of the photo-production of the ω was taken into account. In the case of the background channels only the Fermi momentum distribution of the target nucleons was modeled.	82
4.1.	Parameters of the fit of the data after applying the cuts listed in Section 3.3.1. . .	104
4.2.	Parameters of the fit of the data after applying the cuts listed in Section 3.3.1. . .	110
4.3.	Parameters of the fit of the data for $0 \text{ MeV}/c \leq p_{\pi^0\gamma} \leq 300 \text{ MeV}/c$ after applying the cuts to reduce the contribution of the background channels (see Section 3.5.5). The third column the gives the ratio of the fitted values without and with applying the extra cuts to remove the background contribution.	111
C.1.	Main parameters during the March 2007 beamtime.	122
C.2.	(a) Four-particle trigger, (b) Meaning of the used abbreviations, (c) Three-particle trigger	122

Acknowledgement

First of all, I am heartily thankful to my supervisor, Prof. Dr. Volker Metag for his encouragement, support and endless patience from the beginning to the end of my work.

I am also deeply grateful to Dr. Reiner Novotny who taught me so much.

Thanks to Mariana and Frida for their continuous support, help and friendship. Thanks to Stefan for the lots of work he did for me.

Thanks to the PANDA-boys (Daniel, Marcus, Till, Tobi) for the relaxing minutes (hours?) that I spent on their couch. Especially, thanks to Till not only for the Aerogel detector but for the conversations during the long-long night-shifts.

Thanks to Valera for the long discussions about physics, life and everything.

Thanks to the Mainzelmännchen (“Eagle-eyed” Micha (who spotted many of my spelling mistakes . . . and many more ☺!), Henning, Boris) for their help and kind support. Especially thanks to Boris for the fruitful discussions, the millions of little helps and his unbreakable optimism.

Thanks to the postdocs (Peter, Martin and Volker Hannen) for the discussions during the travels between Gießen and Bonn and for the introduction to the art of the TAPS-handling.

Also thank for the Stefan, Raplf, David and Björn for the sausages and the beers, to Werner and Jürgen the smiles and laughs and Anita who always made me remembered to my bureaucratic tasks. Thanks to the Electronic Workshop for the patience and the boards. And many thanks to Johannes.

Than I would like to thank to Vahe Sokhoyan (HISKP), Daniel Elsner (PI) and everyone else in Bonn who helped me with work and friendship.

I cannot forget the “*local*”-group, the gießener Hungarian community (Kolbász also belongs here!), all my teachers and friend who believed in me (Endre, Dezső, Gábor, Jóska, Sanyi and others).

At the end I have to thank to my parents and for my sister for the kicks, the hugs and the continues love I received from them.

Last but not least I would like to tell a big-big thank to my wife who was and is a true partner in everything, including supporting my work, correcting my English, pushing me forward and simply being there.

Erklärung

Hermit versichere ich, dass ich diese Arbeit selbständig verfasst und keine weiteren Quellen und Hilfsmittel außer den genannten verwendet habe. Diese Arbeit wurde bisher keine anderen Prüfungsbehörde vorgelegt und auch noch nicht veröffentlicht.

Károly Makónyi